

Functional hydrogels: ferrogel thin films

Dissertation

zur Erlangung des Grades
“Doktor der Naturwissenschaften”
im Promotionsfach Chemie

am Fachbereich Chemie, Pharmazie und Geowissenschaften
der Johannes Gutenberg-Universität in Mainz

vorgelegt von

Núria Queraltó Gratacòs
geboren in Barcelona, Spain

Mainz, 2010

Die vorliegende Arbeit wurde am
Max-Planck Institut für Polymerforschung in Mainz,
und am Stanford University in California
in der Zeit von November 2006 bis Mai 2010 angefertigt.

*to Mariona,
whose light vanished
in a cold winter night;*

sempre et duré dins meu

Abstract

The combination of magnetic nanoparticles (NPs) with thermoresponsive polymer systems leads to the formation of composite materials with a wide range of potential applications such as magnetic separation, drug release systems, sensors and actuators. The response time to external stimuli can be reduced by the reduction of the hydrogel matrix volume since swelling is a diffusion-controlled phenomenon.

In this work, a UV-crosslinkable polymer, consisting of N-isopropylacrylamide, methacrylic acid and the UV-crosslinker 4-benzoylphenyl methacrylate was used in conjunction with magnetite nanoparticles. The temperature and pH influence on the gel were studied by means of nanomechanical cantilever sensors (NCS) and surface plasmon resonance with optical waveguide mode spectroscopy (SPR/OWS). The obtained values of polymer pKa and lower critical solution temperature (LCST) were in agreement with literature values. It was found that higher crosslinked networks exhibit a lower LCST. NCS provided additional insight into polymer physics of the hydrogel showing stresses caused by skin-effect in the heating of higher crosslinked networks.

Fe₃O₄ nanoparticles were synthesized from iron(III) acetylacetonate using a high temperature reaction. By changing the reaction temperature a control on the NP size was achieved from 3.5 nm to 20 nm with a size distribution between 0.5 and 2.5. In addition, magnetite nanoparticles were functionalized to allow stabilization in aqueous environment through two strategies: a silica shell or a citric acid surfactant; thus, opening the door for the nanoparticles to bioapplications. The magnetic nanoparticles were analyzed by transmission electron microscopy (TEM) and superconductive quantum interference device (SQUID). A size dependence of the magnetic properties was observed and a superparamagnetic character was confirmed. In addition, the heat loss of the nanoparticles exposed to an AC magnetic field was investigated.

A ferrogel was formed through the mixing of magnetite nanoparticles, functionalized with benzophenone for the first time, and PNIPAAm polymer. The polymer was spincoated into a thin film, whose behavior in front of a magnetic field gradient was investigated. The results showed a small plastic response. The results were compared to theoretical calculations, which explained the different response in comparison with bulk ferrogels.

Table of contents

ABBREVIATIONS	I
<hr/>	
1. INTRODUCTION	1
<hr/>	
1.1. HYDROGELS	1
1.2. RESPONSIVE HYDROGELS	2
1.3. PNIPAAm THIN FILMS	5
1.4. FERROGELS	6
1.5. MAGNETISM IN MAGNETIC NANOPARTICLES	7
1.6. AIM AND OUTLINE	10
2. METHODOLOGY	13
<hr/>	
2.1. NANOMECHANICAL CANTILEVERS SENSORS	13
2.2. SPR/OWS	17
2.3. TRANSMISSION ELECTRON MICROSCOPY	24
2.4. ELLIPSOMETRY	26
2.5. UV/VIS/NIR SPECTROSCOPY	28
2.6. SUPERCONDUCTING QUANTUM INTERFERENCE DEVICE	29
2.7. HYPERTHERMIA SETUP	30
2.8. CONTACT ANGLE	31
3. MATERIALS	33
<hr/>	
3.1. PNIPAAm	33
3.1.1. BENZOPHENONE SYSTEM	33
3.1.2. DIMETHYLMALEIMIDE SYSTEM	34
3.1.3. GRAFTING	35
3.1.4. PHOTOCROSSLINKING	37
3.2. NANOPARTICLES	39
3.2.1. MAGNETITE NANOPARTICLES	39
3.2.1.1. Synthesis	40
3.2.1.2. Silica shell	44
3.2.1.3. Silane (BZ / APTES)	47
3.2.1.4. Citric acid	49

4. RESULTS AND DISCUSSION **51****4.1. THIN FILM HYDROGEL STUDY** **51**4.1.1. INTRODUCTION 514.1.2. EXPERIMENTAL PROCEDURES 544.1.3. RESULTS AND DISCUSSION 574.1.3.1. Benzophenone silanization optimization 574.1.3.2. Effects of the pH 594.1.3.3. Transition temperature measurements 674.1.4. CONCLUSIONS 73**4.2. MAGNETITE NANOPARTICLES** **75**4.2.1. INTRODUCTION 754.2.2. EXPERIMENTAL PROCEDURES 774.2.3. MAGNETIC PROPERTIES 784.2.3.1. Magnetization curves 784.2.3.2. Hyperthermia experiments 834.2.3.3. Nanoparticle self-assembly 884.2.4. CONCLUSIONS 90**4.3. FERROGEL STUDY** **91**4.3.1. INTRODUCTION 914.3.2. EXPERIMENTAL PROCEDURES 934.3.3. RESULTS AND DISCUSSION 944.3.3.1. Ferrogel preparation 944.3.3.2. UV-VIS study on binding of nanoparticles to the hydrogel 954.3.3.3. Refractive index variation with amount of nanoparticles 1044.3.3.4. Effect of magnetic nanoparticles on LCST 1084.3.3.5. Effect of nonuniform magnetic field on ferrogel 1114.3.3.6. Theoretical estimation 1184.3.4. CONCLUSIONS 122

5. SUMMARY **123**

APPENDICES **125****A.1. CHARACTERIZATION OF SILICA NANOPARTICLES FUNCTIONALIZED WITH APTES** **125**

A.1.1. LINK TO HYDROGEL	126
A.2. ANALYSIS OF PLASMA POLYMERIZED PENTAFLUOROPHENYL METHACRYLATE BY MEANS OF NCS	129
<u>BIBLIOGRAPHY</u>	147
<u>PUBLICATIONS AND PRESENTATIONS</u>	167

Abbreviations

A_0	initial amplitude
AAEM	acetoxyethyl methacrylate
ac	alternate current
AFM	atomic force microscopy
AIBN	2,2'-Azobis(isobutyronitrile)
AMF	Alternating magnetic field
AOI	angle of interest
APTES	3-aminopropyltriethoxysilane
B	Applied magnetic field
BSA	bovine serum albumin
BZ	benzophenone
BZ-silane	4-(3-triethoxysilyl)propoxybenzophenone
BZ-thiol	4-(3-mercaptopropoxy)benzophenone
χ_0	equilibrium susceptibility
CCD	charged coupled device
D	dissipation factor
dc	direct current
DLS	dynamic light scattering
DMI	dimethylmaleimide
DMIAAm	N-[2-(3,4-dimethyl-2,5-dioxa-2,5-dihydro-pyrrol-1-yl)-ethyl-acrylamide
f	frequency
FAD	flavin adenine dinucleotide
FC	field cooling
FDA	Food and Drug Administration
FITC	Fluoresceine isothiocyanate
GPC	gel permeation chromatography
H_0	field amplitude
Hc	coercivity
HOMO	highest occupied molecular orbital
HRTEM	high resolution transmission electron microscopy
I	detected intensity
I_0	Intensity incident light
I_{max}	maximum supercurrent in superconductor
K	Anisotropy constant
LCST	lower critical solution temperature
LUMO	lowest unoccupied molecular orbital
M-G	Maxwell-Garnett
μ_0	magnetic permeability of vacuum
MAA	methacrylic acid
MABP	4-benzoylphenyl methacrylate
MG	magnet
MPIP	Max Planck Institute for Polymer Research
Mr	remanent magnetization

Ms	saturation magnetization
MWCO	molecular weight cut off
NCS	nanomechanical cantilever sensors
NIR	near infrared
NMR	nuclear magnetic resonance
NP	nanoparticles
NPs	nanoparticles
n_r	refractive index
OA	oleic acid
OVS	optical waveguide spectroscopy
PDI	polydispersity
PDMS	poly(dimethyl siloxane)
PED	photocrosslinking energy dose
PEG	polyethyleneglycol
PHEMA	poly(hydroxyethyl methacrylate)
PNIPAA _m	poly(N-isopropylacrylamide)
PS	polystyrene
PSD	position sensitive detector
PSP	plasmon surface polaritons
PVA	polyvinylalcohol
QCM-D	Quartz Crystal Microbalance with Dissipation monitoring
rf	radio frequency
RLC	resistor inductor capacitor (resonant circuit)
ROI	region of interest
SAED	Selected Area Electron Diffraction
SAM	self-assembled monolayer
SAR	Specific absorption rate
SEM	scanning electron microscopy
SFM	scanning force microscopy
SPR	surface plasmon resonance spectroscopy
SQUID	Superconducting quantum interference devices
τ	characteristic decay time in Dissipation measuring
T	temperature
T_B	Block temperature
TEM	transmission electron microscopy
TEOS	tetraethylorthosilicate
THF	tetrahydrofuran
TIR	total internal reflection
TM	transversal magnetic
UCST	upper critical solution temperature
UV	ultraviolet
V_H	hydrodynamic volume
VIS	visible
VLC	N-vinylcaprolactam
V_M	magnetic volume
W	watts

ZFC	zero field cooling
$\hat{\alpha}$	dielectric constant
\ddot{o}	phase

1.INTRODUCTION

1.1. Hydrogels

Polymers are materials made of long molecular chains, so-called macromolecules. In the beginning of the 20th century, polymers were considered complex colloid system.¹ It was not until the early 1920s that the German physical chemist H. Staudinger suggested that polymer molecules were chains.² He received the Nobel Prize in Chemistry in 1953 for this work.³ Polymers are part of our everyday life. Some of them come from nature, like natural rubber -extracted from rubber trees and used in tires- or cellulose -used for paper-. Often they are produced by humans; for instance plastic bags, made out of polyethylene or polylactic acid (which is biodegradable); or some clothes are fabricated with polyamides (nylon) or polyvinyl chloride. In some cases, polymers can absorb high amounts of water and therefore can be used in applications such as diapers (polymethylacrylate) or soft contact lenses (polyacrylamide, poly(hydroxyethyl methacrylate)). This last kind of polymers are called hydrogels and can be defined as hydrophilic polymer networks that may absorb from 10-20% (an arbitrary limit) up to thousands of times their dry weight in water.⁴

A three dimensional hydrogel network is formed by crosslinked polymer chains; the interaction between individual chains can be based on covalent bonds, hydrogen bonding, ionic interactions, van der Waals interactions and physical entanglements.⁵ Covalent links are stable whereas the other interactions may degrade and eventually disintegrate and dissolve. Due to the variety in crosslinking mechanism, there are many known types of hydrogels. Polyelectrolytes are a good example of ionic interactions. When they are combined with another ion of the opposite charge, a hydrogel may form.⁶ Polyethylene glycol (PEG) is a widely used hydrogel due to the nontoxicity and the approval from US Food and Drug Administration for some clinical trials. It can be crosslinked through photopolymerization using acrylate-end monomers^{7, 8} Another widely used hydrogel is poly(hydroxyethyl methacrylate) (PHEMA), which due to its mechanical properties, high transparency and stability in water has been used in many bioapplications such as contact lenses.⁹ When biodegradable non-toxic hydrogels are in need, polysaccharides are a good choice. An example is dextran polymers, which are widely used for biomedical applications.¹⁰ In general, as the previous examples

show, most of the applications regarding the use of hydrogels are bioapplications, because of the high water content. The properties of hydrogels have been reviewed by several authors.^{4, 11}

1.2. Responsive hydrogels

By tailoring their structure, hydrogels can interact with the environment in a smart way. These are the so-called *smart*, *intelligent* or *stimuli-responsive* polymers.⁵

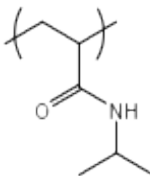
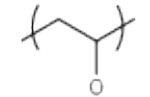
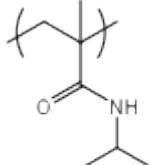
Different stimuli can cause a response in hydrogels: temperature, pH, electric field, solvent composition, light, ionic strength, pressure, or magnetic fields. The response mechanism depends on the chemical structure of the polymer. A clear example are pH-sensitive hydrogels, which contain ionizable monomer units (i.e., acid or basic comonomers). When an acid comonomer is present at a high pH, the polymer will swell due to the repulsive interactions between the negatively charged anions. On the other hand, a base-composed hydrogel will swell at low pH. Hence, the mechanism in this case is based on repulsive interactions. Acrylic acid and methacrylic acid or vinylacetic acid monomers are among the acid monomers that confer pH sensitive behavior.^{12, 13} Acrylamide or 2-vinylpyridine are basic monomers responsible for the swelling at low pHs due to the protonation of the basic nitrogen.¹⁴

Likewise, changing the salt concentration (i.e. ionic strength) of the solution can alter the solubility of the polymer. Park and Hoffman were the first to report a salt induced phase transition of a nonionic poly N-isopropylacrylamide (PNIPAAm) gel in aqueous solution.¹⁵ The salting out effect was explained through an influence of sodium chloride in inter- and intramolecular hydrogen-bonding and polar interactions, as well as hydrophobic interactions associated with water molecules. Later on, other groups studied the effect of NaCl and other salts and concluded that collapse of the networks due to the different types of perturbation (i.e., temperature, salt) are induced by the same mechanism: hydrophobic hydration and dehydration.¹⁶⁻²¹

Electrical field stimuli polymers are polyelectrolytes²² or conductive polymers such as polypyrrole that can be electrochemically oxidized and reduced in a reversible way.²³ These change in properties are linked to movements of ions and solvents inside and outside the conducting polymer that can lead to applications such as artificial muscles.²⁴

Light sensitive polymers have monomers on the backbone or side chains that undergo a structural transformation upon being irradiated with light. The most studied systems are those containing azobenzene, which experiences a *trans*-*cis* isomerization that is accompanied by a fast and complete change in electronic structure, geometric shape, and polarity.^{25, 26} Other mechanisms in light sensitive polymers consist of moieties that will ionize upon exposure to light; thus, swelling will occur due to an increase on osmotic pressure inside the network. Mamada *et al.* reported the photoinduced phase transitions of gels by introducing a leuco derivative molecule, bis(4-(dimethylamino)phenyl) (4-vinylphenyl)methyl leucocyanide, into a polymer network.²⁷ Triphenylmethane leuco derivate could reversibly be transformed into triphenylmethyl cation upon UV irradiation.

Thermoresponsive polymers are influenced by changes in temperature. Tanaka *et al.* were the first to observe the collapse of polymer networks in 1978.²⁸ Most of the polymers exhibit a decrease in solubility when temperature decreases up to an upper critical solution temperature (UCST) below which they precipitate. However, polymers with inverse temperature dependence show a lower critical solution temperature (LCST) beyond which the polymer collapses. Some examples of polymers with LCST are listed in Table 1.1.

Polymer	LCST (°C)	Structure
Poly(N-isopropylacrylamide) ²⁹	32	
Poly(methyl vinyl ether) ³⁰	37	
Poly(N-isopropylmethacrylamide) ³¹	38-42	

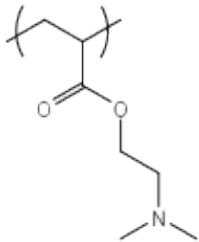

Polymer	LCST (°C)	Structure
Poly(N,N-dimethylaminoethylmethacrylate) ³²	50	
Poly(ethyleneoxide) ³³	96	

Table 1.1 List of thermoresponsive polymers with their LCST in water and their chemical structure.

A change in the volume of the network can be seen in a macroscopical level [Figure 1.1 (a)]. The mechanism behind is based on a balance between hydrophilic and hydrophobic forces.³⁴ At molecular level, when $T < LCST$ chains behave as random coils in the network with hydrophilic parts of the polymer surrounded by water molecules, making the polymer soluble [Figure 1.1 (b)]. At $T > LCST$ there is a transition from random coils to globule due to the increase in entropy, as is next discussed.

From a thermodynamic point of view, these can be explained from the definition of the free energy of Gibbs:

$$\Delta G = \Delta H - T\Delta S \quad (1.1)$$

The polymer will remain in solution as long as the free energy of mixing is negative. The enthalpy from the hydrogen bonding of the water molecules with the hydrophilic group (amide in PNIPAAm) is negative. There is negative entropy of mixing due to the hydrophobic character of the polymer (polymer backbone and isopropyl in PNIPAAm) and the relative orientation of water molecules around these hydrophobic moieties. When temperature increases the free energy of mixing becomes positive and the polymer phase-separate.

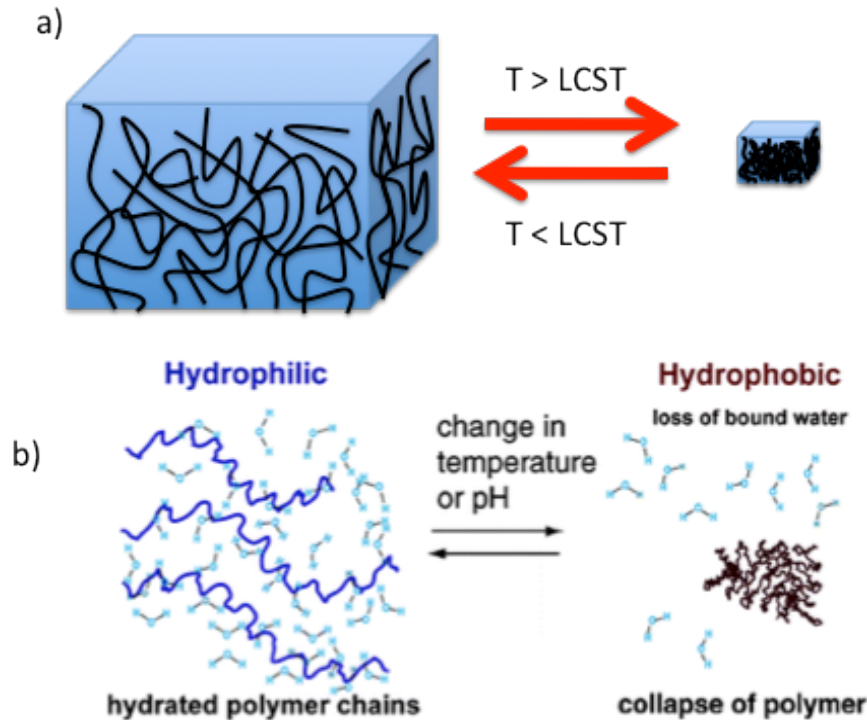


Figure 1.1. a) Macroscopic volume change on thermoresponsive polymers. b) LCST mechanism at molecular level.³⁵

1.3. PNIPAAm thin films

The most widely studied thermoresponsive hydrogel is poly(N-isopropylacrylamide) (PNIPAAm), which exhibits a sharp phase transition at 32 °C.³⁶ The LCST can be modified when the chemical structure of the polymer is changed. For instance, incorporation of carboxylic acid containing monomers increases the LCST.^{13, 37} Comonomer composition, crosslinking density, reference state and environmental parameters can influence the swelling of the polymer, as well.^{29, 38-40}

A disadvantage one encounters when using bulk hydrogels is the slow response (i.e., change in volume) to external stimuli. It has been predicted that the swelling transition time is directly proportional to the square of the linear size of the gel and inversely proportional to the diffusion coefficient of the network (D).⁴¹ Therefore, changing the size of the network from bulk to thin films (micrometer range) will reduce significantly the response time, which can be beneficial for some applications such as microactuators, or drug delivery.^{5, 42, 43}

The storage capacity of hydrogel thin films (their ability to accommodate various nanoparticles, chemicals, dyes, enzymes, etc.) can be explored for the

substantial increase in the range of functional properties. PNIPAAm is already sensitive to temperature and, when gold nanoparticles are incorporated, the electrical resistance of the collapsed polymer decreases.⁴⁴ On a similar approach, incorporating quantum dots brings photoluminescence properties to the gel.⁴⁵ Incorporation of magnetic nanoparticles provides magnetic response into the network.⁴⁶⁻⁴⁸ This last kind of hydrogels are known as ferrogels and are going to be used in this work. Their properties are, therefore, discussed next with a higher level of detail.

1.4. Ferrogels

Ferrogels are *composites* consisting of small magnetic particles, usually in the nanometer range, dispersed in an elastic polymeric matrix.⁴⁹

The magnetic nanoparticles are the elementary carriers of magnetic moment of a ferrogel. In case of superparamagnetic nanoparticles, which will be discussed in this work, the magnetic behavior of the whole ferrogel can be described by the Langevin equation. If we assume that the saturation magnetization is equal to the magnetization of individual nanoparticles, the magnetization, M , of the magnetic material in the presence of a magnetic field can be defined as:^{50, 51}

$$M = \Phi_m M_s L(\xi) = \Phi_m M_s \left(\coth \xi - \frac{1}{\xi} \right) \quad (1.2)$$

where Φ_m is the volume fraction of nanoparticles in the gel, and ξ is a parameter from the Langevin function $L(\xi)$ and is defined as:

$$\xi = \frac{\mu_0 m H}{k_B T} \quad (1.3)$$

where H represents the strength of an external magnetic field, μ_0 is the magnetic permeability of the vacuum, m is the magnetic moment of the nanoparticle and k_B denotes the Boltzmann constant.

From equation (1.2) and (1.3) it can be deduced that the magnetization of a ferrogel is directly proportional to the concentration of magnetic nanoparticles on the gel and their saturation magnetization.

There are two kinds of interactions between polymer networks containing magnetic particles and an external magnetic field: particle-particle interactions and field-particle interactions.⁵² This mainly depends on the magnetic field distribution.

When the field is uniform, particle-particle interactions tend to prevail,⁵³⁻⁵⁷ whereas in a non-uniform magnetic field the particles interact with the field experiencing an attractive force towards the high intensity magnetic field.^{58, 59} In the latter, the magnetic force acting on a piece of gel, f_m is described by:

$$f_m = \mu_0 M \nabla H \quad (1.4)$$

Therefore, the force acting on a ferrogel depends on the magnetization M and the gradient of the magnetic field ∇H . If we consider a ferrogel that has been deformed and lies on a stable state under the gradient magnetic field, the force manifests as a stress distribution balanced by the network elasticity.

1.5. Magnetism in magnetic nanoparticles

It was mentioned that the magnetization on a ferrogel is carried by the nanoparticles on the network; thus, studying the magnetic nanoparticle properties is interesting in view of both ferrogel applications and magnetism.

The magnetization of magnetic materials is mostly affected by some kind of anisotropy. Anisotropy is the property of being directionally dependent as opposed to isotropy, where the physical property is homogeneous in all directions of space. The most common types of magnetic anisotropy for nanocrystals are magnetocrystalline and shape anisotropy. Magnetocrystalline anisotropy is intrinsic to the material and means preferential magnetization depending on the crystallographic direction. The spontaneous magnetization occurs on the so-called easy axis. Shape anisotropy comes from the ease to induce a magnetization along a long direction of a nonspherical piece of material than along a short direction. The coercivity is proportional to the anisotropy constant.

Magnetic properties of magnetic materials depend as well on particle size. Magnetic particles below one critical diameter cannot support more than one domain - small regions in ferromagnetic materials within which all the magnetic dipoles are aligned parallel to each other - and become single domain.⁵¹ The critical diameter where single-domain state is more favorable normally lies in the range of a few tens of nanometers and depends on the material and the anisotropy. Note that particles with significant shape anisotropy can remain single domain up to much larger dimensions than their spherical counterparts.⁶⁰ The critical volume for spherical magnetite Fe_3O_4 , used in this thesis, is 128 nm.^{61, 62} Critical volumes for Fe, Co, Ni,

Fe_2O_3 are 14, 70, 55, and 166 nm, respectively.⁶³ Magnetization reversal on multidomain particles occurs via domain wall displacement. When getting to the single-domain regime, the only option is via spin rotation, which is generally speaking harder than to move a domain wall. Because of this the coercivity (field required to bring the magnetization to zero, H_c) is higher at the critical size for single-domain nanoparticle [Figure 1.2].⁶³ Below the critical diameter, H_c falls off due to thermal activation, leading to superparamagnetism for which $H_c=0$.

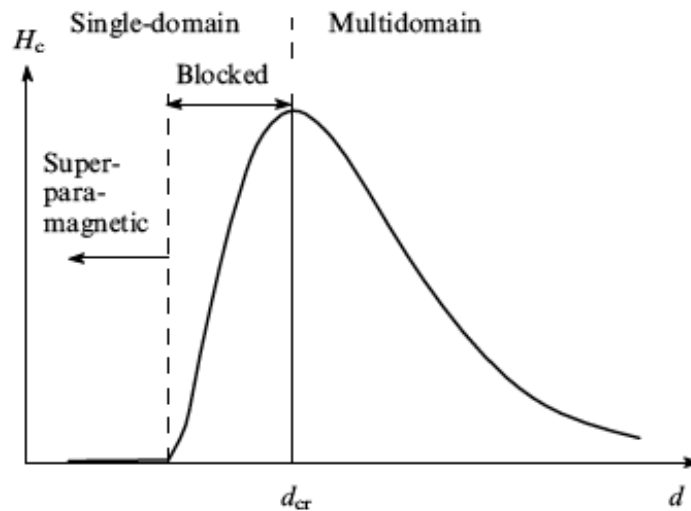


Figure 1.2. Particle coercivity versus size. d_{cr} represents the critical diameter below which particles have a single-domain.⁶²

As the particle size decreases, the amount of atoms on the surface becomes comparable to the number of core atoms. Therefore, the surface and the interface become relevant to the overall performance of the nanoparticle. Owing to this large surface atoms/bulk atoms ratio, the surface spins make an important contribution to magnetization. These surface effects can lead to a decrease in magnetization respect bulk values. This reduction has been associated with different mechanism, such as the existence of a magnetically dead layer on the particle surface, the existence of canted spins (disorder of spin on the surface compared to spin in the core of the nanoparticle), or the existence of a spin-glass-like behavior of the surface spins.^{61, 64}

There are two main areas of applications in magnetic nanoparticles: information storage and bioapplications. The stability of information storage in format of magnetic nanoparticles is very important to achieve higher densities of stored “bits”.^{65, 66} Small nanoparticles with high coercivity would be ideal for this application.

Diminishing the size brings nanoparticles to the superparamagnetic regime, where coercivity is zero. However, blocking the magnetic moments at low temperatures increases the coercivity significantly. On the other hand, the controllable size of magnetic nanoparticles, the magnetic behavior, as well as the heat emitting properties under certain circumstances make magnetic nanoparticles especially suitable for biomedical applications.⁶⁷

1.6. Aim and outline

The main aim of this thesis was the design of a thin film ferrogel as well as the study of its behavior under magnetic field. Although thin film polymers have been widely studied for applications where fast response is necessary, no studies on thin film ferrogels have been reported (despite the fact that bulk ferrogel use in applications such as biomedicine is growing). The magnetic character of nanoparticles in the ferrogel can complement the thermoresponsive character of PNIPAAm polymer (which exhibits an LCST ~ 32 °C) opening a door to combined functionality for new applications. Furthermore, since the addition of an acid comonomer can turn a hydrogel into a pH-responsive material, one can envision a ferrogel with an acid comonomer as a material with several levels of functionality.

The polymer used for this studies in thin film hydrogels was kindly supplied by Robert Roskamp in our group. Since it was synthesized with photocrosslinkable moieties, control over crosslinking degree could be achieved through different UV light exposure times. The synthesis and photocrosslinking mechanism is explained in Section 3.1.

The first step towards the study of thin film ferrogels is the understanding of the scaffold, i.e., the PNIPAAm hydrogel alone. In Section 4.1 the properties of PNIPAAm polymer system without nanoparticles were investigated by means of nanomechanical cantilever sensors and surface plasmon resonance spectroscopy coupled with optical waveguide spectroscopy. Both techniques were compared and served for a fundamental study of the hydrogel.

Magnetite nanoparticles were synthesized and strategies for the functionalization of the nanoparticles and stabilization were discussed in Section 3.2.2. A surfactant based on a photoactivated moiety was coupled to the as-synthesized nanoparticles in order to covalently bind these onto the polymer network.

A systematic study of the magnetite nanoparticles with different sizes was performed and discussed in Section 4.2. Their magnetic properties as well as behavior in front of alternating magnetic field was investigated and results were examined in correlation with their size.

Finally, the study of the ferrogel composite was reviewed in Section 4.3. Investigation on the influence of the nanoparticles on the gel properties was

presented. The effect of a gradient magnetic field is discussed with the support of theoretical calculations.

2.METHODOLOGY

2.1. Nanomechanical cantilevers sensors

Nanomechanical cantilevers sensors (NCS) have been used in this work to study changes in pNIPAAm [Section 4.1]. In contrast to other most common sensors, which produce an electrical, thermic or optical change in response to a change in an external physical parameter, cantilevers are mechanical sensors. The most widespread commercial biosensor, for instance, is the blood glucose biosensor. The enzyme glucose oxidase is used to oxidize blood glucose. Thereby, the enzyme component FAD is reduced to FADH₂ triggering an electric current.⁶⁸ NCS respond to changes of an external parameter, such as temperature or molecule adsorption, by a mechanical response; this is, bending or deflecting. The primary advantages of the nanocantilever method are sensitivity based on the ability to detect cantilever motion with sub-nanometer precision and the suitability for fabrication into a multi-element sensor array.

Cantilevers

Cantilevers for sensing are design like any common scanning probe for atomic force microscopy (AFM) or scanning force microscopy (SFM); however, a sharp tip is not required. Cantilever arrays have many advantages versus single cantilever sensors. The most relevant is the use of some of the cantilevers as reference and the others as sensors so that multiple difference signals can be evaluated simultaneously excluding parasitic effects such as thermal drifts or chemical interactions with the environment.⁶⁹ OCTOSENSIS silicon nanomechanical cantilever arrays (Micromotive GmbH, Germany) were used as transducers. Each chip consisted of eight cantilevers, each one of them with a length of 500 μm , width of 90 μm and thickness of around 700 nm arranged at a pitch of 250 μm [Figure 2.1].

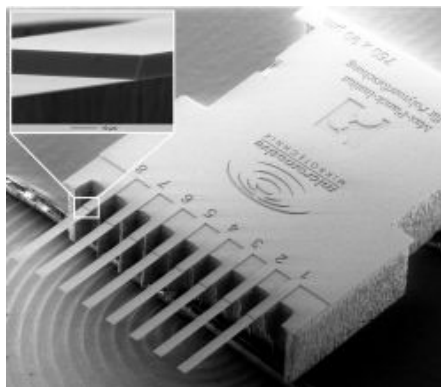


Figure 2.1 SEM of a cantilever chip.⁷⁰

Functionalization

In order to create a differential stress, one of the sides of the cantilevers has to be either not-functionalized or passivated. There are several techniques to cover only one side of the cantilever.

Commonly, a 2 nm layer of titanium followed by a 20 nm one of gold are deposited on the upper side. This surface is called functionalized side and is used to anchor the monolayer that represents the chemical surface sensitive to the molecules to be detected.^{6, 71} Metal-coated cantilever can be influenced by thermal changes, as well as other ambient conditions such as moisture. This so-called bimetallic effect was first observed on cantilevers by Thundat *et al.*⁷² Gimzewski *et al.* used this effect to sense chemical reactions.⁷³ Zhao *et al.*, on the other hand, made use of the bimetallic effect between silicon oxide and a PS layer to measure the temperature coefficient of interfacial tension between the polymer and silicon oxide.⁷⁴ Although widely used, this can be inconvenient when temperature effects on films want to be studied.

Other functionalization methods are based on manual manipulation. Among these one can find microfluidics or array of dimension-matched capillaries. Polymer solutions can be pipetted into the microchannels or can be sucked by the microcapillaries. These methods coat the whole cantilever, including the backside. Further manipulation of the cantilever has to be done in order to get only one side functional.

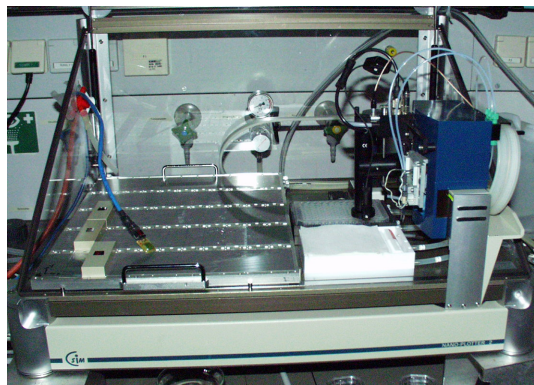


Figure 2.2. Nano-Plotter© 2.0 device used for the coating of the nanocantilevers.

For coating large number of cantilevers the inject-spotting technique allows rapid and reliable coatings.⁷⁵⁻⁷⁷ Furthermore, it allows the functionalization of only one side of the cantilever. This has been the preferred technique for the work mentioned in this thesis. It has been done in the Nano-Plotter© 2.0 (“Gesellschaft fuer Silizium-Mikrosysteme mbH”, Germany) [Figure 2.2].^{78, 79} It consists of a computer-assisted drop-on-demand inkjet system. Essential parts of the system are the piezoelectric working micropipettes. A piezoactuator ejects the drops from the tip of the nozzle. The Nanotip ejects droplets with a volume of 0.4 nL. All functions of the inkjet system can be used either interactive or via programs written in the internal script language “Nano-Plotter-Language” which is related to Pascal. The script used to inject the solution was written by Sebastian Nett.⁸⁰

Readout principle

Different readout mechanisms can be used in cantilevers such as frequency shifts in the cantilevers resonant vibrations (dynamic method), piezoresistive/capacitance changes, or changes in the deflection of the cantilever at the free end (static method). In this work the optical (beam-deflection) readout method has been used.⁶⁹ A commercial device Scentris™ (Veeco, Santa Barbara, USA) is used [Figure 2.3]. Other readout principles include optical interferometric readout, piezoelectric readout or piezoresistive readout.⁸¹⁻⁸⁶

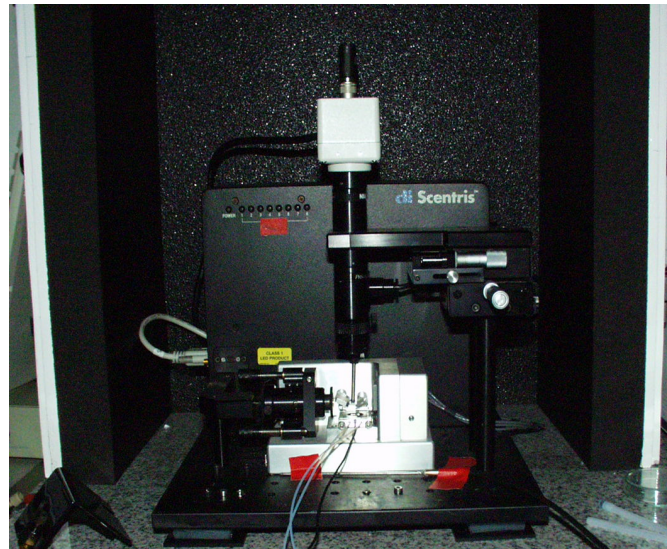


Figure 2.3 Picture of readout setup Scentris instrument

The beam-deflection readout principle is the same as any surface probe microscopy technique. Eight superluminescent emitting diodes are aligned on the free tip of the cantilevers with the help of a mirror [Figure 2.4]. The reflected beam is redirected by a second mirror towards a position sensitive detector (PSD). The actual cantilever position is calculated from the cantilever dimensions and the bending angle.

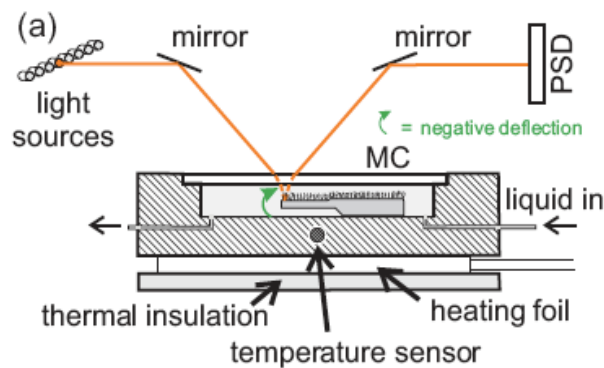


Figure 2.4. Flow cell used for nanocantilever experiments.⁸⁰

The flow cell used to perform the experiments was built by the machine shop in MPIP in collaboration with the electronic shop in MPIP. There is an inlet and an outlet for liquids or gases. The cantilever was held in position inside the flowcell with a spring element. Close to the cantilever chip there is a PT100 thermocouple that controls and records the temperature. A resistive foil heater (28x28 mm², 75 Ω, Minco, USA) is glued underneath the chamber for heating the system up. The

temperature control was calibrated in a temperature range of 20 to 60 °C. The temperature was measured in the fluid at the cantilever position with a second PT100. All measurements were adjusted according to the calibration shown in Figure 2.5 and performed by Sebastian Nett.

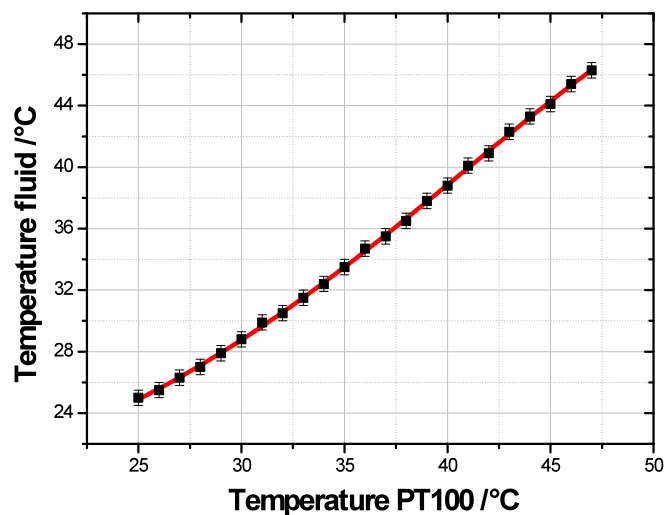


Figure 2.5 Calibration curve of temperature inside the flow cell vs. temperature read by the thermocouple.

When cooling down of the system is needed, the heater is switched off and approximately half an hour is needed to decrease the temperature from 50 °C to 25 °C. A negative deflection means in our system a bending up. Hence, a positive deflection corresponds to a bending downwards.

2.2. SPR/OWS

Surface Plasmon Resonance Spectroscopy together with Optical Waveguide Spectroscopy (SPR-OWS) has been used for the study of PNIPAAm thin films in this work. This technique has been widely used for biosensing⁸⁷ some of the reasons being the label-free and non-destructive character. Currently, commercial SPR imaging instruments are available from several companies such as GWC Technologies, Inc. (Madison, WI),⁸⁸ IBIS Technologies (Hengelo, The Netherlands),⁸⁹ and from GenOptics (Orsay, France).⁹⁰

The basics behind these techniques are going to be discussed in the subsequent section.

Surface Plasmon Resonance

SPR is understood as a technique that makes use of the attenuation of the total internal reflection of photons at an interface. In order to understand this, Snell's law should be mentioned. This describes the behavior of a refracted light in an interface such as:

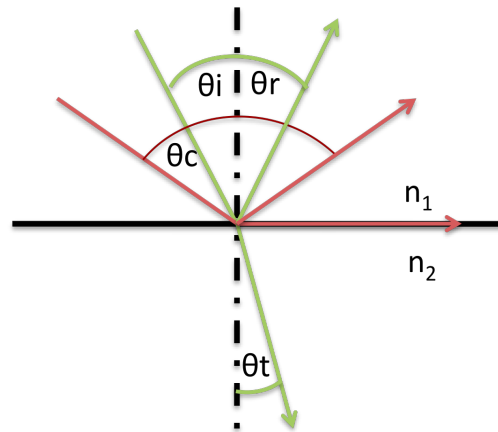


Figure 2.6 Snell's Refraction of light at the interface of two media, being the refractive index $n_1 > n_2$. Different colors are not related to the beam properties.

Figure 2.6 shows a sketch describing Snell's law where:

$$\sin \theta_t = \frac{n_1}{n_2} \sin \theta_i \quad (2.1)$$

where θ_t is the angle of transmitted light, n_1 is the refractive index of the optically denser medium, n_2 is the refractive index of the media where light is refracted, and θ_i is the angle of the incident light. There is a critical angle, θ_c , that determines the minimum angle at which total internal reflection (TIR) starts to happen. This can be extracted from Equation 2.1 inserting $\theta_t = 90^\circ$.

Above TIR, the incident light gives rise to a wave near the interface that is described by Maxwell theory and explains how, above θ_c the perpendicular component of the optical E-field decays exponentially with a decay length l which is a function of the angle of incidence and is called evanescent wave:

$$l = \frac{\lambda}{2\pi \sqrt{(n \cdot \sin \theta_i)^2 - 1}} \quad (2.2)$$

Only p-polarized light (transversal magnetic TM) modes can excite surface polaritons. Analyzing the form for the resulting electromagnetic wave created

indicates that they can only be excited at interfaces between two media with dielectric constants of opposite sign. Dielectric media under study have usually a positive dielectric constant, ϵ ; thus, metallic films such as silver or gold are going to be used as they provide a negative ϵ .

For practical purposes, the quantitative treatment of this problem is based on the Fresnel theory for calculating the overall transmission and reflection of a general multilayer assembly.⁹¹ Fresnel calculations have been implemented by the program WINSPALL, developed at the MPIP.

$$\begin{aligned}
 r_s &= \frac{n_2 \cos \Theta_i - n_1 \cos \Theta_t}{n_2 \cos \Theta_i + n_1 \cos \Theta_t} \\
 r_p &= \frac{n_2 \cos \Theta_t - n_1 \cos \Theta_i}{n_2 \cos \Theta_t + n_1 \cos \Theta_i} \\
 t_s &= \frac{2n_1 \cos \Theta_i}{n_2 \cos \Theta_i + n_1 \cos \Theta_t} \\
 t_p &= \frac{2n_1 \cos \Theta_t}{n_2 \cos \Theta_i + n_1 \cos \Theta_t}
 \end{aligned} \tag{2.3}$$

where r_s is the reflection ratio for s-polarized light, r_p is the reflection ratio for p-polarized light, t_s is transmission ratio s-polarized light and, t_p transmission ratio for p-polarized light.

Plasmons surface polaritons (PSP) or surface plasmons, for short, are described as the excitations created through the coupling of photons with the nearly free electron gas in a metal in the interface of a metal and a dielectric material.⁹¹

Further analyzing of the created electromagnetic wave leads to the dispersion relationships (i.e. the energy-momentum relation) for surface plasmons at a metal/dielectric interface:

$$k_{x,plasmon} = \frac{\omega}{c} \sqrt{\frac{\epsilon_m \epsilon_d}{(\epsilon_m + \epsilon_d)}} \tag{2.4}$$

where ϵ_m is the dielectric constant of the metal and ϵ_d the one of the dielectric material, ω is the angular frequency and c is the speed of light. In order to create surface plasmons the wave vector of the incident light and the plasmon must be the same. The dispersion relation for a free photon in a dielectric medium will always be smaller than the wave vector of the plasmon since:

$$k_{x,ph} = \frac{\omega}{c} \sqrt{\epsilon_d} \tag{2.5}$$

A coupling configuration consisting on the addition of a prism or a grating is then needed to match the wave function of the photon and the surface plasmons.^{92, 93} In this work the Kretschmann configuration was used where a prism with a high refractive index is used to couple the light with the gold layer deposited on the sample. In order to create a continuous medium, a substrate made with the same material as the prism is used and an index matching oil is used in between the two [Figure 2.7].

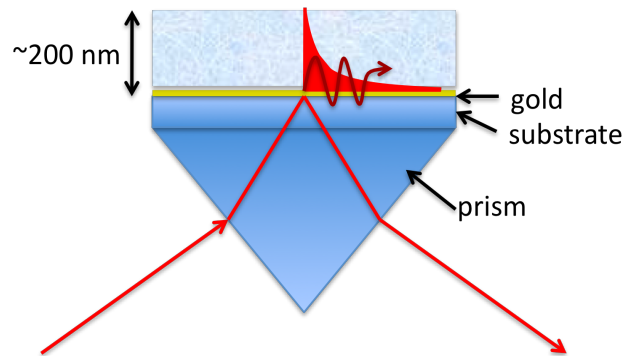


Figure 2.7 Kretschmann configuration where a prism is used to match the wave function of the photon with the surface plasmon one.

The wave function for the photon in the prism takes the form:

$$k_{x,ph} = \frac{\omega}{c} \sqrt{\epsilon_{prism}} \sin \Theta_i \quad (2.6)$$

and it only depends on the angle of incidence allowing for an increase of k_x to gain resonance with the plasmon for a given angular frequency of the laser ω_{laser} [Figure 2.8 (a)]. That is, at a certain angle $k_{x,photon}$ matches the resonance conditions and a surface plasmon is generated for a fixed angular frequency (ω) of the laser. The resonant condition will manifest in a decrease of the reflectivity because light is translated into surface plasmon generated [Figure 2.8 (b)].

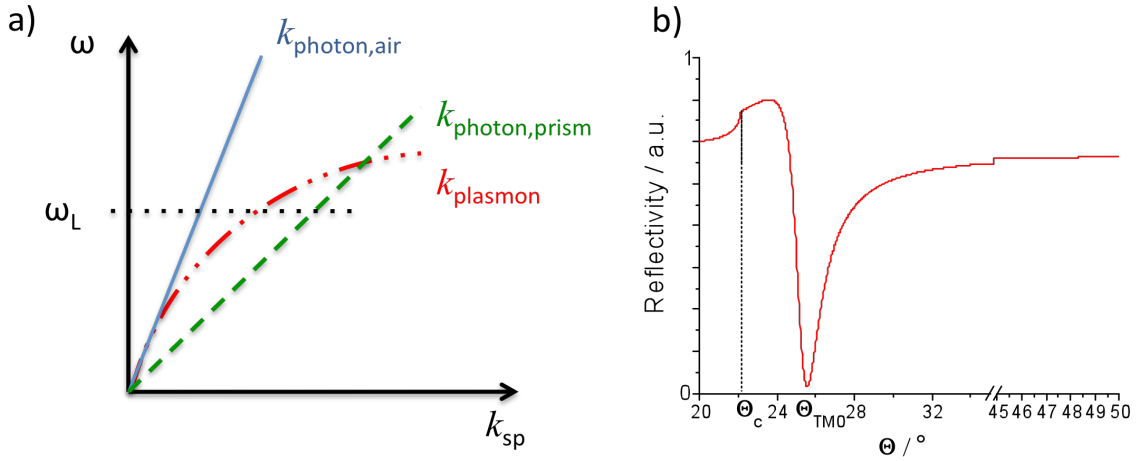


Figure 2.8 (a) Dispersion relation of a photon traveling as a plane wave in the dielectric medium, blue line, photon propagating in the prism, green dashed line and, dispersion of the surface plasmon mode propagating along the metal/dielectric interface, dashed/dotted line red line.(b) Simulation of reflectivity in a three layer system (glass/gold/air).

There are, typically, two kinds of experiments on SPR. The first consists of the scan of the angular dependent reflectivity spectra, as it is show in Figure 2.8 (b). The plasmon wave function will change when the optical density of the dielectric changes, i.e., whenever there is a change in the thickness or the refractive index. This change is translated in a shift of the resonant angle. Different angle scans will measure this shift. On the other hand, a kinetic experiment would allow us the tracking of the changes in real-time. It basically consists of recording the reflectivity at a fix angle on the linear region over time.

The change in SPR angle depends on the dielectric constant of the medium and the thickness of the adsorbed layer:

$$\Delta\Theta_i = f\left(d_{layer}, \left(\sqrt{\varepsilon_d} - \sqrt{\varepsilon_p}\right)\right) \quad (2.7)$$

ε_d is the complex dielectric constant of the dielectric and ε_p the complex dielectric constant of the buffer. Therefore, SPR requires the knowledge of the thickness of the layer or the refractive index in order to calculate the respective other parameter. This brings some limitations on SPR that will require the coupling of this technique with other measurements.

Optical Waveguide Mode Spectroscopy (OWS)

OWS makes use of the same setup as the SPR, many times both techniques are measured together, such as in this work. This technique is based on the appearance of a new type of nonradiative mode, when the thickness of the coating is increased further. This is depicted in Figure 2.9. It makes use of the principle of guiding light in a transparent medium with confined (optical dimensions) such as optical fibers.

Assuming a model waveguide consisting of three layers with refractive indices n_1, n_2 and n_3 , for the case of $n_2 > n_1, n_3$ layer 2 can guide lightwaves. Once we have ray confined in a waveguide media, only certain wavelengths and discrete angles can exist, other conditions will be canceled by destructive reflections.

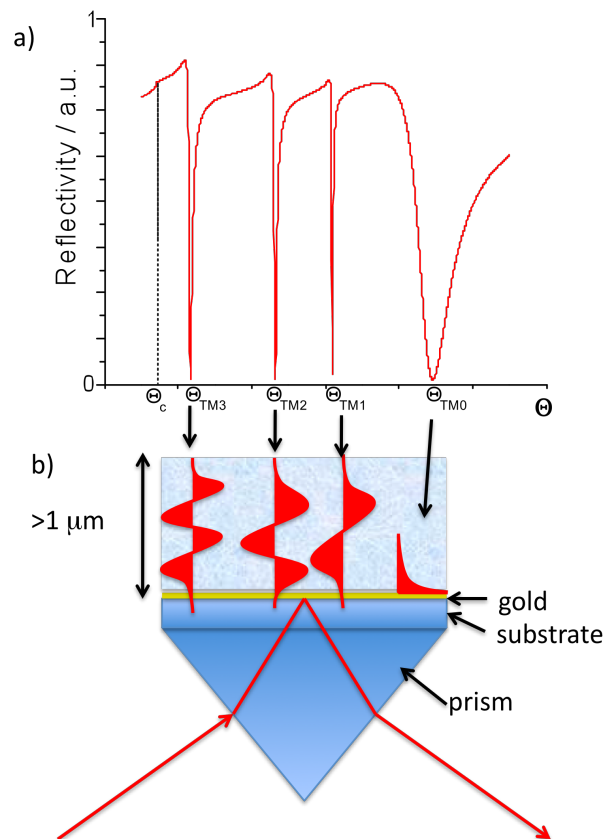


Figure 2.9 a) Waveguide modes excited by the light as well as the PSP wave, provided that the layer is thick enough. b) When these modes are excited sharp dips can be seen in the reflectivity as a function of the angle. The index of the modes is in accordance with the number of nodes of their field distribution waveguide structure.

In this work, our system is composed by 4 layers: air or buffer, dielectric or waveguide media, gold and glass. The gold is far too thin to allow for the complete evanescence decay of the waveguide mode. A complete description can be found in

literature,⁹⁴ here it is stated that it's possible to guide leaky waves and that the coupling efficiency – the depth of the modes – depends on the thickness of the gold layer.⁹⁵

Setup

In Figure 2.10 a scheme of the SPR-OWS setup is depicted.⁹⁵

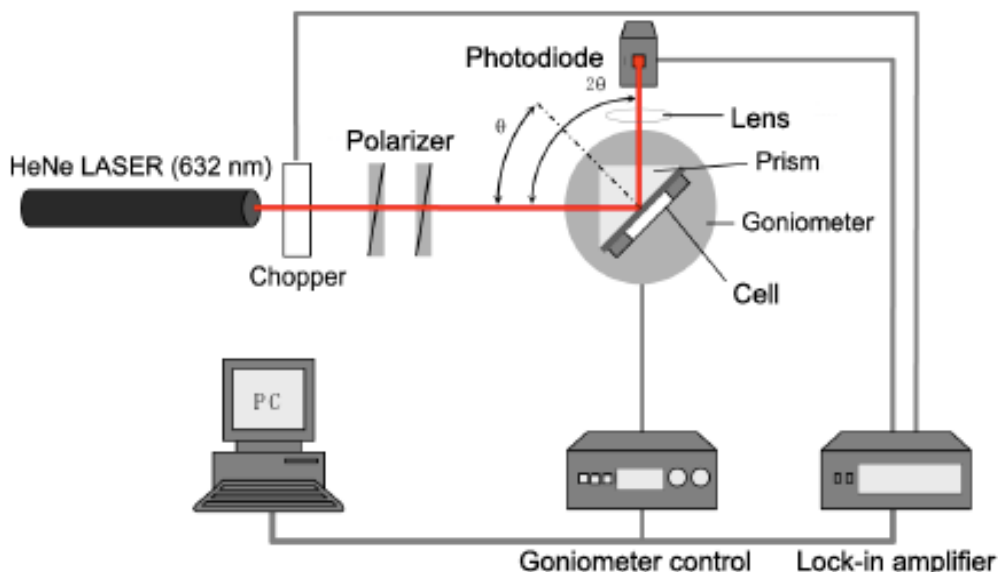


Figure 2.10 SPR-OWS setup used in this work.⁹⁵

The setup was modified with a heating plate positioned next to the flow cell in the sample holder in order to perform temperature dependent experiments. The sample holder was provided with a sealed water-cooling system in order to stabilize and decrease the temperature when necessary. A thermocouple in the heating plate and another one right next to the flow cell were used to control the temperature through program implemented in our group.

Furthermore, the SPR setup was slightly modified when a magnetic field was implemented. A platform was attached to the cell on the goniometer to allow scanning with the magnet. A picture is shown in Figure 2.11.

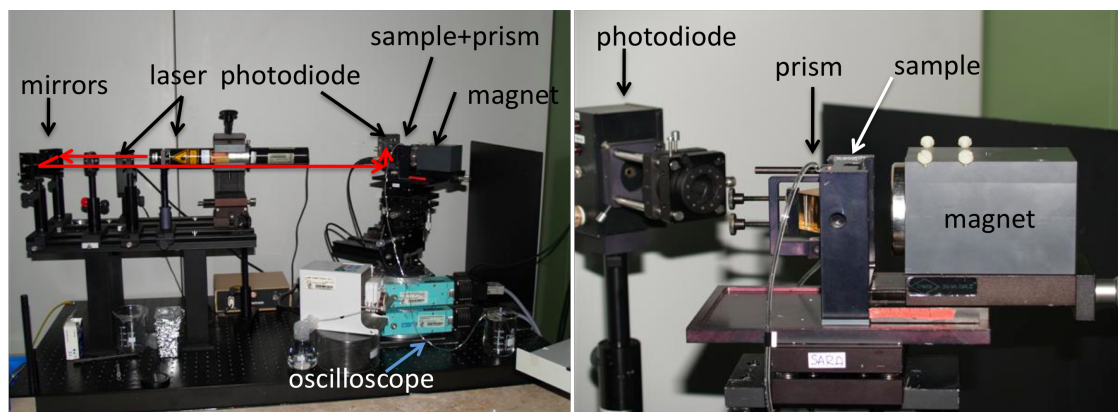


Figure 2.11 Pictures of SPR setup with magnet attached next to the sample. On the right picture a blowup of the sample holder is shown. The distance of the magnet to the sample could be adjusted by the screw on the magnet platform.

Simulation of the data was achieved through WINSPALL program. Fresnel calculations have been implemented by the program WINSPALL, which uses a box model approximation assuming a homogeneous box for every layer with the same set of parameters homogeneously distributed. In evaluating experimental data, the R vs. θ measurement is compared with the response calculated from the Fresnel equations based on trial values of thickness and refractive index. The best fit between the data and the calculation constitutes the measurement of the adsorbed molecular layer. The input data of some of the layers are presented in Table 2.1.

<i>material</i>	<i>thickness / nm</i>	ϵ'	ϵ''
prism LaSFN9	0	3.397	0
chromium	2	-16.0208	15.9723
gold	50	-12.0544	1.3864
ferrogel	depends on the gel	depends	depends
air	0	1	0

Table 2.1 Approximate values of thickness and dielectric constant introduced in the box-model system in Winspall software.

2.3. Transmission Electron Microscopy

The construction of the first TEM was attributed to Knoll and Ruska in 1931; which brought Ruska to win the Nobel Prize in Physics in 1986.⁹⁶

Transmission Electron Microscopy (TEM) is an imaging technique with the same principles of light microscopy with the only exception that electrons are used

instead of photons. The use of electrons brings a much higher resolution compared to light, allowing the imaging of structures in a nanometer scale. This is due to the small de Broglie wavelength of the electrons.

An electron gun is used as source of electrons and is either based on thermoionic emission from a filament, usually tungsten, or field electron emission. High voltages (100-300 kV) are applied in order to emit high-energy electrons that accelerate towards the cathode. A Wehnelt cylinder helps focalizing the electrons into the beam by having highly negative charge walls. The lenses in TEM help the beam to converge. These are not glass lenses but electron lenses (i.e., coil). The condenser lenses are responsible for the primary beam formation, that is the beam with high-energy electrons that are going to be transmitted through the thin sample. The objective lens creates an inverted image of the specimen. The aperture in the back focal plane of the lens determines how many electrons go through influencing this way the appearance of the image. Other lenses are needed for increasing resolution, correcting astigmatism, and shifting the beam. The image is finally displayed on a fluorescent screen and recorded using photographic films or nowadays mostly CCD camera.⁹⁷

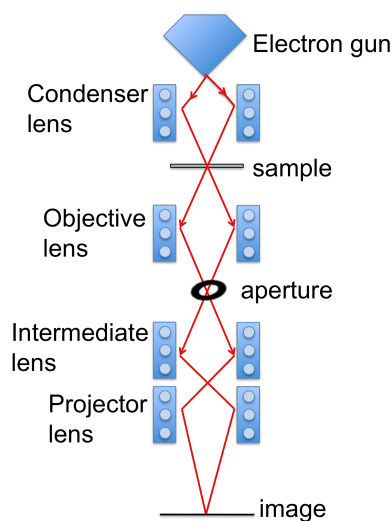


Figure 2.12 TEM setup scheme. An electron beam is generated and focused on the sample through a condenser lens. A series of lenses and apertures positioned after the sample help creating the image.

Electron diffraction patterns can be extracted by selecting the back focal plane instead of the image plane to be displayed on the image with the help of the electromagnetic lenses. Selected area electron diffraction (SAED) allows extract a

pattern of a selected crystalline structure. When SAED of nanocrystals is performed, ring patterns analogous to those obtained by X-Ray powder diffraction are obtained.

The samples were analyzed by Katrin Kirchhoff in a FEI Tecnai F20 with a 200 kV field emission gun.⁹⁸ The samples were prepared by drop casting a solution of nanoparticles in copper grids carefully positioned on top of a tissue. The solvent depended on the sample that was analyzed.

2.4. Ellipsometry

Ellipsometry is a technique used to analyze optical properties of thin films such as refractive index, roughness, crystallinity or optical thickness. The basic principle of the measurement is the change in the polarization state of the light upon reflection or transmission on the sample.

A suitable model of the layer system has to be chosen to calculate the desired parameter from the measured ellipsometric angles Ψ and Δ .

Monochromatic light wave is generally polarized elliptically. The wave is transverse and its electric-field intensity vector, E , moves along an elliptical trajectory in a perpendicular plane to the propagation direction. The time evolution of this wave is represented by a superposition of harmonic vibrations along two perpendicular axes, E_p , parallel to the incident plane, E_s , perpendicular. Basically, if the two vibrations are shifted in phase, the resulting trajectory is elliptic.⁹⁹

When a beam of light enters a transparent film and reflects on a substrate [Figure 2.13], the polarization of the beam changes depending on the wavelength, the refractive indexes of the layers as well as the thickness of the film. The change in the polarization is denoted by the change in phase of E_p and E_s , namely Δ ; and the change in amplitude, ψ .

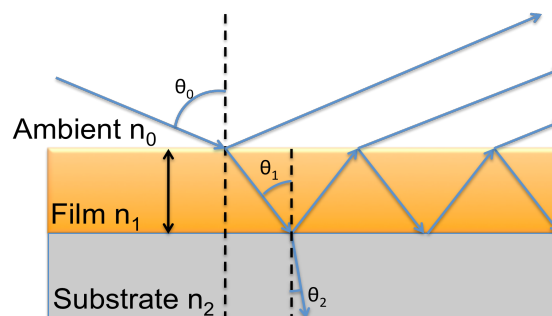


Figure 2.13 Reflection and transmission of a beam of light into a multilayer system.

The resulting change in polarization after reflection from a surface can be measured through a complex reflection coefficient, ρ :

$$\rho = \tan \Psi \exp(i\Delta) = \frac{R_p}{R_s} \quad (2.8)$$

Setup

The ellipsometer is basically an optical instrument that consists of two arms whose axes lie in one plane. At the central axis there is the stage on which the specimen would be mounted. The specimen itself is a specularly reflecting surface that is positioned to contain the axis of rotation. Collimated unpolarized light or circularly polarized monochromatic light from a suitable source is passed along a linear polarizer alone or with the combination of a compensator. These will polarize the light incident on the surface under examination in a definite state. Analyzing optical devices will determine the state of polarization of the light beam after its reflection from the surface. Either a linear analyzer alone is employed or a combination of a compensator and a linear analyzer (in case a polarizer alone is used on the incident-beam). The operation of a nulling ellipsometer [Figure 2.14] involves rotation of the polarizing and analyzing optical components until the light leaving the analyzer is totally extinguished.¹⁰⁰

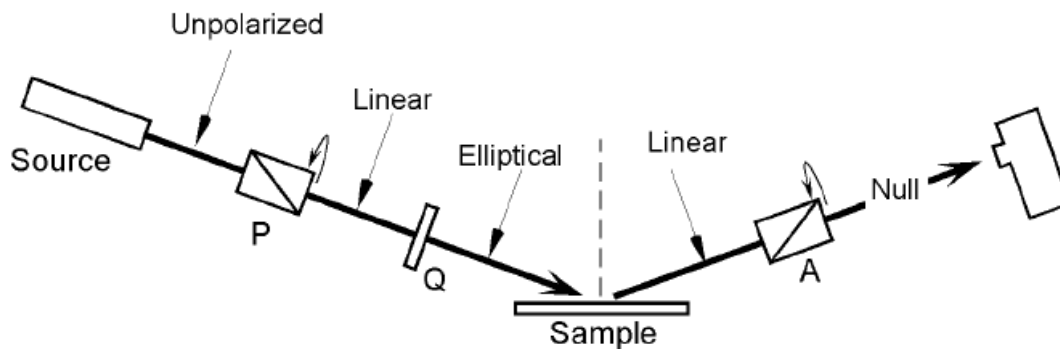


Figure 2.14 Configuration of a PCA Nulling ellipsometer: SPCA stands for the optical elements polarizer-compensator-analyzer.⁹⁹

In order to get valuable information from the ellipsometric angles ψ and Δ a box model is assumed. A fit is applied to solve the unknown parameters. The layer thickness is periodic for a given pair of ψ and Δ . This can be solved by measuring a variety of the incident angles in order to increase the data points to fit.

The measurements were performed on an imaging ellipsometer EP3 from Nanofilm Technologies GmbH, Göttingen. Using interference filters and a Xenon lamp as the light source, the wavelength was set to 403.5 nm. The light source is a laser with the wavelength of $\lambda = 532$ nm and a xenon lamp having a wavelength range from 403 nm to 1000 nm. For all measurement in this thesis the incident angle was set to an angle of interest (AOI) = 60° . The ellipsometric angles can be determined for every pixel or averaged over parts (ROI: Region of interest) of the field of view (0.33 mm x 0.33 mm utilizing a 10x objective). Inside the field of view several ROI's can be defined and analyzed individually. On experiments in cantilever, a ROI with an area of 50 nm x 300 nm was used to average the thickness over this area

2.5. UV/Vis/NIR Spectroscopy

UV/Vis/NIR Spectroscopy measures the absorption of light by molecules in the UV/VIS/NIR region. When a photon hits a molecule an electron can be excited from the ground state to an excited state. On a molecule the most energetically probable transitions will from the highest occupied molecular orbital (HOMO) to the lowest unoccupied molecular orbital (LUMO). Other transitions on the molecular level are possible but not probable in this energy range (UV-VIS) since the energy of the photon has to be equal to the energy necessary to promote the electron. A sample is shined with light at different wavelengths with an initial intensity I_0 . When the energy of the photon at a certain wavelength matches the energy necessary to promote an electron, the light is absorbed. The decrease in intensity is detected by the optical spectrometer. The wavelength at which the transition occurred is related to the molecule whereas the absorption is related to the concentration of molecules in the solution. Lambert-Beer law [Equation 2.9] relates the intensity change with the concentration as long as the concentration, c , remains low and the path of the light constant, d .

$$A = -\log\left(\frac{I}{I_0}\right) = \epsilon cd \quad (2.9)$$

A is the absorbance, I is the detected intensity, I_0 is the initial intensity, c is the concentration in mol/L, d is the path of the cuvette, and ϵ represents the molar absorptivity of the absorbent ($M^{-1}.cm^{-1}$) and is characteristic for every molecule

provided that the pressure, temperature, wavelength and solvent remain the same. It can be measured through a calibration curve or extracted from literature values. Thus, UV-VIS spectroscopy is a good tool to measure concentrations.

In this work UV-VIS spectra were recorded with a UV-VIS/NIR (Perkin Elmer, Lambda 900). The background was always measured in the beginning of the experiment and subtracted from the spectra of the samples. In order to analyze thin films a setup [Figure 2.15] was built consisting of two quartz slides joined together with a Teflon piece in between with an inlet and an outlet for liquids. One of the quartz slides had the thin film spin coated on top.

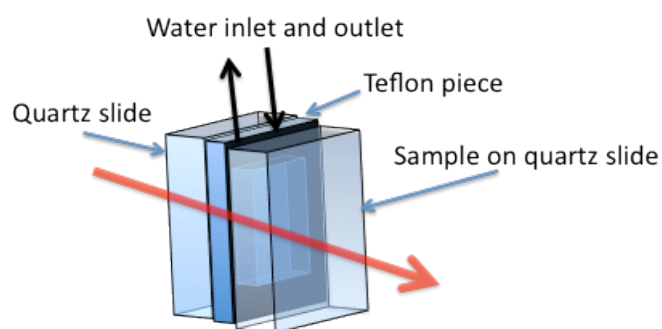


Figure 2.15 Sketch of flow cell used for measurements on thin film samples. The red arrow represents the laser.

2.6. Superconducting quantum interference device

Superconducting quantum interference device (SQUID) is an apparatus that is capable of measuring very small changes in magnetic field. It is based on the combination of the physical phenomena of flux quantization and Josephson tunneling.¹⁰¹

The Josephson effect describes the tunneling of Cooper pairs in superconductors separated by a thin insulating layer.^{51, 102} Cooper pairs is the name used to describe pairs of electrons that are bound together at low temperatures under certain circumstances. The effects due to the superimposition of wave functions in the potential well separating two regions of space in which free particles are confined. The whole system will behave as a single superconductor, allowing the passage of a current without any voltage difference.¹⁰³ When two or more Josephson junctions are connected in parallel, the phase across each junction is coherently related to the phase of the other junction, by the flux quantization condition in every superconducting loop enclosed by each pair of junctions. The maximum supercurrent I_{max} that can be supported by the system with no voltage across the junctions exhibits

a periodic dependence upon the applied magnetic field B . The magnetic flux enclosed inside the ring modulates I_{max} periodically, with a period of one flux quantum. This modulation, caused by an interference of the superconducting wave functions in the two SQUID arms, forms the basis of the working principle of the dc-SQUID.¹⁰¹ While dc-SQUID needs of two Josephson junctions, rf-SQUID needs only one junction and the applied external field will be AC instead of DC current.

All SQUID measurements in this thesis were performed on a Quantum Design MPMS-XL SQUID Magnetometer. The samples were prepared by precipitation of the nanoparticles originally well dispersed in hexane, by the addition of a non-solvent (ethanol). After the NPs are collected with the help of a permanent magnet, the supernatant is discarded and the powder obtained is dried in the oven overnight under vacuum.

2.7. Hyperthermia setup

The heat generated by magnetic nanoparticles in an alternate magnetic field can be studied by calorimetry. A system was designed and built in the MPIP by Luis Heritier. The system consisted on three main components:

- a) RLC circuit (the coil is part of a resonant system with a resistor and capacitor):
 - Inductive component: The coil had a diameter of 5 cm and was 5 cm high. The diameter of the wire was 1.5 mm and approximately 120 turns
 - Capacity component: Three capacitor combinations designed to provide three different frequencies: 51.8 kHz, 98.25 kHz and, 135.15 kHz
 - Resistive component: a resistance of 0.47 Ohm was included in the circuit, in order to determine the current running through the coil. As resistive component also the internal resistance of coil and cables must be considered.
- b) Power supply:
 - Function generator: Agilent 33220A 20 MHz Function / Arbitrary Waveform Generator

- Amplifier: Harman / Kardon model HK 970 120W_{RMS} power output, response up to 200KHz
- Tektronix 2465 300 MHz oscilloscope

c) IR thermometer: Testo 845 infrared thermometer.¹⁰⁴

In Figure 2.16 a picture of the setup with the components is shown.

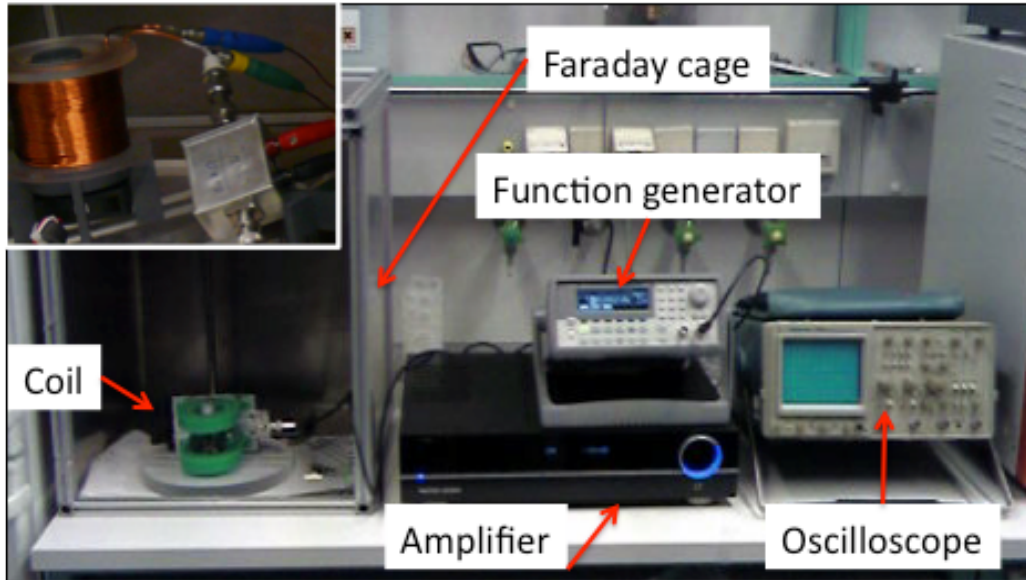


Figure 2.16 Picture of hyperthermia experiment. On the left upper corner a blowup of the coil used for the experiments is show.

The circuit is supplied by the signal generator with a sinusoidal signal of frequency f and voltage V_G . The current I flowing through the solenoid of inductance L depends on the frequency f , the generator voltage and parameters of the RLC circuit. In order to get a resonance in the RLC circuit at a given frequency, the capacitor's capacity C must be chosen so as to reduce the complex component of the electrical impedance (reactance) by compensating the coil impedance, according to:¹⁰⁵

$$f_0 = \frac{\omega_0}{2\pi} = \frac{1}{2\pi\sqrt{LC}} \quad (2.10)$$

2.8. Contact Angle

Contact angle measurement is one of the easiest ways to study surface energy. The contact angle is determined at the interface between the three phases, liquid, solid, and vapor, of a liquid droplet placed on the solid surface of interest. The system applied is the Drop Shape Analysis System DSA 10 (Kruess, Germany) with

a thermo stage and degassed ultrapure water. Only the static contact angle in “Sessile-Drop”-mode is determined here. A 5 μL drop of ultrapure water was placed on the sample and the angle between the surface of the drop and the sample surface was measured. This was repeated several times and the values were averaged.

Hydrophilic surfaces have typical contact angles between 10° to 30° , hydrophobic contact angles are between 70° and 90° . Figure 2.17 (a) represents this phenomenon.

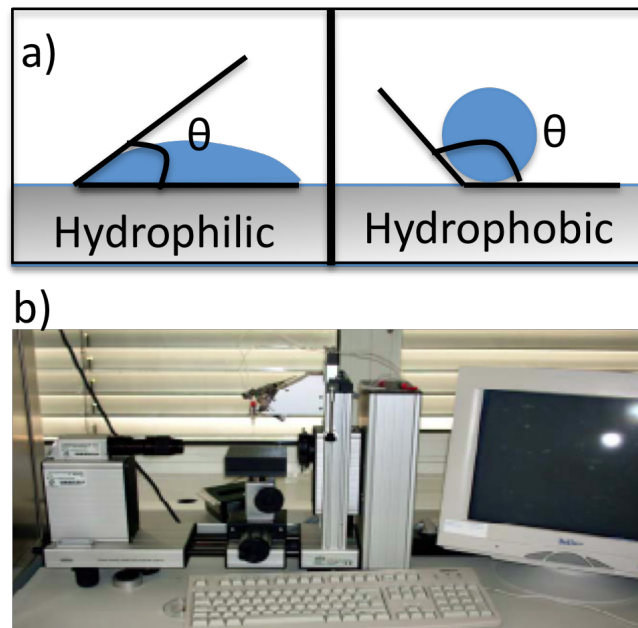


Figure 2.17 (a) Comparison of contact angle of a hydrophilic and a hydrophobic surface. (b) Drop shape analysis system DSA10-MK2

3. MATERIALS

3.1. PNIPAAm

Multiple methods are known to coat hydrogels on surfaces including brushes grafted from the surface by in situ free radical polymerization or by atom transfer radical polymerization techniques^{106, 107} and grafting of functionalized PNIPAAm to a modified substrate. E-beam and plasma polymerization¹⁰⁸ had been employed as well.

In this thesis coating is achieved by spincoating of an uncrosslinked polymer followed by simultaneous crosslinking and surface attachment by UV-light. The main system used in this thesis employs benzophenone (BZ) monomer as crosslinking point. In some cases, another PNIPAAm polymer containing dimethylmaleimide (DMI) as crosslinking unit is used instead of the benzophenone. Both polymers were provided in polymer chains, however, for further understanding the synthesis is briefly described below.

3.1.1. Benzophenone system*

Materials: Monomers were prepared according to literature.^{109, 110} N-isopropylacrylamide (NIPAAm, Aldrich) was purified by recrystallization from a mixture of toluene/hexane (1/4) and 2,2'-Azobis(isobutyronitrile) (AIBN) from methanol. Methacrylic acid (MAA, Aldrich) was distilled prior to use from the stabilizer. 4-benzoylphenyl methacrylate (MABP) was prepared following Toomey *et al.*¹¹¹ and dioxane was distilled over calcium hydride.

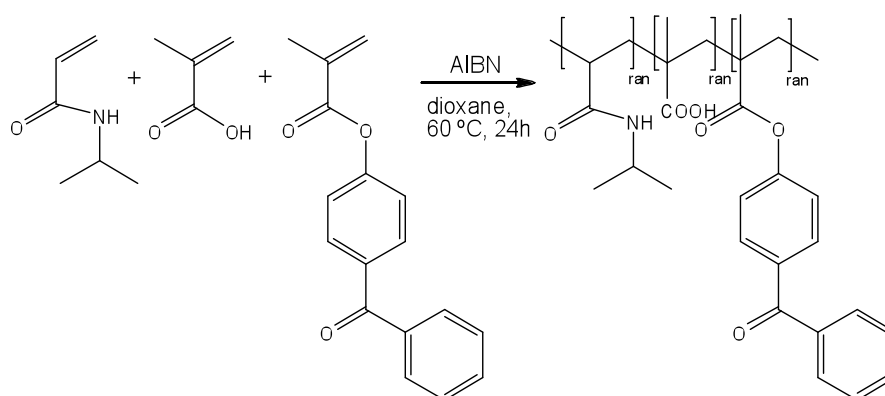


Figure 3.1 Free radical terpolymerization of NIPAAm, MAA and MABP.

* Polymer chains synthesized by Robert Roskamp.⁹⁵

Procedure: In a first step, a terpolymer from N-isopropylacrylamide (NIPAAm), methacrylic acid (MAA), and 4-benzoylphenyl methacrylate (MABP) was prepared by free radical polymerization in solution, as depicted in Figure 3.1. Typically 21 g (185.57 mmol, 100 eq.) NIPAAm, 798.7 mg (9.27 mmol, 5 eq.) MAA and 494.2 mg (1.86 mmol, 1 eq.) MABP were dissolved in 140 ml dry dioxane. After argon was bubbled through the solution for at least one hour, 140 mg (0.85 mmol, 0.0046 eq.) of AIBN were added. The free radical polymerization was carried out at 60 °C under argon and quenched after 24 hours. This was achieved either by precipitating in ice cold diethyl ether when purified by precipitation or by adding untreated dioxane in the case of purification by dialysis techniques. The obtained polymer was freeze-dried from *tert*-butanol in vacuum.

The terpolymer was obtained with an average yield of 80%. For purification it was either precipitated from methanol to ice-cold diethyl ether, ultrafiltrated (MWCO: 20000 g/mol) with THF, or dialyzed (MWCO: 14000 g/mol) with DMF. GPC gave a molecular mass of $M_n = (115000 \pm 5000)$ g/mol and $M_w = (250000 \pm 15000)$ g/mol and a polydispersity of $PDI = 2.2 \pm 0.1$ for all purification methods. The copolymerization with MABP allows for the subsequent crosslinking of the polymer by UV-irradiation.

3.1.2. Dimethylmaleimide system[†]

Materials. N-isopropylacrylamid (NIPAAm) from ACROS ORGANICS was recrystallized from n-hexane and dried in vacuum and 2,2'-Azobis(isobutyronitrile) (AIBN) was recrystallized from methanol before use. 1,4-dioxane was freshly distilled over KOH. N-[2-(3,4-Dimethyl-2,5-dioxa-2,5-dihydro-pyrrol-1-yl)-ethyl-acrylamide (DMIAAm) was prepared following.¹¹³

[†] Polymer chains synthesized and provided by group of Dirck Kuckling in the University of Dresden.¹¹²

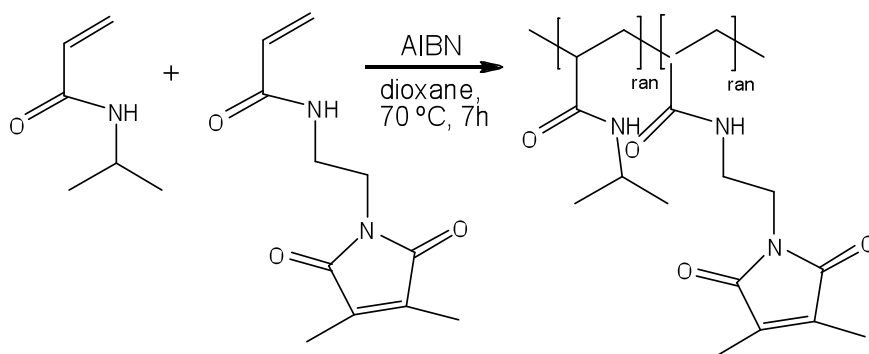


Figure 3.2 Free radical terpolymerization of NIPAAm and DMIAAm.

Procedure. AIBN (0.1 mol%) was added to a solution of NIPAAm and DMIAAm in dried dioxane. The total monomer concentration was about 0.55 M, being DMIAAm 5 mol%. After purging with argon the reaction mixture was kept at 70°C for 7h. The polymer was poured into cold diethylether. For purification the polymer was reprecipitated from THF solution into diethylether (1/3) and dried in vacuum for 24h. The polymer was obtained with a yield of 40%. GPC gave a molecular mass of 47600 g/mol and a molecular weight of 100000 g/mol and a polydispersity of 2.10. The DMIAAm content in the polymer is 4.8mol% according to H-NMR (500 MHz, CDCl₃). In some of the PNIPAAm-DMI systems used, comonomers containing an amine or a carboxylic acid group are added such as 3-acryloylaminopropionic acid (AAmPA).^{38, 114}

3.1.3. Grafting

The polymer obtained from the synthesis in powder can be dissolved in a solvent such as ethanol, cyclohexanone, or chloroform and spin coated on a surface. To attach a polymer to a surface the chains can either be physisorb or chemisorb. Since the polymer in use is a hydrogel and is going to be used in liquid, a stronger attachment is preferred; therefore, a self-assembled monolayer (SAM) was deposited at the interface between the polymer and the sample surface to ensure the chemical binding. The main active group is the benzophenone. Prucker *et al.* were the first group that introduced benzophenone SAM for the same purpose.¹¹⁵ In this work, two main kinds of samples were used: (i) SiO₂-like samples such as BK7 glass, silicon or quartz; and (ii) metal-covered samples such as gold coated samples used for SPR.

Depending on the surface chemistry of the sample, either silane chemistry or thiol chemistry was used.

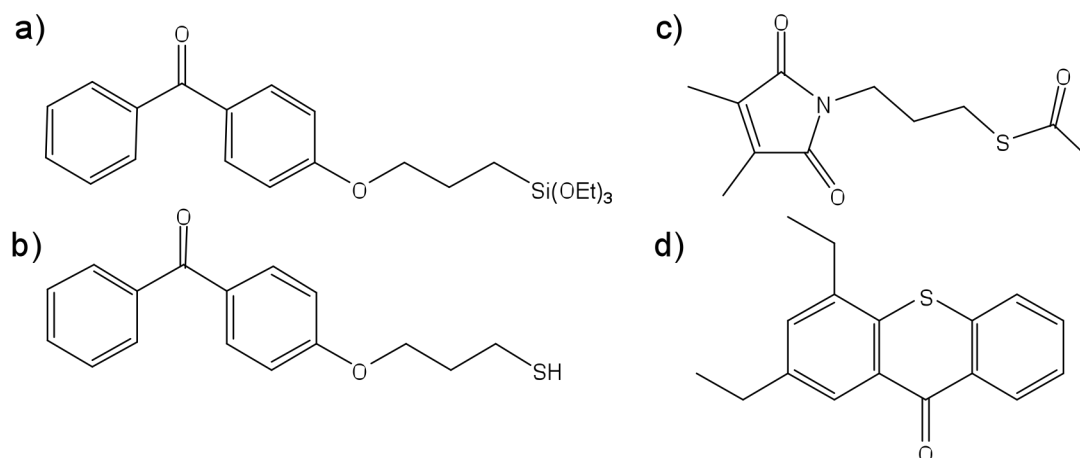


Figure 3.3 Adhesion promoters a) BZ-silane, b) BZ-thiol, and c) DMI-thioester. Sensitizer for DMI-system is shown in (d).

The thiol used was 4-(3-mercaptopropoxy)benzophenone (BP-thiol) [Figure 3.3 (b)] and was synthesized according to ⁴⁰. In order to coat the substrate, these were immersed in a 1 mM ethanolic solution of the BZ-thiol for at least overnight. Studies show that with a 1mM thiol solution the SAM layer (80% – 90%) forms within minutes, while it takes some hours to completely cover the surface.¹¹⁶ Next, the samples were thoroughly rinsed with ethanol and dried with N₂ gas, showing a water contact angle of ~80°.

On the other hand, the silane used was 4-(3-triethoxysilyl)propoxybenzophenone (BP-silane) [Figure 3.3 (a)] and its detailed synthesis can be found in.⁹⁵ Triethoxysilanes have been proven to be more stable compared to trichlorosilanes, which most of the times suffer from polymerization issues already in the container and need to be deposited in vapor. Typically, the BP-silane was diluted in ethanol at a concentration of 1 mM. The samples had to be introduced in the aforementioned solution for at least 3 days. Next, the samples were thoroughly rinsed with ethanol and dried with N₂ gas, showing a water contact angle of ~40°, exhibiting its lower density compared to the BP-thiol. In order to increase the density of BP-silanes on the surface a protocol consisting of heating a toluene solution of 0.15 mM BZ-silane at 110°C overnight increased the contact angle up to ~75°. More details on these can be found on Section 4.1.3.1.

When PNIPAAm-DMI system was used, another adhesion promoter on gold surfaces could be used, in addition to BZ-thiol. It consists of thioacetic acid

3-dimethylmaleimido propyl ester (DMI-thioester) [Figure 3.3.(c)] and the synthesis can be found in.³⁸ To cover a gold surface, the substrate was introduced in a 1 mM ethanolic solution of DMI-thioester for 12 h. Afterwards the samples were rinsed with ethanol and dried with a nitrogen stream.

Once the surface was covered with the adhesion promoter SAM, a solution of the polymer on chloroform was spincoated on top. Crosslinking of the polymer is achieved through UV light exposure. This process is explained in more detail in the following section.

3.1.4. Photocrosslinking

In order to form networks there has to be a crosslinking step. In our main system, PNIPAAm-BZ, the benzophenone moiety is used for this purpose. When benzophenone is illuminated by UV-light, a photon at 350 nm is able to excite one electron from a nonbonding sp²-like n-orbital on oxygen to an antibonding π^* -orbital of the carbonyl group. This biradical triplet state is conformed by an electron-deficient oxygen that can interact with weak C-H bonds, resulting in hydrogen abstraction. Next, the ketyl and the alkyl radicals that are formed readily recombine to create a new C-C bond.¹¹⁷ If the biradical state doesn't react with the vicinity groups, it will return to the ground state mainly by phosphorescence.^{118, 119}

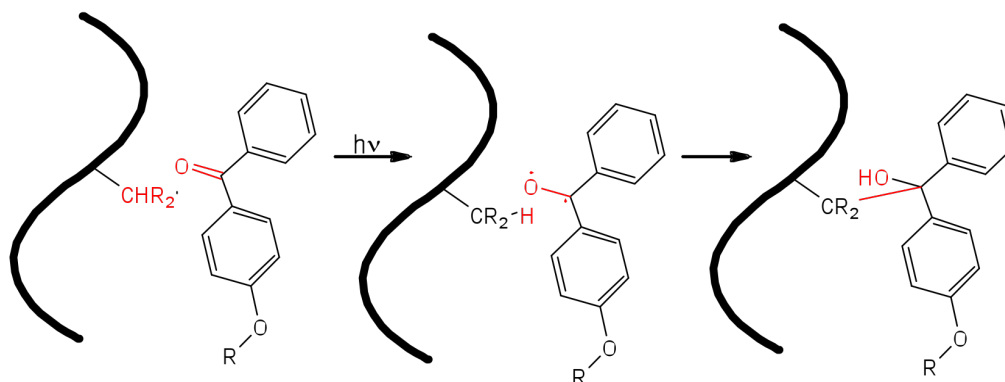


Figure 3.4 Photochemistry of benzophenone moiety.

In this work, a wavelength of 365 nm (Stratalinker 2400, Agilent, Germany) is going to be used to crosslink the network. This wavelength doesn't fall on the maximum absorption wavelength, however, it allows us to finely tune parameters such as crosslinking density.⁹⁵ The benzophenone moiety, shown in Figure 3.4, can represent either the BZ groups on the polymer chains or the benzophenone SAM. The exposure to UV light allows us to crosslink the network at the same time as we

graft the polymer to the substrate. PNIPAAm-BZ polymer was dissolved in chloroform in concentrations from 1-4.5%-wt, depending on the thickness required. The solutions were spincoated at 4500 rpm for 60 s onto SAM-functionalized substrates. Next, the samples were dried at 50 °C in vacuum for 8 hours. The films were cross-linked by UV irradiation (365 nm) in a Stratalinker 2400 (Stratagene). The total photocrosslinking energy dose (PED) was varied from 1.57 to 6.28 J·cm⁻² for different samples by varying the exposure time from 15 to 60 minutes. Typically, 1%-wt solutions gave films in the 100 nm range dry thickness, whereas 4.5% translated in films in the 1-1.3 μm range dry thickness.

It's worth mentioning that since the network is attached to the surface there is a confinement effect that doesn't allow the polymer to swell equally in all directions. The lateral expansion is going to be restricted by the grafting, and the swelling is going to be perpendicular to the surface, in 1D. The same thing happens with PNIPAAm hydrogels systems crosslink through DMI crosslinker moiety.

DMI-PNIPAAm, system used occasionally in this work, contains a DMI moiety instead of BZ. It has been known for several years that N-substituted dimethylmaleimides undergo [2+2]-cycloadditions by exposure to light [Figure 3.5].¹²⁰

121

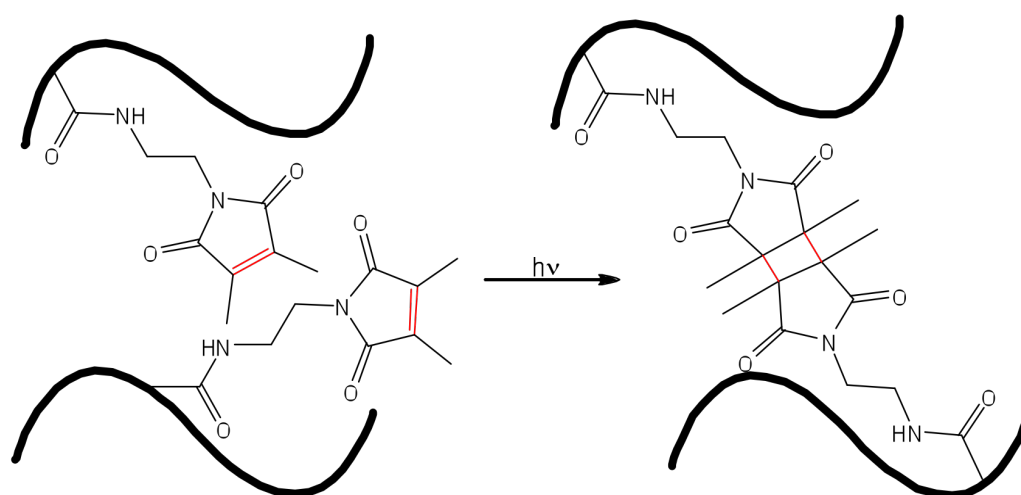


Figure 3.5. Photochemistry of dimethylmaleimide (DMI) moiety.

DMI molecule absorbs in the region of 270 to 300 nm. The UV crosslinking would require an emission maximum in the deep UV; however, most of the polymer backbones are photochemically cleaved at this region. Therefore, the cyclodimerization of DMI must be sensitized towards the near UV. A study on several sensitizers proved that thioxanthone was more efficient respect to other ones such as

benzophenone, acetophenone or benzil.¹²⁰ The reason for this was thought to be the shorter lifetimes of the triplet states for these ketones. Another important parameter is the solubility of the sensitizer and the polymer. Kuckling *et al.* used thioxanthone for the same PNIPAAm-DMI system and spincoated from cyclohexanone.²⁹ In this work, 2,4-diethyl-thioxanthen-9-one is used instead [Figure 3.2.(d)]. This molecule is soluble in solvents with a higher polarity, which are, at the same time, more convenient for the PNIPAAm-DMI polymer because the solubility parameter is closer to the ones of polar solvents such as 1-propanol, ethanol, etc. Usually, PNIPAAm-DMI (solubility parameter PNIPAAm=23.5 (MPa)^{1/2}) powder is dissolved in 1-propanol (solubility parameter=23.5 (MPa)^{1/2}) in concentrations from 2 to 10%-wt (dry thickness from 20 nm to 1.5 μ m). The concentration of the sensitizer is 2%-wt vs. polymer weight. Irradiation times of 10 minutes are usually enough to fully crosslink the polymer.

3.2. Nanoparticles

Nanoparticles are attracting more interest in the scientific community because of the change in properties with respect to bulk materials, furthermore, the properties change with size.¹²²⁻¹²⁴ When decreasing the diameter of particles, the number of atoms in the surface starts to be comparable to the atoms inside the particle. In the case of magnetic particles they have novel properties such as superparamagnetism, low Curie temperature, high coercivity, high magnetic susceptibility.

On the other hand, nanoparticles can be used as fillers for polymers in order to improve some of the properties. In this work, different nanoparticles have been used and whose syntheses are going to be described below.

3.2.1. Magnetite nanoparticles

There are various methods to synthesize magnetic nanoparticles; from physical methods such as thermal vaporization,¹²⁵ to chemical synthesis.¹²⁶ Among chemical synthesis of magnetite one can distinguish three important groups: thermolysis of metal-containing compounds,¹²⁷⁻¹²⁹ reduction of metal-containing compounds,¹³⁰⁻¹³² and synthesis in reverse micelles.¹³³ After different trials, the method that produced the most monodispersed nanoparticles with a control on the size and higher crystallinity was the thermal decomposition of iron compounds under

oxygen-deficient conditions accompanied by partial reduction of Fe^{3+} to Fe^{2+} . The synthesis was adapted from the protocol by Sun *et al.*¹³⁴

3.2.1.1. Synthesis

In order to both control and monitor the temperature within the system, a metal bath heater equipped with a temperature control and monitoring unit was used (see Figure 3.6).[‡] The heater was made out of brass and equipped with two 180 W heating elements operating at 220 V and a Pt100 temperature sensor. Filled with 1.2 kg Wood metal (Roth, $T_m = 70\text{ °C}$), the heater had to be preheated to 70 °C before the flask could be placed in the heated metal. The temperature program was started immediately after.



Figure 3.6 The home-built metal bath heater and temperature control equipped with two Pt100 thermocouples. One is situated inside the brass heater. The second one is introduced in a thin glass tube and placed into the flask measuring the actual reaction temperature. The unit is connected to a computer, which records the temperature read-out of both thermometers.

Materials. The synthesis was carried out under nitrogen and using commercially available reagents: Ethanol (Sigma-Aldrich, absolute Chromasolv), hexane (Fisher Scientific, analytical reagent grade), toluene (Riedel-de Haën, puriss. p. a.), chloroform (VWR, HiPerSolv Chromanorm), diphenyl ether (Alfa Aesar, 99%), dibenzyl ether (Fluka, > 98%), oleic acid (Sigma-Aldrich, 90%), oleyl amine (Fluka, >

[‡] Built by Markus Schwind with the help of the electronic workshop and the mechanical workshop at MPIP.

70%), 1,2-hexadecanediol (Sigma-Aldrich, 90%), iron(III) acetylacetonate (Aldrich-Chemie, 97%). All chemicals were used as received.

Procedure. Iron(III)acetylacetonate $\text{Fe}(\text{acac})_3$ (2 mmol), 1,2-hexadecanediol (10 mmol), oleylamine (12 mmol), and phenyl ether (20 mL) are mixed and magnetically stirred under a flow of nitrogen. The mixture is heated up to 200 °C for 30 min. Then, under a blanket of nitrogen, heated to reflux at ~265 °C for another 30 min. The black-brown mixture is cooled to room temperature by removing the heat source. Under ambient conditions, the nanoparticles are precipitated with the addition of ethanol. The precipitate is separated via centrifugation. The black product is dissolved in hexane in the presence of oleic acid (0.05 mL) and oleylamine (0.05 mL). Centrifugation is applied to remove any undispersed residue. The precipitate is disposed and the nanoparticles in the supernatant are precipitated with ethanol and separated with centrifugation. This cleaning process is repeated at least 4 times. Next, the nanoparticles dispersed in hexane are precipitated with ethanol and magnetically separated. The magnetic separation is repeated 3 times. The final product is redispersed in hexane.

Preparing magnetite nanoparticles with a bigger size requires a solvent with a higher boiling point and for longer boiling times. Dibenzyl ether was used when nanoparticles with a diameter of 8 nm were required.

When even bigger nanoparticles were needed, a seed-growth method extracted from Sun *et al.* is used. Typically, $\text{Fe}(\text{acac})_3$ (2mmol), 1,2-hexadecanediol (10 mmol), oleic acid (2 mmol) oleylamine (2 mmol) and benzyl ether (20 mL) are mixed and magnetically stirred under a flow of nitrogen. An 84 mg sample of 8 nm nanoparticles in hexane is added and the mixture is heated to 100 °C to remove excess hexane. Afterwards the mixture is heated to 200 °C for 60 minutes and 30 minutes more to reflux. Afterwards, the same cleaning protocol with repetitive solvent exchange is repeated.

Characterization. Transmission electron microscopy was used in order to determine the particle shape, size and size distribution. Selected area electron diffraction was used to determine the particle composition. The diluted solution of nanoparticles was dropped-casted on a carbon coated TEM grid that was placed on top of a tissue that absorbed the solvent that was not evaporated.

- SAED. The diffraction pattern on the nanoparticles showed the typical Fe_3O_4 cubic structure, shown by the ring patterns in Figure 3.7.

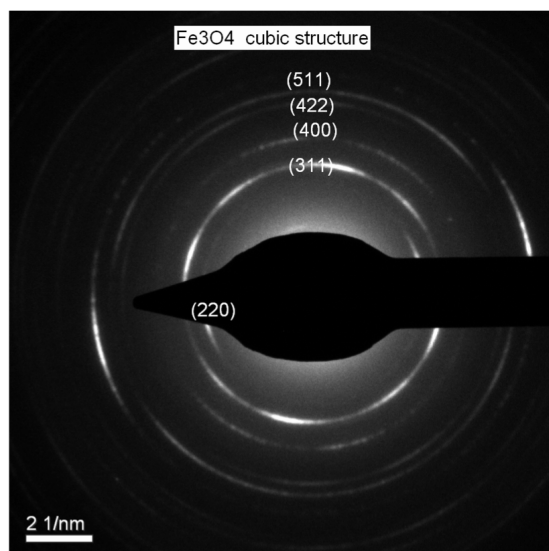


Figure 3.7 SAED pattern for magnetite nanoparticle.

We were able to synthesize magnetite nanoparticles in three different sizes:

- The smallest nanoparticles had a diameter of 3.5 up to 5 nm (depending on the batch) (standard deviation < 0.5). The TEM images can be seen in Figure 3.8. They were highly monodispersed and spherical.

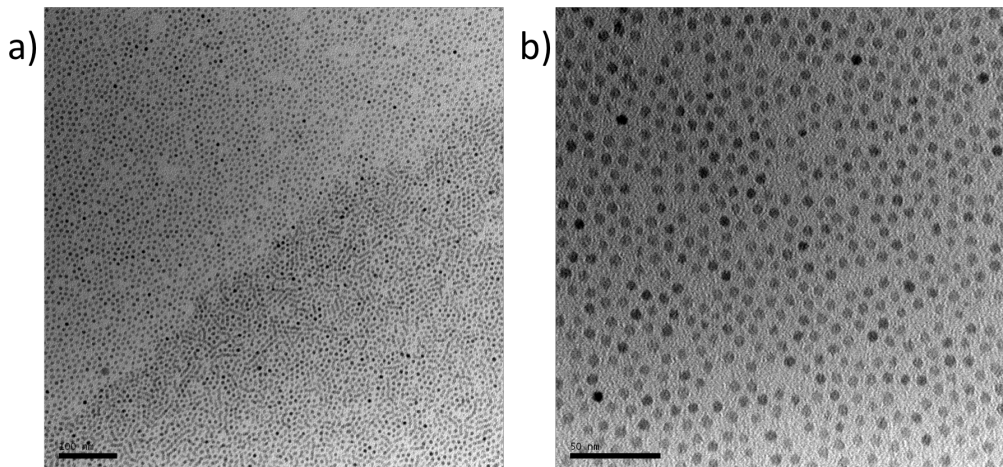


Figure 3.8 TEM pictures of magnetite nanoparticles synthesized with the use of diphenyl ether as a solvent. The scale bar in (a) is 100 nm and 50 nm in (b).

- Bigger nanoparticles with a diameter of 7 to 8 nm (depending on the batch) (standard deviation ~ 1) were synthesized from a higher boiling point solvent (benzyl ether (bp=298 °C) instead of diphenyl ether (bp=258 °C)). Nanoparticles start to lose the sphere shape towards this crystalline cube where different faces can be distinguished. High-

resolution TEM (HRTEM) images of these iron oxide nanocrystals show distinct lattice fringe patterns, indicating the highly crystalline nature of the nanocrystals [Figure 3.9 (b)].

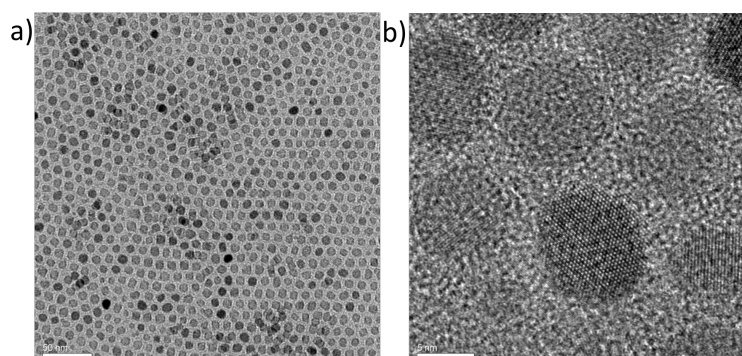


Figure 3.9 TEM pictures of magnetite nanoparticles synthesized with the use of dibenzyl ether as a solvent. The scale bar in (a) is 50 nm and 5 nm in (b).

- The biggest nanoparticles were synthesized from a seed-growth strategy where nanoparticles previously prepared are used as nucleation points. The mean diameter depending on the batch varies between 12 to 15 nm (standard deviation ~ 2). As the standard deviation shows, these particles present a higher particle size distribution.

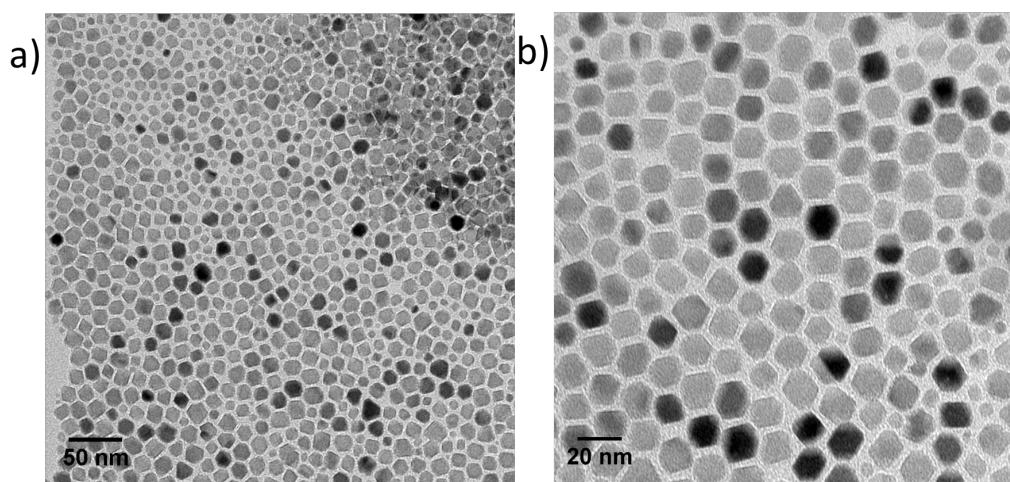


Figure 3.10 TEM pictures of magnetite nanoparticles synthesized with the use of dibenzyl ether as a solvent and Fe_3O_4 nanoparticle seeds. The scale bar in (a) is 50 nm and 20 nm in (b).

Further increase on the nanoparticle size can be achieved through seed-growth technique using nanoparticles with bigger particle size. However, at the same time, the standard deviation increases with size.

Magnetic properties as well as other characteristics of the nanoparticles will be discussed in Section 4.2.

3.2.1.2. Silica shell

The synthetic route used to synthesize magnetite nanoparticles allows us to control the size in a monodisperse manner; however, the as-synthesized nanoparticles are only soluble in non-polar solvents. Surface modification of these nanoparticles is an essential and challenging step. Different strategies are followed to functionalize the surface. The use of hydroxamic acid group has been proven to be useful to introduce dendrons on the surface for stabilization.^{135, 136} On the other hand, Mohapatra *et al.* made use of phosphonic acid based anchoring agents to introduce folic acid on the surface for biomedical applications.¹³⁷ In this work, water-in-oil microemulsion was used as an approach to cover the magnetic nanoparticles with silica shell. Silica surfaces as well as their functionalization with silane chemistry have been widely studied. The protocol is adapted from literature.¹³⁸

Materials. Cyclohexane (Acros Organic, anhydrous >99.5%), Igepal CO-520 (Sigma-Aldrich), ammonium hydroxide (Acros Organics, 28-30 wt%), tetraethylorthosilicate (TEOS) (VWR International GmbH, zur synthese), methanol (Carl Roth GmbH + Co KG, >99.5%), ethanol (Sigma-Aldrich, absolute Chromasolv). All chemicals were used as received.

Procedure. Magnetite nanoparticles in hexane were redispersed in cyclohexane: ethanol was added to precipitate NPs from hexane solution. After centrifugation for 15 minutes the supernatant was exchanged for cyclohexane at a concentration of 1mg/mL. Cyclohexane (170 mL) and 8 mL of Igepal CO-520 were stirred in a flask. Next, the NPs dispersed in cyclohexane were injected into the Igepal/cyclohexane solution. Aqueous solution ammonium hydroxide 30% (1.3 mL) was added dropwise and stirred 2-3 minutes. Tetraethylorthosilicate TEOS (1.5 mL) was added to the mixture. The mixture was stirred for 72 h. Methanol was added to collect particles. Methanol phase was extracted. The particles were precipitated with excess hexane and collected by centrifugation. The particles were redispersed in ethanol. These cleaning steps were repeated at least 3 times to wash the nanoparticles. Then, magnetic separation was performed at least 3 times. The nanoparticles were finally stored in ethanol.

Optical characterization. TEM micrographs of the nanoparticles show how silica forms a shell around the nanoparticles. A very small proportion of nanoparticles do not have magnetite nucleus inside.

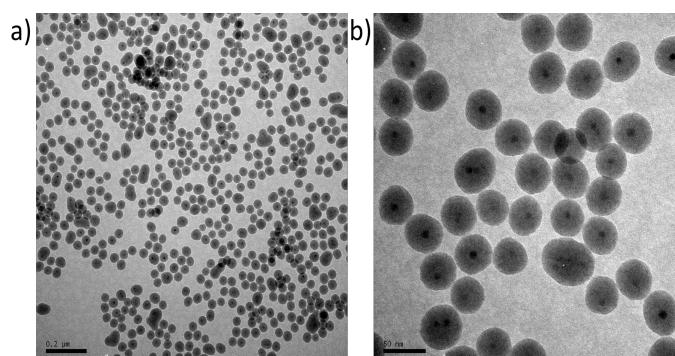


Figure 3.11 TEM pictures of magnetite nanoparticles covered by silica. The scale bar in (a) is 0.2 μm and 50 nm in (b).

The surface of silica microspheres can be easily functionalized by reaction with organosilanes. Modification of SiOH-like surfaces have been widely studied, however, one has to be more careful when dealing with nanoparticles. Nanoparticles tend to aggregate due to interparticle forces such as van der Waal interactions or, in case of magnetic nanoparticles, magnetic dipoles. Stabilization of nanoparticles can be achieved through electrostatic repulsion or steric hinderance.

- **APTES**

There are several routes to modify silica nanoparticles, most of them consist in the stirring of the nanoparticles with silane in a basic medium.¹³⁹⁻¹⁴²The protocol chosen was a modified version of the protocols aforecited.

Materials: Aminopropyltriethoxysilane (APTES) was purchased from Acros Organics and distilled under vacuum before using it. Ethanol (Sigma-Aldrich, absolute Chromasolv) was used as a solvent.

Procedure: Magnetite covered with silica was dispersed in ethanol in a round-bottom flask. Once the NPs were well dispersed, 0.5 mL of APTES were quickly added while stirring. The solution was stirred overnight at room temperature. The solution was centrifuged at 4000 rpm for 15 minutes after which a white precipitate could be appreciated. Next, the supernatant was discarded and more ethanol was added to the nanoparticles. After dispersing the nanoparticles through sonication and shaking, the nanoparticles were precipitated again by centrifugation. These last steps were repeated at least 4

times to make sure all the unreacted APTES was removed. Residual APTES can polymerize and form impurities on the solution.

This protocol was first tried in commercial silica nanoparticles and the characterization can be seen in Appendix A1.

- **FITC-APTES**

Materials. Fluoresceine isothiocyanate (FITC) (Sigma-Aldrich, >90% (HPLC)), ammonium hydroxide (Acros Organics, 28-30 wt%), tetraethylorthosilicate (TEOS) (VWR International GmbH, zur synthese), methanol (Carl Roth GmbH + Co KG, >99.5%), ethanol (Sigma-Aldrich, absolute Chromasolv), N,N-dimethylformamide (Sigma-Aldrich, >=99.8%), sodium hydroxide (Merck Chemicals Ltd, pellets). All these chemicals were used as received. Aminopropyltriethoxysilane (APTES) was purchased from Acros Organics and distilled under vacuum before using it.

Procedure. First, 0.008 g (0.021 mmol) of FITC was dissolved in 3 mL of anhydrous ethanol. Vacuum-distilled 3-aminopropyltriethoxysilane (APTES) (15 μ L (0.064 mmol)) are added to the mixture. The reactants were allowed to react in the dark for 24 hours under stirring in a dried flask. Ammonium hydroxide (0.4 mL) was first added onto a 32 mL solution of $\text{Fe}_3\text{O}_4\text{-SiO}_2$. APTES-FITC (1 mL) was added into the above dispersion and stirred for 15 minutes. Next, 5 μ L of TEOS was added to initiate the formation of a 2nd SiO_2 layer. The reaction was kept at 35°C for 15h. The resulting solution was purified by centrifugation at 12,000 rpm for 5 minutes. The supernatant was removed and replaced with ethanol. The process was repeated for 3 times until no fluorescence of FITC was observed for the supernatant.

Labeling efficiency. The particles were transferred quantitatively to the solvent dimethylformamide by repeated centrifugation, removal of supernatant, and redispersion in DMF. The particles were dissolved in a 0.2 M sodium hydroxide solution liberating the dye molecules. The absorption of the solution was measured by UV-VIS. In order to extract the number of FITC molecules a calibration curve with different known concentrations of FITC was measured.

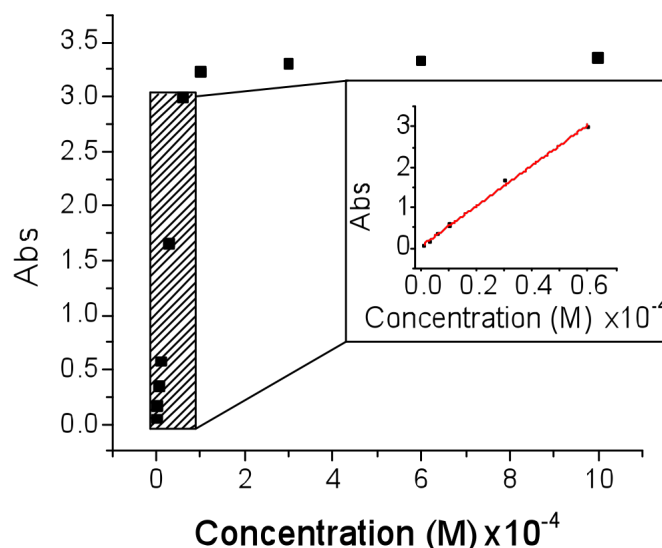


Figure 3.12 FITC concentration calibration curve. Absorption at 490 nm is plotted vs. the FITC concentration. Inside plot corresponds to the linear zone of the calibration plot zoomed in.

From the calibration curve [Figure 3.12] a FITC molar absorption coefficient of $5.1 \times 10^6 \text{ M}^{-1}\text{m}^{-1}$ was found for our mixture at 490 nm. This value is similar to the one found by Imhof *et al.* in similar mixtures, $3.64 \times 10^6 \text{ M}^{-1}\text{m}^{-1}$, and close to the one specified in the product information sheet of Thermo Scientific, that is $6.8 \times 10^6 \text{ M}^{-1} \text{m}^{-1}$ at pH 8 at a wavelength of 495 nm. From this value and the absorption at 490 nm of the modified nanoparticles, a concentration of $1.986 \times 10^{-5} \text{ M}$ is found.

3.2.1.3. Silane (BZ / APTES)

Functionalization of magnetite nanoparticles has been previously done with different surfactants. The use of silanes was approached by different authors such in the literature.^{132, 143, 144} Linking benzophenone moieties around nanoparticles would provide a tool to covalently bind them to a polymer network. A protocol is designed and proceeds as follows:

Materials: Toluene (Riedel-de Haën, puriss. p. a.), chloroform (VWR, HiPerSolv Chromanorm), triethylamine (Sigma-Aldrich, $\geq 99.5\%$ (GC)) were purchased and used without further purification. BZ-silane was obtained as described in Section 3.1.3.

Procedure: In order to modify the nanoparticles, 100 mg of them were redispersed in 20 mL of toluene. The toluene mixture was introduced in a flask with a

blanket of nitrogen together with 0.25 mL of triethylamine. After stirring for 5 minutes, 0.5 g of BP-silane were introduced in the mixture dropwise and the solution was stirred at room temperature for 12h. After this time, ethanol was added to the solution and the nanoparticles were magnetically separated at least 3 times. The nanoparticles were finally dispersed in chloroform and stored in the fridge protected from light.

Characterization. Transmission FTIR is performed on KBr pellets of the nanoparticles modified with the BZ-silane [Figure 3.13]. There are two peaks at 2900 cm^{-1} corresponding to the methylene group. These can correspond to remaining oleic acid methylenes on the chain. A small peak at 1650 cm^{-1} denotes the presence of the ketone -C=O , typical for benzophenone. There is another peak at 1050 cm^{-1} corresponding to Si-O-C stretching. As a conclusion, there are indications that the benzophenone silane has been attached to the magnetite nanoparticles, however, some residual oleic acid moiety could still be present.

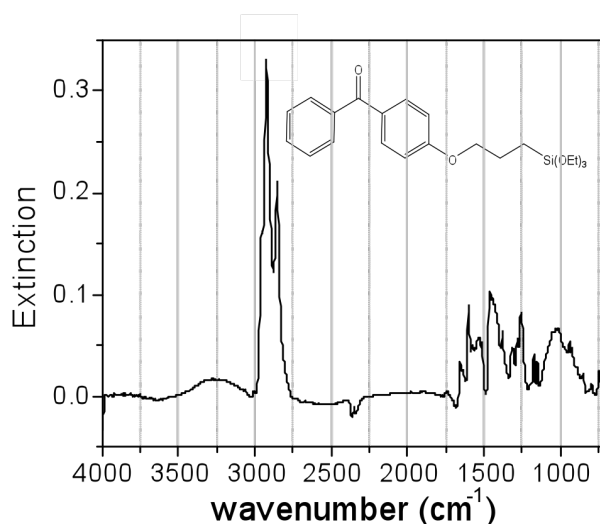


Figure 3.13 FTIR spectrum of magnetite nanoparticles functionalized with benzophenone silane.

UV-VIS spectra of magnetite nanoparticles dispersion in chloroform at the same concentration of nanoparticles (0.0325 mg/mL) covered with BZ-silane and covered with oleic acid (OA) is shown in Figure 3.14. The ratio between the two of them shows clearly the absorption of the benzophenone.

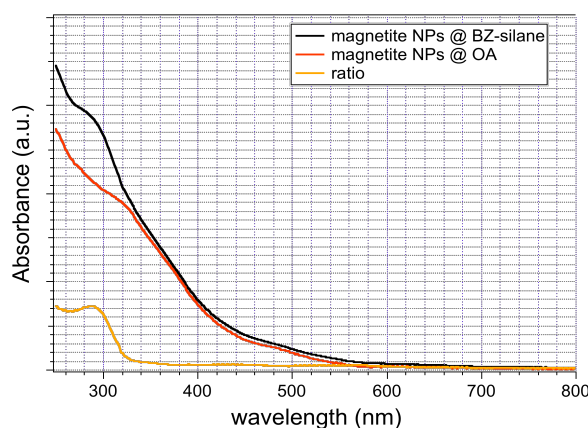


Figure 3.14 UV-VIS spectra of magnetite nanoparticles dispersion in hexane at the same concentration of nanoparticles (0.0325 mg/mL) covered with BZ-silane (black line), covered with oleic acid (OA) (red line), and the ratio between the two of them, which shows the absorption of the benzophenone.

3.2.1.4. Citric acid

It has been shown how magnetic nanoparticles can be covered by silica and, thus, be dispersed in aqueous solutions. It has been reported how diamagnetic organic coatings can decrease the saturation magnetization of magnetic nanoparticles.¹³⁷ It was suggested that the carboxyl group interacts with a trivalent iron atom located on the surface by forming a bridge with the two oxygen atoms. Therefore, citric acid is a very attractive surfactant for magnetite nanoparticles due to the three carboxylic acid groups, which provide the nanoparticles with the ability to disperse in water. A protocol based on heating for a long period of time is followed to achieve a surfactant exchange between oleic acid and citric acid and is based on Lattuada *et al.* protocol.¹⁴⁵

Materials. N,N-dimethylformamide (Sigma-Aldrich, $\geq 99.8\%$), 1,2-dichlorobenzene (Sigma-Aldrich, 99%), citric acid (Sigma-Aldrich, $\geq 99.5\%$), diethyleter (Sigma-Aldrich, $\geq 99.7\%$).

Procedure. A mixture of 10 mL of 1,2-dichlorobenzene and 10 mL of dimethylformamide (DMF) was prepared. An amount of 0.1 g of citric acid was added to the mixture and stirred until no solid could be distinguished by naked eye. 120 mg of as-prepared magnetite nanoparticles were precipitated from the mother solution and redispersed in the mixture aforementioned. The mixture was stirred at 100 °C for ~24h. Next, diethyleter was added to the mixture and magnetic separation is used to precipitate the nanoparticles. The supernatant is discarded and acetone is used to

disperse the NPs. Magnetic separation is repeated at least 5 times and, finally, the nanoparticles are dispersed in water.

Optical characterization. TEM has been used to study the dispersion of the nanoparticles in the new solvent.

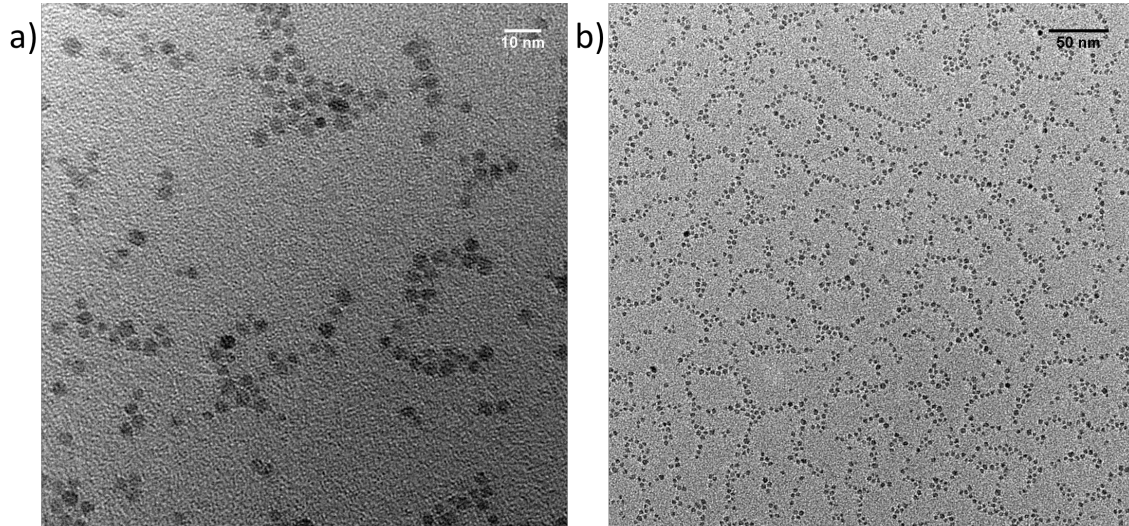


Figure 3.16 TEM micrograph of magnetite nanoparticles redispersed in water after being coated with citric acid. The scale bar in a) is 10 nm, in b) is 50 nm.

TEM micrographs in Figure 3.16 show a perfect distribution of nanoparticles with no agglomeration observed.

4. Results and Discussion

4.1. Thin film hydrogel study

4.1.1. Introduction

Hydrogels are hydrophilic polymer networks that swell in water. When their swelling depends upon external conditions, hydrogels can be considered smart materials. Some potential factors affecting swelling are: pH, magnetic properties, pressure and temperature. In this work, temperature-dependent hydrogels are investigated. As mentioned in Section 1.2, the polymer chains experience a change from random coil below the Lower Critical Solution Temperature (LCST) to a dense globular structure above this temperature. One of the most extensively studied thermal responsive hydrogels is poly(*N*-isopropylacrylamide) (PNIPAAm), which exhibits a sharp phase transition in water at 32 °C. This chapter contains results regarding the use of nanomechanical cantilever sensors (NCS) to study the effect of temperature and pH on these gels. NCS allow the monitoring of films, deposited on cantilevers, through mechanical changes. Surface plasmon resonance with optical waveguide spectroscopy (SPR-OWS) is used for comparison. SPR-OWS is a thin-film technique that uses light to excite plasmons and waveguides on the gel and tracks changes in optical thickness or dielectric constant. For a further description of NCS and SPR-OWS refer to Sections 2.1 and 2.2, respectively.

PNIPAAm polymers have mostly been studied at the macroscopic scale. Because swelling and deswelling is a diffusion-limited process, size plays a role. One of the biggest issues of smart hydrogels is their slow collapse response. For practical applications, it becomes therefore necessary to work with thinner and smaller hydrogels.¹⁴⁶ In this regard, PNIPAAm thin films have been proposed as candidates for actuators in microfluidic devices, or biomaterial in drug delivery. One could think, for instance, of a PNIPAAm layer as a coating for scaffolds in tissue engineering. PNIPAAm could collapse at body temperature releasing drugs to the system. When referring to thin film polymers one could think about polymer networks or polymer brushes. Polymer brushes are polymer chains tethered to an interface (typically a surface) on one end and stretched away from it to avoid overlapping.¹⁴⁷ This configuration differs from the one of polymer networks where chains can be link to

the substrate in multiple anchoring points, which makes them more stable. Unlike polymer brushes, the thin gel film can be transferred from the surface of one material to the surface of another material or used as a free-standing film.¹⁴⁸ In a hydrogel network, chains are no longer able to move long distances relative to each other because they are all tied into the network. Meanwhile, on a smaller scale (i.e., shorter than the average distance between two neighboring crosslinks) the mobility of the chains is not constrained by the crosslinking. When a tension is applied to the polymer network (i.e. change in T, pH, etc.) its chains stretch quite considerably, resulting in exceptionally large elastic reversible deformation. Therefore, networks and brushes can be considered completely different systems. Crosslinked smart polymers attract greater interest than linear smart polymers for drug delivery applications because they allow the drug to be released in response to a change in the environment.^{13, 149, 150} This study is focused on PNIPAAm networks.

Many techniques can be used to study PNIPAAm networks. Most approaches are restricted to bulk gels. For instance, a macroscopic gel can be observed using a camera⁵⁶ or a microscope or, most commonly, bulk gels can be weighed before and after changing the temperature.¹⁵¹ Dynamic light scattering can be used to study these changes in particles composed of smart materials.^{12, 37, 152} In order to study thin films at an interface, techniques based on optical properties of the layer can be used, like ellipsometry¹⁵³ or surface plasmon resonance (SPR). With SPR either the thickness or the refractive index of the layer have to be a known parameter. When coupled to optical waveguide spectroscopy (OWS), which requires the use of thicker films, one can independently determine the refractive index and the thickness of the layer. Many groups have used this technique successfully to study PNIPAAm systems.^{38, 39, 109, 154} Quartz crystal microbalance with dissipation monitoring (QCM-D) is another technique used for the study of thin films. Mass changes as well as viscoelastic variations are detected and can be used to determine changes on PNIPAAm gels, as Guangzhao Zhang *et al.* already showed.¹⁵⁵⁻¹⁵⁷ All these thin film techniques rely on the change of optical properties, mass or viscoelastic properties. In this work, nanomechanical cantilever sensors (NCS), which offer insights on the mechanical changes, are used together with SPR-OWS, as a comparison, to study changes in PNIPAAm networks.

Nanomechanical cantilevers (NCS) have been successfully used as sensors in different applications such as gas sensing,^{158,77} UV irradiation¹⁵⁹ and DNA

hybridization^{160, 161} amongst others. One area of special interest is the detection of conformational changes in polymers. For instance, Feng Zhou *et al.* have shown how ion transport in and out of polyelectrolyte brushes changed their conformation and created a deflection on NCS.^{6, 162} This proved that polyelectrolyte brushes can be used in the electroactuation of cantilevers. Snow D. *et al.* studied the effect of different solvents on poly(vinylalcohol), poly(vinyl butyral-co-vinyl alcohol-co-vinyl acetate), and poly(vinyl chloride-co-vinyl acetate-co-2-hydroxypropyl acrylate). Deflection of the cantilevers varied depending on the mixing energy of the polymer and the solvent.¹⁶³ In another approach, Oliviero *et al.* studied the use of a functional terpolymer based on two functional monomers that confer to the polymer the ability to bind to the nanocantilever and, at the same time, react with nucleophilic species on biomolecules. The polymer, deposited onto NCSs by dip coating, served as anchor for more specific biomolecules that would be used as binding sites.¹⁶⁴ This method provided a fast, inexpensive, and robust route to bind biomolecules. Despite all the above-mentioned efforts, there are not reported studies on PNIPAAm networks by means of NCS.

Previous PNIPAAm NCS studies have been limited to polymer brushes (not networks). For instance, Bradley and coworkers investigated PNIPAAm polymer brushes by means of NCS. They showed how PNIPAAm brushes and plasma polymerized N,N-diethylacrylamide showed a collapse behavior upon heating.¹⁶⁵ More precisely, two regimes were observed upon heating: before the LCST, dehydration is reflected through a tensile stress; after the LCST, compressive surface stress is associated with the bimetallic effect between the collapsed polymers and the cantilever materials. Despite the value of these studies, it is worth noting that polymer brushes are simpler systems compared to polymer networks, because there is only one anchor point to the surface and, hence, fewer interchain effects have to be taken into account. Other studies on NCS were done using either self-assembled monolayers (SAM) terminated in carboxylic acid or amine, or polyelectrolyte brushes and were based on the pH effect. Work on carboxylic acid-terminated SAMs showed an increase in the pKa of the acids in comparison to bulk values.¹⁶⁶⁻¹⁶⁸ This lower acidity was attributed to local mutual interactions among the densely packed carboxyl groups on the surface. More precisely, the reason was the accumulation of negatively charged ions (carboxylate groups) close to the dielectric material

constituted by the alkyl chains. Therefore, as the number of deprotonated species at the surface increases, it becomes more difficult to deprotonate other acidic groups.

PNIPAAm hydrogel thin films have been widely studied by means of SPR-OWS.^{29, 38, 39, 109, 169} This technique provides data on films tethered to a rigid substrate. Thus, the use of NCS on thin film PNIPAAm hydrogels, where the bending of the substrate (i.e., cantilever) is allowed, might provide more information regarding stress exerted by the thin film. In this section, we describe the deposition of PNIPAAm networks on nanomechanical cantilevers and the characterization of its temperature-dependent and pH-dependent collapsing and swelling, analyzed by nanomechanical cantilever sensors. Surface plasmon resonance in conjunction with optical waveguide spectroscopy is used for comparison purposes.

4.1.2. Experimental procedures

The material used in this study is PNIPAAm-based hydrogel described in Section 3.1.1. Two different techniques were used: NCS and SPR-OWS.

For SPR-OWS experiments, hydrogel layers were prepared by spincoating of photocrosslinkable polymers on SPR substrates, followed by photocrosslinking as described in Section 3.1.4. SPR substrates consist of LASFN9 glass coated with a 2 nm thick chromium layer and a 50 nm thick gold layer on top. The chromium layer works as an adhesive layer. In order to attach the polymer covalently to the substrate, the use of a thiol is needed. The synthesis of a benzophenone-derivative with a thiol anchor (4-(3-mercaptopropoxy)benzophenone, BZ-thiol) is described elsewhere.⁹⁵ In a standard protocol, after Cr and Au were evaporated, the substrates were immersed in a 5mM thiol solution overnight. The next day, the substrates were rinsed thoroughly with ethanol. Spincoating of the polymer was made from a chloroform solution of the PNIPAAm. Concentrations of the solution ranged from 2% to 10%, depending on the desired thickness. Coated samples were dried in vacuum at 50 °C for at least 2 h and irradiated either 30 minutes or 1h (corresponding to PED 3.14 and 6.28 J.cm⁻²) with a Stratagene UV Stratalinker 2400 operating at 75 W with a peak wavelength of 365 nm. The photocrosslinked hydrogel layers were studied by means of SPR and OWS in the Kreschmann configuration, as described in Section 2.2.

For the nanomechanical cantilever sensor experiments a chip with an array of cantilevers is needed, as mentioned in Section 2.1. The NCS preparation involved

several steps. For the use of the cantilever as a mechanical sensor, one of the sides of the cantilever has to be either uncovered or passivated. To be able to observe a bending, there should be a differential stress between the upper and the lower side of the cantilever.

The improved silanization protocol is described in the following Section 4.1.3.1. The best strategy was as follows: the first step consisted of cleaning the cantilever surface with an Ar/O₂ plasma (2:1) for 10 minutes at 150 W. Next, silanization was performed at 110°C in toluene reflux overnight at a concentration of 0.15 mM benzophenonesilane. After silanization, the chip was extensively rinsed with toluene. The PNIPAAm-based hydrogel was diluted in cyclohexanone to a concentration of 2% (w/w) and drop-cast on the NCS by an inkjet dispensing method that dispersed drops of 0.4 nL. For every cantilever, 5 drops were needed [Figure 4.1.1], one next to the other, to cover the whole surface. Two cycles were applied per cantilever.

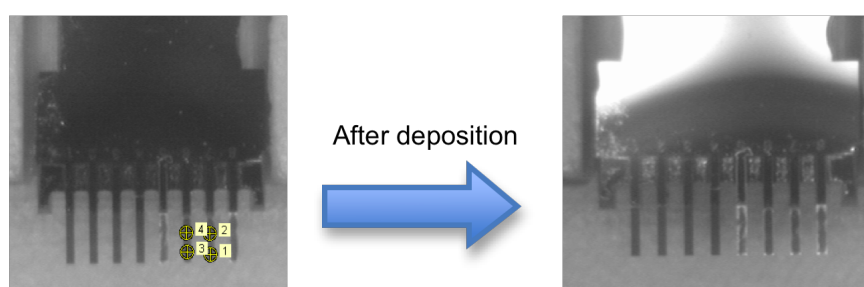


Figure 4.1.1. Snapshot made with Nano-Plotter program of before and after positioning of the drops. Note that only 2 drops per cantilever are pictured in the snapshot and the usual amount, to cover the whole cantilever, was 5 drops.

At least two cantilevers per chip were not inkjet-printed and used as reference. As already mentioned, laser-beam detection was used. In order to avoid interferences caused by polymer-related changes in refractive index or surface roughness, the polymer was deposited on the backside of the NCS. Other solvents, such as ethanol and water, were tried but their vapor pressure is too high and the nanopipette nozzle was clogged with dry polymer. The solvent on the nozzle evaporated too fast in between injections and the dry polymer left on the exit of the nozzle did not allow more solution to be deposited. NCS chips were dried in vacuum at 50 °C for at least 2 h and irradiated for different times (from 30 to 60 minutes corresponding to PED of 3.14 to 6.28 J.cm⁻²) with a Stratagene UV Stratalinker 2400 operating at 75 W with a peak wavelength of 365 nm.

The overall coating thicknesses of the benzophenone silane and the polymer were checked with an imaging ellipsometer (EP3 imaging spectroscopic ellipsometer, Nanofilm, Göttingen, Germany) directly on each of the NCS. A further description of ellipsometry can be found in Section 2.4. Since the polymer was deposited on the back, the cantilever had to be positioned on the backside, to be measured. This is a very delicate step because the 700 nm thick cantilever is easily broken. The measurements were carried out at an angle of incidence of 60°. Using interference filters and a Xenon lamp as the light source, the wavelength was set to 403.5 nm. The field of view, utilizing a 10x objective, was 0.330 mm x 0.330 mm. On each cantilever, a region of interest with an area of 50 nm x 300 nm was used to average the thickness over this area. To achieve highest accuracy, four zone measurements were carried out. For the calculation of the layer thickness of the polymer, a multilayer model for homogeneous films covering the cantilever was applied. The refractive indices of the layers used were:

Layers	n	k
Silicon	5.4815	0.3463
Silica	1.491	0
SAM	1.5	0
PNIPAAm	1.517	0

Table 4.1.1 Multilayer characteristics for ellipsometer modeling.

The deflection of each of the 8 NCS was monitored with a Scentris™ platform (Veeco, USA) based on the beam deflection detection principle, as mentioned in Section 2.1. Since the deflection of each cantilever was determined independently, it was possible to calculate the differential deflection between a PNIPAAm coated and a reference. Liquids were exchanged by a system of tubes and valves and were pumped out by a manually operated syringe.

For experiments at different pHs, buffer solutions were prepared from pH 2 to 8 using acetate/acetic acid system and different combinations of phosphoric acid/hydrogen phosphate/dihydrogen phosphate. The buffer was prepared in 1 L with a 10 mM concentration of buffer and the ionic strength was 20 mM. To ensure the same ionic strength sodium chloride was added as needed. The exact amounts are described in Table 4.1.2.

pH	acid component	basic component	NaCl
8	0.8 mmol (0.096 g) NaH ₂ PO ₄	9.1 mmol (1.2933 g) Na ₂ HPO ₄	0.102 g
7	5 mmol (0.6 g) NaH ₂ PO ₄	4.9 mmol (0.696 g) Na ₂ HPO ₄	0.01 g
6.2	8.6 mmol (1.032 g) NaH ₂ PO ₄	1.3 mmol (0.185 g) Na ₂ HPO ₄	0.429 g
5	3.3 mmol (0.2 g) CH ₃ COOH	6.6 mmol (0.542 g) CH ₃ COONa	0.78 g
4	8.3 mmol (0.5 g) CH ₃ COOH	1.6 mmol (0.131 g) CH ₃ COONa	1.073 g
3	1 mmol (0.098 g) H ₃ PO ₄	8.9 mmol (1.068 g) NaH ₂ PO ₄	0.649 g
2	5.5 mmol (0.539 g) H ₃ PO ₄	4 mmol (0.48 g) NaH ₂ PO ₄	0.649 g

Table 4.1.2. Amounts of buffer components mixed.

When water was required in the experiments, Milli-Q (ultra pure water, > 18.2MΩcm²) was used.

4.1.3. Results and discussion

4.1.3.1. Benzophenone silanization optimization

To determine the best silanization protocol, a series of experiments were performed on nine silicon samples (1x1 cm²). Three different protocols were considered to clean the surface:

1. Acid piranha (1:1 hydrogen peroxide and sulfuric acid) for 30 minutes followed by rinsing with copious amounts of water.¹⁷⁰
2. Acid piranha for 5 minutes followed by rinsing with copious amounts of water + oxygen plasma for 1 minute.
3. Acid piranha for 5 minutes followed by rinsing with copious amounts of water + argon/oxygen plasma (0.2 mbar:0.1mbar) for 10 minutes with a Power of 150 Watts.¹⁷¹

After the treatment, the samples were silanized with the standard protocol, which consists of immersion of the samples in a 10mM ethanolic solution of benzophenonesilane overnight.

One sample from every protocol was removed after 13 h, another after 61 h and another after 82 h.

The contact angle was then measured as explained in Section 2.8. The higher the contact angle, the more benzophenones on the surface. Values for contact angle vs. time are depicted in Figure 4.1.2.

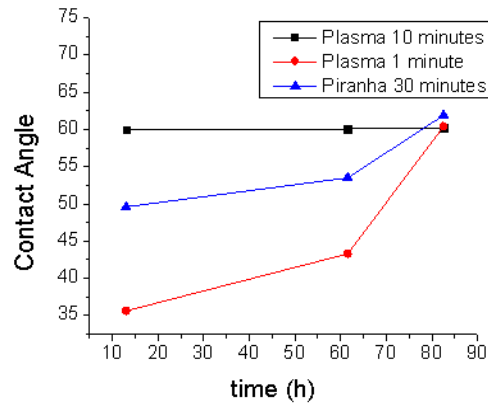


Figure 4.1.2 Contact angle of samples cleaned with different protocols vs. silanization time.

Contact angle measurements reveal that plasma cleaning for 10 minutes with argon and oxygen creates a surface that couples to the silane most efficiently. After 13 hours of treatment, the contact angle is as high as possible with this silanization protocol. This result suggests that this cleaning protocol creates the most hydroxyl groups, which are necessary for the silanization process.

In order to increase the contact angle, three different silanization processes are tested. Again, nine samples are cleaned with piranha treatment for half an hour. Afterwards, the samples are treated in three different ways and contact angles are measured after different silanization times [Figure 4.1.3].

1. 20 mL dry toluene + 3 mM benzophenone silane + 0.4 mL triethylamine
2. 20 mL dry toluene + 3 mM benzophenone silane + 0.2 mL triethylamine + heating to 110 °C
3. 20 mL ethanol + 3 mM benzophenone silane + 0.2 mL sulfuric acid

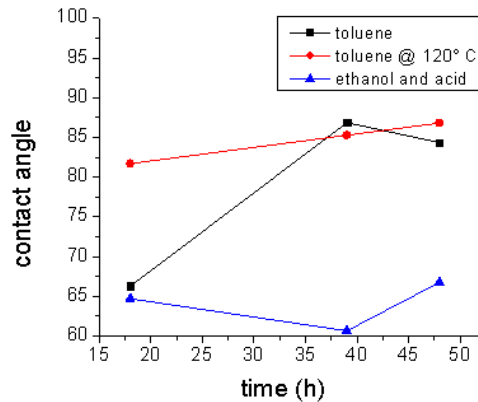


Figure 4.1.3 Contact angle of samples using different silanization procedures vs. silanization time.

This experiment brings us to believe that the toluene treatment at higher temperature is the most efficient one. High contact angles are reached within the first 12 h.

According to these results, the best protocol is cleaning the cantilever with Ar/O₂ plasma for 10 minutes and silanizing the cantilever with toluene at high temperature. When these protocols were transferred to the cantilevers, the NCS experienced what we call “edge-effect”. The silane layer is thicker than expected. When checked by ellipsometry, layers of 40 nm were measured.

It was found, after different trials, that a concentration of 0.15 mM of benzophenonesilane was enough to deposit a monolayer of silane. The thickness of the silane checked by ellipsometry was around 2 nm. The use of triethylamine to accelerate the process was avoided since the same results were obtained without using it.

4.1.3.2. Effects of the pH

The pH solutions were freshly made and consisted of different buffers. All buffers had a concentration of 0.01 M. The ionic strength was adjusted with sodium chloride to ensure a final value of 0.02 M for all of them. The pH was measured using a standard pH meter [Table 4.1.3].

Ph	Buffer species	Measured pH
8	Dihydrogen phosphate	7.99
7	Dihydrogen phosphate	6.83
6.2	Hydrogen phosphate	6.28
5	Acetate	4.7
4	Acetate	3.96
3	Phosphate	3.13
2.5	Phosphate	2.64

Table 4.1.3 Buffer characteristics

To study the influence of pH in the swelling of the polymer gel, experiments by means of two different techniques, namely NCS and SPR-OWS, were performed and compared.

An SPR-OWS experiment was performed on a sample spin coated from a 2% solution of PNIPAAm in ethanol. After drying overnight, the hydrogel layer was crosslinked for 40 minutes. Dry thickness measured with a profilometer was 144nm.

In these experiments, samples are flushed with ultrapure water. A kinetic measurement following the plasmon angle is started. When the plasmon resonance remains at the same minimum angle (after stabilization), a scan of the reflectivity vs. angle is measured. Next, a pH 8 solution is inserted and another kinetic measurement is started until the layer is stabilized. A scan of the reflectivity vs. angle is measured for every pH (from pH 8 to 2). Each of these experiments can be fitted with a box model approximation, as explained in Section 2.2, and the refractive index of the hydrogel and thickness can be extracted. In order to visualize the effect at every pH, the minimum plasmon angle and the thickness extracted from the fitting can be plotted vs. the pH.

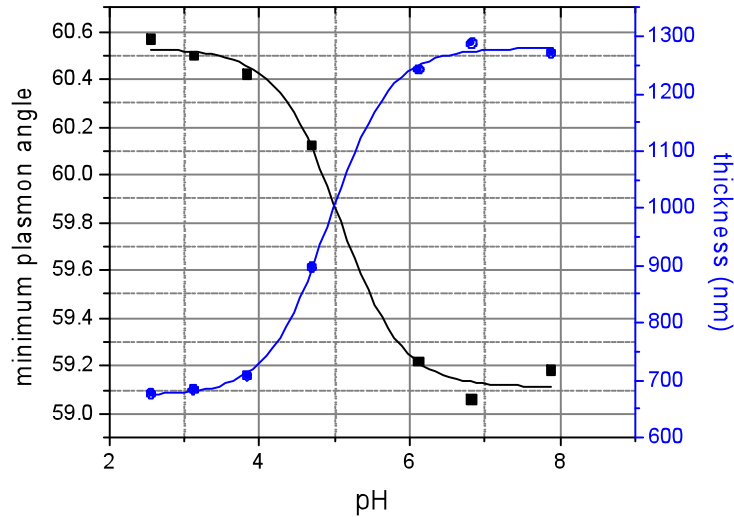


Figure 4.1.4 Effect of pH on minimum of the plasmon angle (■) and the thickness (●). Lines represent the sigmoidal fitting to the data points.

Figure 4.1.4 shows the displacement of the minimum angle position when pH is decreased from 8 until 2. From the graph, it can be seen that decreasing the pH causes an increase in the plasmon angle. From pH 2.5 to pH 4 the change in thickness is only 30 nm whereas, from pH 4 to pH 6 there is an increase of 534 nm, 90% of the total increase. From pH 6 to 8 the thickness remains stable increasing only 5% of the total growth.

The pH-dependent change in SPR-OWS and NCS experiments, as can be seen subsequently, can be fitted to a sigmoidal expression (Equation 4.1.1). Sigmoidal fit has already been used to estimate the transition temperature on PNIPAAm gels.^{19, 172, 173} The equation is as follows:

$$y = y(\text{collapsed}) + \frac{y(\text{swollen}) - y(\text{collapsed})}{y + \exp\left(\frac{pH - pH_c}{\Delta pH}\right)} \quad (4.1.1)$$

where y is the pH-dependent parameter (deflection, plasmon angle, thickness), $y(\text{collapsed})$ is the parameter at lower pH, $y(\text{swollen})$ is the parameter at higher pH, and pH_c is critical pH.

Fitting of pH-dependent-curves can be used to relate this data to more significant physical parameters. The inflection point is defined as the transition point; in our case it is going to be called critical pH, pH_c . At this pH, the layer swells

The sigmoidal fit, showed in Figure 4.1.4 with a black line for the plasmon and blue line for the thickness, gives a critical pH of 4.98 ± 0.1 . In the case of the PNIPAAm used in these experiments, the concentration of carboxylic acid groups in the network is only 5%. This value is in close agreement with reported pKa values for bulk PNIPAAm. For instance, Brazel and coworkers studied PNIPAAm polymers containing methacrylic acid and found values between 5.5 and 6.¹⁵⁰

Experiments with the same buffer solutions and polymer are performed using NCS. For a typical experiment, ethanol was initially flowed through the system to remove bubbles in the cell. Next, at least 20 mL of solution pH 8 were injected. After injecting the solutions, the system was left for 10 to 15 minutes until the signal was stable. In Figure 4.1.6 one of the pH experiments is shown. The polymer used in this experiment had a dry thickness of 13 nm, according to ellipsometry data. Experiments performed in samples prepared in the same way and measured by SPR-OWS confirmed that the swelling rate of the polymer from dry to swollen is 9 ± 1 times. Consequently, after 30 minutes of crosslinking time, the thickness increases to ~ 120 nm when water is flown through.

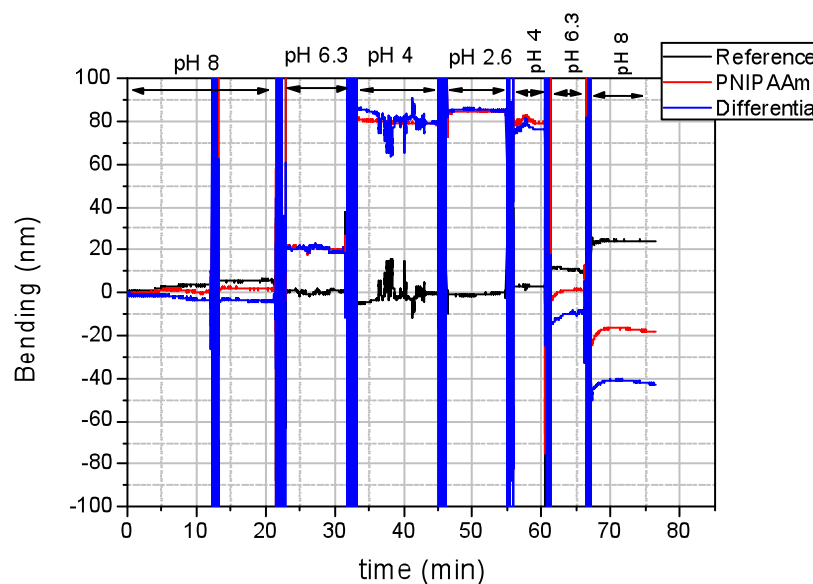


Figure 4.1.6. Bending of cantilevers covered with PNIPAAm in response to change in pH.

Figure 4.1.6 shows the summarized bending of the reference cantilevers, PNIPAAm-covered cantilevers, and the differential of both. When solution was injected, the flow and the difference in refractive index of the liquids in exchange

generate noise that can be observed on the significant high and low values of bending (i.e., minute 13, 22, 33, 46, 55, 62, 67). From minute 36 to minute 42 there was a small bubble close to the reference cantilevers that caused some noise. It is considered that this noise affects the stability of the signal for a short period of time but once the bubble disappears, the bending signal is stable.

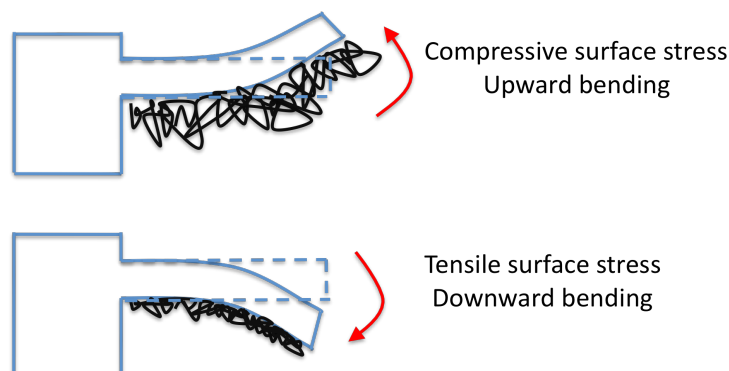


Figure 4.1.7. Scheme of cantilever subjected to tensile and compressive surface stress by the hydrogel located on the backside of the cantilever.

In the setup used, positive bending means downwards bending of the cantilever. Since the polymer was deposited on the lower surface, downwards bending corresponds to a tensile stress [Figure 4.1.7]. It is called tensile because the adsorbed layer pulls the cantilever and produces therefore a bending towards the functionalized side.⁸⁶ Note that a tensile stress in the cantilever corresponds to a compressive stress in the polymer layer. In the opposite situation, when the cantilever bends upwards, the adsorbed layer produces a bending away from its functionalized side, corresponding to compressive stress in the cantilever.

From pH 8 to pH 2.6 the bending increases from 4 nm to 86 nm. Acid groups that were ionized become protonated and the polymer therefore loses some water. This contraction of the polymer translates to a tensile stress in the cantilever. The sharpest increase was observed between pH 6.3 and pH 4, where the bending was 58.3 nm. When pH was raised back to 8, the bending of the cantilever decreased from 86 to -41.7 nm. Again, the major bending occurred when pH was increased from 4 to 6.3. In this case, the polymer is swelling due to the repulsive forces between the ions and the entrance of water molecules into the network.

From these results, one can plot the differential bending at each pH and extract, through a sigmoidal fitting, the critical pH [Figure 4.1.8]. On the right axis the surface stress is plotted. This stress comes from the mechanical changes in the polymer

attached on one side of the cantilever, which cause it to bend. The sensitivity of a cantilever increases with the ratio of cantilever length and thickness. The actual deflection scales with the cantilever dimensions; therefore, deflection responses should be expressed in terms of surface stress to be able to compare cantilever responses acquired with different setups. The most-used formula to calculate surface stress values is Stoney's equation:

$$\Delta\sigma_{st} = \frac{E_{Si}t^2\Delta x}{3L^2(1-\nu)} \quad (4.1.2)$$

where E_{Si} is Young's modulus, $1.7 \times 10^{11} \text{ N/m}^2$, t is the thickness of the cantilever, 700 nm, ν is Poisson's ratio, 0.24, L is the length of the cantilever, 500 μm , and Δx is the bending.

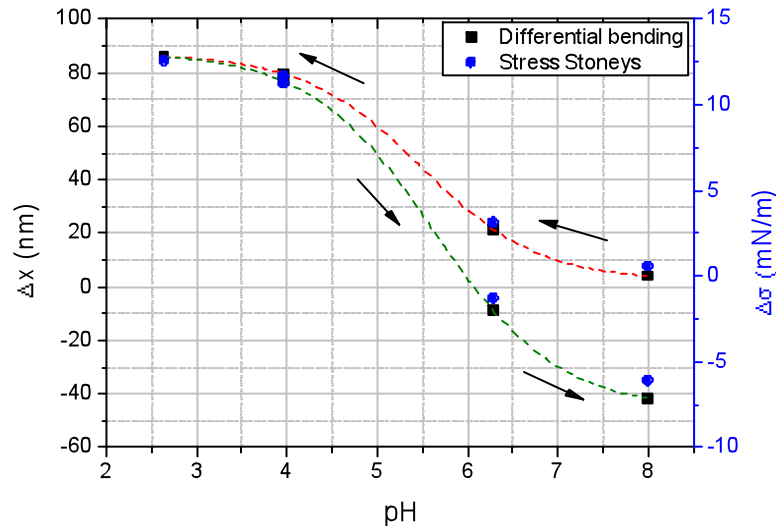


Figure 4.1.8 Deflection and surface stress on cantilever coated with PNIPAAm vs. pH (note that reference is already subtracted) Dashed line corresponds to the sigmoidal fitting for first decrease in pH in red, and latter increase in green.

The average pKa calculated for the polymer when pH is initially decreased is 5.31 ± 0.25 . This value is in agreement with bulk pKa values of PNIPAAm, already described beforehand as 5.5-6. Hysteresis between decreasing and increasing the pH can be observed in the graph. The pKa value, according to the sigmoidal fitting (in green), is higher when pH is raised back: 5.62. This means that after the initial loss of water, while pH was decreased, the polymer is able to swell up to a higher thickness when pH is brought back to 8. Hysteresis on pH-responsive SAMs has also been

observed. For instance, in work made by Raiteri and coworkers, who investigated amine and acid-terminated SAMs on NCS, a hysteresis when pH was changed was reported, yet, no explanation was given.¹⁶⁸ A polymer network consists of a series of chains bonded at crosslinking points. The bonding nature can be chemical, i.e., covalent bonds, or physical, as entanglements of the chains. When the polymer free energy is changed by varying the pH of the solvent and making the network contract, these physical entanglements can disappear and new ones can develop. This process is more pronounced on the first cycles, when some uncrosslinked chains might be flowing out of the network. The new conformation of the network creates different stresses on the cantilever that explain the observed hysteresis.

On the other hand, the pKa obtained from the SPR-OWS was 4.98 ± 0.1 , compared to 5.31 ± 0.25 obtained with NCS. The difference lies in the range of the experimental error of the values.

Stresses calculated from Stoney's equation are on the same range of those obtained by Watari *et al.* or Fritz *et al.*^{166, 175} Both worked with SAMs of mercaptohexadecanoic acids and obtained values that go from 0.5 to 32 mN/m. In our case, when pH is first decreased from 8 to 6.3, the stress enforced on the cantilever is 1.63 ± 1.27 mN/m (differential deflection of 11.16 ± 8 nm); when pH is decreased further to 4, the stress is 6.82 ± 2.41 mN/m (differential deflection of 46.65 ± 16.5 nm), and, finally, stress is 0.82 ± 0.13 mN/m (differential deflection of 5.64 ± 0.9 nm). Nevertheless, Stoney's equation has been greatly debated in the last years and different approaches have been contemplated depending upon the layer characteristics.¹⁷⁶⁻¹⁷⁸ Bradley *et al.* and Bumbu *et al.* used Atkinson's approximation, which accounts for cantilevers coated by layers with a thickness ratio δ higher than 0.1 ($\delta = t_c/t_s$, t_c is thickness of coating, t_s is the thickness of the substrate).^{165, 179}

$$\Delta\sigma_{At} = \frac{E_{st} t_s^3 \Delta x}{3L^2 t_c^2 \left(1 + \frac{t_s}{t_c}\right) (1 - \nu)} \quad (4.1.3)$$

where t_s is the thickness of the substrate and t_c is the thickness of the coating. The thickness ratio in our case is ~ 0.17 , which means Atkinson's approximation would be more adequate. Values calculated from Stoney's equation were given beforehand and used to compare to literature. Although more appropriate, Atkinson's approximation has not been widely used in the literature. In order to calculate the

stress with Atkinson's approximation, the thickness of the coating is estimated from SPR data. More precisely, swollen thickness is estimated using the swelling ratio known for samples crosslinked with the same conditions. From the pH experiment performed in SPR the thicknesses at every pH are known for the SPR sample. Thicknesses for cantilever coating at every pH are estimated from these values. Table 4.1.4 shows the calculated surface stresses according to Atkinson's formula.

pH	Surface stress Atkinson's (N/m ²)
8 to 6.3	1.16E+04 ± 9.06E+03
6.3 to 4	9.34E+04 ± 3.30E+04
4 to 2.6	1.15E+04 ± 1.85E+03

Table 4.1.4 Values of stress calculated according to Atkinson's equation.

Experiments analyzing the dependence of PNIPAAm hydrogel to the change in pH showed that exists a critical pH in both measurement techniques. After fitting the results and extracting the inflection point, the critical pH has been determined. At this pH_c the layer swells dramatically when pH is increased, or deswells when pH is decreased [Figure 4.1.4]. The swelling behavior can be seen in the NCS by an increase in the compressive stress. It is well known that compressive stress on cantilevers coated by polymers can be due to swelling of the network.⁶ In the case of the SPR-OWS, fitting with Fresnel equations gives us an idea of the optical thickness, which directly correlates with the swelling of the network.

4.1.3.3. Transition temperature measurements

LCST of PNIPAAm gels that had different crosslinking density were estimated using NCS and SPR-OWS. It is well known that ionic strength can influence the LCST^{15, 16, 18, 20}; hence, measurements varying the T were performed with MilliQ water as a solvent.

The gel crosslinking density can be tailored changing the UV exposure time. For these experiments, two different exposure times were used: 30 minutes and 60 minutes.

A temperature ramp with an increase of 3 °C per minute was applied to the NCS while the deflection of the cantilever was recorded. Figure 4.1.9 shows the

deflection of a cantilever crosslinked for 60 minutes. In this case, three cantilevers were coated with PNIPAAm and three were used as references (the other two from the 8-cantilever array were broken on the process) [Figure 4.1.9 (a)]. Reference cantilevers are affected by the T variation. It is important to subtract these effects from the bending of cantilevers coated with PNIPAAm in order to achieve a better interpretation [Figure 4.1.9 (b)]

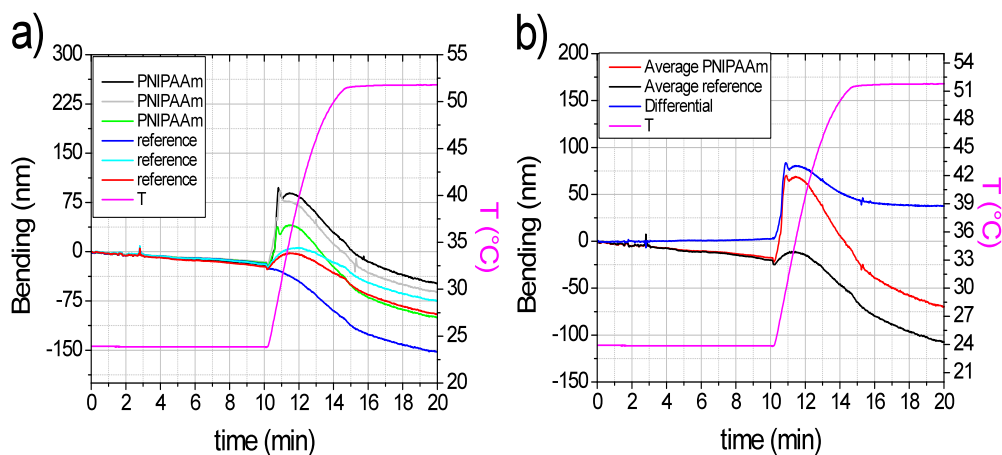


Figure 4.1.9 Bending of cantilevers crosslinked for 60 minutes (a) showing all the individual cantilever deflection and (b) summarizing PNIPAAm coated cantilevers and reference ones together with the differential.

The results presented in Figure 4.1.9 (b) show that, when T is increased, the deflection increases; in other words, there is a tensile stress on the cantilever [Figure 4.1.7]. This is caused by polymer contracting due to dehydration of the polymer when LCST is approached. Note that the reference cantilever deflection has a small increase in deflection as well. As already mentioned, the reference consists of cantilevers containing the benzophenone silane SAM but no polymer deposited on top. The SAM layer might have a small response to the temperature. This effect and other noise that might affect the measurement are removed by the subtraction of the reference cantilever deflection.

At even higher temperatures, the bending of the polymer-coated cantilever decreases slightly until it gradually reaches a plateau. For a better understanding, a plot of cantilever bending as a function of temperature is presented in Figure 4.1.10. In red there is the experiment with the PNIPAAm crosslinked 60 minutes,

corresponding to the data shown in Figure 4.1.9; in black there is the experiment with the PNIPAAm crosslinked 30 minutes.

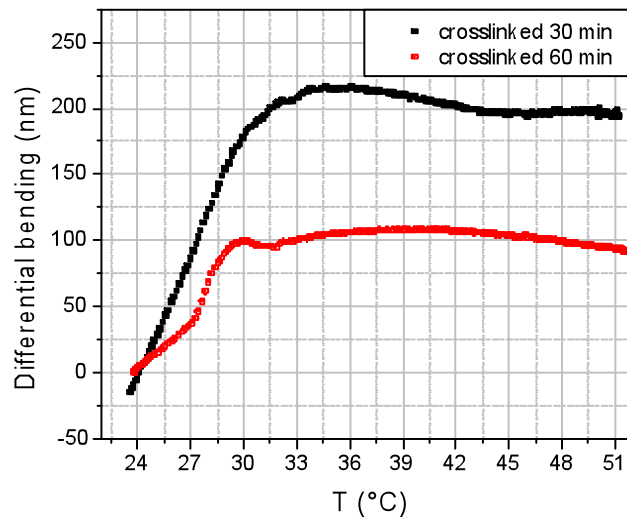


Figure 4.1.10 Bending of PNIPAAm polymer with different crosslinking density vs. temperature.

In cantilevers covered with PNIPAAm crosslinked for 30 minutes (black squares Figure 4.1.10) there is a tensile stress when T is increased that makes the cantilever bend downwards at a rate of $32 \text{ nm}/^\circ\text{C}$, i.e., positive deflection. At around $33 \text{ }^\circ\text{C}$ the bending decreases and a plateau is reached. In the case of the 60 min crosslinked PNIPAAm, there is an initial tensile strength that becomes steeper at $27 \text{ }^\circ\text{C}$. The bending rate changes from $11 \text{ nm}/^\circ\text{C}$ to $33 \text{ nm}/^\circ\text{C}$. After this increased bending region, deflection stabilizes in a plateau region. A factor that can affect polymer phase transitions is the “skin-effect”.^{47, 180-183} Upon heating of the polymer, especially with high heating rates, the outer layer collapses creating a dense polymer shell that prevents water from going out the network. Eventually, heat diffuses through the polymer and the whole layer is fully collapsed. Methacrylic acid comonomer is known to help decrease this by creating hydrophilic channels.^{150, 184} However, as it can be seen in Figure 4.1.10, when polymer is highly crosslinked, the “skin-effect” can occur. “Skin-effect” is thought to be the cause of the different shapes of curves in Figure 4.1.10. When the polymer is crosslinked for 1h, there is an initial compressive stress that becomes more abrupt when T is closer to LCST. Past this point, there is a maximum and there is a short period of tensile strength, probably

caused by relaxation of the polymer network when heat is fully diffused and the scaffold disappears. After that, at around 34 °C, the polymer gradually collapses.

The LCST in the cantilever measurements is defined as the sharp change in the slope as the temperature increases in figure 4.1.10. There is a maximum in both cases, more pronounced in the case of the 60 minutes crosslinked PNIPAAm. This maximum has been fitted with a quadratic equation, which was derived to find the temperature at which there is a change in bending direction. For the polymer crosslinked 30 minutes, the T at the maximum of the curve is 36 °C; when the crosslinking is 60 min, this T is 30 °C. The transition temperature in PNIPAAm has been shown to depend upon many factors. Harmon and coworkers studied the effects in thin films to great extent.^{29, 38, 39, 43, 169, 172} It can be deduced from the NCS experiment that higher crosslinked networks have a lower LCST. Harmon *et al.* already described this phenomenon.³⁸ Lower crosslinking density means a higher mobility of polymer networks. This increases the energy that is required to collapse these networks. As a consequence, higher temperatures are required to switch the energy between the hydrogen bonding with water molecules and hydrophilic parts of the network, and entropy factor that favors the precipitation (i.e., collapse) of the polymer.

The stress measured with Atkinson's equation is 1.9×10^5 and 9.48×10^4 N/m² for the cantilever crosslinked 30 minutes and 60 minutes, respectively. From SPR-OWS data it was calculated that the swelling ratio for samples crosslinked 30 minutes is 9 ± 1 times the collapsed thickness and for samples crosslinked 60 minutes is 7.5 ± 1 . This brings us to the conclusion that higher surface stress found for the lower crosslinked polymer is due to initial higher swelling of the polymer. These values are on the order of surface stress found on other thermoresponsive polymers.¹⁶⁵

The heating ramp was repeated in the same sample to check the reversibility of the response of PNIPAAm polymer [Figure 4.1.11]. After a heating up cycle, the cell is cooled down and another ramp is started recording the bending. The bending of the polymer, with the reference subtracted, is plotted vs. the temperature. While the curves keep the same shape with a change in slope and a maximum that ends up in a plateau, the maxima shift from each other ± 0.5 °C.

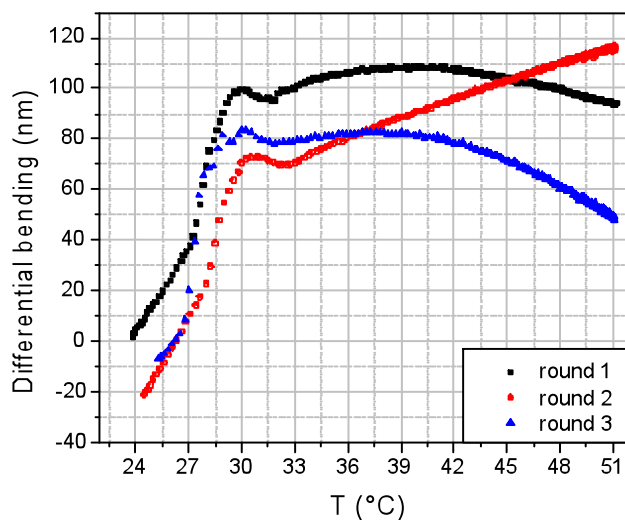


Figure 4.1.11 Bending of a cantilever crosslinked for 1 h vs. temperature during three consecutive T ramps.

The reason for this small shift is attributed to an error in the measurement. Zhang *et al.* noticed small differences in heating and cooling cycles but was attributed to the relaxation time of the network and the different kinetics of heating and cooling.¹⁸⁵ With the purpose of increasing reproducibility some authors recommend the priming of the polymer by ramping the temperature from room temperature until well above the collapse temperature.^{109, 186} Other approaches to increase reproducibility include loading of supercrosslinker nanoparticles.¹⁸⁶

It is well mentioned that PNIPAAm networks can exhibit hysteresis when heating and cooling down.^{146, 186, 187} However, not big insight has been given to the phenomena compared to the importance it may have when designing a device. Some work on nanoparticles with a PNIPAAm gel made by Daoji Gan *et al.*, showed the existence of hysteresis in the swelling-deswelling experiments and concluded that an external shell (skin-effect) was blocking the water from diffusing out.¹⁸⁸ Likewise, thin films studied through SPR showed hysteresis, as several groups proved.^{107, 186, 189} Similarly, in this work a complete heating up and cooling down cycle was performed on PNIPAAm polymer crosslinked 30 minutes in order to check the response of the polymer to the whole cycle. Heating up was achieved at a rate of 3 °C/min and controlled through the input voltage of the heating element. Although cooling down was programmed at the same rate, it is a process controlled by the dissipation of heat. Figure 4.1.12 shows the experiment mentioned above.

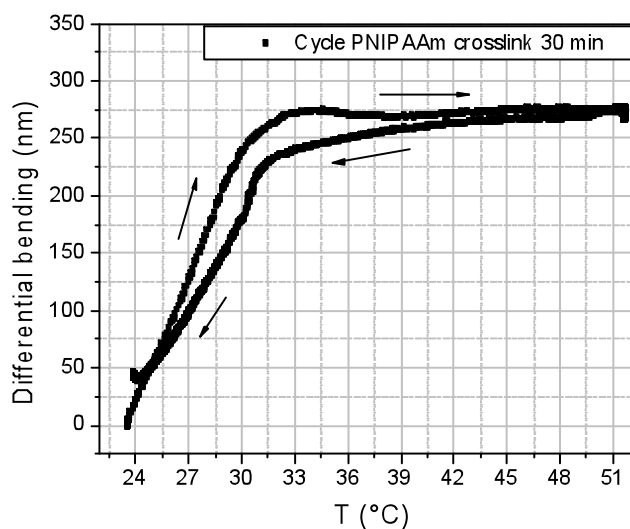


Figure 4.1.12 Heating up and down a cantilever covered with PNIPAAm crosslinked 30 minutes.

In our case, a hysteresis between swelling and collapsing appears. Collapsing seems to be a process initialized at nucleation points,¹⁹⁰ whereas swelling is a water-diffusion-limited process. In other words, the polymer chain stretching during the cooling down is a slower process compared to the gel contraction. The activation energy for the swelling is higher than the one for the deswelling.¹⁴⁶

For comparison with these temperature-related experiments, similar ones were performed in SPR-OWS with our polymer. The thickness of dry PNIPAAm SPR samples was between 600 nm and 1 μm . A typical experiment consists of rinsing the sample with water and drying with nitrogen gas at least 3 times. Next, the sample is mounted on an SPR setup and water is rinsed for at least 10 minutes. Then, temperature is brought up to 50 °C and decreased again to room T quickly not less than 2 times. Again, water is flowed through for 20 minutes. This procedure allows for all uncrosslinked polymer chains to leach out of the polymer. At this point, the sample is ready to be measured. Temperature was raised with intervals that depended on the proximity to already reported LCST, from 5 to 1 degree difference. At each temperature, a scan of reflectivity vs. angle was performed. Each minimum angle of the plasmon is plotted in Fig. 4.1.13 as a function of temperature.

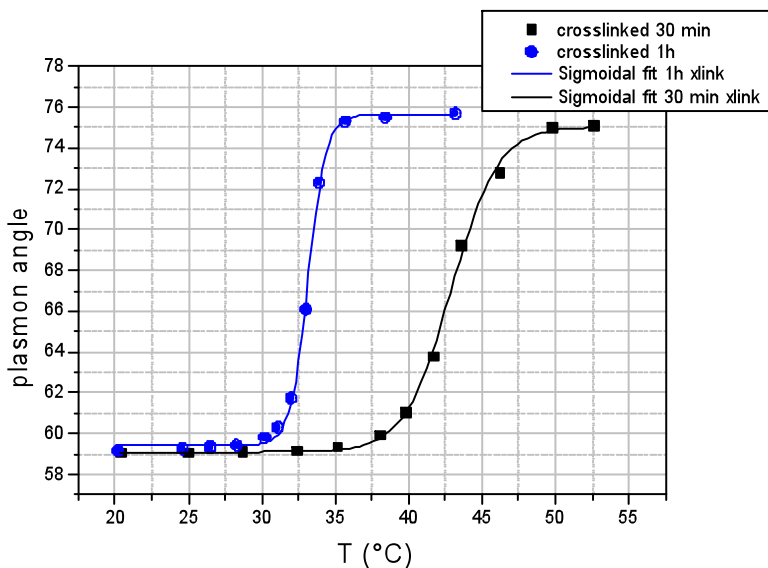


Figure 4.1.13 Dependence of plasmon angle minimum on the temperature for two samples; one crosslinked 30 minutes, the other 1h. In the legend xlink=crosslink.

Similarly to NCS experiments, the LCST obtained from the sigmoidal fitting is higher for layers less crosslinked. More specifically, samples crosslinked during 30 minutes showed a critical temperature of around 42 °C, whereas samples crosslinked for 1 hour exhibit a volume transition at around 33 °C. Surprisingly, skin effect is not shown in the SPR/OWS experiments [Figure 4.1.13]. This shows that NCS is a better technique when mechanical effects on polymers have to be studied. NCS transduce this effect to the cantilever and, hence, it can be sensed.

Measurements by NCS gave an LCST of 30 °C and 36 °C for 60 minutes and 30 minutes crosslinked PNIPAAm, whereas SPR-OWS showed higher values compared to these (33 °C and 42 °C respectively). The difference might be most likely due to how the two methods define LCST. In NCS experiments, LCST is determined at the onset of the transition whereas, in SPR-OWS, the transition has already started and the middle point is the one defined as critical temperature. Also, NCS is a dynamic technique whereas SPR-OWS measurements were performed in the equilibrium state.

4.1.4. Conclusions

The combination of SPR-OWS and NCS was applied to study the influence of pH and T on photo-crosslinkable poly(N-isopropylacrylamide)-based polymer. A silanization strategy was successfully established in order to get monolayers of

BZ-silane on the cantilever. Furthermore, a deposition protocol for placing PNIPAAm polymer solution onto the thin cantilever sensors was achieved by means of inject printing.

SPR-OWS and NCS showed the response of PNIPAAm-based polymer to pH and T. Compressive surface stress on the cantilever sensors at pH values higher than 6 confirmed the swelling of the polymer due to the osmotic pressure required to stabilize the carboxylate ions. Sigmoidal fitting of the curves extracted from SPR-OWS and NCS was used to calculate the pKa of the polymer. Values of pKa estimated from NCS, 5.31, and from SPR-OWS, 4.98, were in close agreement with bulk polymer pKa values. Surface stress values were close to those for acid terminated SAMs because acid groups on the polymer are composed of only 5% of the network.

By employing nanomechanical cantilevers, access to mechanical changes on the polymer while collapsing is gained. The sensing of the interplay between lateral and perpendicular swelling in NCS allowed the investigation of stresses that were not sensed by SPR-OWS, where a rigid substrate do not allow bending and, therefore, only compressive behavior on one direction can be sensed. PNIPAAm polymers that are highly crosslinked experience skin-effect phenomenon and have a lower LCST. More energy is required to collapse a polymer with a lower crosslink density due to the higher mobility of the chains.

4.2. Magnetite nanoparticles

4.2.1. Introduction

In the previous chapter, changes in PNIPAAm-based hydrogels with respect to pH and temperature were discussed. In this chapter a completely different topic is reported: magnetic nanoparticles.

Nanomaterials are of great interest among the scientific community due to the discovery of unusual physical and chemical properties of materials in the nanometer size range. These properties are related to the manifestation of the so-called “quantum size effects”.^{62, 122-124} Magnetic nanoparticles (NP) belong to this class of materials. It was shown that magnetization (per atom) and the magnetic anisotropy of nanoparticles can be much greater than those of bulk materials, while differences in the Curie or Neel temperatures between the NP and the microscopic phases can reach hundreds of Kelvin.^{62, 191}

The interest in magnetic nanoparticles is mainly due to their potential applications. For instance, they can be used for super-high density information recording,⁶⁶ for bioapplications such as drug delivery,^{192, 193} and for the creation of heavy-duty magnets and various sensors.¹⁹⁴

The chemical composition of the particles, their shape and their magnetic properties are all interrelated; thus, all properties need to be considered when studying these materials. It has been reported that the coating of magnetic nanoparticles affects the saturation magnetization.^{137, 195} For instance, Mohapatra *et al.* studied the effect of 3-aminopropyltriethoxysilane (APTES) on magnetite and observed a decrease in saturation magnetization from 56 emu/g to 41 emu/g.¹⁴⁴ They attributed the decrease to the formation of a diamagnetic APTES coating that contributed as a nonmagnetic mass to the total sample volume. Likewise, Wu *et al.* studied APTES and mercaptopropyltrithoxysilane functionalization of magnetite. They observed a slight decrease of M_s after functionalization as well; however, it was attributed to some exchange interactions at the surface.¹⁴³ Nevertheless, the first explanation seems to be the acting mechanism.^{130, 196} APTES confers to the particles an amine functionalization that can be further used to modify the nanoparticles or disperse them in an acid aqueous solution. The selection of the right surfactant is crucial to disperse the nanoparticles in different solvents. Nanoparticles that form stable dispersions in water are commonly required. Among the wide variety of

magnetic materials that can be prepared in the form of nanoparticles, iron oxides have certainly been and still are the most intensively studied. This is one of the factors that contributed to the election of magnetite for this work. Another important factor is the approval by the Food and Drug Administration (FDA) of the use of superparamagnetic iron oxide nanoparticles as contrast agents in magnetic resonance imaging. That is one of the main reasons why magnetite is intensively studied for bioapplications. A review about applications in biomedicine can be found in reference ⁶⁷. Interesting possible applications arise in the field of cancer treatment, where magnetite nanoparticles can be used in different ways. An example is the use of nanoparticles as drug carriers. A high-gradient magnetic field would be used to direct the nanoparticle-carriers to a specific area of the body. Once the drug/carrier is concentrated, the drug could be released by enzymatic activity or changes in the environment.¹⁹⁷ This idea could be revolutionary in medicine if accomplished, however, driving of the magnetic carriers upstream in blood vessels is very difficult with most typically applicable magnetic strengths. Moreover, the magnetic carriers can block the blood stream once they are accumulated in the target sites. Another prospective idea is the use of magnetic nanoparticles applied in hyperthermia treatment, where the destruction of cancer tissue is facilitated by the means of heating the infected tissue. It is widely known that magnetic nanoparticles can release heat when an alternating magnetic field (AMF) is applied.¹⁹⁸ We can distinguish between two approaches: 1) heating the target tissue to 41-42°C, taking advantage of the synergetic effect together with radiation and chemotherapy (i.e., higher effectiveness of drugs at higher temperatures) or 2) using higher temperatures up to 56°C, which produce necrosis and coagulation (thermo-ablation).^{199, 200} Magnetic heating of the nanoparticles is determined by the field amplitude, the frequency and the properties of the materials. Since magnetic nanoparticles are poor electrical conductors, inductive heating does not occur. However, the electrical conductivity of biological tissues is high enough to generate heating of tumor cells and healthy cells at the same time due to eddy currents.^{201, 202} This leads to the establishment of limits on the field amplitudes and frequency applied. In a study made by Ivkov *et al.* it was concluded that for a safe application of high-amplitude AMF, high duty cycles to allow diffusion of Eddy currents (on/off ratios of AMF) are necessary.²⁰² In general, a maximum field frequency 300-400 kHz and a field amplitude of 7-15 kA/m may be safe and technically feasible at the same time. There

are three main heating mechanisms: (i) resonance losses, (ii) hysteresis losses, and (iii) relaxation losses. (i) Resonance losses occur at high frequencies (~GHz) and are therefore neglectable in hyperthermia experiments. (ii) Hysteresis losses arise as multidomain magnetic nanoparticles (i.e., with a volume bigger than the critical volume $V > V_c$) react to an external magnetic field by Bloch wall displacement, thus creating a hysteresis between the magnetization, M , and the applied magnetic field. The energy dissipated during one re-magnetization cycle is the area enclosed in the hysteresis loop. (iii) In the case of monodomain magnetic nanoparticles, the energy barrier for magnetization reversal decreases and the thermal fluctuations lead to relaxation losses. Among these we distinguish between Néel relaxation and Brown relaxation. In the presence of an external magnetic field, rotation of the magnetic moment of the particle to reach the orientation corresponding to an energy minimum requires overcoming an energy barrier, $\Delta E = K_v V$ (K_v =anisotropy constant, V =volume). This is the so-called, Néel relaxation. On the other hand, the Brown relaxation causes heat as a result of viscous friction between the rotating particle and the surrounding medium when the whole particle reorients itself with the magnetic field.^{51, 62, 200}

In this chapter a characterization of the magnetic properties of the magnetic nanoparticles and their application in hyperthermia experiments is presented with respect to different sizes (synthesis Section 4.2.2). Additionally, nanoparticle self-assembly is discussed.

4.2.2. Experimental procedures

Magnetic nanoparticles were synthesized according to the method reported by Sun *et al.* as described in Section 4.2.2. Different nanoparticle sizes were studied, ranging from 3.5 to 20 nm.

Nanoparticles for magnetization studies were precipitated from hexane solution with ethanol and the precipitate separated using the magnetic field of a permanent magnet (0.7 T at the surface). The nanoparticle precipitate was then dried overnight under vacuum at 50 °C. The resulting powder was used for measuring the magnetic properties by means of SQUID.

When measuring the heat generated by the nanoparticles in AMF, several solutions of particles with different diameters and different concentrations in hexane were used. The volume of each sample was 2.1 mL and concentrations of 20 mg/mL

and 40 mg/mL were studied. A reference experiment was performed with pure hexane. For a complete description of the measurement setup see Section 2.7.

4.2.3. Magnetic properties

4.2.3.1. Magnetization curves

The magnetization of dry nanoparticle powder samples in an external magnetic field was studied using a superconducting quantum interference device (SQUID). The magnetization was measured until saturation was reached. In order to determine the temperature dependence of the magnetic moment M , two types of measurements are carried out: (i) zero-field cooling (ZFC) and (ii) field cooling (FC). (i) In ZFC, the sample is cooled down to the liquid helium temperature in the absence of a magnetic field. Then a moderate measuring field is applied (1-100 Oe) and the temperature is gradually raised while the magnetic moment of the nanoparticle powder m_{ZFC} is recorded. (ii) In FC, the magnetic moment is obtained while cooling the sample in the presence of a moderate magnetic field.

Figure 4.2.1 shows high-resolution TEM micrographs of the samples used for these experiments. Four different nanoparticle sizes were studied: 3.7 nm, 7.0 nm, 8.0 nm and, 11.6 nm. The sizes were obtained from TEM.

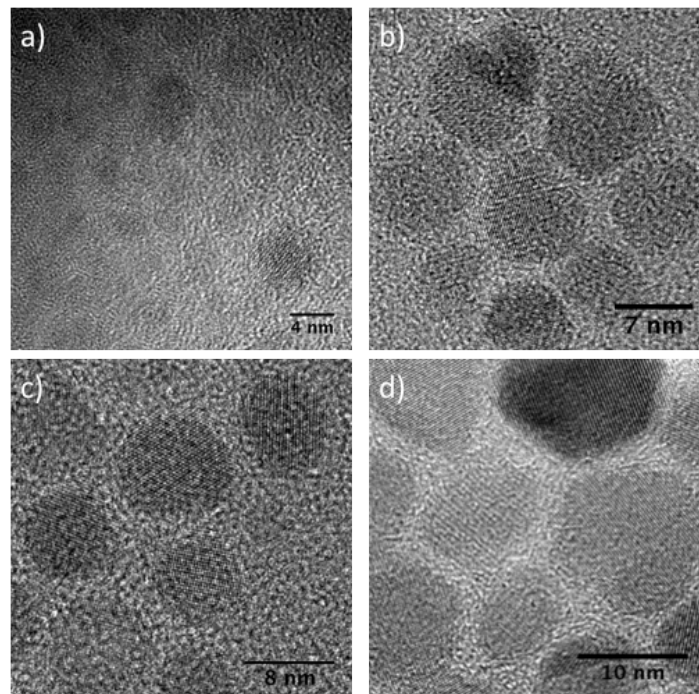


Figure 4.2.1. HRTEM micrographs of nanoparticles (a) 3.7 nm, (b) 7.0 nm, (c) 8.0 nm and (d) 11.6 nm in diameter.

Magnetization versus external field (M-H) diagrams for the four different nanoparticle sizes are shown in Figure 4.2.2 at two distinct temperatures: 300 K and 5 K. At 300 K, the nanoparticles are superparamagnetic, i.e., there is no hysteresis in magnetization. On the other hand, at 5 K the nanoparticles show ferrimagnetic behavior, i.e., a hysteresis in magnetization for increasing and decreasing external magnetic field strength. Corresponding values for saturation magnetization, M_s , remanent magnetization, M_r , and coercivity, H_c are listed in Table 4.2.1.

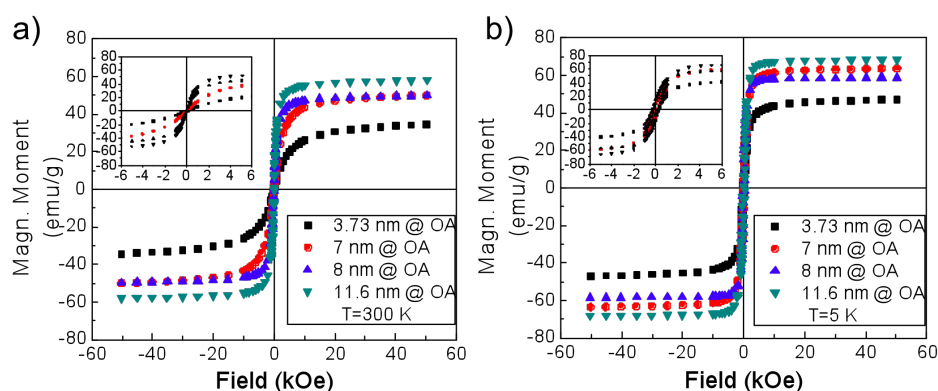


Figure 4.2.2. Magnetization versus external magnetic field (M-H) for nanoparticles coated with oleic acid of different sizes. The M-H curves are shown at (a) 300 K and at (b) 5 K. The insets show enlargements at lower field amplitudes.

Coercivity, remanent magnetization and saturation magnetization are all significantly higher at lower temperatures. This is due to the fact that the nanoparticle powder samples show ferrimagnetic behavior at 5 K as opposed to superparamagnetic one at 300 K. The magnetic spin at low temperatures is not relaxed by thermal energy. At higher temperatures, the relaxation rate becomes exponentially large and the system reaches the thermodynamic equilibrium faster.

Saturation magnetization. For smaller nanoparticles the saturation magnetization decreases due to surface spin canting (disorder of the surface spin compared to the core of the nanoparticle). M_s values found in this work (presented below) are in accordance with literature values; Caruntu *et al.* found values of 80.0 emu/g for M_s of Fe_3O_4 NPs covered by oleate with a size of 6.6 nm at 5 K and 70.7 emu/g at 300 K. For nanoparticles sized 11.6 nm in diameter, they reported values of 89.2 and 77.4 emu/g at 5 K and 300 K, respectively.²⁰³ Sun *et al.* found lower values for M_s (room temperature), increasing from 41.6 to 49.24 emu/g for particle sizes 8 to 20 nm.¹³¹ In both cases, the nanoparticles were fabricated using the coprecipitation

method, however, Caruntu annealed the nanoparticles at temperatures close to 210 °C in order to obtain a better nanoparticle crystallinity. Schwind *et al.*, using the same synthetic method as applied in this work, found saturation magnetizations of 78 emu/g at 5 K and 61 emu/g at 300 K for spherical nanoparticles 7 nm in diameter.²⁰⁴ Table 4.2.1 summarizes the values found in this work, which are slightly lower than the values reported by Caruntu *et al.* as well as Schwind *et al.* but higher than those reported by Sun *et al.*

Diameter / nm	Surfactant	T _B / K	H _c / Oe		M _r / emu.g ⁻¹		M _s / emu.g ⁻¹	
			5 K	300 K	5 K	300 K	5 K	300 K
3.73 ± 0.78	OA	23.07	270.04	10.39	9.21	0.07	46.96	34.41
7.02 ± 1.66	OA	32.46	195.51	8.95	10.46	0.15	63.55	49.9
8.04 ± 1.12	OA	65.5	247.24	9.34	15.01	0.38	58.47	49.68
11.60 ± 3.33	OA	215.04	240.09	18.97	13.55	1.08	68.25	57.97
11.60	BZ	250.42	238.38	5.12	14.5	0.43	61.28	52.04

Table 4.2.1. Physical properties of Fe₃O₄ nanoparticles with different sizes and surfactants.

OA = oleic acid, BZ = benzophenone.

Remanent magnetization and coercivity. The remanent magnetization and coercivity of the nanoparticles is zero at 300 K, due to the superparamagnetic character. At a temperature of 5 K, values of 9.21 emu/g up to 13.55 emu/g for M_r have been measured for nanoparticles ranging from 3.7 nm to 11.6 nm. Goya *et al.* found similar values: 10 and 13 emu/g for nanoparticles 4 and 11.5 nm in size, respectively. The coercive field at 5 K is similar for all nanoparticle sizes studied and lies around 200-250 Oe, in the same range found by Song *et al.* and Schwind *et al.*²⁰⁴⁻²⁰⁶

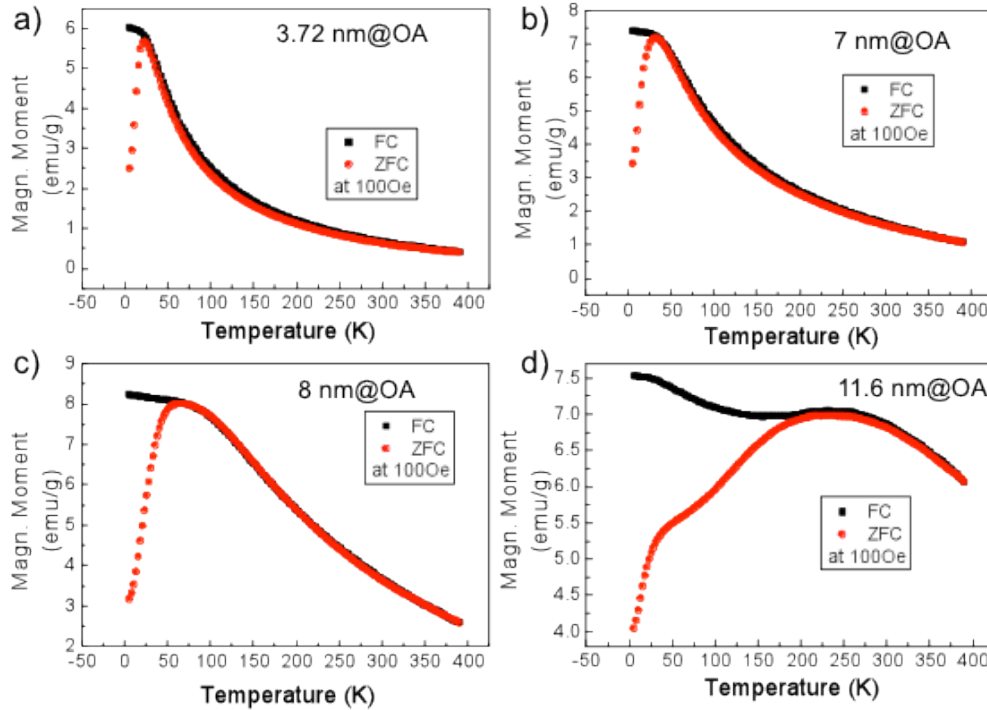


Figure 4.2.3. Temperature (T) dependent Magnetization (M) measured both in ZFC and FC modes for nanoparticles with the following sizes: a) 3.7 nm, b) 7.0 nm, c) 8.0 nm and, d) 11.6 nm. All the NPs are covered by oleic acid.

The ZFC and FC diagrams describe the temperature dependence of the magnetization of Fe_3O_4 nanoparticles. The maximum in the ZFC curves indicates the transition temperature from superparamagnetic to ferrimagnetic behavior. Before the ZFC measurement, the net magnetization is zero, i.e., the sample is at the equilibrium state. After a low field is applied, the equilibrium breaks. If the particles are magnetically isotropic, i.e., there are no energy barriers for flipping the magnetic moments, the ZFC curve is a measure of the thermodynamic equilibrium states and is well described by the Curie law (decrease of magnetization with increase of T). When energy barriers exist in the system, the sample cannot reach the corresponding thermodynamic equilibrium state at such a low temperature and low external magnetic field. When temperature raises, the relaxation rate increases exponentially and a higher percentage of particles have their magnetic moments aligned with the direction of the field, i.e., the magnetization of the nanoparticle ensemble increases with temperature. At a certain temperature, the blocking temperature (T_B), the magnetization increases to the value of the equilibrium state. If the temperature increases further, the magnetization decreases following the Curie law, and consequently a maximum appears at this temperature. In other words, at

low temperatures, the thermal energy is too low to overcome the anisotropic energy barrier, the nanoparticles are therefore ferromagnetic (ferrimagnetic in the case of iron oxide) and at high temperatures, the thermal energy is greater than the anisotropic energy and the nanoparticles show superparamagnetic behavior.

It was found that T_B increases with size [Table 4.2.1]. This is consistent with the Stoner-Wohlfarth theory, which predicts an increase in the anisotropy barrier as the nanoparticle volume increases.²⁰⁷ As can be seen from Table 4.2.1, the particle size distribution increases with particle volume. This effect leads to the broadening of the maximum at T_B in the ZFC curve.²⁰³ Simulations of ZFC and FC curves for nanoparticles with different particle distributions confirm this effect.²⁰⁸ In other words, a large size distribution is reflected in a broader distribution of energy barriers of the individual nanoparticles which leads to broadening of the peak at T_B in the ZFC curves [Figure 4.2.3]. Roca *et al.* reported blocking temperatures of 20 K for diameters of 5.7 nm, 45 K for diameters of 7 nm, which agrees well with this study.²⁰⁹ Park *et al.* studied magnetite nanoparticles and found an increase in T_B with NP size: T_B is reported to be 40 K for 5 nm nanocrystals, and increases with size up to 260 K for 22 nm nanocrystals.²¹⁰

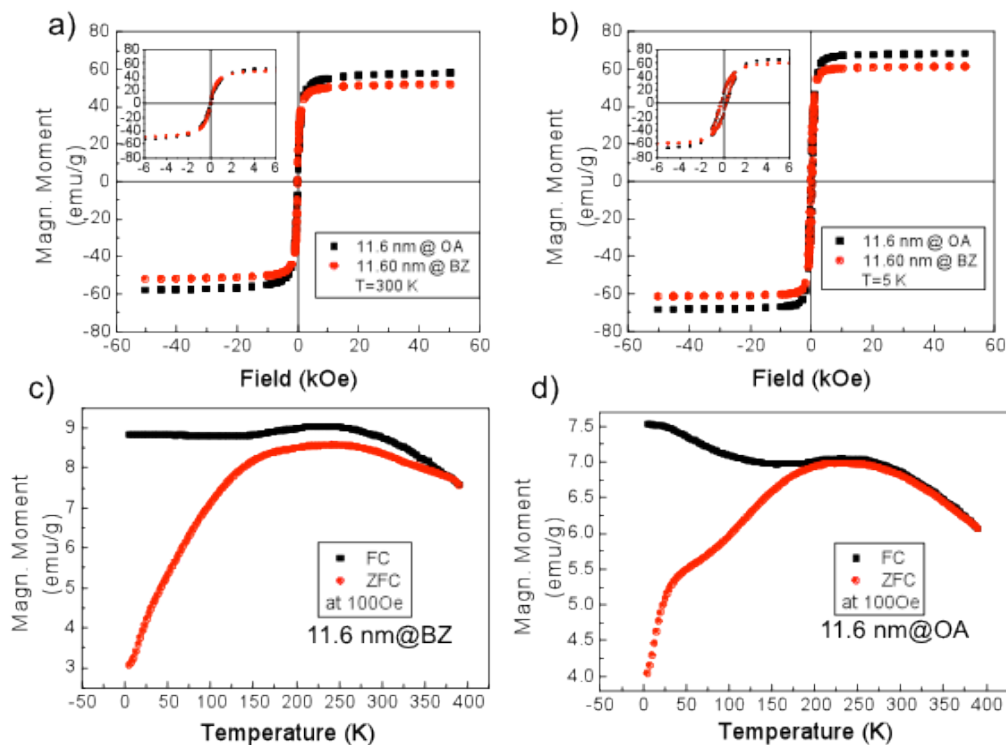


Figure 4.2.4. M-H diagram of magnetite nanoparticles with a size of 11.6 nm and modified with oleic acid or benzophenone at (a) 300 K and (b) 15 K. ZFC and FC curves for (c) benzophenone and (d) oleic acid coated NPs.

Coating the iron oxide nanoparticles with benzophenone, changes the magnetic properties as can be seen in Figure 4.2.4 and Table 4.2.1. The saturation magnetization decreases for the nanoparticles coated with benzophenone. As already mentioned before, M_s has been reported to decrease when the nanoparticles are coated and this effect is attributed to the contribution of the diamagnetic layer created around the nanoparticle.^{130, 196} In this case, the oleic acid shell is partially replaced by a shell of benzophenone silane, which is a shorter molecule. However, silanes can form multilayers very easily. The benzophenone shell must therefore be composed of a multilayered structured benzophenone silane. M_r and H_c values are on the same order of magnitude for both oleic acid and benzophenone coatings. T_B increases for benzophenone from 215 to 250 K compared to oleic acid. The increase in block temperature is a sign of increase in nanoparticle size, which could be the result of nanoparticles same particle aggregation during the modification (exchanging the coatings/surfactants).²¹¹

4.2.3.2. Hyperthermia experiments

Experiments concerning the heating of the nanoparticles in an alternating magnetic field (AMF) are performed. The specific absorption rate is extracted experimentally from the increase in temperature of the ferrofluid (a stable solution of magnetic iron oxide nanoparticles) as a response to the AC-field. The experimental setup is described in Section 2.7. Typically, an AMF was created through a coil and the nanoparticle solution was placed in the coil's center. The sample temperature is measured using an infrared gun. Currents are supplied by a signal generator and amplified in the desired frequency. In the following measurements, magnetic fields of 7 kA/m (88 Oe) and frequencies of 51.8, 98.25 and 135.15 kHz were applied. The heating power depends on the magnetic field and the nature of the nanoparticles, i.e., particle size and size distribution, anisotropy constant, saturation magnetization and surface modification. Three different nanoparticle sizes were used: 3.8 ± 0.5 nm, 10.9 ± 1.8 nm and, 19.6 ± 2.4 nm. Two different concentrations were measured for each nanoparticle size: 20 mg/mL and 40 mg/mL in hexane. In a typical experiment, a current is applied to the coil for 180 seconds. The temperature is measured for 60 seconds both before and after the measurement to ensure stability of the measurement. Analysis is based solely on the 180 seconds when the AC-field was

applied. Two reference experiments were performed at every frequency on pure hexane. The results are shown in Figure 4.2.5.

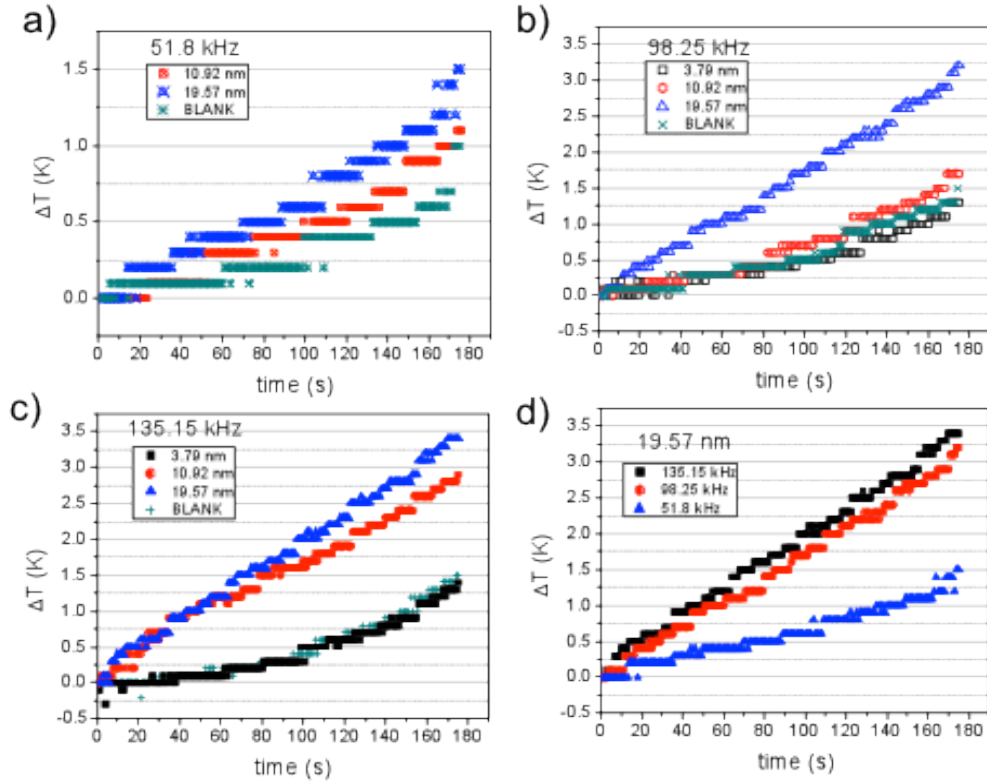


Figure 4.2.5. Specific absorption rate (SAR) experiment of Fe_3O_4 magnetite nanoparticles. A 7 kA/m field with frequency (a) 51.8 kHz, (b) 98.25 kHz, and (c) 135.15 kHz was applied. A direct comparison between different frequencies is shown in (d) for nanoparticles 19.6 nm in diameter.

The specific absorption rate (SAR) quantifies the amount of magnetic energy transformed by the nanoparticles into heat per unit time and mass. In order to estimate the SAR the data was linearly fitted to

$$SAR = c \left. \frac{dT}{dt} \right|_{t=t_i} \quad (4.2.1)$$

where c is the heat capacity of the sample, and $(dT/dt)_{t=t_i}$ is the initial slope. To extract the Joule effect, that is convection heating produced by the coil, the SAR for the reference sample is calculated and subtracted from the SAR of the ferrofluid. The solution c was approximated by using the weight average of the bulk values for glass ($c_{\text{glass}} = 0.75 \text{ Jg}^{-1}\text{K}^{-1}$), hexane ($c_{\text{hexane}} = 0.0109 \text{ Jg}^{-1}\text{K}^{-1}$), and magnetite ($c_{\text{magnetite}} = 0.938 \text{ Jg}^{-1}\text{K}^{-1}$). The results obtained are listed in Table 4.2.2.

SAR / mW•mg ⁻¹	Diameter / nm		
	3.8	10.9	19.6
Frequency / kHz			
135.15	11.98	74.29	115.12
98.24	8.51	24.57	71.32
51.8	--	8.86	22.98

Table 4.2.2. Experimental values of SAR for a field amplitude of 7kA/m.

Nanoparticles with a bigger particle size have higher SAR. It has been discussed in the literature that at low frequencies, like the ones used in this study, power losses increase with diameter up to a critical diameter (for magnetite, it is reported to be 18.3 nm).²¹² At this critical diameter $P_{\text{Néel}}$ (Power loss generated by Néel relaxation) reaches a maximum and the SAR values decreases with further increase of nanoparticle size. When hysteresis losses become considerable, this effect is reversed again, meaning SAR increases with increasing particle size. This makes comparison with literature data extremely difficult as reported values might have been obtained at different frequencies and field amplitudes and different processes might determine the heat loss. For instance, Wang *et al.* found values of 50 mW/mg for 6 nm magnetite nanoparticles, 78 mW/mg for 8 nm magnetite nanoparticles and 123 mW/mg for 10 nm. These values were obtained at 7 kA/m and 63 kHz.²¹² Ma *et al.* found for magnetite nanoparticles of 13 nm, a values of 190 W/g for magnetite nanoparticles with a diameter of 11 nm at a magnetic field strength of 11 kA/m and a frequency of 410 kHz.²¹³

As already described, heating in superparamagnetic nanoparticles is produced by relaxation processes. These relate to the gradual alignment of the magnetic moments with the magnetic field. The relaxation can take place through Brownian relaxation and/or Néel relaxation. To distinguish both effects, nanoparticles can be immobilized in a matrix in order to prevent rotation of the nanoparticles and therefore, avoid the losses through friction, i.e., Brownian relaxation.^{201, 214} This effect has been used by others to engineer biosensors, for instance, Chemla *et al.* chose nanoparticles with a Néel relaxation time much longer than the Brownian relaxation time. As a result, SQUID measurements detect the decaying field produced only by superparamagnetic nanoparticles bound to a target on the film.²¹⁵

The Brownian relaxation time is given by:¹⁹⁸

$$\tau_B = \frac{3\eta V_H}{k_B T} \quad (4.2.2)$$

where η is the viscosity coefficient of the matrix fluid, k_B is the Boltzmann constant ($1.38 \times 10^{-23} \text{ J K}^{-1}$), and T the absolute temperature (K). V_H is taken as the hydrodynamic volume of the particle of radius R and can be approximated by $V_H = (1 + \delta/R)^3 V_M$, where δ is the thickness of the surfactant and V_M is the magnetic volume.¹⁹⁸

The Néel relaxation time is given by:²¹²

$$\tau_N = \tau_0 \exp \frac{KV}{k_B T} \quad (4.2.3)$$

where τ_0 is a time constant, $\tau_0 \sim 10^{-9} \text{ s}$, and K is the anisotropy constant, $K = 1.35 \times 10^4 \text{ J/m}^3$ for magnetite.²¹⁶ The total relaxation time, τ , is given by:

$$\frac{1}{\tau} = \frac{1}{\tau_B} + \frac{1}{\tau_N} \quad (4.2.4)$$

The relaxation time will be mainly determined by the fastest relaxation. For instance, for big nanoparticles where Néel relaxation is less likely to occur due to high anisotropy energy barriers, the nanoparticles will tend to relax through Brownian processes.¹⁹⁸

The power loss, or specific absorption rate, corresponding to Néel and Brownian relaxation is approximately given by:²¹²

$$P = \pi \mu_0 \chi_0 H_0^2 f \frac{2\pi f \tau}{1 + (2\pi f \tau)^2} \quad (4.2.5)$$

where μ_0 is the permeability of vacuum, χ_0 is the equilibrium susceptibility, and H_0 is the amplitude and f the frequency of the applied AC magnetic field.

The values obtained from Equation 4.2.5 using the experimental values for field amplitude, frequency and diameter of nanoparticles are shown in Table 4.2.3:

SAR / mW.mg ⁻¹	Diameter / nm			
Frequency / kHz	3.8	10.9	19.6	19.6 ± 2.4 (lognormal distribution)
135.15	0.0037	0.4280	88.2	138.834
98.24	0.0019	0.2260	86.2	110.63
51.8	0.0003	0.0629	76.8	68.81

Table 4.2.3 Calculated values of SAR for a field amplitude of 7kA/m with Equation 4.2.5.

Calculated values differ by several orders of magnitude from experimental values for smaller nanoparticles (3.8 and 10.9 nm). These calculations were performed assuming monodispersed nanoparticles. In reality, the size distribution might affect the SAR as large nanoparticles in the ensemble might influence SAR to a higher degree compared to smaller nanoparticles. Using a lognormal distribution (which reflects the experimental size distribution very well) the frequency dependence of the SAR is much better reproduced (see Figure 4.2.5). Figure 4.2.5 is showing a comparison, for the case of 19.6 nm nanoparticles, of the SAR values obtained experimentally as well as from calculations for a monodispersed sample and one showing a lognormal distribution.

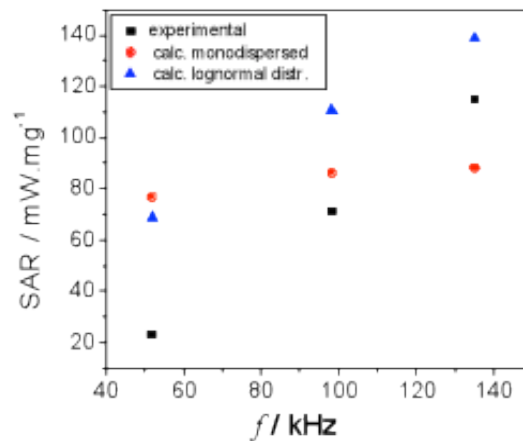


Figure 4.2.5. SAR values for nanoparticles with a diameter of 19.57 nm extracted from experimental results and calculations using Equation 4.2.5.

The calculations fit to the experimental values; however, lognormal distribution calculations have the same trend of frequency-dependence compared to experimental values. This clearly shows that the nanoparticles size distribution needs to be taken into account. At lower frequencies, the amount of nanoparticles with smaller size inside the size distribution decrease the SAR values whereas the bigger

size NPs do not play a role; on the other hand, as frequency increases bigger size NPs contributions increase SAR of the ferrofluid considerably.

4.2.3.3. Nanoparticle self-assembly

Recent research has been focused on self-assembly of nanocrystals.^{126, 217} A tightly packed assembly of exchange-decoupled magnetic nanoparticles may serve, for instance, as future ultrahigh-density data storage media.²¹⁸ Self-organization into superlattices requires a sphere repulsion, a very narrow size distribution and the inherent van der Waals attraction between NPs. Therefore, it does not depend on the material and the effect can be observed in different kinds of nanocrystals such as magnetic, metallic and semiconducting (quantum dots) nanoparticles.²¹⁹⁻²²¹ Magnetic interactions might play a role in the self-assembly of magnetic nanoparticles, however, as the nanoparticles used here are superparamagnetic at room temperature, there is no remanent magnetization [See T_B in Section 4.2.3.1]. If size and shape distribution of nanoparticles are narrow, colloidal nanocrystals spontaneously self-assemble into a two-dimensional (2D) and three dimensional (3D) superlattices. The formation of superlattices is commonly induced by slow evaporation of the solvent, which increases the particle concentration and gives the particles time to assemble. Using a solvent or a solvent mixture that evaporates at slower rates will increase the order. If higher degree of packing is required, a technique that uses colloidal crystallization can be used.²²² A poor coordinating solvent is slowly diffused into the mixture allowing the particles to find their minimum energy positions in a close-packed lattice.

There are many important factors in the formation of superlattices, such as particle size distribution and evaporation rate. Murray *et al.* found that nanoparticles with a standard deviation in the order of $\sigma = 7\%$ could only achieve short to medium range order distribution, whereas $\sigma = 5\%$ provided long range order.²²³ It was interesting to observe that the wettability of the substrate influences the dimensions of the growth. More precisely, if the NPs dispersion wets the surface, a 2D structure is more likely to happen in the first place; however, when the dispersion doesn't wet the substrate, 3D structures form predominantly.

The formation of superlattices can also influence the magnetic properties. However no studies of this kind have been performed in our work. It has been found

an increase in T_B and the width of the ZFC peak due to dipolar coupling interactions.²²³

The nanoparticle suspensions are drop-casted on top of TEM grid and the solvent is evaporated under normal conditions. Some of the obtained structures are shown in Figure 4.2.6.

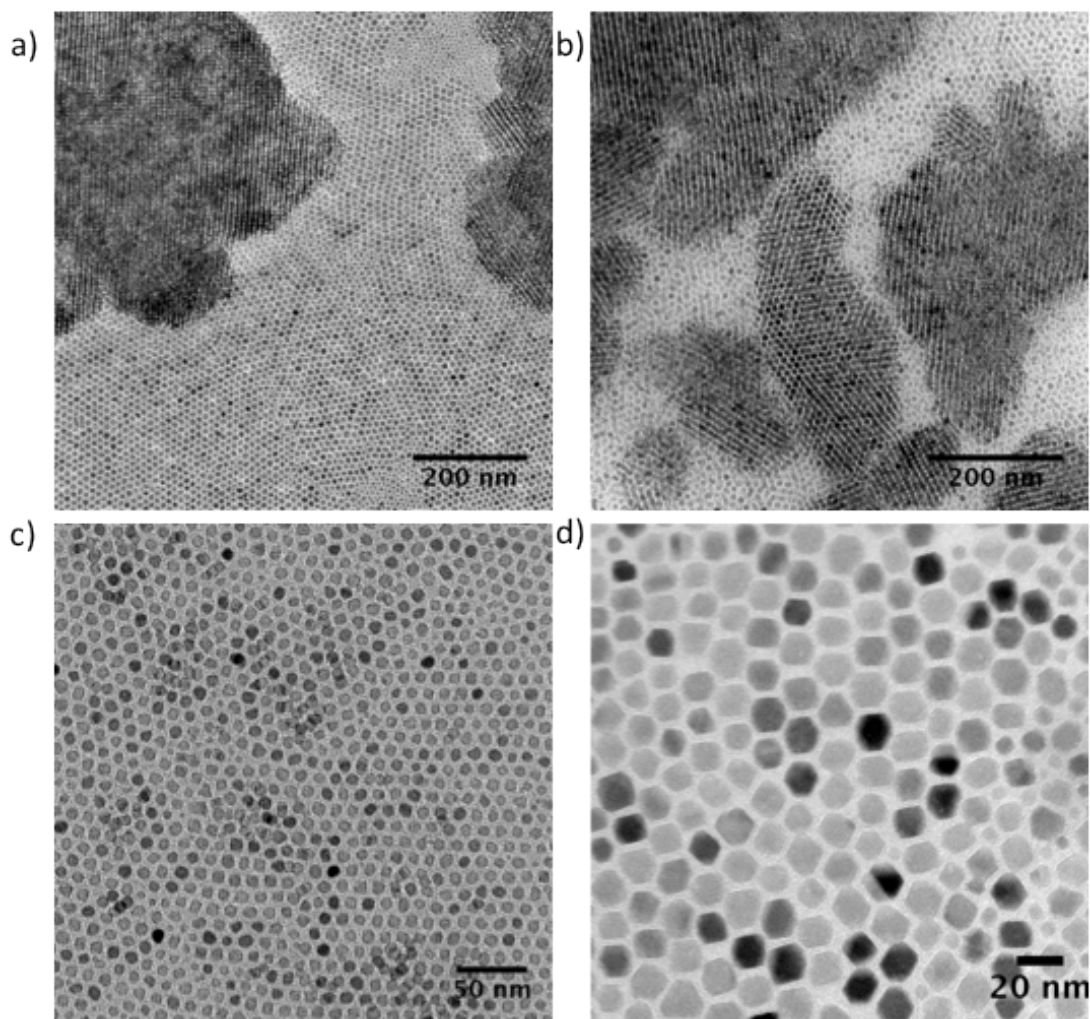


Figure 4.2.6. TEM micrographs of nanoparticle self-assemblies. (a) and (b) show the formation of a 3D superlattice, (c) and (d) show a 2D structure.

The nanoparticles self-assemble into a 2D structure that gradually grows into the third dimension [Figure 4.2.6 a) and b)]. Every new monolayer forms shifted slightly so that nanoparticles from the new layer sit on top of the interstitial spaces between two nanoparticles of the previous monolayer. Diluting the dispersion of NPs by 1:10 yields a 2D superlattice [Figure 4.2.6c)]. It can be clearly observed on the

2D structure shown in Figure 4.2.6 (d) how the nanoparticles tend to follow a general rule of face-to-face in order to maximize the van der Waals interactions.²²⁴

The HRTEM images confirm that the particles are single crystalline nanoparticles (see Figure 4.2.1), which is also confirmed by the TEM images in Figure 4.2.6 as they show differences in Bragg contrast (which was verified by slightly tilting the sample).

The area of the 3D superlattices is usually around 1000 to 2500 nm², the area covered by the 2D superlattices is much bigger, on the order of square micrometers.

4.2.4. Conclusions

The size effect of nanoparticles on magnetic properties was systematically studied using magnetite nanoparticles of different diameters between 3.7 and 19.6 nm. The size dependence of key magnetic properties, namely saturation and remanent magnetization, coercivity and blocking temperature for the superparamagnetic behavior, was determined and agrees well with results reported in literature. M-H-diagrams and ZFC curves confirm the superparamagnetic character of the nanoparticles. Magnetization values are found to be smaller for nanoparticles considered here than for bulk magnetite. The influence of coatings on the nanoparticles was studied. For only one particle size, benzophenone and oleic acid surfactants were compared and the magnetization was found to be lower for benzophenone compared to oleic acid, which is in accordance to diamagnetic contributions of the surfactant. This led to the conclusion that benzophenone forms a multilayer with a higher diamagnetic character. Furthermore, the blocking temperature was found to increase as the surfactant was changed from oleic acid to benzophenone which is probably due to aggregation of some of the nanoparticles.

Applying these nanoparticles in heating studies, the nanoparticles were found to heat their environment in an AC magnetic field. Power losses, i.e., increasing transfer of magnetic energy to heat, are found to increase with particle size. Temperature were found to increase by a few Kelvin which is, however, not enough for biomedical applications. Higher amplitudes and frequencies would be necessary to improve the effect.

Finally, the nanoparticles were found to self-assemble into two and three-dimensional superstructures was studied.

4.3. Ferrogel study

4.3.1. Introduction

The behavior of PNIPAAm hydrogel under different pHs and temperatures has been described in Section 4.1. The synthesis and some applications of magnetic nanoparticles have also been studied in Section 4.2. In this chapter, results regarding combination of nanoparticles and the hydrogel are presented. This combination is more properly designated as ferrogels and, as already stated in Section 1.4, represent a new type of *composites* consisting of small magnetic particles, usually in the nanometer range, dispersed in an elastic polymeric matrix.⁴⁹ The term *composite gel* indicates that in addition to the polymer network and swelling agent, a third component is present as a filler (i.e., magnetic nanoparticles).⁵⁰ Fillers can be used to take up space (i.e., reduce cost), reinforce mechanical performance of the gel, or, as it is the case in this work, improve its electrical or magnetic properties.

Ferrogels are a promising class of materials for many applications, such as magnetoelastic mobile robot, artificial muscles,⁵² or magnetic controlled drug delivery.^{49, 226}

As already mentioned in Section 1.4, there are two distinct types of interactions between polymer networks containing magnetic particles and an external magnetic field: particle-particle interactions and field-particle interactions.⁵²

If a uniform magnetic field is applied, particle-particle interactions become dominant. The magnetic dipole in the nanoparticle aligns with the magnetic field direction and two things can happen if particles are so closely spaced that they are inside the local field radio of their neighbors: (i) they will attract each other when aligned end to end, (ii) they will repel each other in the side-by-side situation. Pearl-chain structures can build up leading to magnetorheological effects inside the gel or even deformation effects. Gollwitzer *et al.* showed how a sphere of a ferrogel elongates along the field lines of an homogeneous magnetic field, an effect predicted by calculations (check reference 15 and 16 from⁵⁸) but not observed until then.⁵⁸ An interesting configuration was obtained by Osterman *et al.* who constructed membranes of nanoparticles with the help of three orthogonal pairs of Helmholtz coils.²²⁷ Nevertheless, the most commonly observed effect is the alteration of the mechanical properties.^{53-55, 57, 228, 229} Stepanove *et al.*, for instance, obtained a magnetoactive elastomer polymerizing carbonyl iron (2-4 μm) nanoparticles and

silicone elastomer under a magnetic field of 800 Oe. They claimed the existence of a correlation between the magnetic and mechanical hysteresis behavior in a way that when magnetic field was turned on, the sample behaved as a plastic material; however, when the field was turned off, the magnetic interparticle forces disappeared and the elasticity of the matrix was recovered.⁵⁷ On another example, S. Abramchuk *et al.* showed the anisotropic mechanical behavior of a poly(dimethylsiloxane) (PDMS) magnetoelastomer containing carbonyl iron nanoparticles crosslinked under a uniform magnetic field. Young's modulus turned out to be higher on the direction of the particle chains and when a magnetic field was applied parallel to the columnar structures.^{228, 229}

On the other hand, if the field is nonuniform, the field-particle interactions are dominant. In this case, the particles experience a magnetophoretic force; namely, the particles are attracted towards the stronger field intensities. When the binding between the solid nanoparticles and the polymer network chains is strong enough, and the amount of nanoparticles overpass the percolation threshold (amount of nanoparticles that allow the infinite connectivity),^{230, 231} the forces can accumulate and lead to a macroscopic shape change.^{59, 232, 233} Zrínyi *et al.* studied the elongation of cylindrical polyvinyl alcohol (PVA) gels with magnetite nanoparticles.^{233, 234} They observed a giant magnetostriction (elastic response to magnetic polarization) up to 40% of the initial length.

If one could think of a way to implement the responsiveness to a magnetic field with the responsiveness to another controllable parameter, interesting new applications would come into view. Following this idea, thermoresponsive ferrogels have attracted much attention in the last years. The thermal properties can be used to complement the performance of ferrogels. For instance, Shamim *et al.* studied the behavior of thermoresponsive-polymer-coated magnetic nanoparticles.²³⁵ They used the hydrophobic character of PNIPAAm at temperatures higher than the LCST of PNIPAAm (~40 °C) to adsorb BSA (Bovine Serum Albumin) on the surface, separate it from the rest by magnetic separation and desorbing the protein later on at temperatures lower than the LCST. Other applications are related to the inner heating behavior of nanoparticles when subjected to an AC magnetic field.^{226, 236-238} This is the so-called *hyperthermia* and it was already discussed in Section 4.2. Owing to its popularity, much effort has been put on the synthesis and characterization of PNIPAAm containing ferrogels. From a dimension point of view, one can find

macroscopic samples,²³⁹ or microscopic particles.²⁴⁰ Typically, ferrogels in a macroscopic dimension are studied for applications such as micromachines and artificial muscles. The ferrogel is usually synthesized through the polymerization of a mixture of magnetic particles with the monomer.^{55, 236, 237, 241, 242} To the best of our knowledge, no influence of the nanoparticles in the LCST of PNIPAAm was ever observed. However, Pich *et al.* studied the effect of magnetite nanoparticles dispersed in microgels based on N-vinylcaprolactam (VLC) and acetoxyethyl methacrylate (AAEM), instead of PNIPAAm.²⁴³ They observed that lower amounts of NPs lowered the LCST, which they attribute to magnetite-polymer interactions, whereas higher loads of NPs shift the LCST to higher values, which they assumed to be caused by interparticle forces. However, they did not bring more insight into the phenomenon. Microspheres are mainly used in biomedical applications such as drug-release.^{49, 244, 245} Typically, magnetic nanoparticles are used as seeds for polymerization around the surface,^{235, 240, 245} although other methods are used such as synthesizing the magnetic nanoparticles inside micelles created by PNIPAAm surfactant chains.²⁴⁶

To the best of our knowledge, thin film ferrogels have never been studied. In this section, thin film ferrogels based on PNIPAAm were investigated. In the first place, we answered the question whether the nanoparticles remain in the hydrogel after rinsing or not. Next, the effect of the nanoparticles on the hydrogel properties was discussed. Finally, the effect of nonuniform magnetic field on the thin film ferrogel is studied both experimentally and theoretically.

4.3.2. Experimental procedures

As aforementioned, ferrogels consist of a polymeric matrix with embedded magnetic particles. In this study, PNIPAAm based hydrogel described in section 3.1.1 is used as polymer. The magnetic nanoparticles were synthesized as described in Section 3.2.2 with a size of 3.7 ± 0.8 nm and 19.5 ± 2.4 nm. They were coated either with benzophenone silane (4-(3-triethoxysilyl)propoxybenzophenone) or with oleic acid.

UV-visible light spectra were recorded on a Lambda 900 spectrometer (Perkin Elmer). A flow cell was designed for the measurement of thin film polymers on liquid (see Figure 2.15). PNIPAAm solutions containing 0.99 wt% of nanoparticles were spin coated in quartz slides previously silanized with benzophenone silane. The

silanization protocol included two parts: (1) cleaning of the slides with an Ar/O₂ plasma (2:1) for 10 minutes at 150 W, and (2) immersing slides overnight in an ethanolic solution of 1 mM benzophenone-silane. After rinsing and spincoating of the slides with polymer, UV crosslinking was performed during different times (5 minutes, 20 minutes, and 60 minutes).

For the SPR-OWS experiments LaSFN9 slides were prepared as described in Section 4.1.2. The ferrogel blend was spincoated on LaSFN9 glass slide previously covered with Cr, Au, and BZ-thiol.

The photo-crosslinked hydrogel layers were studied by means of SPR and OWS in the Kretschmann configuration, as described in Section 2.2. Two different setups were used in this study. In order to study the effect of temperature, the setup was modified with a heating plate and a cooling system, as described in Section 2.2. On the other hand, a platform that allows the incorporation of a magnet was used when the effect of the magnetic field was studied [Figure 2.11].

Ferrogel preparation

To prepare the ferrogel blend a certain amount of dry PNIPAAm was mixed with a dispersion of nanoparticles in chloroform. The amounts of each component depended on the experiment. The chloroform-PNIPAAm solution was spincoated on the substrate. Polymer concentrations varied between 2 and 4.5 wt% and nanoparticle concentrations varied between 0.99 and 16.7 wt%.

4.3.3. Results and Discussion

4.3.3.1. Ferrogel preparation

Ferrogel thin film was prepared as described beforehand. A drop from a diluted ferrogel solution in chloroform was drop casted on top of a TEM grid. The nanoparticles in this case had been functionalized with BZ-silane. Figure 4.3.1 show two TEM micrographs.

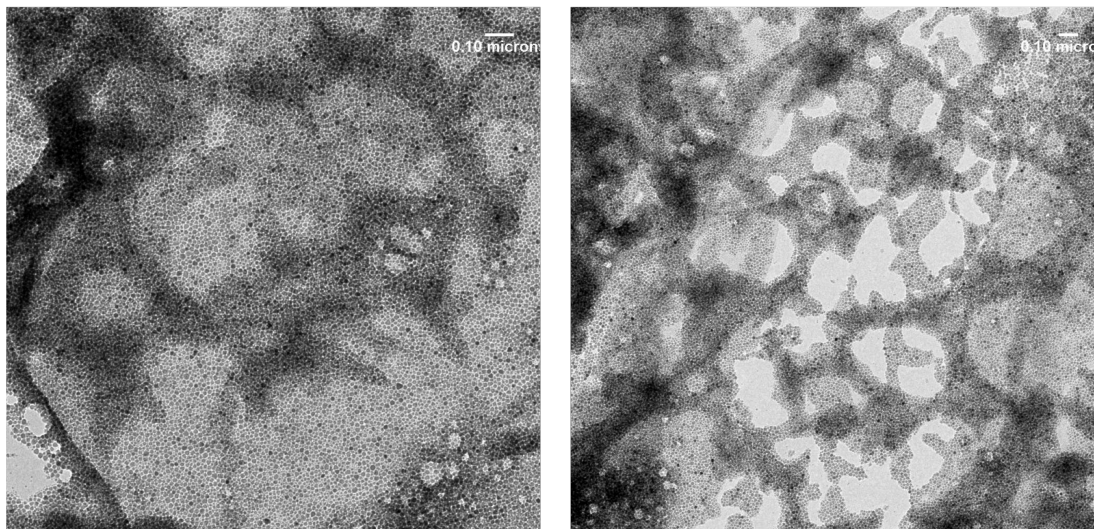


Figure 4.3.1 TEM pictures of ferrogel dropcasted. The scale bars on the top right hand represent 0.1 μm .

Note that drop cast can generate thicker films compared with spincoating; thus, multiple layers of nanoparticles can be observed in the TEM pictures. However, nanoparticles are well dispersed with no big aggregates.

4.3.3.2. UV-VIS study on binding of nanoparticles to the hydrogel

The main purpose of studying ferrogels was to understand the effect of the magnetic nanoparticles on the network properties. The first objective was to ensure that the nanoparticles remained inside the hydrogel after rinsing. It is known that Fe_3O_4 nanoparticles present a shoulder in UV-VIS spectra, typical from semiconductor materials, at wavelength between 300 and 400nm.²⁴⁷⁻²⁵¹ A spectra of the particles modified with BZ-silane and as-synthesized with oleic acid can be seen in Figure 3.14. Monitoring this shoulder allowed us to verify the presence of magnetite nanoparticles in the gel.

In order for the nanoparticles to stay inside the network, one of these two effects (or both) should happen: 1) the nanoparticles are bond to the network 2) the mesh size of the network is small enough to retain the NPs inside. The mesh size of the network can be varied with different irradiation times under a constant polymer composition due to photo-crosslinking process. Hence, to investigate hypothesis number 2) different crosslinking times (i.e., different mesh sizes) were used.

PNIPAAm solutions containing 0.99 wt% of nanoparticles were spincoated in quartz slides previously silanized with benzophenone. The polymer concentration

was 4.5 wt% in chloroform, which yielded a thickness of 1 micrometer in dry state. The nanoparticles had a diameter of 19.5 nm. They were coated either with the BZ-silane or with the oleic acid surfactant. The different crosslinking times chosen were: 5 minutes, 20 minutes, and 60 minutes of UV exposure. A typical experiment consisted of:

- 1) Mounting the quartz slide with the polymer in the flow cell, being the slide one of the walls. Filling it with MilliQ water and scan from 200 to 800 nm
- 2) Start rinsing at a rate of 0.5 mL/min for 5 minutes before stopping and scanning the sample again.
- 3) Rinse for 10 more minutes and scan afterwards.
- 4) Rinse for 30 minutes more and do a final scan.

A blank experiment with PNIPAAm without nanoparticles is made. As already mentioned, magnetite nanoparticles present a shoulder between 300 and 400 nm in the UV-VIS spectra [Figure 4.3.2 (a)]. This shoulder is difficult to distinguish; hence, Figure 4.3.2 (b) shows a comparison of a PNIPAAm hydrogel with and without nanoparticles.

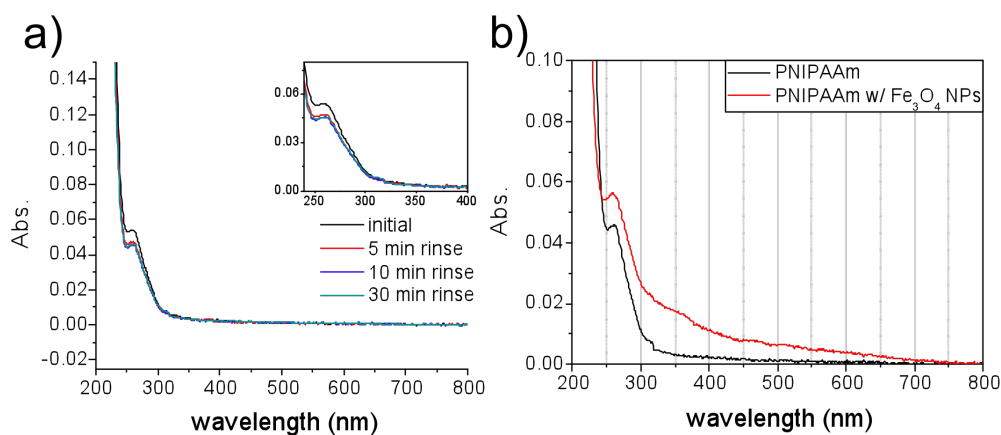


Figure 4.3.2 UV-VIS spectra of a) PNIPAAm hydrogel at different rinsing times and b) the same gel compared to another PNIPAAm hydrogel with nanoparticles with a diameter of 19.5 nm after being rinsed for 30 minutes.

The UV-VIS spectrum of PNIPAAm crosslinked for 60 minutes is shown in Figure 4.3.2(a). An absorption at 260 nm corresponding to the benzophenone is present.⁹⁵ After the polymer has been rinsed for 5 minutes, the peak decreases due to an initial loss of uncrosslinked material. Posterior rinsings do not change the absorption significantly meaning that the polymer uncrosslinked chains are mostly

removed. When the spectra of PNIPAAm is compared with a spectra from a PNIPAAm polymer containing Fe_3O_4 NPs a shoulder between 300 and 400 nm can be clearly appreciated. This shoulder corresponds to the semiconductor absorption mentioned above.

In order to extract information about the presence of NPs in the gel after rinsing a ratio, r , between the absorption at 260 nm (typically of the benzophenone) and the absorption at 350 nm (typically of magnetite nanoparticles) is calculated and used as a comparison parameter. For PNIPAAm without nanoparticles the initial ratio is 14 and remains constant throughout the whole experiment [Figure 4.3.2(a)].

In all the experiments where the polymer with or without NPs was crosslinked for 5 minutes, the film was washed away after 5 minutes of rinsing. Therefore, 20 minutes and 60 minutes crosslinking times will only be considered for further interpretation.

The first set of experiments was done using 19.5 nm diameter NPs either covered with benzophenone units or oleic acid surfactant. For each type of NP, two different crosslinking times were used: 20 and 60 minutes. Thus, the effect of decreasing mesh size is shown in Figure 4.3.3.

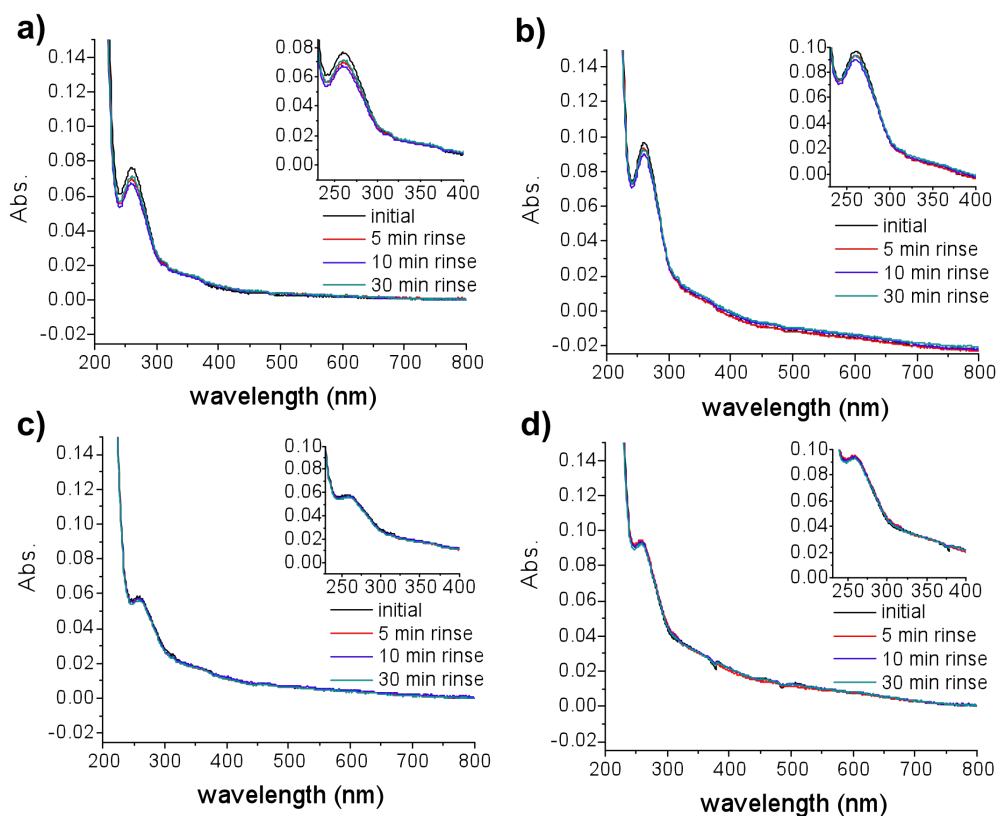


Figure 4.3.3. UV-VIS spectra of samples containing PNIPAAm and Fe_3O_4 NPs (19.5 nm diameter) covered with oleic acid and crosslinked for a) 20 minutes, and c) 60 minutes. The spectra of samples containing PNIPAAm and Fe_3O_4 NPs covered with BZ-silane and crosslinked for b) 20 minutes, and d) 60 minutes.

The samples crosslinked 20 minutes have a more pronounced decrease in the benzophenone absorption ($\lambda = 260$ nm) after the initial 5 minutes rinsing compared to the ones crosslinked for 60 minutes. Unlike the 5 minutes crosslinked samples, further rinsing did not wash the polymer additionally in any of the two cases. Another difference between the samples with different crosslinking densities was that the benzophenone peak absorption decreased in the 60 minutes crosslinked due to the transformation of benzophenone into a benzophenone ketyl radical that is inserted in any available non-aromatic C-H bond forming a C-C bond, as explained in Section 3.1.3. There is not noticeable difference between the NPs covered with oleic acid and the NPs covered with benzophenone units.

A deeper insight into these experiments is extracted through the study of the ratios, r , presented in Table 4.3.1.

<i>rinsing time</i>	<i>initial</i>	<i>5 min</i>	<i>10 min</i>	<i>30 min</i>
OA 20min	5.37	4.98	4.78	4.74
OA 60 min	3.22	3.30	3.09	3.18
BZ 20 min	3.97	3.84	3.65	3.73
BZ 60 min	3.00	3.11	3.00	2.98

Table 4.3.1. Ratio of absorption at a wavelength of 260 nm (typical absorption for benzophenone) divided by the absorption at 350 nm (typical for magnetite NPs). (OA = refers to surfactant around NPs is oleic acid. BZ = refers to surfactant around NPs is benzophenone. 20 min or 60 min refer to the crosslinking time).

The first and most important point is that the ratios of absorption, r , for these samples at the final stage (i.e., after 30 minutes rinsing) are between 3 and 4. This is significantly smaller compared to the PNIPAAm without particles ($r=14$). It can be concluded that the 19.5 nm diameter NPs are not rinsed out of the gel. Whether this is because the nanoparticles are covalently bound to the gel or because the mesh size of the gel is small enough to retain them inside is unclear.

To study the effect of the mesh size, the ratios of samples with the same surfactant but different crosslinking times were compared. When the crosslinking density is higher (60 min crosslinking time) one can see that the ratios decrease. This is due to a decrease in the 260 nm absorption compared to the NPs shoulder at 350 nm. This decrease in the benzophenone peak occurs because of the transformation to benzophenone ketyl radical, already mentioned above. Another contribution to this effect could be that a decrease in the mesh size would have prevented the nanoparticles to leach out of the network.

The effect of the surfactant on the surface of the nanoparticles can be studied through the ratios of gels with the same crosslinking time. For gels crosslinked 20 minutes, the ratio for the benzophenone coated NPs is smaller compared to the OA one. The same effect was observed for the gels crosslinked for 60 minutes. The reason for this effect is that there are more nanoparticles that remain in the system when they are coated with benzophenone, probably because benzophenone covalently binds to the network decreasing the possibility of leakage of NPs.

From the observations up to this point, it was clear that a big fraction of the nanoparticles remained inside the network after rinsing and, moreover, benzophenone surfactant around the nanoparticles helped the nanoparticles to stay inside the network. It still remained unclear the reason why the nanoparticles coated

with oleic acid stay inside the network: was it a mesh size effect, or that the benzophenone on the polymer linked to them? In the next set of experiments NPs that have a diameter of 3.7 nm were incorporated instead of the 19.5 nm ones. If the mesh size of the gel is bigger than 3.7 nm and the NPs are not bonded to the network, they should be able to escape through the pores.

In Figure 4.3.4, the above-discussed difference between 20 minutes and 60 minutes crosslinking time can be observed as well. Likewise, samples crosslinked for 20 minutes release more uncrosslinked chains after the first rinsing. In the same way, the benzophenone absorption decreases due to the increase of benzophenone units transformed into benzophenone ketyl radical.

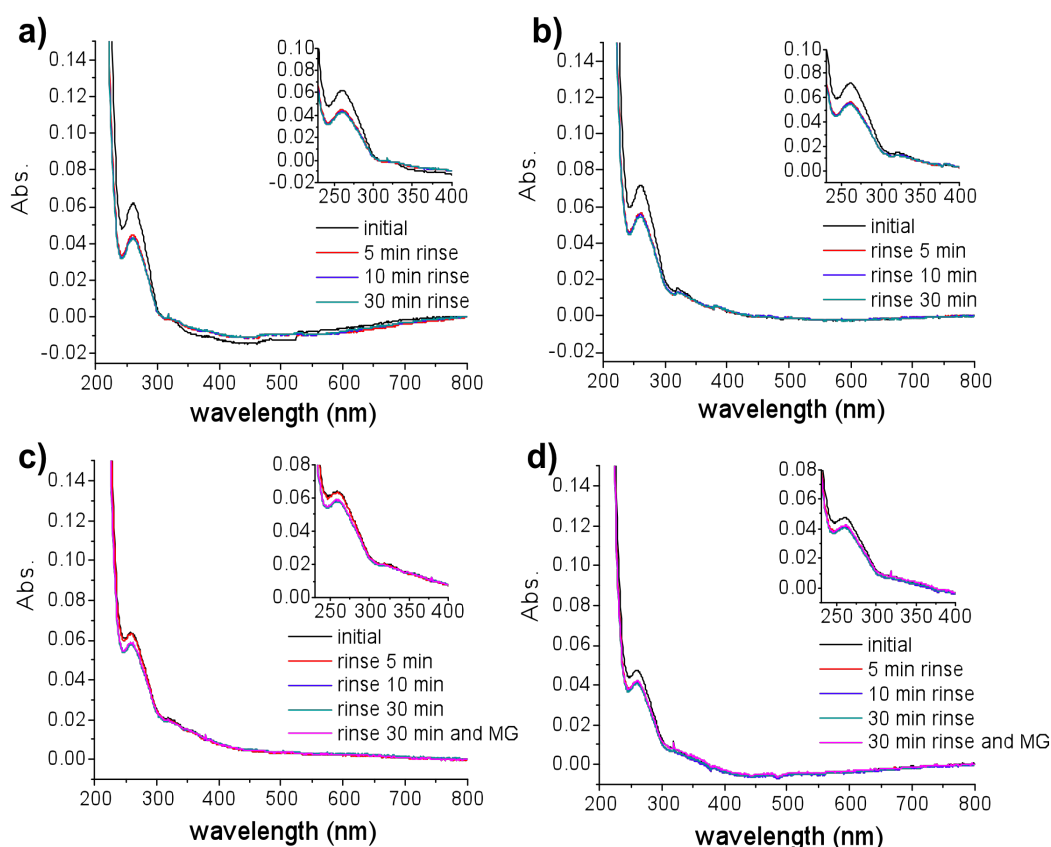


Figure 4.3.4. UV-VIS spectra of samples containing PNIPAAm and Fe_3O_4 NPs (3.7 nm diameter) covered with oleic acid and crosslinked for a) 20 min, and c) 60 min. Also, UV-VIS spectra of samples containing PNIPAAm and Fe_3O_4 NPs covered with benzophenone and crosslinked for b) 20 min, and d) 60 min are shown.

The objective of using smaller nanoparticles with the same mesh size (same UV exposure time) was to unravel whether these would escape from the network if

hypothetically the mesh size had been bigger. The ratios for these nanoparticles [Table 4.3.2] were, again, lower than the $r=14$ found for pure PNIPAAm; hence, the nanoparticles stayed inside the network. It could still be possible that the oleic acid around the nanoparticle is binding into the benzophenone crosslinking points on the polymer. It remains unclear the nanoparticles stayed inside due to a mesh size effect or due to the benzophenone on the polymer acting as a linker.

	OA 20min	OA 60min	BZ 20min	BZ 60min
r	1.93	3.09	2.5	1.6

Table 4.3.2. Ratio of absorption at a wavelength of 260 nm (typical absorption for benzophenone) divided the absorption at 350 nm (typical for magnetite NPs). (OA = refers to surfactant around NPs is oleic acid. BZ = refers to surfactant around NPs is benzophenone. 20 min or 60 minutes refer to the crosslinking time). All ratios calculated for 30 minute rinsing.

In order to study if benzophenone crosslinks to the network, another polymer system with the same nanoparticles was studied for comparison purposes. The new system consisted of PNIPAAm polymer with DMI comonomer as crosslinking agent. Description can be found in Section 4.1.2. The new system did not have benzophenone comonomers, thus, oleic acid coated nanoparticles could not stay inside the network due to the covalent bonding to the network. If the nanoparticles functionalized with OA were washed away and the benzophenone coated ones were not, it would mean that the benzophenone on the nanoparticles would be crosslinking to the network.

A blank UV-VIS spectrum of the PNIPAAm-DMI system without the nanoparticles is measured in order to compare the effect of the nanoparticles [Figure 4.3.5]. For comparison, a spectrum of the PNIPAAm-BZ system without nanoparticles is depicted next to PNIPAAm-DMI system and PNIPAAm-DMI with NPs. The spectrum of the PNIPAAm-DMI system has two main absorption peaks: the corresponding to DMI crosslinking unit at 270 nm, and the other at 395 nm from the photosensitizer.^{29, 252} It's worth noting that DMI concentration in PNIPAAm-DMI system was 5 wt% in comparison to the 1 wt% concentration of BZ in PNIPAAm-BZ. When magnetite NPs coated with benzophenone are added to the system, the absorption shoulder corresponding to them can be clearly distinguished on the spectrum. The benzophenone absorption related to the NPs linked to the polymer is disguised under the DMI absorption peak.

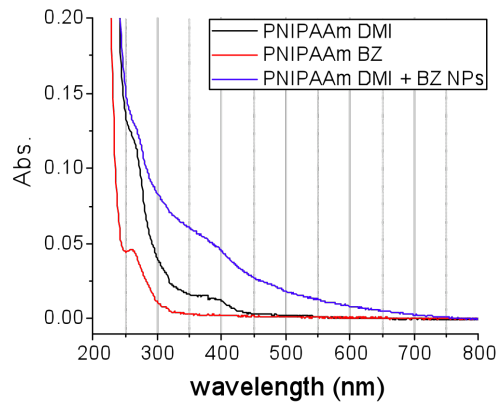


Figure 4.3.5 UV-VIS spectra of PNIPAAm polymer system with DMI crosslinker (black line) with benzophenone crosslinker (red line) and PNIPAAm with DMI crosslinker and nanoparticles covered with benzophenone.

In this system, the ratio, r' , is defined as the absorption of DMI ($\lambda=270\text{nm}$) divided by the absorption of nanoparticles ($\lambda=350\text{nm}$). The same kind of experiments with magnetite nanoparticles with a diameter of 3.7 nm and with two different surfactants (benzophenone and oleic acid) and different crosslinking times (20 minutes and 60 minutes) were performed and are shown in Figure 4.3.6.

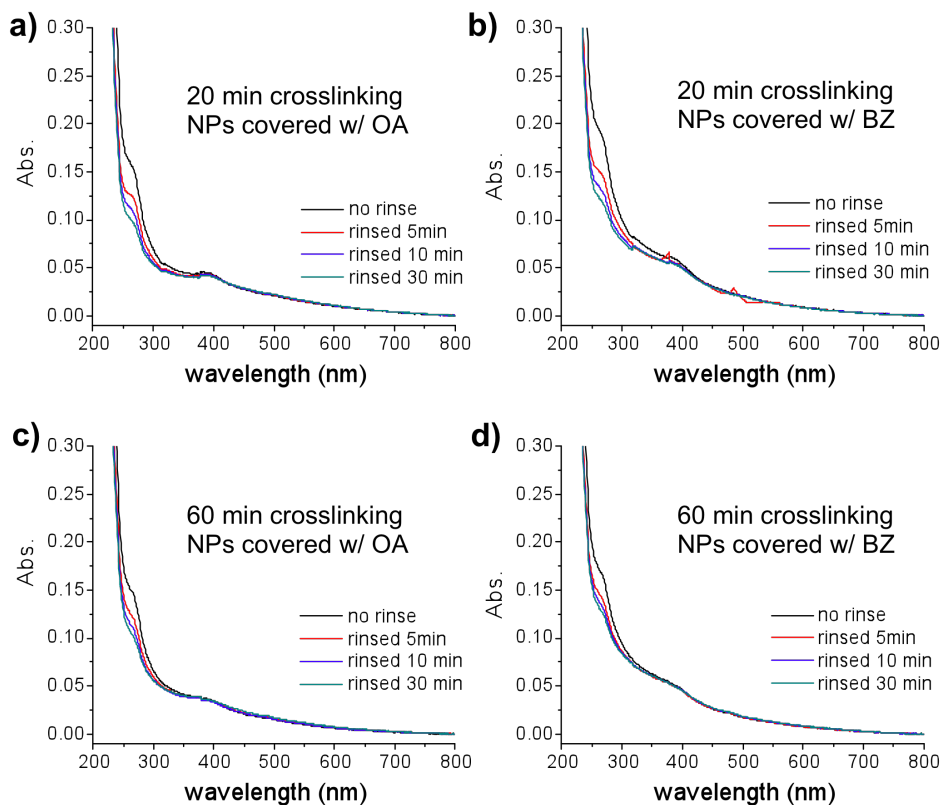


Figure 4.3.6. UV-VIS spectra of samples containing PNIPAAm-DMI and Fe_3O_4 NPs (3.7 nm diameter) covered with oleic acid and crosslinked for a) 20 minutes, and c) 60 minutes. Also, UV-VIS spectra of samples containing PNIPAAm-DMI and Fe_3O_4 NPs covered with benzophenone and crosslinked for b) 20 minutes, and d) 60 minutes.

Films with a higher crosslinking degree lose less material when being rinsed. This can be seen in the decrease in absorption of the spectra after the initial 5 minutes rise, which is more pronounced when samples have been crosslinked for 20 minutes. The same trend was found in the other experiments with PNIPAAm-BZ. From spectra in Figure 4.3.6 the ratios, r' , are calculated and can be seen in Table 4.3.3.

	OA 20 min	OA 60 min	BZ 20 min	BZ 60 min	PNIPAAm-DMI
r'	2.26	2.42	1.87	2.04	6.56

Table 4.3.3. . Ratio of absorption at a wavelength of 260 nm (typical absorption for benzophenone) divided the absorption at 350 nm (typical for magnetite NPs). (OA = surfactant around NPs is oleic acid. BZ = surfactant around NPs is benzophenone. 20 min or 60 minutes refer to the crosslinking time). All ratios are calculated with the corresponding absorptions after samples have been rinsed for 30 minutes. PNIPAAm-DMI is the ratio for the polymer without NPs and crosslinked for 60 minutes.

The samples containing nanoparticles have a ratio, r' , three times lower compared to the PNIPAAm-DMI sample without nanoparticles. This difference leads to the conclusion that the nanoparticles stay inside the network even after the 30 minutes rinsing in both cases: NPs coated with oleic acid and benzophenone. It can therefore be concluded that the nanoparticles remain inside because of the mesh size. The ratios, r , corresponding to nanoparticles containing benzophenone are, however, smaller. That indicates that, apart from the mesh size effect retaining the NPs inside the network, benzophenone on the surface of the nanoparticles is binding to the network. In conclusion, magnetite nanoparticles remain inside the system DMI-PNIPAAm because of a combination between small mesh size than NPs and a covalent bond between the NPs and the network, in case that the NPs have benzophenone on the surface.

As summary, nanoparticles inserted in the network are not washed away in any of the systems studied. In case of the nanoparticles covered with benzophenone lower ratios compared to the oleic acid coated ones are found. Therefore, benzophenone on the surface helped nanoparticles stay inside the network. The nanoparticles coated with oleic acid were retained inside the PNIPAAm-DMI network because the mesh size of the polymer was smaller than 4 nm. In the case of the

PNIPAAm-benzophenone system, whether it's only a mesh size effect or the binding to the benzophenone crosslinking unit contributes cannot be stated.

From an application point of view, it would be interesting to test the resistance of the nanoparticles to escape from the network under the influence of a magnetic field. This resistance test was performed on the experiments corresponding to PNIPAAm crosslinked for 60 minutes with the 3.7 nm diameter nanoparticles. The experiment consisted of positioning a permanent magnet (0.7 Tesla at the surface) with a gradient magnetic field next to the cell while rinsing for 5 minutes, after which another UV-VIS spectrum was measured [Figure 4.3.4 (c) and (d) in pink]. The result shows an increase on the ratio r (<1.5%) not significant enough to attribute it to a leaching of nanoparticles attracted by the magnetic field. The nanoparticles are not dragged out of the polymer by the exterior magnetic field.

4.3.3.3. Refractive index variation with amount of nanoparticles

The optical properties of ferrogels are of interest when designing photonic crystals of superparamagnetic nanoparticles for optoelectronic applications such as lasers, or components in telecommunication devices. It is highly desirable that a photonic crystal possesses a tunable stop band that can be conveniently controlled by external stimuli. Considerable effort has been devoted to achieving this goal by changing the refractive indices of the materials and the lattice constants or spatial symmetry of crystals through application of chemical stimuli, mechanical forces, electrical fields, or light.²⁴⁹ A very important parameter is the refractive index of the system and, in particular, of the nanoparticles. However, there are not many publications, to the best of our knowledge, describing refractive index of magnetite nanoparticles. In this section, results regarding the use of SPR-OWS [See Section 2.2 for detailed explanation of this method] to fully characterize the refractive index of the system are reported.

The studied materials consisted of mixtures of PNIPAAm and magnetite nanoparticles coated with benzophenone surfactant. Nanoparticle concentrations were adjusted to 0.99, 9.1 and 16.7 wt%. An angular scan of the reflected intensity $I(\theta)$ was recorded in dry state and shown in Figure 4.3.7.

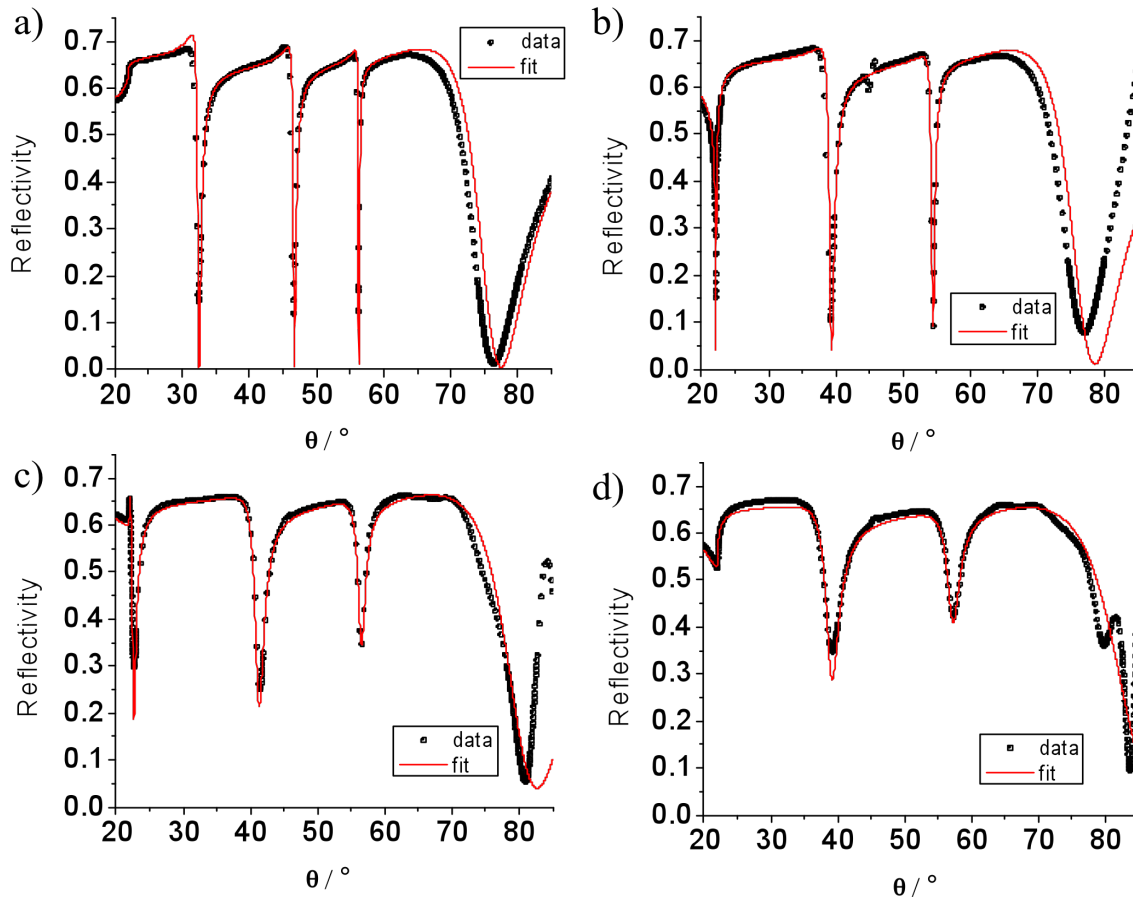


Figure 4.3.7 SPR/OWS spectra for dry films of a) pure PNIPAAm b) PNIPAAm with 0.99% magnetite NPs, c) PNIPAAm with 9.1% magnetite NPs and, d) PNIPAAm with 16.7 wt% magnetite NPs. All films were deposited on a LaSFN9 glass slide with a chromium layer and a gold layer coated with adhesion promoter. The diameter of all the magnetite NPs was 19.5 nm. All spectra were recorded with p -polarized light. The dots are measured data points; the red lines correspond to simulated spectra for a box model.

Figure 4.3.7(a) shows a typical spectrum of pure PNIPAAm film without nanoparticles in dry state and a thickness around $1\ \mu\text{m}$. There are 4 minima in the spectra. The wider one -between 75° and 80° - corresponds to the excitation of the plasmon at the interface between the gold and the polymer. The other 3 sharp minima correspond to the coupling of the light guided optical modes that are confined inside the polymer (normally called leaky optical waveguide modes). These are labeled TM1-TM3 from left to right. The fact that the TM n modes present a sharp shape with reflectivity close to 0.1 is due to a good coupling efficiency, which happens when films are optically homogeneous and smooth. Figures 4.3.7(b)-(d) show the spectra of PNIPAAm with 0.99, 9.1 and 16.7 wt% in dry state. It can be observed that the coupling efficiency decreases with the increase of the amount of

nanoparticles. The two main reasons for this is that magnetite nanoparticles scatter and absorb light (absorption provides a complex dielectric constant). The double minima at angles higher than 80° is due to alignment effects and backscattering. Figure 4.3.8 shows the spectra for nanoparticles with a main diameter of 3.5 nm. The most evident feature is that the coupling efficiencies (sharper TM modes) are better for these films due to the smaller size on the nanoparticles.

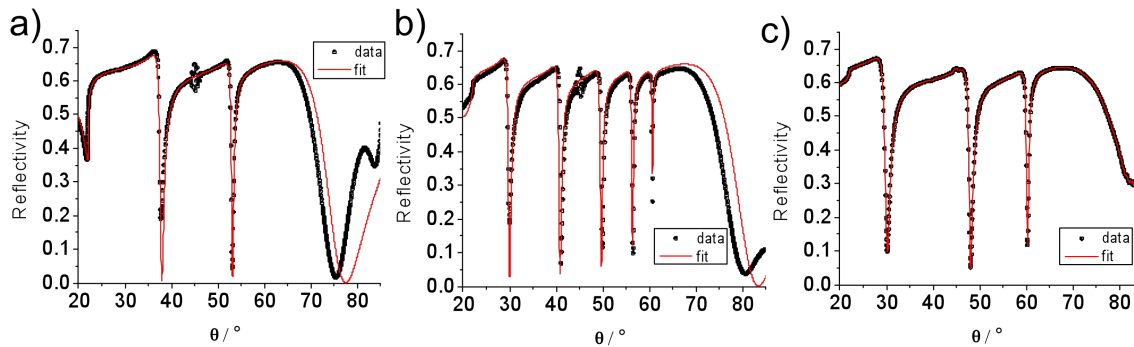


Figure 4.3.8. SPR/OWS spectra for dry films of a) PNIPAAm with 0.99 wt% magnetite NPs, b) PNIPAAm with 9.1 wt% magnetite NPs and, c) PNIPAAm with 16.7 wt% magnetite NPs. All the magnetite NPs correspond to 3.5 nm diameter NPs.

The angle-dependent reflectivity of hydrogel/nanoparticle film samples was modeled by solving the Fresnel equations by a transfer-matrix algorithm, using software developed in our group. The system was divided in planar homogeneous layers, each one of which is described by three parameters, its thickness d_{layer} and the complex dielectric constant ($\epsilon_{\text{layer}} = \epsilon'_{\text{layer}} + i\epsilon''_{\text{layer}}$). The different layers are described in Section 2.2. When describing the composite film, only one layer was used; thus the so-called “box-model” was applied. The dielectric constants extracted from the modeling are presented in Table 4.3.4.

<i>sample</i>	<i>15 nm NPs</i>		<i>3.5 nm NPs</i>	
	ϵ'	ϵ''	ϵ'	ϵ''
PNIPAAm 0% NPs	2.17	0	2.17	0
PNIPAAm 0.99% NPs	2.187	0.003	2.149	0
PNIPAAm 9.1% NPs	2.25	0.015	2.238	0.003
PNIPAAm 16.7% NPs	2.328	0.031	2.320	0.004

Table 4.3.4. Dielectric constants extracted from the modeling of the SPR/OWS spectra using the so-called “box model”.

Several methods have been developed to model dielectric function on mixtures. They are widely used in porous alumina²⁵³ or ceramic mixtures²⁵⁴. The base on these methods is host-inclusion models assuming spherical pores. Maxwell-Garnett (M-G) and Bruggeman's effective medium approximation and are going to be used in this work. The equations describing these models are, respectively: ²⁵⁵

$$\varepsilon_m = \varepsilon_{HG} \left[\frac{2\varepsilon_{NP} + \varepsilon_{HG} + 2f(\varepsilon_{NP} - \varepsilon_{HG})}{2\varepsilon_{NP} + \varepsilon_{HG} - f(\varepsilon_{NP} - \varepsilon_{HG})} \right] \quad (4.3.1)$$

$$0 = f \frac{\varepsilon_{NP} - \varepsilon_m}{\varepsilon_{NP} + 2\varepsilon_m} + (1 - f) \frac{\varepsilon_{HG} - \varepsilon_m}{\varepsilon_{HG} + 2\varepsilon_m} \quad (4.3.2)$$

Where ε_{NP} represents the dielectric constant of the nanoparticles, ε_{HG} represents the dielectric constant of the hydrogel, ε_m represents the dielectric constant of the medium, and f represents the volume fraction of nanoparticles. There are some assumptions on these approximations: M-G assumes that the included spheres are isolated from each other and the diameter of inclusion is much less than the inclusion spacing. Bruggeman assumes that the subunits (or grains) of each phase in the composite material are randomly mixed, and that the subunit dimensions are much less than the wavelength of light but large enough for each subunit to be characterized by its bulk optical response.

The dielectric constant of the nanoparticles was calculated from the dielectric constant of pure PNIPAAm and dry composites.

The average value of refractive index for the magnetite nanoparticles was extracted from samples containing 9.1% and 16.7 wt%. Values extracted from 0.99 wt% had too much experimental error to be considered.

n_r	<i>Bruggeman</i>	<i>M-G</i>
4 nm	2.74 ± 0.20	2.766 ± 0.22
15 nm	2.96 ± 0.05	2.998 ± 0.07

Table 4.3.5. Refractive index of magnetite nanoparticles calculated through Bruggeman-EMA and M-G.

Both models give similar results, however, M-G is generally used with a low volume fraction because it assumes large spacing between nanoparticles.

Smaller nanoparticles have a refractive index of 2.766 ± 0.22 , smaller compared to the 15 nm nanoparticle, which refractive index is 2.998 ± 0.07 . Both values differ from the 2.42 value found in literature for bulk material for Fe_3O_4 .²⁵⁶ This effect could be due to the quantum-size effect, commonly observed in semiconductors.^{257, 258} In such small size regions, there are many atomic vacancies and defects on the surfaces which can become trap states. When excited by an external radiation source, the trapped states would become effective routes for nonradiative transition of excited states, leading to a possible change in refractive index.²⁵⁹ There is no literature that explores the size effects on optical properties of magnetic nanoparticles that could reinforce this hypothesis. On the other hand, being this influenced by size, the refractive index for the smaller nanoparticle should present the bigger effect; and this does not occur. Another explanation is the mixture of Fe_3O_4 with Fe_2O_3 in the nanoparticle chemical composition since the refractive index of Fe_2O_3 is reported to be $\sim 3-3.10$.^{260, 261} Hence, a method for measuring refractive indices of nanoparticles is reported here.

4.3.3.4. Effect of magnetic nanoparticles on LCST

Temperature responsive hydrogels are of special interest as platform networks in ferrogels. Their collapse behavior when heated makes them ideal candidates for drug release applications. As already mentioned, magnetic nanoparticles can be heated up when an alternate magnetic field is applied. The heat generation depends on many factors: magnetic field strength, frequency, nanoparticles size, solvent, etc. A proper study of these factors is required for an optimized performance. Another equally important factor to be studied is the hydrogel platform. It is widely known that when monomers are covalently added to PNIPAAm, the LCST can be influenced. On the other hand, when additives are just in solution, LCST is not affected.³⁶

In this section the effect of magnetic nanoparticles on the LCST is studied. Changes in the thin film ferrogel were monitored by means of SPR-OWS. The samples consisted of PNIPAAm-benzophenone polymer mixed with magnetite nanoparticles with 15-20 nm diameter coated with benzophenone. The concentration of nanoparticles was adjusted to 0.99 wt%, 9.1 wt% and 16.7 wt%. The samples were crosslinked for 60 minutes. As already described in Section 4.1, the LCST of

PNIPAAm is sensitive to the pH in solution because there is an acid comonomer; therefore, all the experiments were performed with MilliQ water as solvent.

The protocol to characterize the LCST of the thin film ferrogels was:

- 1) Inserting the sample on the SPR flow cell setup and record an angle-dependent reflected intensities $I(\theta)$ in dry state.
- 2) Rinsing of the sample for, at least, 15 minutes.
- 3) Heating up and cooling down the sample rapidly at least twice so any uncrosslinked polymer is leached out.
- 4) Stabilize the temperature to 20 °C and scan the angle vs. the reflectivity.
- 5) Increase the temperature to 25 °C and after stabilizing the sample for at least 15 minutes, run another scan of the angle vs. the reflectivity.
- 6) Repeat step 5 for temperatures 27, 28, 29, 30, 31, 33, 35, 40, and 45 °C.

The angular scans of $I(\theta)$ were recorded using p-polarized light to excite the plasmon resonance (TM0) and couple into the transverse magnetic waveguide modes TM_n . Figure 4.3.9(a) shows an example of the evolution of the spectra of the polymer when this is heated up. In this particular case, the PNIPAAm polymer is mixed with magnetite nanoparticles in a concentration of 16.7 wt%. As the polymer heats up and, consequently, collapses, the minimum angle of the plasmon moves to higher angles. On the other hand, the minima corresponding to the waveguided light TM_n decrease in number and separation from themselves. This trend was observed for all samples whose LCST was studied by means of SPR-OWS.

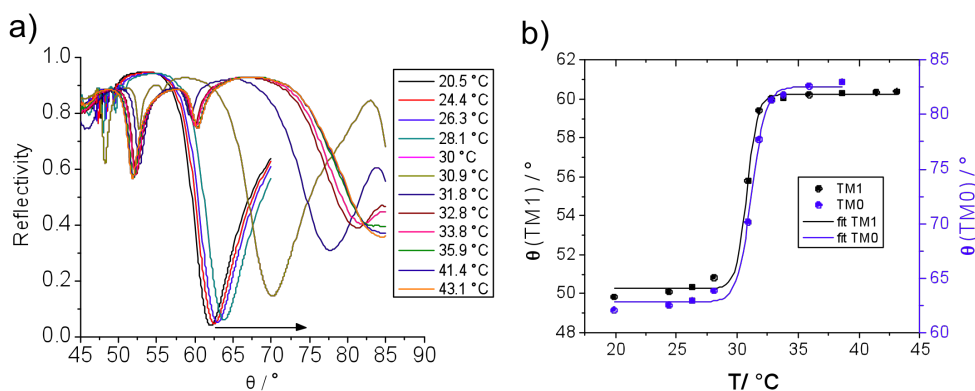


Figure 4.3.9 (a) SPR/OWS spectra of PNIPAAm thin film gel containing 16.7 wt% of magnetite nanoparticles with 15 nm diameter at different temperatures. b) Effect of a temperature on the angle of incidence θ at which the surface plasmon TM_0 is excited and the first waveguide mode TM_1 . The line represents the sigmoidal fit.

To investigate the LCST of the gel, both the angle of incidence θ corresponding to the excitation of the surface plasmon TM0 and the angle of incidence corresponding to the guided mode TM1 are plotted vs. the temperature [Figure 4.3.9(b)]. To determine the LCST these plots are fitted through a sigmoidal expression, as explained in Section 4.1 [Equation 4.1.1]. These plots contain two plateau regions separated by a section with steep slope. Initially the polymer starts losing water gradually as T is increased; suddenly, there is a change in slope because the polymer is collapsing rapidly as it reaches the LCST; once almost all the water is expelled, the last plateau is reached. We define the critical temperature as the temperature at which the sigmoidal curve reaches its inflection point.

For a better understanding of the effect of the nanoparticle loading on PNIPAAm, the LCST values extracted from the curves corresponding to different amounts of magnetite NPs added to PNIPAAm are plotted together vs. the amount of NPs [Figure 4.3.10]. Two LCST values were extracted for every loading, related to the displacements of TM0 and TM1 respectively. At least, two experiments were done for every loading. In some experiments, TM1 was not observed at collapse stage of the polymer due to a decrease in the thickness. For this reason, some values do not present error bars.

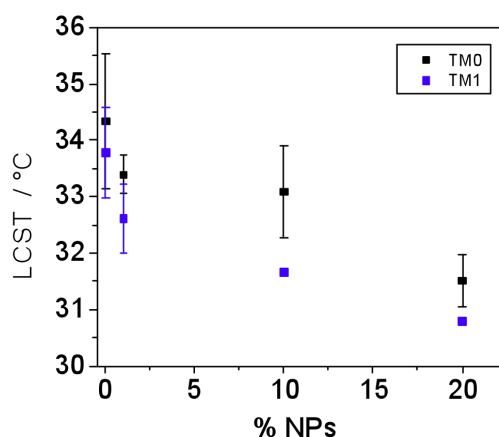


Figure 4.3.10. Dependence of the LCST of PNIPAAm on the nanoparticle loading. LCST values are extracted from the tracking of angle of excitement of the plasmon (TM0) or the angle at which the light couples with the first waveguided mode (TM1).

Two main features can be distinguished from Figure 4.3.10: a decrease in LCST with the increase of nanoparticles and lower values of LCST for data extracted from TM1 compared to TM0. When nanoparticles covered by benzophenone molecules are introduced in the network, the LCST of the polymer decreases, as

Figure 4.3.10 shows. Increasing the hydrophobicity of the network makes it easier for the network to collapse since less energy is needed to counterbalance the hydrogen bonding energy of the water with the hydrophilic parts of the polymer. It has been already reported how hydrophilic comonomers added to the network increase the LCST.^{13, 17} Many factors can affect the LCST of PNIPAAm polymer: crosslinking density, ionic strength of the solution, pH, etc. This is especially interesting when one wants to correlate the collapse response with external phenomena. A clear example of this is the use of PNIPAAm as scaffold for drug delivery on humans. One would ideally tailor the LCST of the polymer close to the body temperature.

As already stated before, LCST values corresponding to TM0 are higher than the ones corresponding to TM1. The surface plasmon (TM0) is excited at the gold-composite interface and is evanescent in the film. Therefore, it is only sensitive to changes in the refractive index in the bottom 150-200 nm of the film. The first order waveguide mode TM1 has its highest field intensity in the centre of the film, so it is a good probe of the “bulk structure” of the film. Therefore, TM1 values give a better idea of the whole gel, sensing earlier the collapse of the film; thus, LCST values for TM1 are lower. The surface plasmon is mainly sensitive for the last part of the process when the film gets thinner; hence, LCST values are higher for TM0.

4.3.3.5. Effect of nonuniform magnetic field on ferrogel

It is well known that ferrogels are sensitive to nonuniform magnetic fields due to the coupling of magnetic and elastic properties.^{58, 59} The magnetic field translates into a shape distortion of the ferrogel. The solid particles in the ferrogel are the only carriers of a magnetic moment. When an external magnetic field is applied, the magnetic moments of the particles align with the field to produce a bulk magnetic moment.

In this section, a nonuniform magnetic field created by a permanent magnet was applied on the ferrogel. A permanent magnet was preferred vs. a coil because the magnetic field created by this was higher than those from coils feasible to build in our lab. The magnet used was a cylindrical magnet made out of Nd₂Fe₁₄B with a diameter of 5.1 cm and a height of 5.1 cm. It was purchased from K&J Magnetics, Inc. To increase the power of the magnetic field, another cylindrical cone magnet with 5.1 cm diameter was purchased and used together with the previously mentioned

(see section 4.3.3.6 for details). The magnetic flux density on the surface of the magnet was close to 0.7 Tesla.

The thin film ferrogel was measured by means of SPR-OWS. The samples consisted of PNIPAAm-benzophenone polymer mixed with magnetite nanoparticles with 19.5 nm diameter coated with benzophenone on the surface. The concentration of nanoparticles was 16.7 wt%. The samples were crosslinked for 30 minutes instead of the usual 60 minutes. The reason for this being that, lower crosslinking densities increase the deformation of the ferrogels.²⁶²

An SPR/OWS setup was designed and built where the magnet was placed on the sample holder and was allowed to rotate with the sample while maintaining the same position with respect to it. A blank sample, consisting of PNIPAAm without the magnetite nanoparticles, was measured. The thickness did not change when the magnet was placed, however, a change in the kinetic was detected due to the weight of the magnet that slightly tilted the prism holder.

Every new sample of ferrogel was first rinsed and dried with MilliQ water at least 3 times. After being placed in the SPR/OWS holder, angular scans of $R(\theta)$ were recorded and the curves were compared until a permanent thickness was achieved [Figure 4.3.11 (a) and (b)]. It was found that the film needed long periods of time (i.e., at least overnight) to stabilize completely.

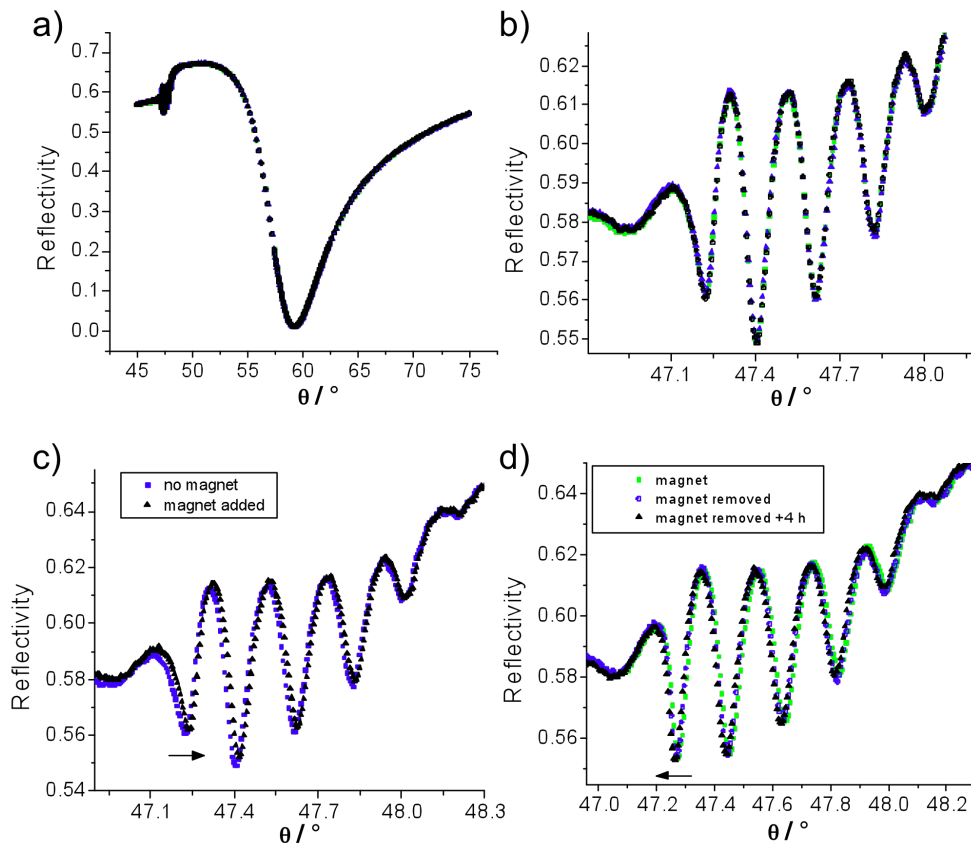


Figure 4.3.11 SPR/OWS spectra in water of a ferrogel sample around 10 μm thick containing 16.7 wt% of nanoparticles with a 19.5 nm diameter. In a) and b) the 3 scans correspond to the initial stabilization of the ferrogel in water over a period of 1h. In b) a close-up of the waveguide modes is shown. In c) the waveguide modes are shown without and with the magnet positioned at a distance of 1 cm from the sample. In d) the same corresponding to the removing of the magnet is shown.

Figure 4.3.11 shows one sample of ferrogel before and after adding the magnet. The scans shown in Figure 4.3.11 (a) and (b) correspond to the initial stabilization. The waveguide modes are more sensitive to changes; hence, close-up of the waveguides are shown instead of the whole spectrum. When the magnet was added for the first time [Figure 4.3.11(c)] there was a 0.7% increase in thickness, that is, from 9910 nm to 9980 nm, according to the fitting in a box. When the magnet was removed the next day [Figure 4.3.11(d)] there was only a small decrease of thickness from 10430 nm to 10390 nm. These changes are very small and in the order of the experimental error. In order to track more sensitively the changes, a kinetic study was performed. In this study the change in reflectivity at a certain angle was measured every 5 to 10 seconds. The angle chosen is in the linear part of the plasmon at a reflectivity value around 20-30 %. The kinetic is shown in Figure 4.3.12.

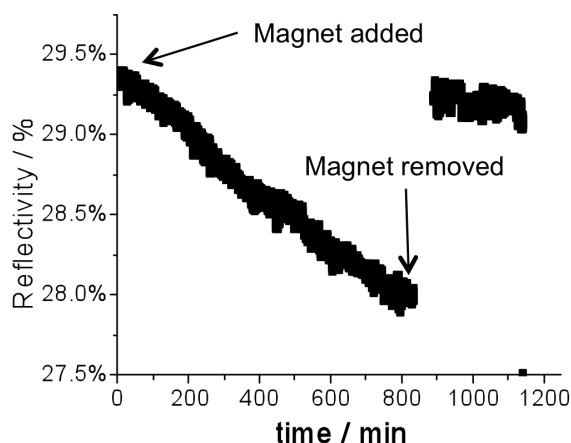


Figure 4.3.12. Evolution of the reflectivity with time at a certain angle θ .

The kinetic study was started after placing the magnet for the first time. A swelling was observed from minute 0 to 800. When the magnet was removed, the slope decreased drastically to a stable state where the ferrogel did neither swell nor collapse anymore. This means that the change caused by the magnet is not reversible. The swelling increases the hydrogel thickness in more than 4%, more precisely, from 10090 nm to 10430 nm. The reflectivity jump is due to the magnet weight that tilts the holder stage. As already mentioned, it was observed as well with pure PNIPAAm. This behavior was observed in other samples and only at the beginning of the experiment, that is, the behavior was not reversible. One explanation is that the nonuniform magnetic field attracts the nanoparticles just enough to slightly deform the ferrogel, however, when the magnetic force is removed, the ferrogel does not respond in an elastic way, but plastic. A discussion on the magnetic field gradient is performed in section 4.3.3.6 These experiments are not clear indications of the magnetic influence on the ferrogel, therefore, another experiment taking advantage of the phase separation behavior was carried out.

The collapse of the network happens on very specific circumstances. Thus, a sensitive way to detect changes in the polymer is through the study of the collapse behavior. In this chapter it was already shown how the addition of magnetic nanoparticles was shifting the LCST of PNIPAAm to lower values due to hydrophobic interactions. Another way to collapse PNIPAAm networks is by changing the environment. For instance, changing from water to mixtures of ethanol or acetone collapse the polymer.⁴⁰ Hence, the quality of the solvent used is an important parameter that can change the mixing energy of the polymer molecules with the

molecules surrounding them (see Section 1.2 for further understanding). In this section the salt induced phase transition of PNIPAAm is studied with and without magnetic nanoparticles and, with and without the influence of a nonuniform magnetic field.

The salt solutions used for these experiments were prepared from sodium chloride in MilliQ water. A protocol for the salt-collapse experiment was established and is as follows:

- 1) Rinse the sample thoroughly with MilliQ water and dry it with nitrogen gas at least 3 times.
- 2) Insert the sample in the SPR/OWS holder designed for magnetic experiments and, after rinsing it with water, position the magnet next to the sample. Allow them to stabilize for at least 5 hours (usually overnight).
- 3) Record an angular scan of $I(\theta)$.
- 4) Rinse the sample for 10 minutes at a rate of 0.3 mL/min with a solution of sodium chloride in MilliQ water of 0.025M.
- 5) Record an angular scan of $I(\theta)$.
- 6) Repeat step 3 and 4 for concentrations 0.1 M, 0.25 M, 0.5 M, 0.75 M, 1 M, 1.2 M, 1.4 M, 1.5 M, 1.6 M, 1.8 M, 2 M, 2.5 M, and 3 M.
- 7) Decrease the ionic strength back to pure MilliQ water slowly and remove magnet. Let stabilize for at least 5 hours (usually overnight).
- 8) Repeat the experiment, this time without any influence of magnetic field.

To understand the influence of the salt on the gels, a similar data processing to the one in section 4.3.3.4 was done. In summary, the angles of incidence θ for the coupling with TM0 and TM1 were plotted vs. the salt concentrations. The resulting curves were fitted with a sigmoidal expression and the critical salt concentration, C^* , was extracted from the inflection point. The curves corresponding to a blank sample of polymer without magnetic nanoparticles are shown in Figure 4.3.13(a) and (b). More precisely, the sample was prepared by spin coating deposition using a PNIPAAm solution with a concentration of 4% in chloroform. The sample was dried under vacuum at 50 °C and crosslinked for 30 minutes. The thickness of the hydrogel, determined through the fitting of the angular scan of $I(\theta)$ using the “box-model”, in MilliQ water is 7.60 μm .

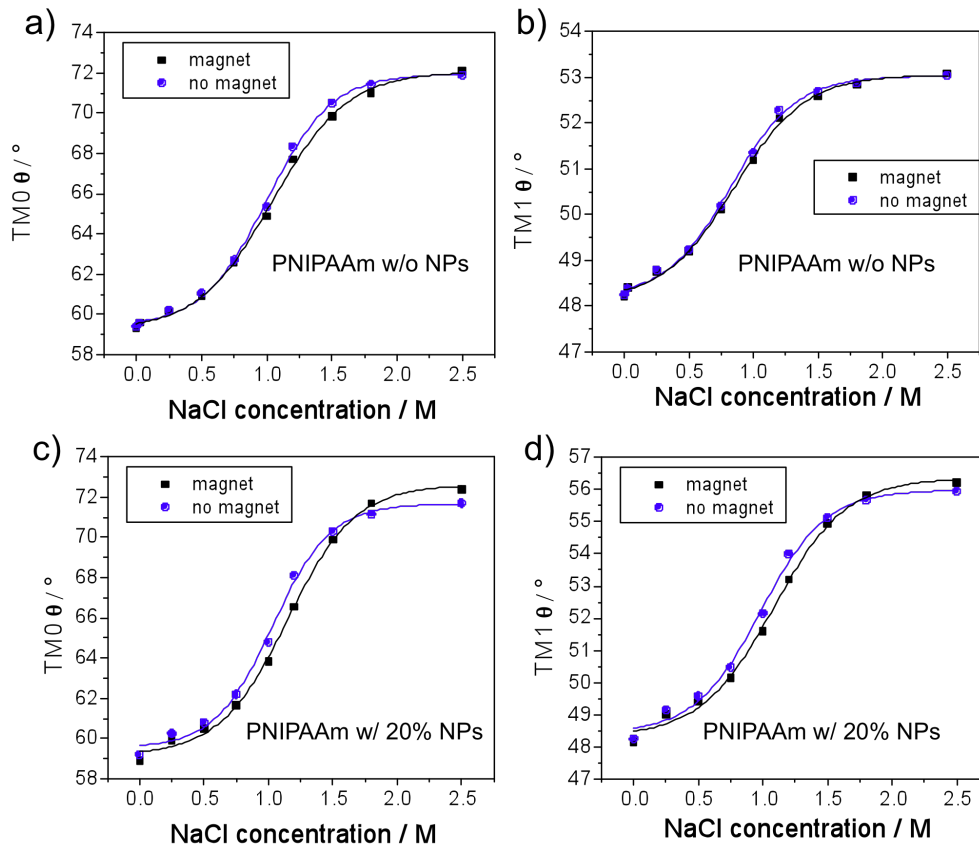


Figure 4.3.13. Dependence of angle at which a) and c) the plasmon is excited (TM0) or b) and d) the guided mode TM1 is coupled with the change in sodium chloride concentration. Figure a) and b) correspond to measurements performed on samples that contain only PNIPAAm whereas in graphs c) and d) the polymer was filled with 16.7 wt% magnetite NPs. Black squares were extracted from measurements made under the influence of a magnetic field. Lines correspond to the sigmoidal fitting of the data.

The typical sigmoidal curve observed when temperature was changed can be seen in Figure 4.3.13. There is a gradual increase on TM0 and TM1 from NaCl concentrations ranging from 0 to 0.6 M. The hydrogel responds to an increase of ionic strength by gradually dehydrating; this is the so-called “salting-out” effect. On one hand, the increase in NaCl promotes hydrogen bonding among water molecules and, therefore, decreases the hydrogen bonding among hydrophilic chains and water. On the other hand, the presence of NaCl increases the polarity of the medium, strengthening the interactions among hydrophobic segments of the network. There is a critical concentration of NaCl upon which the hydrophobic interactions are predominant and the whole network collapses; the values for TM0 and TM1 increase drastically. The C^* values extracted from the sigmoidal fitting can be found in Table

4.3.6. Experiments on PNIPAAm polymer without magnetic nanoparticles show that the critical concentration of NaCl extracted from the change in TM0 varies from 1.00 M without the magnet, to 1.04 M with the magnet, which represents a change of 4.1%. The critical concentration, extracted from the analysis of TM1, changes from 0.82 M to 0.85 M, a change of 3.14%. These values are low enough to be considered measurement errors and are going to be compared with the ferrogel values.

Two samples containing the same ferrogel (16.7 wt% concentration and 30 minutes crosslinking time) were scanned, and the results were analyzed in the same way. The average critical concentration for the TM0 was 1.107 ± 0.07 M and under magnetic field influence it increased to 1.184 ± 0.084 M, which represents a rise of 6.96%. In the case of TM1, the average critical concentration was 1.074 ± 0.102 M NaCl and it raised 7.17% up to a value of 1.151 ± 0.138 M under the influence of a magnetic field. All these values can be found in Table 4.3.6.

		Critical NaCl Concentration / M		Increase %
		No MG	MG	
TM0	PNIPAAm	1.00	1.04	4.10%
	PNIPAAm w/ NPs	1.107	1.184	6.96%
TM1	PNIPAAm	0.82	0.85	3.14%
	PNIPAAm w/ NPs	1.074	1.151	7.17%

Table 4.3.6. Critical concentration of sodium chloride values extracted from experiments on PNIPAAm films and PNIPAAm with magnetite NPs films.

The increase on C^* with a magnetic field gradient is 2-fold higher for samples containing magnetite nanoparticles compared to the reference experiment. This means that the magnetic field influences the ferrogel. But, how does the nonuniform magnetic field influence the C^* of the ferrogel? A hypothesis is that when a field is applied to the ferrogel, this experiences a force towards the increasing magnetic field. The way this experiment is set up, the ferrogel experiences a force towards the opposite side of the anchored surface; in other words, swelling. In that case, a higher energy would be needed for the ferrogel to collapse (i.e., higher C^*). This is exactly what can be seen on these experiments: there is an increase on C^* of 6.96% for TM0 and 7.17% for TM1. Even though there is a high standard deviation, the increase is high enough to be considered a real physical phenomenon.

In section 4.3.3.4 the influence of the magnetic NPs on the LCST of the hydrogel was studied. It was concluded that the hydrophobic character of the NPs surface-attached benzophenone decreased the energy required to collapse the hydrogel and, hence, the LCST decreased with the increase of nanoparticles on the network [Figure 4.3.10]. When looking at the critical concentration, C^* , of sodium chloride needed to collapse the polymer a similar effect is expected; that is, the presence of the nanoparticles should decrease the amount of NaCl needed to collapse the network. However, when nanoparticles are attached to the network, an increase of 30% is detected on C^* extracted from TM1. Similarly, an increase of 10% is found on C^* from TM0. First of all, TM1 is sensitive to the whole network while TM0 is sensitive to the first 200 nm close to the surface; hence, this effect is more pronounced on the “bulk” of the thin film compared to the interface with the substrate. The fact that the LCST decreases with the addition of nanoparticles whereas C^* increases implies that the two collapsing processes follow different mechanisms. An explanation could be that the hydrophobic nanoparticles create hydrophobic cavities that make the diffusion of ions more difficult. As a result, a higher ionic strength is needed to break the hydrogen bonding of water and the hydrophilic network chains.

4.3.3.6. Theoretical estimation

Nonuniform magnetic fields are known to attract magnetic NPs; some promising results have been obtained in the previous section. However, the effect was smaller than experiments for bulk ferrogels²³⁴ which leads to the question: is this field strong enough to deform a constrained ferrogel?

A theoretical description of the deformation induced by a nonuniform magnetic field is formulated in order to understand the results aforementioned in the previous section. The equation used is based on the description made by Zrínyi *et al.*²³³ They published the description of magnetic deformation on macroscopic ferrogels. A macroscopic cylindrical ferrogel, made out of polyvinylalcohol (PVA), was hanging from a force-measuring device. The ferrogel was submerged in a beaker full of water and, underneath the beaker, an electromagnet was placed. A CCD camera was used to monitor the deformation of the gel with an accuracy of $\pm 10^{-2}$ mm. In comparison, our experiment was done on thin film ferrogels attached to a surface and immersed in water. Our setup with the meaning of the symbols used in Equation 4.3.3 is presented in Figure 4.3.14.

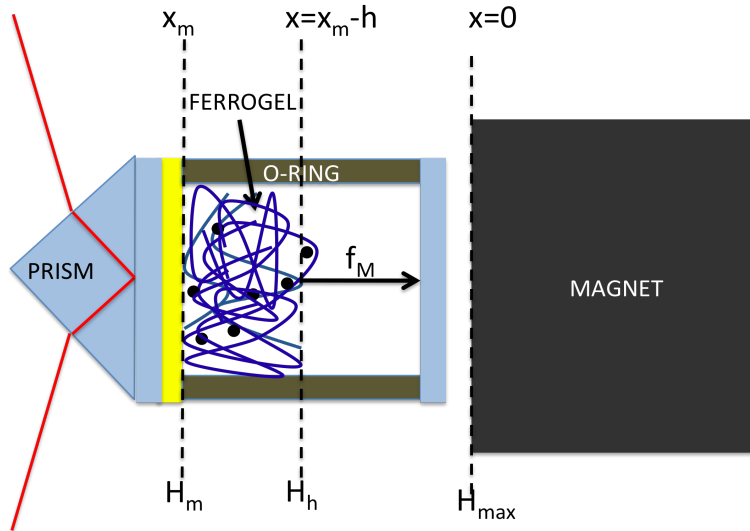


Figure 4.3.14. Schematic diagram of experimental setup for experiments in nonuniform magnetic field.

The magnetic field drives and controls the displacement of the individual particles, which are covalently linked to the network. The equation used is mainly based on the idea that, if the force exerted on the nanoparticles is able to move the network chains, the final shape would be the result of the balance of magnetic and elastic interactions.

$$\lambda^3 - \frac{\mu_0 \chi}{2G} (H_h^2 - H_m^2) \lambda - 1 = 0 \quad (4.3.3)$$

Where λ corresponds to the deformation ratio (i.e., the thickness, h , divided by the corresponding undeformed thickness), μ_0 is the magnetic permeability in vacuum, χ is the susceptibility, H represents the strength of the external magnetic field (h and m are the positions of H , indicated in the scheme of Figure 4.3.14), and G stands for the modulus of the ferrogel.

Equation 4.3.3 was derived on the basis of the following assumptions:

- (1) homogeneous deformation,
- (2) linear dependence between magnetization and field strength,
- (3) and Gaussian-type strain energy function

Since particles are dispersed throughout the gel, we will assume that the deformation is homogeneous. For the susceptibility value to be correct, the magnetic field should be in the linear region, which is assumed for all simulations. And, finally, for more simplicity Gaussian-type chains are presupposed, as well.

The modulus of the ferrogel can be, at the same time, expressed as a function of filler concentration:²⁶³

$$G = G_0(1 + k_E \Phi_m) \quad (4.3.4)$$

where G_0 denotes the modulus of the gel without colloidal filler particles, k_E is the Einstein-Smallwood parameter and corresponds to 2.5 for noninteracting spherical particles, and Φ_m corresponds to the volume fraction of nanoparticles in the gel. The Young modulus, G_0 , used for simulation purposes is 29 kPa and was measured by Junk *et al.* at 20 °C in the same thin film gel by means of AFM.²⁶⁴ A similar value was obtained by Brom *et al.* in the same gel loaded with a 38 wt% of silica nanoparticles.¹⁸⁶ In this case Young's modulus was 45 kPa measured at 30 °C with the same technique. Given that the volume fraction of the nanoparticles on the gel is extremely low due to the big difference in density of the two components (0.0004255 for a concentration of 16.7 wt% NPs), G was 29.030 kPa, almost equal to G_0 .

The value used for susceptibility, χ , is extracted from the SQUID measurements of the magnetite NPs with 15 nm of diameter and benzophenone surrounding the nanoparticle (Section 4.2.3.1). This value corresponded to the mass susceptibility and is 52.04 emu g⁻¹ KOe⁻¹.

In Figure 4.3.14 the results of the simulations extracted from Equation 4.3.3 can be observed.

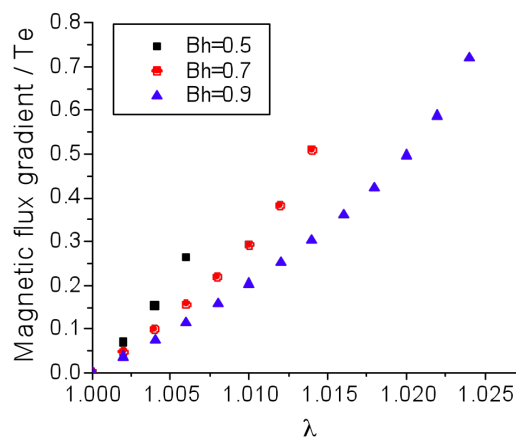


Figure 4.3.15 Simulation of the magnetic flux gradient necessary to cause a deformation λ depending on the magnetic flux at the beginning of the hydrogel, B_h .

These estimations predict a deformation of only 2% with fairly high magnetic flux gradients (i.e. 400 mT). The main problem is that this gradient should exist in the thickness of the hydrogel (i.e., $\sim 10 \mu\text{m}$).

The program FEMLAB was used to simulate the magnet field lines through finite element method.²⁶⁵ A 2D-uniaxial symmetry configuration was used. A cylindrical magnet with the same properties as the ones stipulated in the technical sheet provided with the magnet used on the experiments is simulated [Figure 4.3.16 (a)]. Considering a distance of 1 cm from the magnet surface the gradient on magnetic flux in $10 \mu\text{m}$ distance is 0.2 mT with a B_h of 0.475 T.

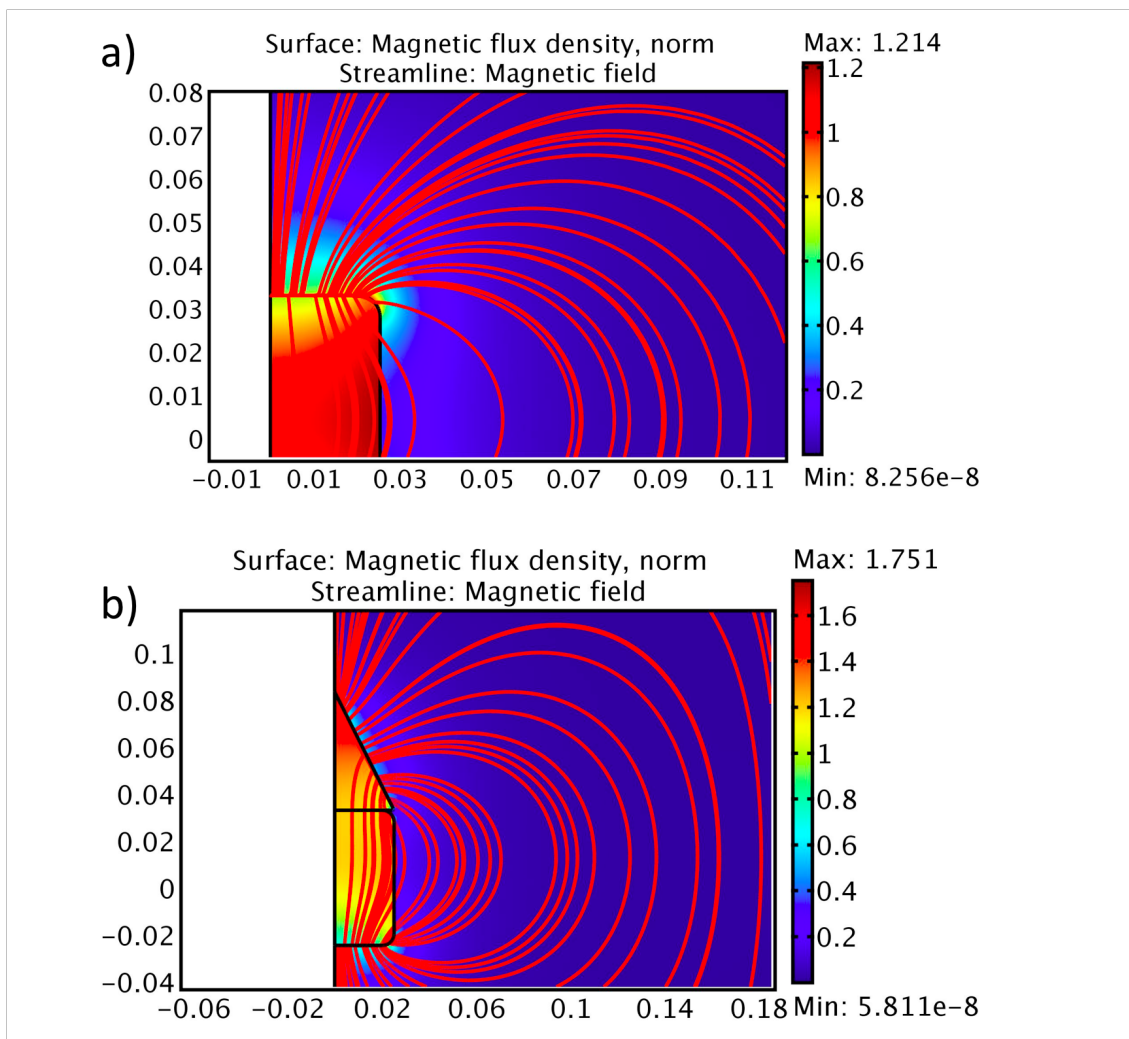


Figure 4.3.16 Simulations of magnetic flux density in a 2-D uniaxial symmetry configuration. X- and Y-axes represent length in meters. The magnetic flux, B (in Tesla), is represented in different colors. The color code is on the right. (a) Magnet with cylindrical shape is represented. In the picture only the quarter from the top right is shown. (b) Magnetic cylinder with cone is shown.

This value is tremendously inferior to the one needed to deform the gel. In order to increase the magnetic flux gradient a cylindrical cone with same diameter as the cylinder is added to the end of the cylinder [Figure 4.3.16.(b)]. A cylindrical cone with a sharp point should focus the flux in this point and allow a stronger gradient. As expected, simulations showed the gradient increased to 0.4 mT. However, this flux is not enough to elongate the hydrogel.

4.3.4. Conclusions

The study of magnetic nanoparticles on thin film hydrogels, namely ferrogels, has been reported for the first time, to the best of our knowledge.

The presence inside the gel of nanoparticles with sizes ranging between 3.7 nm to 19.6 nm was confirmed by means of UV-VIS spectroscopy. The mechanism was a combination of mesh size trapping and covalently binding, the last one only confirmed for nanoparticles coated with benzophenone.

It was found that increasing the amount of nanoparticles inside PNIPAAm decreases the LCST due to the hydrophobic character of the benzophenone shell. In contrast, the critical NaCl concentration, C^* , that makes the hydrogel collapse increases with the presence of nanoparticles in the network probably due to the interaction of the ions with the hydrophobic moieties around the NPs. In both cases values reported for TM0 were higher compared to TM1 values because of the short sensitive range of surface plasmon vs. leaky optical waveguided modes.

Some swelling of the ferrogel was detected by means of SPR-OWS when a magnetic field gradient was applied on the sample, however the ferrogel shows a plastic behavior because it did not recover the original shape after the removal of the magnetic field. Furthermore, the increase in C^* in the magnetic field gradient support the swelling of the ferrogel, although again, the influence was rather small. Calculations taking into account the physical properties of the nanoparticles and the gel suggest that the magnetic field gradient created in a short space is not enough to deform the hydrogel. This explains the divergence between the big magnetodeformation found on bulk samples compared to the thin gels under study.

5. Summary

The work presented above discusses the interactions of magnetic nanoparticles introduced in a hydrogel scaffold. The thesis is structured in three parts: (1) fundamental study on hydrogel thin films, (2) investigation on magnetic nanoparticle properties, and (3) examination of ferrogel thin films.

The polymer of choice was PNIPAAm copolymerized with a carboxylic acid moiety that provided the polymer with pH sensitivity as well as the already well known sensitivity to temperature of PNIPAAm (LCST ~ 32 °C). In addition, a benzophenone moiety was introduced in the polymer as a photocrosslinking inducer. A fundamental study on the behavior dependence on pH and T from the hydrogel thin films was performed by nanomechanical cantilever sensor (NCS) and surface plasmon resonance in conjunction with optical waveguide spectroscopy (SPR/OWS). First, a strategy was successfully designed to functionalize the cantilever sensors with a benzophenone silane monolayer. Furthermore, a protocol was established to cover only one side of the cantilever sensors with the hydrogel, in a manner that differential stress could be sensed. The studies performed with SPR/OWS and NCS showed the pH response of the hydrogel allowing the determination of the pKa of the polymer, which were in agreement with pKa values found in the literature for similar polymer composition. NCS experiments yielded surface stress values that were comparable to stresses obtained in carboxylic acid terminated SAMs found in the literature. Temperature studies demonstrated that higher crosslinked networks have a lower LCST. Furthermore, NCS platform provided information about changes in stress on the higher crosslinked sample due to the formation of a skin-layer that was not observed by SPR. Thus, NCS proved to be a good technique for the study of thin films allowing a deeper understanding on the stress that the thin film exerted over the substrate.

Magnetite nanoparticles were synthesized by a high temperature reaction that provided control over the size of the nanoparticles in a monodispersed manner. Two different strategies were followed to confer water stability to the as-synthesized non-polar magnetite nanoparticles covered by oleic acid: silica shell formation, which could be further silanized; or exchange of the oleic acid surfactant by citric acid. On another functionalization strategy the nanoparticles were covered by benzophenone-silane, which provided the nanoparticles with the capability of covalently bind to

polymer networks by photoactivation. A study on the magnetic properties of different size nanoparticles covered with oleic acid was performed. The dependence of the magnetic properties on particle size was determined and agreed well with results reported in literature. It was confirmed from these values and the shape of M-H diagrams and ZFC curves that the nanoparticles were superparamagnetic at room temperature. The magnetization of benzophenone-covered nanoparticles was lower compared to the oleic acid ones. This observation and the shape of the ZFC curves brought us to the conclusion that the benzophenone-silane formed a multilayer around the nanoparticles. On another study, the heat loss of the nanoparticles on response to an AC-magnetic field showed that the power losses increase with particle size. However the increase is only of a few Kelvin. Higher frequencies and field amplitudes would be necessary to use these nanoparticles in bioapplications. Another approach would involve the increase on the nanoparticle size to the superparamagnetic limit; however, a better synthetic strategy should be designed to decrease the particle size distribution, which directly affects the heating capabilities.

Finally, a study on ferrogels was, for the first time, performed on thin films. The ferrogels were prepared through the mixing of magnetite nanoparticles, covered with benzophenone, and PNIPAAm polymer. Thin films were formed by spincoating of the ferrogel mixture followed by UV crosslinking. It was found that magnetite nanoparticles increased the hydrophobic character of the ferrogel decreasing the LCST of the polymer. The response of the ferrogel thin films to ionic strength was used to study in a more sensitive way the magnetic response. In summary, a small plastic response was detected when a gradient magnetic field was applied. Calculations taking into account the physical properties of the nanoparticles and the gel suggest that the magnetic field gradient created in a short space is not enough to deform the hydrogel. This explains the divergence between the big magnetodeformation found on bulk samples compared to the thin gels under study.

APPENDICES

A.1. Characterization of silica nanoparticles functionalized with APTES

Amorphous silica nanoparticles were purchased from Polysciences, Inc. in a colloidal dispersion of 5% (w/v) in water with NaOH as a stabilizer. The surface of silica microspheres can be easily functionalized by reaction with organosilanes. The surface was modified with APTES as explained in Section 3.2.2. Here a characterization of silica particles functionalized with the same protocol is presented.

Characterization: In order to chemically verify the silanization of the nanoparticles FTIR and Z-Potential measurements were performed. KBr pellets with dry modified and nonmodified nanoparticles were prepared for the FTIR, whereas water dispersions of the modified nanoparticles are analyzed in the DLS-Zpotential. The zeta potential of the silica spheres was measured with a ZetaPlus zeta potential analyzer (Brookhaven Instruments Corp.) at 25 °C at pH 3 and 7.

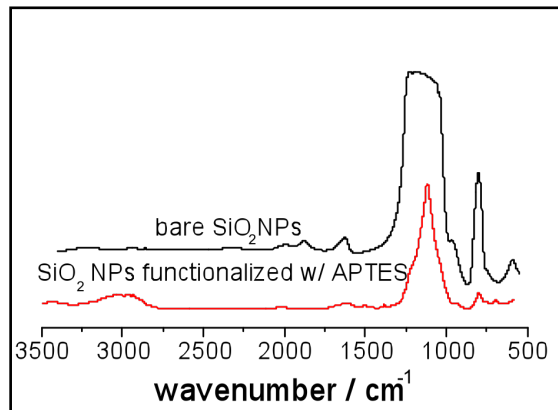


Figure A.1.1 FTIR spectra of bare silica nanoparticles and silica (black line) particles functionalized with APTES (red line).

FTIR measurements [Figure A.1.1] show the appearance of a weak band at 1650 cm^{-1} and 700 cm^{-1} corresponding to the NH_2 δ . These bands are not present on the FTIR corresponding to the bare SiO_2 NPs.

The values extracted from the zeta potential measurements at pH 3 show an effective diameter of 200 nm and a zeta potential of +46.43 mV. On the other hand, when the pH is 7, the effective diameter is 1.5 μm and the zeta potential is +0.208 mV. When the $\text{SiO}_2@$ APTES are at lower pH, the amine groups are positively charged; therefore the nanoparticles repel each other. On the other hand, at pH 7

the amine groups are not charged, as a result, there is no repulsion that stabilizes the particles and they aggregated, as the increase in diameter show.

A.1.1. Link to hydrogel

In an example of the interaction of the modified 50 nm diameter nanoparticles with the hydrogel an experiment using the PNIPAAm-DMI polymer is performed. The polymer contained the carboxylic acid moiety (AAmPA) that is used to bind to the SiO₂@APTES NPs. A high ionic strength buffer would hinder the electrostatic repulsion that maintain the NPs nicely distributed on the solution causing the aggregation of these. In these experiments low ionic strength (8 mM) phosphate buffer is used with a pH of 3.26. The protonation of the amine groups on the nanoparticles is ensured at this pH as Zeta Potential measurements show. Experiments were performed in Quartz Crystal Microbalance with Dissipation (QCM-D). Quartz Crystal Microbalance is a thin film characterization technique that measures changes in resonant frequency in real-time. Quartz crystal microbalance with dissipation monitoring measures the dissipation factor of the crystal, as well as the resonance frequency. The principle of operation involves shorting the drive circuit of the crystal measuring the subsequent oscillations of the crystal with time.

Q-Sense D300 QCM-D (Q-Sense, Inc., Newport Beach, CA) measurement platform fitted with a QAFC301 axial flow chamber was used for these experiments. The D-300 is a single flow module platform that only measures p to the 7th harmonic. The notation Δf_n and ΔD_n is used to represent the resonant frequency and dissipation factor of the quartz excited at the n_{th} harmonic.

Crystals were purchased from Q-Sense. All of them were made out of quartz covered with ~100 nm gold. Adhesion promoter is a maleimide thioester.

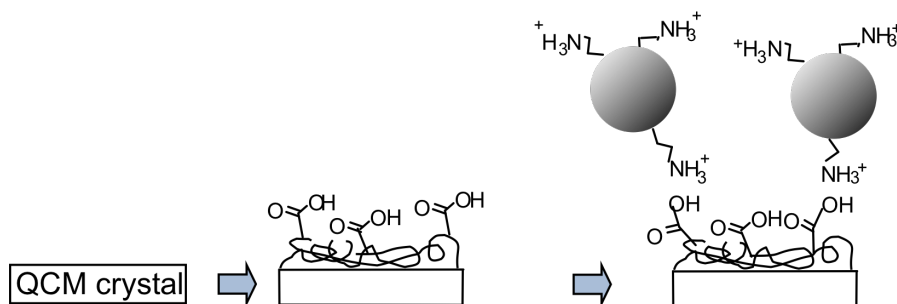


Figure A.1.2 Sketch of the experiment. In the first step the polymer is spincoated; in the second step the nanoparticle interaction with the hydrogel is depicted.

Surface treatment. Au crystals were immersed during one hour in an ethanolic solution with the adhesion promoter. Afterwards it was rinsed with ethanol and dried with nitrogen stream. The hydrogel is composed by 85.7% NIPAAm, 4.5% DMIAAm (crosslinker), and 9.8% AAmPA (carboxylic acid moiety). This copolymer was mixed with thioxanthen-9-one in a 2%-wt vs. polymer using cyclohexanone as solvent. This solution was spincoated over the crystal at spin rate of 8K rpm during 60 s. Samples were placed under vacuum immediately for 1 hour to get rid of the remaining solvent. Copolymer was crosslinking under UV light (365nm) for 10 minutes.

Experiment. The crystal with the polymer is introduced in the QCM-D cell and buffer solution is run through the system. At least half an hour to 45 minutes was allowed for the polymer to stabilize, with buffer injection every 20 minutes. Next, nanoparticles are introduced and the system is allowed to stabilize. Rinsing of the particles with buffer is performed to remove any physisorb material.

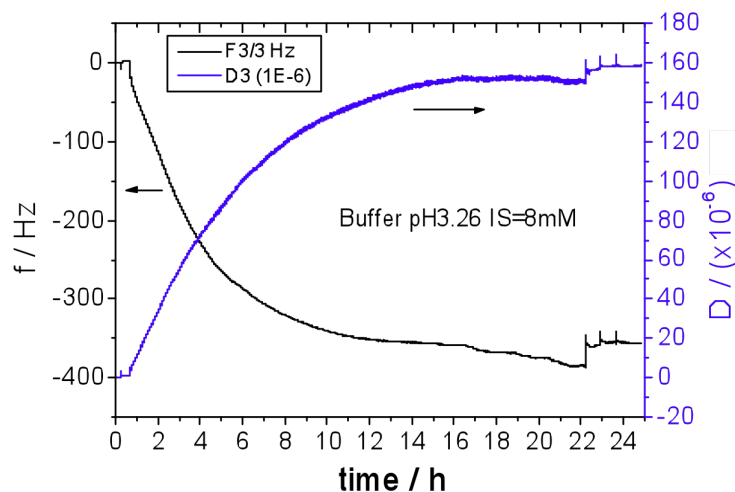


Figure A.1.3 QCM experiment with PNIPAAm-DMIAAm-AAmPA and silica nanoparticles with APTES functionalization. In black the frequency of the third overtone is plotted vs. time whereas in blue the dissipation is plotted.

When the APTES functionalized nanoparticles are injected in the cell after one hour of stabilization, there is a decrease on the frequency of 355 Hz [Figure A.1.3]. While the frequency is decreasing, the dissipation increases up to a value of 150.339×10^{-6} . This decrease in frequency is due to the binding of the functionalized NPs on the hydrogel. There is a strong interaction between the acid groups and the amine on the NP surface. If we use Sauerbrey relation to estimate the mass deposited, we obtain a value of $6283.5 \text{ ng}\cdot\text{cm}^{-2}$. If we take into account that the nanoparticles have a diameter of 50 nm and a density of $2 \text{ g}\cdot\text{cm}^{-3}$ and we assume that a monolayer of

them is deposited on the surface, the coverage of the nanoparticles can be estimated to be 94.93%. However, Sauerbrey relation assumes systems with homogeneous rigid layers. When a viscoelastic material is deposited onto the crystal, the frequency is no longer directly proportional to the mass since it depends as well on the dissipation.

A similar experiment is performed with a PNIPAAm-DMI polymer without the acid comonomer (AAmPA) [Figure A.1.4]. The hydrogel is stabilized for one hour. The nanoparticles are then injected and the system is allowed to stabilize. After 150 minutes, the system is rinsed.

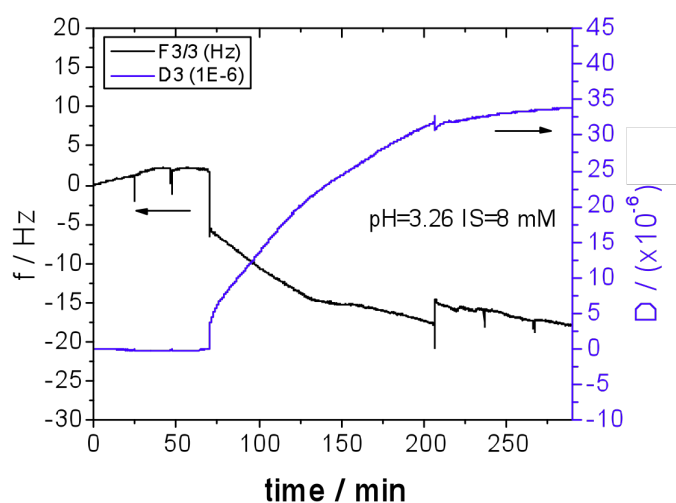


Figure A.1.4 QCM experiment with PNIPAAm-DMIAM and silica nanoparticles with APTES functionalization. In black the frequency of the third overtone is plotted vs. time whereas in blue the dissipation is plotted.

The decrease on the frequency when NPs are injected is only 19.54 Hz and the dissipation increase is 33.8×10^{-6} . These values are lower compared to the ones of the PNIPAAm-DMI-AAmPA. If Sauerbrey relation is used a mass density of 336.6 ng.cm^{-2} is obtained. The reason for this low adsorption is the lack of acid groups on this polymer, compared to the previous experiment. The amine groups on the nanoparticles are not able to interact with the surface, thus, there is no NP adsorption.

A.2. Analysis of plasma polymerized pentafluorophenyl methacrylate by means of NCS

In this appendix an investigation performed aside from the main thesis project is presented. The work is presented in format of the paper, just approved for submission in the journal Plasma Processes and Polymers, in the following pages.

Investigating the reactions of plasma polymerized pentafluorophenyl methacrylate towards different simple amines

Luis Duque,¹ Nuria Queraltó,¹ Laia Francesch,^{1,2,ε} G.G. Bumbu,^{1,ψ} Salvador Borros,² Rüdiger Berger¹ and Renate Förch^{1}*

¹ Max Planck Institute for Polymer Research, Ackermannweg 10, 55128 Mainz, Germany

² Institut Química de Sarrià-Universitat Ramon Llull, Via Augusta 390, 08017 Barcelona, Spain

*Corresponding author: R. Förch, Tel/Fax: +49-(0)6131-379-766/100, e-mail: foerch@mpip-mainz.mpg.de

^ψNew address: Dr. Gina Gabriela Bumbu, Motorenstrasse 102, Wetzikon, 8620, Switzerland

^εNew address: Dr. Laia Francesch, Fundació Privada CETEMMSA, C/Jaume Balmes 37-39 08301 Mataró (Spain), Tel: +34 93 741 91 00, lfrancesch@cetemmsa.com

Keywords: pentafluorophenyl methacrylate, pulsed plasma polymerization, amines, microcantilever sensors, reactivity, interfacial stress

Abstract

Ultra thin films of plasma polymerized pentafluorophenyl methacrylate (pp-PFM) offer highly reactive ester groups throughout the structure of the film that allow for subsequent reactions with different aminated reagents. The reactivity of this surface towards simple primary amines was studied in DI-water and in phosphate buffer saline (PBS) using Infrared Reflection Absorption Spectroscopy (IRRAS) and X-ray photoelectron spectroscopy (XPS). Plasma polymerized PFM films are typically characterised by a high roughness. Immersion in aqueous media leads to a smoothening of the surface as was observed using Scanning Electron Microscopy (SEM) and Atomic Force Microscopy (AFM). Chemical reactivity towards primary (1°), secondary, (2°) and tertiary (3°) amines was investigated using IRRAS in combination with micromechanical cantilever (MC) sensors. While IRRAS provided information on the chemistry occurring at the surface of the MC sensors technique gave insights into the surface stress induced by the changes in the chemistry of the polymer film upon reaction. These changes in surface stress were related to reactions occurring either at the liquid-solid interface or within the matrix of the polymer. The reactivity of the ppPFM towards amines seems to be influenced not only by the chemical structure of the amines but also by their size, which influences the diffusion into the polymer film.

Introduction

The use of plasma polymerization techniques to deposit highly reactive films that show potential for biomaterial and bio-medical applications is well described in the literature.^{1, 2, 3} Already since the 1970's the literature describes the deposition of polymers using plasma assisted processes and points out how functional group control can be achieved by simple adjustment of the process parameters. Plasma polymerization allows for the deposition of thin polymeric films showing a variety of chemical structures and properties, which are dependant on the experimental conditions (such as the input power, gas composition, monomer pressure and substrate position) employed during the process. The density of a particular functional group and the degree of cross-linking within the polymer network can be largely tailored by careful control over the energy input during the deposition. The energy input can be varied either by minimizing the peak power (P_{peak}),⁴ moving substrates into the afterglow zone^{4, 5} or by pulsing the applied power.^{6-8, 9, 10, 11}

The types of films that have been found to be particularly suitable for many bio-material and bio-medical applications are those containing reactive groups such as amines,^{12,13,14,15} acids^{16,17,18,19} and anhydrides.^{20,21} Less attention has been given to precursors containing active esters, generally because of the difficulties encountered during their deposition, and the very rapid loss of the functional group during the plasma deposition. Thin plasma polymer films from pentafluorophenyl methacrylate (PFM) have been discussed in our previous work.²² Plasma polymerised PFM, (pp-PFM) is of particular interest as an active coating, since it offers a highly reactive ester group, which could be utilized for binding biomolecules and promote cell adhesion and proliferation.²³ It was previously shown that while PFM can be deposited under a number of conditions, there is only a very narrow range of process parameters that allow for a high retention of the functional ester group.

The most common application of MC sensors is in molecular detection.^{26,27} MC sensors have been used to detect the hybridization of DNA,^{25, 28} and as gas sensors.^{29, 30} However, MC sensors have also proved to be valuable for the investigation of material or interface properties of small samples.^{31, 32, 33} The MC sensor set-up consists of an array of microcantilevers which act as transducers. On one side of the MC a reactive coating is

deposited. In such a biomaterial system the deflection of the MC is related to the differential mechanical stress generated between opposite sides of the cantilever. This so called static bending mode offers unique possibilities to monitor small changes in stress at the interface between the MC and the thin film. Optical means are often used for read-out of the MC deflection. The stress at the interface is calculated from the deflection of the MC and can be used to evaluate volume changes of the reactive coating. Such volume changes could, for example, be a result of swelling processes owing to changes in environmental conditions such as temperature or humidity,³⁴ or they could be a result of a chemical reactions on top of, or within the thin functional coating.³⁵ MC sensors have in the past been successfully functionalized with thin polymer coatings,³⁶ polymer brushes^{37, 38} and polyelectrolytes.³⁹

The present work investigate the behaviour of pp-PFM films in different solvents such as PBS and de-ionized water (Milli-Q), and to study the reaction of different simple amines in solvent with the pp-PFM. The latter was carried out using a combination of Infra Red analysis and MC sensors. One particular aspect of interest was the influence of the molecular structure of the simple amines on the reactivity towards the perfluoroester thin film. The amines studied ranged from primary amines (1°) containing different substituents, as well as secondary (2°), and tertiary (3°) amines. We have previously published preliminary work in this area studying the reaction of primary amines with pp-PFM only using the combination of IRRAS and MC sensors.²⁴ The present paper further investigates MC sensors as a tool to study simple chemical reactions at the surface of thin films and shows a clear correlation between chemical structure of the reacting moiety and measured cantilever deflection. The results show a correlation between film thickness and MC deflection for a particular reacting moiety.

Experimental

Materials - Pentafluorophenyl methacrylate (PFM) was purchased from Sigma-Aldrich, Germany. In order to degas the liquid monomer it was freeze-thawed three times, but not further purified. A 25 ml round bottom flask containing fresh PFM was attached directly to the plasma reactor and the gas flow was controlled by a needle valve.

Substrates: The substrates used in the course of this work were Si-wafers for X-ray photoelectron spectroscopy (XPS), BK7 glass slides coated with 2 nm of Cr and 80 nm Au (thermal evaporation) for Infrared Reflection Absorption Spectroscopy (IRRAS) and Scanning Force Microscopy (SFM). For Surface Plasmon Resonance Studies (SPR) LaSFN9 glass slides (Hellma Glass, Jena, Germany) (2.5 x 3 cm) were also coated with 2 nm thermally evaporated Cr and 50 nm Gold. To improve adhesion between the gold layer and the subsequent plasma polymer layer octanethiol was self assembled onto the surface. This was done by keeping the gold-coated substrates in a 2 mM octanethiol solution overnight. After thoroughly rinsing with absolute ethanol, the substrates were dried in a stream of dry N₂ just prior to plasma polymerization.

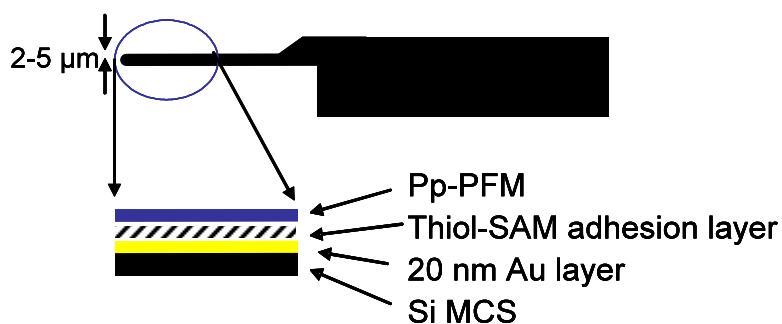
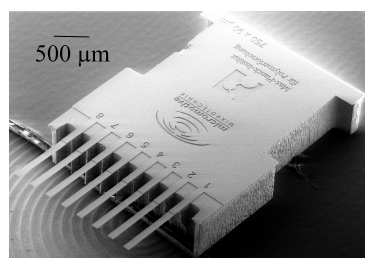


Figure 1 Scanning electron micrograph of a micromechanical cantilever array and a schematic of the multilayer set up used during this work.

OCTOSENSIS silicon micromechanical cantilever arrays (Micromotive GmbH, Germany) were used as transducers for microcantilever sensor studies. Each chip consists of eight rectangular cantilevers, with a length of 500 μm , width of 90 μm and thickness of 2 μm arranged at a pitch of 250 μm , Figure 1. Typical variations of resonance frequencies within one array are less than 1% indicating similar mechanical properties. Since most of the tests were performed under aqueous environment the Si cantilever arrays were prepared to ensure optimum adhesion between the functional coating and the Si surface by the immobilization of a SAM as described above. In order to avoid the deposition of pp-PFM on the bottom part of the cantilevers, a glass cover slip was located beneath the cantilevers.

After deposition, references MC were prepared by exposing 4 MC within an array of 8 to concentrated isopropylamine for 1 hour. The concentrated isopropylamine rapidly reacted with the active perfluorophenyl ester and deactivated the active ester groups. This deactivation procedure was performed using a MC treatment station allowing for the optimum alignment of the MC inside a capillary containing the amine.

Measurements were thus made with 4 cantilevers within one cantilever array. The data shown below are representative of the trend observed for these different measurements.

Plasma polymerization - Plasma polymerization was carried out in a home-built 30 cm long cylindrical Pyrex reactor using an excitation frequency of 13.56 MHz which was fed to the reactor via two concentric rings wound around the outside of the chamber separated by a distance of 13 cm.¹ The substrates were placed on a glass platform half way between the electrodes in the centre of the plasma glow. Before introduction of the substrate, the chamber was cleaned in a continuous wave O₂/Ar (1:4) plasma for approximately 1 hour at a power 150 W. The optimum deposition conditions for plasma polymerized PFM (pp-PFM), that gave films showing the highest -CF content, were found to be a pulsed plasma process using a duty cycle ($DC = t_{on}/(t_{on} + t_{off})$) of 2/52 at an input power (P_{input}) of 50 W, giving an equivalent power ($P_{eq} = DC \cdot P_{input}$) of 2 W. The process pressure during deposition was 0.2 mbar. Plasma polymer film thickness was typically 40 nm \pm 4 nm measured on Si-wafers. For greater thicknesses the time of deposition was increased. A Tencor Alphastep 200 was used to determine film thickness.

Chemical structure analysis - Contact angles were measured using the sessile drop method. A 5 μl drop of Milli-Q water was placed on the sample, the syringe needle was removed from the drop and the angle between the surface of the drop and the sample surface was measured. This was repeated 5 times and the values were averaged.

Analysis of film chemical structure and changes within the film upon immersion in aqueous solution were carried out by IRRAS using a Nicolet 850 spectrometer with an angle of incidence of 5°. For some selected samples XPS was performed approximately 3 days after treatment using a Perkin Elmer PSI 5000 series instrument equipped with an X-ray source monochromator and an Al K α (1486.6 eV) x-ray source. The pass energy used was 17.9 eV giving a resolution of 0.6 eV for Ag (3d_{5/2}). The samples were stored under dry Ar until analysis. An electron flood gun was used to compensate surface charging.

Surface Plasmon Resonance Spectroscopy (SPR) – SPR was carried out on a home-built spectrometer using a He-Ne laser with a wavelength of 633 nm, a home built sample handling system and liquid flow cell. Changes in the incident angle (θ) and relative positioning of the photodetector (2θ) were controlled by two high precision goniometers with a resolution of 0.001°. The system has been described in detail elsewhere.^{40, 41} During the SPR experiment

the intensity of the reflected laser beam is measured, this reaches its minimum when a surface plasmon has been excited at the metal–dielectric interface.^{42, 43, 44} The angle at which this minimum occurs is highly sensitive to changes in thickness and refractive index of the adlayers. As such SPR is a highly versatile tool for the study of reactions occurring at thin film surfaces.

Scanning force microscopy: SFM measurements were made under ambient conditions using intermittent contact mode (Dimension 3100 CL, Veeco, Santa Barbara, USA). All measurements were performed with silicon cantilevers (Olympus OMCL-AC160TS, Japan) having a nominal spring constant of $K = 42$ N/m and a resonance frequency of 300 kHz. All images have been flattened by using a first order plane. The root mean square roughness (RMS) values were then calculated for all images.

Microcantilever Sensor Deflection measurements: The deflection of each of the 8 MCs was monitored with a Scentris™ platform (Veeco, USA) based on the beam deflection detection principle. This technique allows for the sequential measurement of the deflection of 8 MC at a resolution < 1 nm, over a range of several μm . Since the deflection of each MC was determined independently, it was possible to calculate the differential deflection between a pp-PFM-coated and a reference MC. In this way parasitic deflections such as drift owing temperature and unspecific absorption can be compensated.³⁰ Beam deflection read-out techniques are sensitive to refractive index changes as well as to changes in surface energy as a result of changes in media.

The MC sensors measurements were performed in a 30 μL PEEK cell equipped with a glass window. An inlet and an outlet equipped with valves allowed for the exchange of the liquid. After injection of each solution, the inlet and the outlet valves of the reaction cell were closed such that there was no flow during measurements. The surface reactivity of the pp-PFM film to 10 mM solutions of the different amines in PBS could thus be monitored in real time and in-situ.

Results and Discussion

Films deposited from PFM are typically hydrophobic with a contact angle (sessile drop) of $98^\circ \pm 8^\circ$. The IRRAS spectrum of the as-deposited film shows characteristic peaks for the pentafluorophenyl group at 1525 cm^{-1} and 1000 cm^{-1} , the ester linkage at 1736 cm^{-1} , Figure 2(a).

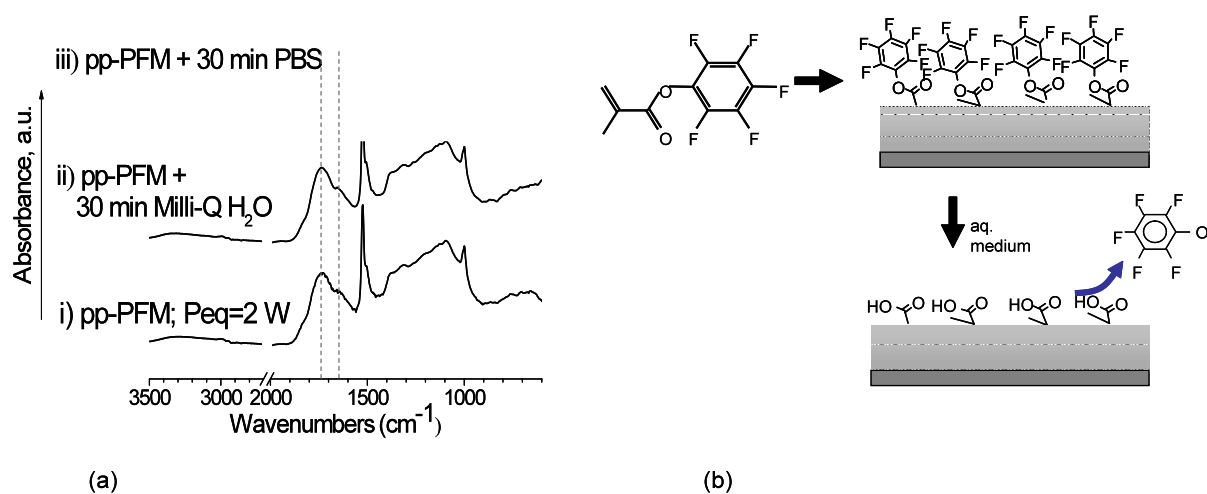


Figure 2 IRRAS spectra of pp-PFM before and after immersion in water and PBS (a). Schematic representation of the hydrolysis of the active ester group with the release of the pentafluorophenol group (b)

The corresponding XPS analysis previously showed the as-deposited films to have an O/C ratio of 0.23 and a F/C ratio of 0.48, which is close to the theoretical values of 0.2 and 0.5 respectively.²² This suggests that the material deposited has a high density of pentafluorophenyl groups and that during the plasma assisted deposition the active ester functionality of the monomer was mostly retained and polymerization occurred mainly through the double bond present in the precursor.

The pp-PFM films are most reactive at the ester group. Nucleophilic attack of water molecules at the ester group can readily lead to a cleavage of the pentafluorophenyl groups, which are assumed to diffuse out of the polymer and into solution, Figure 2 b. However, we find that the reaction of the pp-PFM in deionized water compared with that in Phosphate buffer saline (PBS) is considerably slower, which can probably be attributed to ion-ion interactions in the case of the buffer. This reactivity can be monitored qualitatively by IRRAS analysis, Figure 2a. Upon immersion in phosphate buffer saline solution (Figure 2 a (iii)) for 30 minutes a loss in the intensity of the band at 1736 cm^{-1} (ester group) was seen to be accompanied by an increase in intensity of the band at 1650 cm^{-1} suggesting the conversion of the ester to the acid. The reactivity of the pp-PFM films in water appears to be slower than in PBS, Figure 2 and we observed no significant differences between the spectra after 30 minutes. This is probably due to the hydrophobic nature of the polymer layer, which limits the diffusion of water into the film for the duration of the experiment such that only the uppermost layer of the film had reacted within this time, while the bulk of the layer remained unchanged and dominates the IRRAS spectrum. Thus, the pp-PFM appears to hydrolyse relatively slowly at the solid/liquid interface, this hydrolysis being influenced by the ionic nature of the solvent. The initial hydrolysis at the solid/ liquid interface may be followed by a much slower process during which the active ester groups further within the polymer films react with the environment. Thus, once the uppermost active ester groups have reacted, the surface is probably characterised by a high density of carboxylic acid groups with an underlying “bulk” material that continues to react with the solvent leading to the slower elution of the pentafluorophenyl group, Figure 2 b.

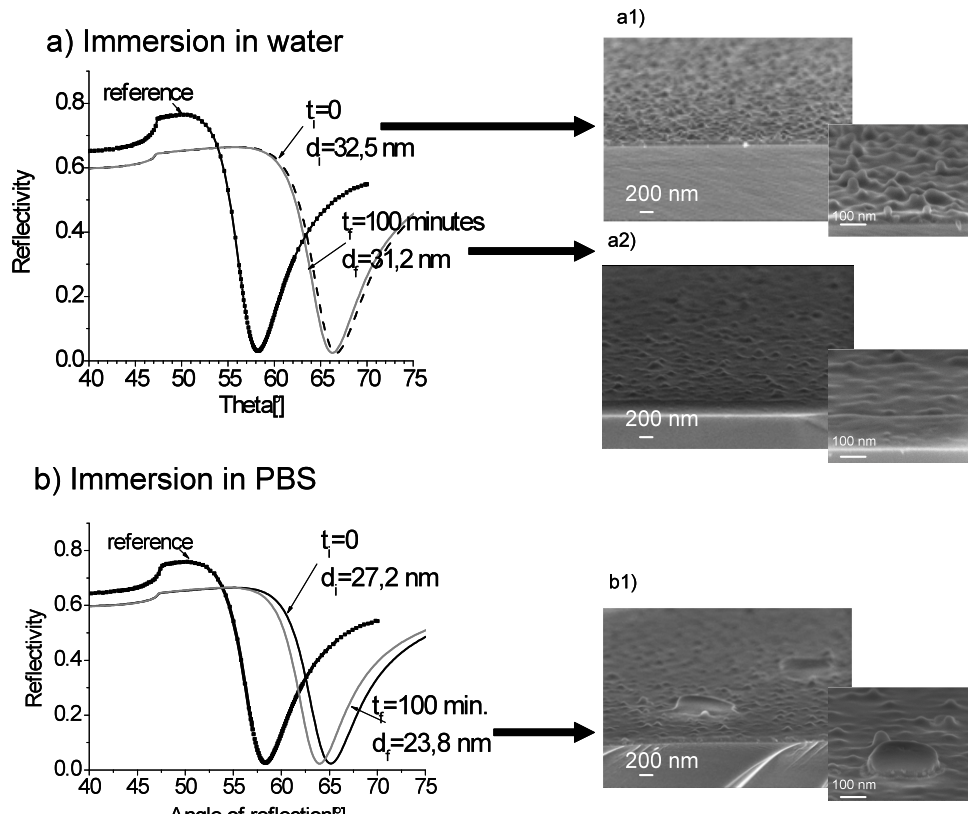


Figure 3 SPR measurements and SEM images of the pp-PFM surface before and after immersion in a) Milli-Q water and b) PBS

Changes in optical constants (SPR) over immersion time showed that the loss of material was larger after immersion in PBS than it was in de-ionized water. SPR scans were recorded at $t = 0$ and $t = 100$ minutes and used to calculate the thickness of the films assuming the refractive index (n) of the polymer to be 1.47. On average, a decrease in thickness of 4 % was observed after 1 hour immersion in de-ionized water, Figure 3a, while a 12% decrease in thickness was observed after immersion in PBS for the same time period, Figure 3b. These results could be correlated to changes observed in the thickness measured using a surface profiler. This decrease in thickness may be associated with a loss of low molecular material from the surface of the thin films. However, the change in thickness is probably mostly a result of molecular rearrangement as the film reacts in solution. This is seen in the SEM micrographs as a smoothing of the surface as the active ester group reacts and the bulky pentafluorophenol group is lost from the surface, Figure 3 a1, a2 and b1.

SEM analysis of the pp-PFM as deposited on a Si-wafer showed the polymer surface to be rough with no resemblance to any other surface morphologies of typical plasma polymer films published in the literature,^{45,46,41,47} Figure 3 (a1). Immersion in de-ionized water leads to a smoothing of the surface that can easily be visualised by SEM. After immersion in PBS, however, the films were seen to form “bubble-like” structures, which account for the difference in roughness after immersion in the two solvents. These “bubbles” may indicate the onset of delamination of the film from the Si-surface. This delamination was more pronounced in PBS than in de-ionized water, where no such structures could be observed.

SFM measurements showed a similar result even on the smaller scale ($5 \mu\text{m} \times 5 \mu\text{m}$), Figure 4. The as deposited films showed a significant roughness (rms roughness of $38 \text{ nm} \pm 3 \text{ nm}$) in comparison to those after immersion in water (rms roughness of $8 \text{ nm} \pm 1 \text{ nm}$). Immersion in

PBS appeared to lead to bubble like structures on the surface and an apparently higher roughness (rms roughness of $18 \text{ nm} \pm 2 \text{ nm}$). The topography of the surface was considerably different to immersion in water or PBS alone.

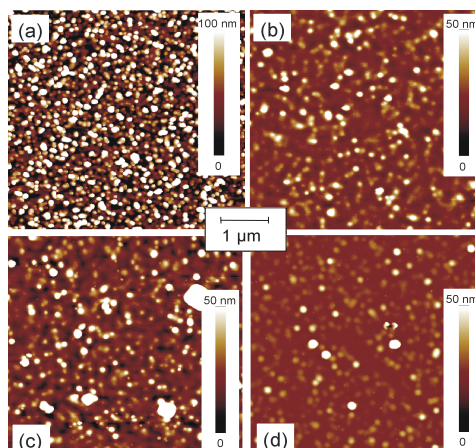
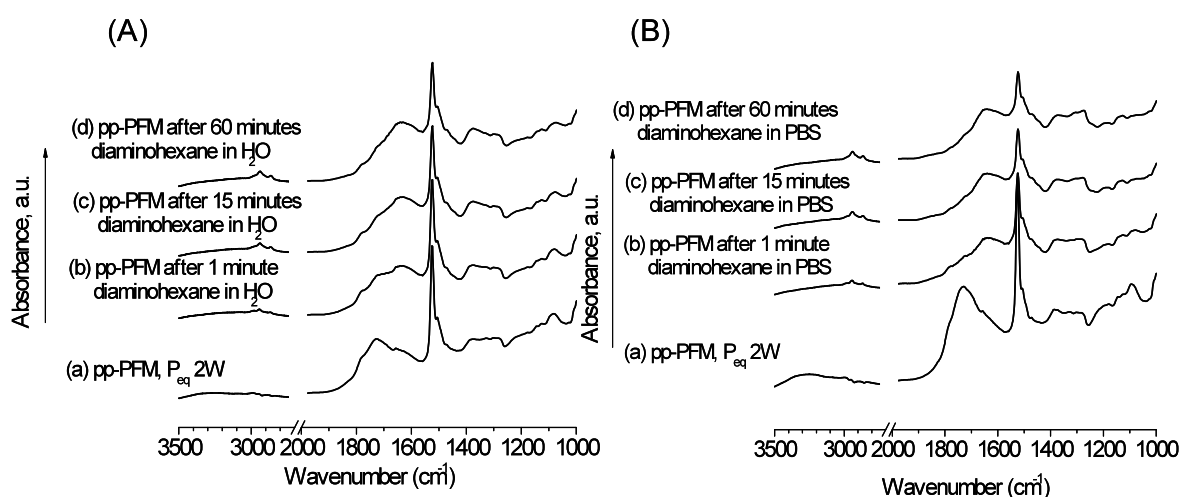


Figure 4: Scanning force micrographs of the topography at a lateral scale of $5 \mu\text{m} \times 5 \mu\text{m}$. (a) pp-PFM as deposited, (b) after immersion in MilliQ water, (c) after immersion in PBS and (d) after reaction with diaminoethane in PBS.

The reactivity of the pp-PFM surface with diaminoethane was investigated using either water or PBS as the solvent, the data is shown in Figure 5 (A) and (B) respectively. Figure 5 (C) shows the corresponding XPS elemental analysis of the surface before and after 1 hour immersion in the diaminoethane solution. The observed IRRAS spectra show differences between the solvents which are however difficult to quantify. A comparison of Figure 2 and Figure 5, however, suggests that the amination of the ester by the amine in water or PBS was in all cases much faster than the hydrolysis in water or PBS alone. The XPS analysis of the samples before and after 1 hour in a 5 mM solution of diaminoethane in solvent (Figure 5 C) showed a difference in reactivity and clearly demonstrate that the reactivity in PBS is more efficient than in deionized water.



(C)

Sample	O/C	F/C	N/C
As deposited pp-PFM	0.2 ± 0.02	0.76 ± 0.02	--
After 1 hour diaminoethane in H_2O	0.2 ± 0.02	0.34 ± 0.02	0.07 ± 0.02
After 1 hour diaminoethane in PBS	0.3 ± 0.02	0.12 ± 0.02	0.14 ± 0.02

Figure 5 IRRAS spectra showing the changes in film chemistry after reaction of diaminohexane in (A) Milli-Q water and (B) PBS with the pp-PFM surface. (C) the accompanying XPS analysis for the samples before and after 1 hour immersion.

Because of the relatively fast reaction times, the reactions of the amine with ppPFM was carried out in more detail using PBS as the solvent. MC sensors and IRRAS substrates coated with 20 nm of pp-PFM were reacted with different amines at a concentration of 10 mM in PBS. The shape of the IRRAS spectra and the relative intensities of the bands after 1 hour exposure to 10 mM solutions of the different amines allow for some predictions to be made about the reactions occurring.

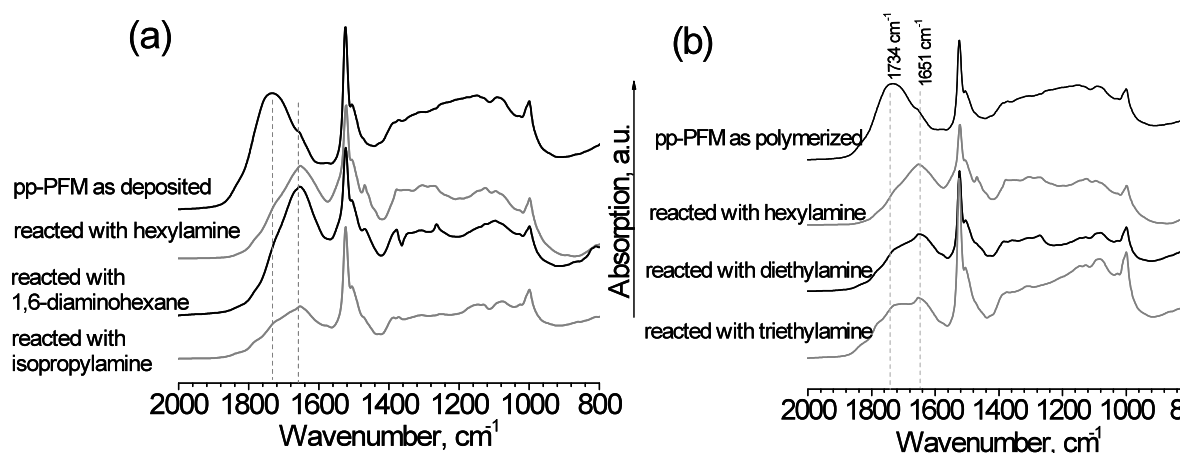


Figure 6 IRRAS spectra of pp-PFM reacted with different simple amines

The three primary amines, 1°, Figure 6 (a) in PBS studied react readily with the pp-PFM surface and the IRRAS spectra show a clear conversion of the ester to the amide in all cases. Small relative intensity variations between the bands at 1654 and 1735 cm⁻¹ were observed, which may suggest some differences in the surface reactivity. We note, however, that not all of the active ester has reacted during the time given in comparison to the concentrated amine as seen by the continuously high relative intensity of the perfluorophenyl band at 1524 cm⁻¹.

Comparisons of 1°, secondary, 2° and tertiary 3° amines show that the relative intensity of the ester peak (1735 cm⁻¹) and the amide peak (1654 cm⁻¹) changes with respect to the chemical structure of the amine, such that $I_{\text{amide}}/I_{\text{ester}}$ decreases in the order 1° > 2° > 3°, Figure 6 (b). This indicates a better conversion for the lower order amine. The intensity decrease of the band at 1524 cm⁻¹ (fluorinated ring) relative to the amide peak ($I_{\text{fluor}}/I_{\text{amide}}$) increases in the order 1° < 2° < 3°. This suggests a decreasing amount of the fluorinated rings is lost from the film surface for the higher order amine. Therefore the higher order amines appear less reactive towards the PFM ester. This could result from steric hindrance and a lower rate of diffusion of the 2° and 3° amines into the pp-PFM polymer network.

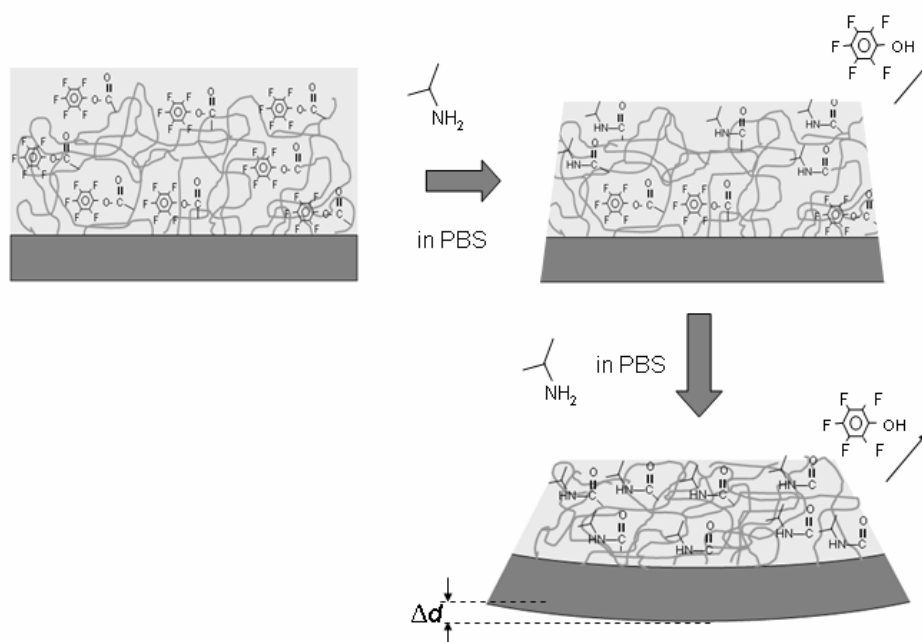


Figure 7 Schematic of a possible structure of the pp-PFM and the reaction with isopropylamine. As the active ester reacts and the bulky pentafluorophenyl group leaves the film undergoes compressive stress, which may lead to the deflection of the micromechanical cantilever

The IRRAS and XPS data so far suggest that, within a given time different degrees of surface modification take place for the different amines tested in this work. A possible explanation for this is that, once the interfacial ester groups have been aminated, modification of ester groups further within the film require the amine to diffuse into the film and that the different amines tested have a different diffusivity through the plasma polymer network. It is anticipated, that the molecular structure of the respective amine governs its ability to diffuse into the PFM plasma, as is schematically indicated for isopropylamine in Figure 7. The reactivity is further governed by the primary, secondary or tertiary nature of the reacting amine. In order to test the latter hypothesis the response of micromechanical cantilever sensors coated with the same multilayers as above to different amines were investigated.

Change in mechanical properties with chemical reactivity

Assuming that the amines are able to diffuse into, and the bulky pentafluorophenyl groups are able to diffuse out of the polymer network and into solution, differences in the conformation of the polymer molecules and thus the film volume would be expected. When a more bulky group leaves the film, the film shrinks and thus the cantilever bends towards the polymer coating side (negative deflection values in our setup) as schematically shown in Figure 7. Figure 8 shows the average differential deflection (Δd) of the modified MC arrays as a function of reaction time to primary (Figure 8a), secondary and tertiary (Figure 8b) amines in PBS. The associated values and errors for the graphs are given in Table 1.

In all measurements amines were injected at $t = 0$ s. The injection of the liquid into the measurement cell causes an initial sharp increase in the cantilever deflection associated with a perturbation of the cantilevers. After exposure to the amines for 1 h – 1.5 h the measurement cell was rinsed with pure PBS. The reaction with hexylamine and isopropylamine resulted in a negative differential deflection related to the reaction of the amine with the perfluoroester

groups and the desorption of the pentafluorophenol group from the film into the buffer solution. The most negative deflection value was observed for the reaction with isopropylamine, i.e. the smallest molecule (Table 1). A negative cantilever deflection indicates a reduction in the volume of the polymer layer. A volume decrease could be explained by the replacement of the large molar volume perfluorophenyl radical by the smaller molar volume isopropyl amine from the polymer surface, as depicted in Figure 7. Rinsing of the surface with pure buffer followed by the injection of fresh amine solution led to a negligible change in deflection indicating that the reaction was complete and irreversible after about 1 hour of amine exposure. Other data (not shown) indicates that, given enough time, the deflection curve for isopropylamine and hexylamine converge to the approximately the same differential deflection value. We conclude here, that the different time periods required to reach equilibrium could be correlated to the size of the reacting molecule and its ability to reach and react with the embedded functional groups.

It can be seen, that the bi-functional 1,6-diaminohexane led to a positive deflection when reacted with the functionalized cantilever (Figure 8a). Upon changing the solvent to pure PBS, the cantilever deflection returned to approximately the initial deflection value ($\Delta d=0$). This observation indicates a reversible reaction to occur between the diaminohexane and the plasma polymer upon rinsing with PBS buffer.

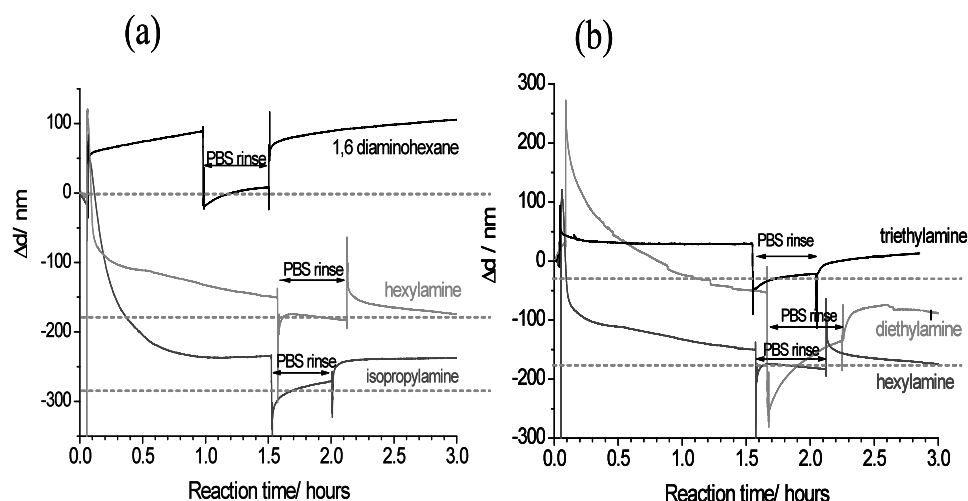


Figure 8 Micromechanical cantilever sensor deflections measured after the reaction of a pp-PFM film with (a) different 1° amines and (b) 1°, 2° and 3° amines.

Reagent	Average deflection /nm	Associated error
triethylamine	-20.3	±5
Diethylamine	-104.3	±88
Hexylamine	-177.5	±1
Isopropylamine	-278.2	±25
Diaminohexane	4.2	± 18

Table 1 Summary of average deflections measured over 4-8 cantilevers and the associated errors

In the presence of the 3° amine (triethylamine) the average differential deflection increased to a positive value ($+\Delta d$), and remained constant until rinsing. Upon rinsing, the average differential cantilever deflection changed to a negative value. For the 2° amine (diethylamine) a much slower change in differential deflection to negative values was observed and after 1.5 hours of reaction a maximum deflection was not yet reached. It is quite obvious from the data in Figure 8 that there seems to be a relationship between the amplitude of the deflection and the structure of the amine used in the reaction. This in turn can be directly correlated to and is in agreement with previous IRRAS data on the reactivity of the different amines to pp-PFM.

It is, for example, possible that the reaction of the 3° amine with the pp-PFM surface leads to positively charged, quaternary amine groups on the surface, which may lead to electrostatic interactions with the electronegative perfluorophenyl group, causing these to be re-adsorbed on the surface and acting as a barrier towards any further reagent. Rinsing of the surface may remove the electrostatically bound perfluorophenyl group. This would allow for further diffusion of solvent and amine molecules into the polymer film, which in turn leads to a bending of the MC sensor.

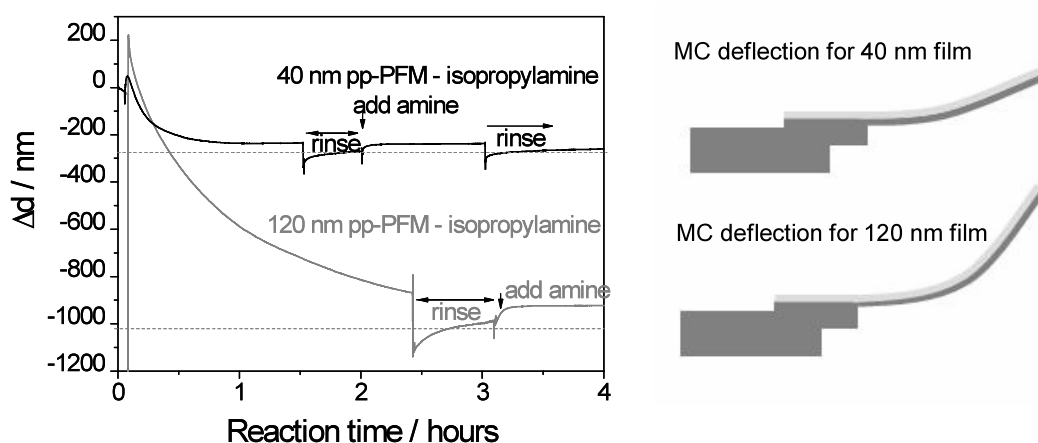


Figure 9 Deflection of micromechanical cantilevers during reaction of pp-PFM films of different thickness with isopropylamine.

If the exposure of isopropylamine to pp-PFM leads to reactions within the film, then an increase in the deposited film thickness would lead to an increase in the subsequently observed cantilever deflection. On the other hand, if only the surface of the pp-PFM film plays the dominant role a thickness independent deflection is expected. Thus, the reaction of isopropylamine with pp-PFM was studied in dependence of film thickness, keeping all other conditions constant. A 40 nm and a 120 nm thick pp-PFM film were reacted with isopropylamine in PBS (as above) until no further changes could be monitored (Figure 9). The reaction of the 40 nm thick film seemed to be complete within about one hour, while the 120 nm thick film required approximately 3 hours until equilibrium was reached. We observed an approximately 3 times larger MC deflection for a 3 times larger pp-PFM polymer film thickness. Based on the finding that the deflection change is proportional to the thickness of the pp-PFM film we conclude that shrinking of this film upon exposure to isopropylamine is the reason for the cantilever bending. In order to quantify this finding, we compared the response of both films using an equation which was derived for bimetallic cantilevers (eq.1) where the cantilever deflection (d) is related to the curvature ($k=1/r$) and the length (L) of the cantilever,⁴⁸ such that:

$$d = kL^2 / 2 \quad (1)$$

where:

$$k = \frac{6E_1E_2t_1t_2(t_1 + t_2)\Delta T_1\Delta\alpha}{(E_1t_1^2)^2 + (E_2t_2^2)^2 + 2E_1E_2t_1t_2(2t_1^2 + 3t_1t_2 + 2t_2^2)} \quad (2)$$

For a typical bimetallic cantilever this equation describes the bending (d) as a result of a change in temperature ΔT . In this case L is the length of the cantilever, t_1 is the thickness of the cantilever, t_2 is the thickness of the second metallic layer, E_1 and E_2 are Young's modulus of Silicon and the second metallic layer. $\Delta\alpha$ is the difference in the expansion coefficient of the two materials.

However, in the case of the reaction of the plasma polymer with a certain isopropylamine concentration in buffer solution, the bending of the cantilever is induced by a volume change. Thus, we are considering a bi-material (Si/ polymer) cantilever bending as a result of a chemical reaction occurring in solution. Formula 1 can thus be rewritten by replacing ΔT with a change in the concentration of the amine (ΔC). In addition, the difference in expansion coefficients, $\Delta\alpha$, is associated with the volume change of the polymer film occurring as a result of reaction in the amine solution ($\Delta\vartheta$). In order to compare the response of the swelling of both films of different thickness (40 nm and 120 nm) in PBS and in 10 mM isopropylamine in PBS, we determined the saturated deflection of both cantilever measurements with a ΔC of 10 mM. Assuming that the entire pp-PFM reacts and de-swells $\Delta\vartheta$ should be independent with the film thickness. Thus the product of $\Delta\vartheta$ and ΔC is constant after the reaction took place and will be called the "volume change coefficient" for the purpose of the following discussion.

For the present situation equations (1) and (2) can be rewritten as follows:

$$k = \frac{6E_1E_2t_1t_2(t_1 + t_2)\Delta\vartheta\Delta C}{(E_1t_1^2)^2 + (E_2t_2^2)^2 + 2E_1E_2t_1t_2(2t_1^2 + 3t_1t_2 + 2t_2^2)} \quad (3)$$

$$d = \frac{kL^2}{2} = \frac{L^2}{2} \cdot \frac{6E_1E_2t_1t_2(t_1 + t_2)\Delta\vartheta\Delta C}{(E_1t_1^2)^2 + (E_2t_2^2)^2 + 2E_1E_2t_1t_2(2t_1^2 + 3t_1t_2 + 2t_2^2)} \quad (4)$$

This allows us to describe the volume change coefficient as:

$$\Delta\vartheta\Delta C = \frac{2d}{L^2} \cdot \frac{(E_1t_1^2)^2 + (E_2t_2^2)^2 + 2E_1E_2t_1t_2(2t_1^2 + 3t_1t_2 + 2t_2^2)}{6E_1E_2t_1t_2(t_1 + t_2)} \quad (5)$$

where L is the length of the cantilever (500 μ m)

t_1 is the thickness of the Si cantilever (5 μ m)

t_2 is the thickness of the polymer (40 and 120 nm)

E_1 , is Young's modulus of Silicon, 150 GPa⁴⁹⁻⁵²

E_2 is Young's modulus of a typical acrylate polymer, 1 GPa^{53, 54}

ΔC = is the change in concentration of isopropylamine in PBS used in the experiments

The results of such calculations for ultra thin films ($t_2 < 5\%$ of t_1), using the above values are given in Table 2 and were found to be constant within the given experimental error. This, in turn, supports our conclusion, that the increase in deflection occurs as a result of diffusion and reaction of the amine molecules into the deeper layers of the film.

Table 2 Values for the volume change coefficient calculated from equation (5) above using experimentally measured deflection values shown in Figure 9.

Measured film thickness	Measured differential deflection after ~ 3 hours, $\Delta d/ nm$	Calculated ($\Delta\vartheta\Delta C$) / m^{-1}
40 nm	280	0.035
120 nm	910	0.037

Summary

This paper summarises and discusses the reactivity of plasma polymerized pentafluorophenyl methacrylate towards different simple amines in de-ionized and ionized aqueous medium with respect to the surface morphology (as observed by SEM and SFM) as well as surface chemistry and reactivity using IRRAS, XPS and SPR. The reactivity towards simple amines was investigated for the first time using highly sensitive micromechanical cantilevers to detect changes in stress within the films as a result of chemical reactions. The changes in stress were measured by the relative deflection of the cantilever. The work has led to the following conclusions:

- The reactivity of simple amines with the pp-PFM was much slower in de-ionized water than in PBS solution.
- Immersion in aqueous medium led to change in surface morphology and a smoothing of the surface suggesting substantial surface rearrangement. This could be correlated to chemical structure changes
- Microcantilever sensors could be successfully and reproducibly coated with a stable multilayer of different films including adhesion layers and pp-PFM.
- The deflection of the MC sensors as a result of reaction of the pp-PFM coated cantilever with different amines showed substantial differences. The amplitude of the deflection can be correlated to the chemical structure and the different chemical reactivity of the amines for one type of film chemistry and thickness.
- The deflection of the cantilever was studied in dependence of the plasma polymer film thickness, and suggests that the amplitude of the MC sensor deflection is volume-related for ultra thin films. A volume change coefficient in the order of $0.035 m^{-1}$ for the reaction with 10 mM isopropylamine was found.

Acknowledgements

The authors would like to thank Daniela Mössner from IMTEK, University of Freiburg, Germany, for the XPS analysis. We thank Helma Burg (MPIP) for her help with the AFM measurements.

References

1. Siow, K. S.; Britcher, L.; Kumar, S.; Griesser, H. J., Plasma methods for the generation of chemically reactive surfaces for biomolecule immobilization and cell colonization - A review. *Plasma Processes and Polymers* 2006, 3, (6-7), 392-418.
2. Forch, R.; Chifen, A. N.; Bousquet, A.; Khor, H. L.; Jungblut, M.; Chu, L. Q.; Zhang, Z.;

- Osey-Mensah, I.; Sinner, E. K.; Knoll, W., Recent and expected roles of plasma-polymerized films for biomedical applications. *Chemical Vapor Deposition* 2007, 13, (6-7), 280-294.
3. Favia, P.; d'Agostino, R., Plasma processed surfaces for biomedical devices: PEO-like, Ag/PEO-like, -COOH functional and micro-patterned coatings. *Vide-Science Technique Et Applications* 2002, 57, (303), 40-48.
 4. Alexander, M. R.; Duc, T. M., The chemistry of deposits formed from acrylic acid plasmas. *Journal of Materials Chemistry* 1998, 8, (4), 937-943.
 5. Fally, F.; Doneux, C.; Riga, J.; Verbist, J. J., Quantification of the functional groups present at the surface of plasma polymers deposited from propylamine, allylamine and propargylamine. *Journal of Applied Polymer Science* 1995, 56, (5), 597-614.
 6. Yasuda, H.; Hsu, T., Some aspects of plasma polymerisation investigated by pulsed RF discharge. *Journal of Polymer Science Part A: Polymer Chemistry* 1977, 15, (1), 81-97.
 7. Yasuda, H., Plasma Polymerization. *Accademic Press, INC* 1985, New York.
 8. Ryan, M. E.; Hynes, A. M.; Badyal, J. P. S., Pulsed plasma polymerization of maleic anhydride. *Chemistry of Materials* 1996, 8, (1), 37-42.
 9. Savage, C. R.; Timmons, R. B.; Lin, J. W., Molecular Control of Surface-Film Compositions Via Pulsed Radiofrequency Plasma Deposition of Perfluoropropylene Oxide. *Chemistry of Materials* 1991, 3, (4), 575-577.
 10. Rinsch, C. L.; Chen, X.; Panchalingam, V.; Savage, C. R.; Wang, Y. H.; Eberhart, R. C.; Timmons, R. B., Film Chemistry Control During Pulsed Rf Plasma Polymerization of Allyl Alcohol and Allyl Amine. *Abstracts of Papers of the American Chemical Society* 1995, 209, 141-POLY.
 11. Llewellyn, I. P. S., G.; Heinecke, R.A., Low temperature pulsed plasma deposition. 4. The preparation of layered structures of amorphous chalcogenide glasses with nonlinear optical properties. *Proceedings of the SPIE - The International Society for Optical Engineering* 1990, 1148 84-96.
 12. Schonherr, H.; van Os, M. T.; Foerch, R.; Timmons, R. B.; Knoll, W.; Vancso, G. J., Distributions of functional groups in plasma polymerized allylamine films by scanning force microscopy using functionalized probe tips. *Chemistry of Materials* 2000, 12, (12), 3689-3694.
 13. Kurosawa, S.; Hirokawa, T.; Kashima, K.; Aizawa, H.; Park, J. W.; Tozuka, M.; Yoshimi, Y.; Hirano, K., Adsorption of anti-C-reactive protein monoclonal antibody and its F(ab')(2) fragment on plasma-polymerized styrene, allylamine and acrylic acid coated with quartz crystal microbalance. *Journal of Photopolymer Science and Technology* 2002, 15, (2), 323-329.
 14. Zhang, Z.; Knoll, W.; Foerch, R.; Holcomb, R.; Roitman, D., DNA hybridization on plasma-polymerized allylamine. *Macromolecules* 2005, 38, (4), 1271-1276.
 15. Choukourov, A.; Biederman, H.; Slavinska, D.; Hanley, L.; Grinevich, A.; Boldyryeva, H.; Mackova, A., Mechanistic studies of plasma polymerization of allylamine. *Journal of Physical Chemistry B* 2005, 109, (48), 23086-23095.
 16. Otoole, L.; Beck, A. J.; Short, R. D., Characterization of plasma polymers of acrylic acid and propanoic acid. *Macromolecules* 1996, 29, (15), 5172-5177.
 17. Daw, R.; Candan, S.; Beck, A. J.; Devlin, A. J.; Brook, I. M.; MacNeil, S.; Dawson, R. A.; Short, R. D., Plasma copolymer surfaces of acrylic acid 1,7 octadiene: Surface characterisation and the attachment of ROS 17/2.8 osteoblast-like cells. *Biomaterials* 1998, 19, (19), 1717-1725.
 18. Mattioli-Belmonte, M.; Lucarini, G.; Virgili, L.; Biagini, G.; Detomaso, L.; Favia, P.; D'Agostino, R.; Gristina, R.; Gigante, A.; Bevilacqua, C., Mesenchymal stem cells on plasma-deposited acrylic acid coatings: An in vitro investigation to improve biomaterial performance in bone reconstruction. *Journal of Bioactive and Compatible Polymers* 2005, 20, (4), 343-360.
 19. Kelly, J. M.; Scutt, A. M.; Short, R. D.; Brook, I. M., Osteoblast attachment and spreading on an acrylic acid plasma polymer. *Journal of Dental Research* 2000, 79, (5), 1184-1184.
 20. Chifen, A. N.; Forch, R.; Knoll, W.; Cameron, P. J.; Khor, H. L.; Williams, T. L.; Jenkins, A. T. A., Attachment and phospholipase A(2)-induced lysis of phospholipid bilayer vesicles to plasma-polymerized maleic anhydride/SiO₂ multilayers. *Langmuir* 2007, 23, (11), 6294-6298.
 21. Jenkins, A. T. A.; Hu, J.; Wang, Y. Z.; Schiller, S.; Foerch, R.; Knoll, W., Pulsed plasma deposited maleic anhydride thin films as supports for lipid bilayers. *Langmuir* 2000, 16, (16), 6381-6384.
 22. Francesch, L.; Borros, S.; Knoll, W.; Forch, R., Surface reactivity of pulsed-plasma polymerized pentafluorophenyl methacrylate (PFM) toward amines and proteins in solution. *Langmuir* 2007, 23, (7), 3927-3931.

23. Francesch, L.; Garreta, E.; Balcells, M.; Edelman, E. R.; Borros, S., Fabrication of bioactive surfaces by plasma polymerization techniques using a novel acrylate-derived monomer. *Plasma Processes and Polymers* 2005, 2, (8), 605-611.
24. Queraltó, N.; Bumbu, G. G.; Francesch, L.; Knoll, W.; Borros, S.; Berger, R.; Förch, R., Investigation into the Chemical Reactivity of Plasma-Deposited Perfluorophenyl Methacrylate Using Infrared Reflection Absorption Spectroscopy and Microcantilever Studies. *Plasma Processes & Polymers* 2007, 4, S790-S793.
25. Fritz, J.; Baller, M. K.; Lang, H. P.; Rothuizen, H.; Vettiger, P.; Meyer, E.; Guntherodt, H.-J.; Gerber, C.; Gimzewski, J. K., Translating Biomolecular Recognition into Nanomechanics. *Science* 2000, 288, (5464), 316-318.
26. Pinnaduwa, L. A.; Thundat, T.; Hawk, J. E.; Hedden, D. L.; Britt, P. F.; Houser, E. J.; Stepnowski, S.; McGill, R. A.; Bubb, D., Detection of 2,4-dinitrotoluene using microcantilever sensors. *Sensors and Actuators B: Chemical* 2004, 99, (2-3), 223-229.
27. Raiteri, R.; Grattarola, M.; Butt, H.-J.; Skladal, P., Micromechanical cantilever-based biosensors. *Sensors and Actuators B - Chemical* 2001, 79, (2-3), 115-126.
28. Wu, G.-H.; Ji, H. F.; Hansen, K.; Thundat, T.; Datar, R.; Cote, R.; Hagan, M. F.; Chakraborty, A. K.; Majumdar, A., Origin of nanomechanical cantilever motion generated from biomolecular interactions. *Proceedings of the National Academy of Science of the United States of America* 2001, 98, (4), 1560-1564.
29. Baller, M. K.; Lang, H. P.; Fritz, J.; Gerber, C.; Gimzewski, J. K.; Drechsler, U.; Rothuizen, H.; Despont, M.; Vettiger, P.; Battiston, F. M.; Ramseyer, J. P.; Fornaro, P.; Meyer, E.; Guntherodt, H. J., A cantilever array-based artificial nose. *Ultramicroscopy* 2000, 82, (1-4), 1-9.
30. Lang, H.; Hegner, M.; Meyer, E.; Gerber, C., Nanomechanics from atomic resolution to molecular recognition based on atomic force microscopy technology. *NANOTECHNOLOGY* 2002, 13, (5), R29-R36.
31. Berger, R.; Gerber, C.; Gimzewski, J. K.; Meyer, E.; Guntherodt, H. J., Thermal analysis using a micromechanical calorimeter. *Applied Physics Letters* 1996, 69, (1), 40-42.
32. Toda, M.; Joseph, Y.; Berger, R.; *Journal of Physical Chemistry C*, 2010, 114, 2012-2017
33. Berger, R.; Lang, H. P.; Gerber, C.; Gimzewski, J. K.; Fabian, J. H.; Scandella, L.; Meyer, E.; Guntherodt, H. J., Micromechanical thermogravimetry. *Chemical Physics Letters* 1998, 294, (4-5), 363-369.
34. Igarashi, S.; Itakura, A. N.; Toda, M.; Kitajima, M.; Chu, L.; Chifene, A. N.; Forch, R.; Berger, R., Swelling signals of polymer films measured by a combination of micromechanical cantilever sensor and surface plasmon resonance spectroscopy. *Sensors and Actuators B-Chemical* 2006, 117, (1), 43-49.
35. Igarashi, S.; Itakura, A. N.; Kitajima, M.; Chifene, A. N.; Forch, R.; Berger, R., Surface stress control using ultraviolet light irradiation of plasma-polymerized thin films. *Applied Physics Letters* 2006, 88, (14).
36. Kooser, A.; Gunter, R. L.; Delinger, W. D.; Porter, T. L.; Eastman, M. P., Gas sensing using embedded piezoresistive microcantilever sensors. *Sensors and Actuators B - Chemical* 2004, 99, (2-3), 474-479.
37. Bumbu, G. G.; Kircher, G.; Wolkenhauer, M.; Berger, R.; Gutmann, J. S., Synthesis and characterization of polymer brushes on micromechanical cantilevers. *Macromolecular Chemistry and Physics* 2004, 205, (13), 1713-1720.
38. Bumbu, G. G.; Wolkenhauer, M.; Kircher, G.; Gutmann, J. S.; Berger, R., Micromechanical cantilever technique: A tool for investigating the swelling of polymer brushes. *Langmuir* 2007, 23, (4), 2203-2207.
39. Toda, M.; Itakura, A. N.; Igarashi, S.; Buscher, K.; Gutmann, J. S.; Graf, K.; Berger, R., Surface stress, thickness, and mass of the first few layers of polyelectrolyte. *Langmuir* 2008, 24, (7), 3191-3198.
40. Advincula, R.; Baba, A.; Xia, C. J.; Knoll, W., Spr techniques for the in-situ analysis of conjugated polymer ultrathin films: Electropolymerization, layer-by-layer growth, and patterning. *Abstracts of Papers of the American Chemical Society* 2002, 223, 004-ANYL.
41. Forch, R.; Zhang, Z. H.; Knoll, W., Soft plasma treated surfaces: Tailoring of structure and properties for biomaterial applications. *Plasma Processes and Polymers* 2005, 2, (5), 351-372.
42. Aust E.F., I. S., Sawodny M., Knoll W., Investigation of polymer thin films using surface plasmon modes and optical waveguide modes. *Trends in Polymer Science* 1994, 2, (9), 313-323.
43. Knoll, W., Guided Wave optics for the characterisation of polymeric thin films and interfaces. In *Handbook of optical properties*, Wißmann, R. E. H. P., Ed. CRC Press: London, New York, Tokyo, 1997; Vol. II, pp 373-399.

44. Knoll, W., Optics of small particles, interfaces and surfaces. In *Handbook of Optical Properties*, R.E. Hummel, P. W. m., Ed. CRC Press: Boca Raton, New York, London, Tokyo, 1997; Vol. II, pp 373-399.
45. Barranco, V.; Carpentier, J.; Grundmeier, G., Correlation of morphology and barrier properties of thin microwave plasma polymer films on metal substrate. *Electrochimica Acta* 2004, 49, (12), 1999-2013.
46. Haiedopoulos, M.; Mirabella, F.; Horgnies, M.; Volcke, C.; Thiry, P. A.; Rouxhet, P.; Pireaux, J. J., Morphology of polystyrene films deposited by RF plasma. *Journal of Microscopy-Oxford* 2007, 228, 227-239.
47. Hu, J. J.; Zong, Y.; Wang, Y. Z.; Forch, R.; Knoll, W., Sn-containing composite thin films by plasma deposition of tetramethyltin. *Thin Solid Films* 2005, 472, (1-2), 58-63.
48. Chu, W.-H.; Mehregany, M.; Mullen, R. L., Analysis of tip deflection and force of a bimetallic cantilever microactuator. *Journal of Micromech. Microeng.* 1993, 3, 4-7.
49. Spiering, V. L.; Bouwstra, S.; Spiering, R., On chip decoupling zone for package-stress reduction. *Sensors and Actuators* 1993, A39, 149-156.
50. Petersen, K. E., Silicon as a mechanical material. *Proc. IEEE.* 1982, 70, (5).
51. Ericson, F., Hardness and fracture toughness of semiconducting materials studied by indentation and erosion techniques. *Materials Science and Engineering* 1988, A105/106, 131-141.
52. Serrea, C.; Gorostiza, P.; Pérez-Rodríguez, A.; Sanz, F.; Morante, J. R., Measurement of micromechanical properties of polysilicon microstructures with an atomic force microscope. *Sensors and Actuators A* 1998, 67, (1-3), 215-219.
53. Harris, K.; Cuypers, R.; Scheibe, P.; Van Oosten, C. L.; Bastiaansen, C. W. M.; Lub, J.; Broer, D. J., Large amplitude light-induced motion in high elastic modulus polymer actuators. *Journal of Material Chemistry* 2005, 15, (47), 5043-5048.
54. Van Vlack, L. H., In *Materials for Engineering* Addison-Wesley Publishing Company: Reading, MA, 1982; Vol. , p 588.

Bibliography

1. Grosberg, A. Y.; Khokhlov, A. R., *Giant Molecules. Here, there, and everywhere...* 1997.
2. Staudinger, H., Concerning polymerisation. *Berichte Der Deutschen Chemischen Gesellschaft* **1920**, *53*, 1073-1085.
3. 1953, N. P. C. http://nobelprize.org/nobel_prizes/chemistry/laureates/1953/.
4. Hoffman, A. S., Hydrogels for biomedical applications. *Bioartificial Organs Iii: Tissue Sourcing, Immunoisolation, and Clinical Trials* **2001**, *944*, 62-73.
5. Qiu, Y.; Park, K., Environment-sensitive hydrogels for drug delivery. *Advanced Drug Delivery Reviews* **2001**, *53* (3), 321-339.
6. Zhou, F.; Shu, W.; Welland, M. E.; Huck, W., T.S., Highly reversible and Multi-stage cantilever actuation driven by Polyelectrolytes brushes. *Journal of American Chemical Society* **2006**, *128*, 5326-5327.
7. Wu, Y. H.; Park, H. B.; Kai, T.; Freeman, B. D.; Kalika, D. S., Water uptake, transport and structure characterization in poly(ethylene glycol) diacrylate hydrogels. *Journal of Membrane Science* **2010**, *347* (1-2), 197-208.
8. Hudalla, G. A.; Eng, T. S.; Murphy, W. L., An approach to modulate degradation and mesenchymal stem cell behavior in poly(ethylene glycol) networks. *Biomacromolecules* **2008**, *9* (3), 842-849.
9. Kidane, A.; Szabocsik, J. M.; Park, K., Accelerated study on lysozyme deposition on poly(HEMA) contact lenses. *Biomaterials* **1998**, *19* (22), 2051-2055.
10. Kim, S. H.; Won, C. Y.; Chu, C. C., Synthesis and characterization of dextran-based hydrogel prepared by photocrosslinking. *Carbohydrate Polymers* **1999**, *40* (3), 183-190.
11. Peppas, N. A.; Hilt, J. Z.; Khademhosseini, A.; Langer, R., Hydrogels in biology and medicine: From molecular principles to bionanotechnology. *Advanced Materials* **2006**, *18* (11), 1345-1360.
12. Hoare, T.; Pelton, R., Highly pH and temperature responsive microgels functionalized with vinylacetic acid. *Macromolecules* **2004**, *37* (7), 2544-2550.
13. Yoo, M. K.; Sung, Y. K.; Lee, Y. M.; Cho, C. S., Effect of polyelectrolyte on the lower critical solution temperature of poly(N-isopropyl acrylamide) in the poly(NIPAAm-co-acrylic acid) hydrogel. *Polymer* **2000**, *41* (15), 5713-5719.
14. Karanikolas, A.; Tsolakis, P.; Bokias, G.; Tsitsilianis, C., Stimuli-responsive poly(ethylene oxide)-b-poly(2-vinylpyridine)-b-poly(ethylene oxide) triblock copolymers and complexation with poly(acrylic acid) at low pH. *European Physical Journal E* **2008**, *27* (3), 335-343.

15. Park, T. G.; Hoffman, A. S., Sodium Chloride-Induced Phase-Transition in Nonionic Poly(N-Isopropylacrylamide) Gel. *Macromolecules* **1993**, *26* (19), 5045-5048.
16. Liu, X. M.; Wang, L. S.; Wang, L.; Huang, J. C.; He, C. B., The effect of salt and pH on the phase-transition behaviors of temperature-sensitive copolymers based on N-isopropylacrylamide. *Biomaterials* **2004**, *25* (25), 5659-5666.
17. Pei, Y.; Chen, J.; Yang, L. M.; Shi, L. L.; Tao, Q.; Hui, B. J.; Li, R., The effect of pH on the LCST of poly(N-isopropylacrylamide) and poly(N-isopropylacrylamide-co-acrylic acid). *Journal of Biomaterials Science-Polymer Edition* **2004**, *15* (5), 585-594.
18. Annaka, M.; Motokawa, K.; Sasaki, S.; Nakahira, T.; Kawasaki, H.; Maeda, H.; Amo, Y.; Tominaga, Y., Salt-induced volume phase transition of poly(N-isopropylacrylamide) gel. *Journal of Chemical Physics* **2000**, *113* (14), 5980-5985.
19. Baltes, T.; Garret-Flaudy, F.; Freitag, R., Investigation of the LCST of polyacrylamides as a function of molecular parameters and the solvent composition. *Journal of Polymer Science Part a-Polymer Chemistry* **1999**, *37* (15), 2977-2989.
20. Freitag, R.; Garret-Flaudy, F., Salt effects on the thermoprecipitation of poly-(N-isopropylacrylamide) oligomers from aqueous solution. *Langmuir* **2002**, *18* (9), 3434-3440.
21. Panayiotou, M.; Freitag, R., Influence of the synthesis conditions and ionic additives on the swelling behaviour of thermo-responsive polyalkylacrylamide hydrogels. *Polymer* **2005**, *46* (18), 6777-6785.
22. Shiga, T., Deformation and viscoelastic behavior of polymer gels in electric fields. *Neutron Spin Echo Spectroscopy Viscoelasticity Rheology* **1997**, *134*, 131-163.
23. Entezami, A. A.; Massoumi, B., Artificial muscles, biosensors and drug delivery systems based on conducting polymers: A review. *Iranian Polymer Journal* **2006**, *15* (1), 13-30.
24. Hara, S.; Zama, T.; Takashima, W.; Kaneto, K., Gel-like polypyrrole based artificial muscles with extremely large strain. *Polymer Journal* **2004**, *36* (11), 933-936.
25. Roy, D.; Cambre, J. N.; Sumerlin, B. S., Future perspectives and recent advances in stimuli-responsive materials. *Progress in Polymer Science* **2010**, *35* (1-2), 278-301.
26. Sugiyama, K.; Sono, K., Characterization of photo- and thermoresponsible amphiphilic copolymers having azobenzene moieties as side groups. *Journal of Applied Polymer Science* **2001**, *81* (12), 3056-3063.
27. Mamada, A.; Tanaka, T.; Kungwachakun, D.; Irie, M., Photoinduced Phase-Transition of Gels. *Macromolecules* **1990**, *23* (5), 1517-1519.
28. Tanaka, T., Collapse of Gels and Critical Endpoint. *Physical Review Letters* **1978**, *40* (12), 820-823.
29. Kuckling, D.; Harmon, M. E.; Frank, C. W., Photo-cross-linkable PNIPAAm copolymers. 1. Synthesis and characterization of constrained temperature-responsive hydrogel layers. *Macromolecules* **2002**, *35* (16), 6377-6383.

30. Arndt, K. F.; Schmidt, T.; Reichelt, R., Thermo-sensitive poly(methyl vinyl ether) micro-gel formed by high energy radiation. *Polymer* **2001**, *42* (16), 6785-6791.
31. Fujishige, S.; Kubota, K.; Ando, I., Phase-Transition of Aqueous-Solutions of Poly(N-Isopropylacrylamide) and Poly(N-Isopropylmethacrylamide). *Journal of Physical Chemistry* **1989**, *93* (8), 3311-3313.
32. Cho, S. H.; Jhon, M. S.; Yuk, S. H., Temperature-sensitive swelling behavior of polymer gel composed of poly (N,N-dimethylaminoethyl methacrylate) and its copolymers. *European Polymer Journal* **1999**, *35* (10), 1841-1845.
33. Ataman, M., Properties of Aqueous Salt-Solutions of Poly(Ethylene Oxide) - Cloud Points, Theta-Temperatures. *Colloid and Polymer Science* **1987**, *265* (1), 19-25.
34. Hirokawa, Y.; Tanaka, T., Volume phase transition in a nonionic gel. *The Journal of Chemical Physics* **1984**, *81* (12), 6379-6380.
35. Alarcon, C. D. H.; Pennadam, S.; Alexander, C., Stimuli responsive polymers for biomedical applications. *Chemical Society Reviews* **2005**, *34* (3), 276-285.
36. Schild, H. G., Poly (N-Isopropylacrylamide) - Experiment, Theory and Application. *Progress in Polymer Science* **1992**, *17* (2), 163-249.
37. Hoare, T.; Pelton, R., Functional group distributions in carboxylic acid containing poly(N-isopropylacrylamide) microgels. *Langmuir* **2004**, *20* (6), 2123-2133.
38. Harmon, M. E.; Kuckling, D.; Pareek, P.; Frank, C. W., Photo-cross-linkable PNIPAAm copolymers. 4. Effects of copolymerization and cross-linking on the volume-phase transition in constrained hydrogel layers. *Langmuir* **2003**, *19* (26), 10947-10956.
39. Harmon, M. E.; Kuckling, D.; Frank, C. W., Photo-cross-linkable PNIPAAm copolymers. 2. Effects of constraint on temperature and pH-responsive hydrogel layers. *Macromolecules* **2003**, *36* (1), 162-172.
40. Anac, I.; Aulasevich, A.; Junk, M. J. N.; Jakubowicz, P.; Roskamp, R.; Menges, B.; Jonas, U.; Knoll, W., Temperature dependent swelling behavior of thin Poly(N-isopropylacrylamide) copolymer gel layers in ethanol-water mixtures. *in preparation* **2010**.
41. Tanaka, T.; Fillmore, D. J., Kinetics of Swelling of Gels. *Journal of Chemical Physics* **1979**, *70* (3), 1214-1218.
42. Hoffmann, J.; Plotner, M.; Kuckling, D.; Fischer, W. J., Photopatterning of thermally sensitive hydrogels useful for microactuators. *Sensors and Actuators a-Physical* **1999**, *77* (2), 139-144.
43. Harmon, M. E.; Tang, M.; Frank, C. W., A microfluidic actuator based on thermoresponsive hydrogels. *Polymer* **2003**, *44* (16), 4547-4556.
44. Sheeney-Haj-Ichia, L.; Sharabi, G.; Willner, I., Control of the electronic properties of thermosensitive poly(N-isopropylacrylamide) and Au-nanoparticle/poly(N-isopropylacrylamide) composite hydrogels upon phase transition. *Advanced Functional Materials* **2002**, *12* (1), 27-32.

45. Li, J.; Hong, X.; Liu, Y.; Li, D.; Wang, Y. W.; Li, J. H.; Bai, Y. B.; Li, T. J., Highly photoluminescent CdTe/Poly(N-isopropylacrylamide) temperature-sensitive gels. *Advanced Materials* **2005**, *17* (2), 163-+.
46. Nemethy, A.; Szilagy, A.; Filipcsei, G.; Tombacz, E.; Zrinyi, M., Characterization of Poly(N-isopropylacrylamide) and Magnetic Poly(N-isopropylacrylamide) Latexes. *Colloids for Nano- and Biotechnology* **2008**, *135*, 194-199
234.
47. Filipcsei, G.; Szilagy, A.; Csetneki, I.; Zrinyi, M., Comparative study on the collapse transition of poly(N-isopropylacrylamide) gels and magnetic nanoparticles loaded poly(N-isopropylacrylamide) gels. *Macromolecular Symposia* **2006**, *239*, 130-137.
48. Xulu, P. M.; Filipcsei, G.; Zrinyi, M., Preparation and responsive properties of magnetically soft poly(N-isopropylacrylamide) gels. *Macromolecules* **2000**, *33* (5), 1716-1719.
49. Francois, N. J.; Allo, S.; Jacobo, S. E.; Daraio, M. E., Composites of polymeric gels and magnetic nanoparticles: Preparation and drug release behavior. *Journal of Applied Polymer Science* **2007**, *105* (2), 647-655.
50. Zrinyi, M.; Szabo, D.; Filipcsei, G.; Feher, J., Electrical and Magnetic Field-sensitive smart polymer gels. In *Polymer Gels and Networks*, Osada, Y.; Khokhlov, A. R., Eds. Marcel Dekker, Inc: New York, 2002; pp 309-355.
51. Spaldin, N., *Magnetic Materials. Fundamentals and Device Applications*. Cambridge, UK, 2003.
52. Zrinyi, M., Intelligent polymer gels controlled by magnetic fields. *Colloid and Polymer Science* **2000**, *278* (2), 98-103.
53. Jolly, M. R.; Carlson, J. D.; Munoz, B. C.; Bullions, T. A., The magnetoviscoelastic response of elastomer composites consisting of ferrous particles embedded in a polymer matrix. *Journal of Intelligent Material Systems and Structures* **1996**, *7* (6), 613-622.
54. Li, B. Q.; Jia, D. C.; Zhou, Y.; Hu, Q. L.; Cai, W., In situ hybridization to chitosan/magnetite nanocomposite induced by the magnetic field. *Journal of Magnetism and Magnetic Materials* **2006**, *306* (2), 223-227.
55. Mayer, C. R.; Cabuil, V.; Lalot, T.; Thouvenot, R., Magnetic nanoparticles trapped in pH 7 hydrogels as a tool to characterize the properties of the polymeric network. *Advanced Materials* **2000**, *12* (6), 417-+.
56. Otsuka, I.; Abe, H.; Ozeki, S., Magnetic field control of structure and function of poly(N-isopropylacrylamide) gels. *Science and Technology of Advanced Materials* **2006**, *7* (4), 327-331.
57. Stepanov, G. V.; Borin, D. Y.; Raikher, Y. L.; Melenev, P. V.; Perov, N. S., Motion of ferroparticles inside the polymeric matrix in magnetoactive elastomers. *Journal of Physics-Condensed Matter* **2008**, *20* (20), -.
58. Gollwitzer, C.; Turanov, A.; Krekhova, M.; Lattermann, G.; Rehberg, I.; Richter, R., Measuring the deformation of a ferrogel sphere in a homogeneous magnetic field. *Journal of Chemical Physics* **2008**, *128* (16), -.

59. Nikitin, L. V.; Mironova, L. S.; Kornev, K. G.; Stepanov, G. V., The magnetic, elastic, structural, and magnetodeformational properties of magnetoelastics. *Polymer Science Series A* **2004**, *46* (3), 301-309.
60. Hergt, R.; Andra, W.; d'Ambly, C. G.; Hilger, I.; Kaiser, W. A.; Richter, U.; Schmidt, H. G., Physical limits of hyperthermia using magnetite fine particles. *IEEE Transactions on Magnetics* **1998**, *34* (5), 3745-3754.
61. Lu, A. H.; Salabas, E. L.; Schuth, F., Magnetic nanoparticles: Synthesis, protection, functionalization, and application. *Angewandte Chemie-International Edition* **2007**, *46* (8), 1222-1244.
62. Gubin, S. P.; Koksharov, Y. A.; Khomutov, G. B.; Yurkov, G. Y., Magnetic nanoparticles: Preparation methods, structure and properties. *Uspekhi Khimii* **2005**, *74* (6), 539-574.
63. Sorensen, C. M., Magnetism. In *Nanoscale Materials in Chemistry*, Klabunde, K. J., Ed. John Wiley & Sons, Inc.; 2001; pp 169-221.
64. Kodama, R. H., Magnetic nanoparticles. *Journal of Magnetism and Magnetic Materials* **1999**, *200* (1-3), 359-372.
65. Reiss, G.; Hutten, A., Magnetic nanoparticles - Applications beyond data storage. *Nature Materials* **2005**, *4* (10), 725-726.
66. White, R. M., Magnetic recording - Pushing back the superparamagnetic barrier. *Journal of Magnetism and Magnetic Materials* **2001**, *226*, 2042-2045.
67. Pankhurst, Q. A.; Connolly, J.; Jones, S. K.; Dobson, J., Applications of magnetic nanoparticles in biomedicine. *Journal of Physics D-Applied Physics* **2003**, *36*, R167-R181.
68. Urban, G. A., Micro- and nanobiosensors-state of the art and trends. *Measurement Science & Technology* **2009**, *20* (1), -.
69. Lang, H. P.; Berger, R.; Andreoli, C.; Brugger, J.; Despont, M.; Vettiger, P.; Gerber, C.; Gimzewski, J. K.; Ramseyer, J. P.; Meyer, E.; Güntherodt, H.-J., Sequential position readout from arrays of micromechanical cantilever sensors. *Applied Physics Letters* **1998**, *72* (383-385).
70. Micromotive http://www.micromotive.de/Octosensis_e.php.
71. Norman, L. L.; Badia, A., Redox Actuation of a Microcantilever Driven by a Self-Assembled Ferrocenylundecanethiolate Monolayer: An Investigation of the Origin of the Micromechanical Motion and Surface Stress. *Journal of American Chemical Society* **2009**, *131*, 2328-2337.
72. Thundat, T.; Warmack, R. J.; Chen, G. Y.; D.P., A., Thermal and ambient-induced deflections of scanning force microscope cantilevers. *Applied Physics Letters* **1994**, *64* (21), 2894-2896.
73. Gimzewski, J. K.; Gerber, C.; Meyer, E.; Schlittler, R. R., Observation of a chemical reaction using a micromechanical sensor. *Chemical Physics Letters* **1994**, *217*, 589-594.
74. Zhao, J.; Berger, R.; Gutman, J., S., Thermal contributions to the bending of bimaterial cantilever sensors. *Applied Physics Letters* **2006**, *89* (033110).

-
75. Deegan, R. D.; Bakajin, O.; Dupont, T. F.; Huber, G.; Nagel, S. R.; Witten, T. A., Capillary flow as the cause of ring stains from dried liquid drops. *Nature* **1997**, *389* (6653), 827-829.
76. Ko, H.-Y.; Park, J.; Shin, H.; Moon, J., Rapid Self-Assembly of Monodisperse Colloidal Spheres in an Ink-Jet Printed Droplet. *Chemistry of Materials* **2004**, *16* (22), 4212-4215.
77. Lang, H. P.; Ramaseyer, J. P.; Grange, W.; Braun, T.; Schmid, D.; Hunziker, P.; Jung, C.; Hegner, M.; Gerber, C., An Artificial Nose Based on Microcantilever Array Sensors. *Journal of Physics:Conference Series* **2007**, *61*, 663-667.
78. www.gesim.de.
79. *Benutzerhandbuch Nano-Plotter 2.0/ Software NPC16; Gesellschaft fr Silizium-Mikrosysteme mbH, 2004.*
80. Nett, S., K. Functional Polymer Coatings. μ -Patterning and μ -Analysis. Gutenberg Universität, Mainz, Germany, 2009.
81. A.M.Moulin; O'Shea, S. J.; Welland, M. E., Microcantilever-based biosensor. *Ultramicroscopy* **2000**, *82*, 23-31.
82. Raiter, R.; Grattarola, M.; Butt, H.-J.; Skládal, P., Micromechanical cantilever-based biosensors. *Sensors and Actuators B* **2001**, *79*, 115-126.
83. Raiteri, R.; Grattarola, M.; Berger, R., Micromechanics senses biomolecules. *Materials Today* **2002**, 22-29.
84. Lang, H. P., Nanomechanical Cantilever Array Sensors. In *Handbook of Nanotechnology 2nd Ed*, Bhushan, B., Ed. Springer: 2007; pp 443-459.
85. Goeders, K. M.; Colton, J., S.; Bottomley, L. A., Microcantilevers: Sensing Chemical Interactions via Mechanical Motion. *Chemical Reviews* **2008**, *108* (2), 522-542.
86. Lang, H. P.; Gerber, C., Microcantilever Sensors. *Topics in Current Chemistry* **2008**, *285*, 1-27.
87. Homola, J., Surface plasmon resonance sensors for detection of chemical and biological species. *Chemical Reviews* **2008**, *108* (2), 462-493.
88. GWC Technologies, I. <http://www.gwctechnologies.com/>.
89. Ibis-Technologies <http://www.ibis-spr.nl/>.
90. Genoptics <http://www.genoptics-spr.com/content.php?idcontent=spr%20in%20the%20lab&lg=en>.
91. Knoll, W., Interfaces and thin films as seen by bound electromagnetic waves. *Annual Review of Physical Chemistry* **1998**, *49*, 569-638.

-
92. Kretschm.E; Raether, H., Radiative Decay of Non Radiative Surface Plasmons Excited by Light. *Zeitschrift Fur Naturforschung Part a-Astrophysik Physik Und Physikalische Chemie* **1968**, A 23 (12), 2135-&.
93. Otto, A., Excitation of Nonradiative Surface Plasma Waves in Silver by Method of Frustrated Total Reflection. *Zeitschrift Fur Physik* **1968**, 216 (4), 398-&.
94. Smith, R. E.; Houdewalter, S. N., Leaky Guiding in Nontransparent Wave-Guides. *Journal of the Optical Society of America a-Optics Image Science and Vision* **1995**, 12 (4), 715-724.
95. Roskamp, R. F. Functional Hydrogels. Gutenberg Universität, Mainz, 2009.
96. Ruska, N. P. http://nobelprize.org/nobel_prizes/physics/laureates/1986/.
97. William, D. B.; Barry Carter, C., *Transmission Electron Microscopy. A Textbook for Materials Science*. 1996.
98. FEI-Company <http://www.fei.com/products/transmission-electron-microscopes/tecnai.aspx>.
99. Tompkins, H. G.; Irene, E. A., *Handbook of Ellipsometry*. 2005.
100. Azzam, R. M. A.; Bashara, N. M., *Ellipsometry and Polarized light*. 1987.
101. Clarke, J.; Braginski, A. I., *The SQUID Handbook Vol.1 Fundamentals and Technology of SQUIDs and SQUID Systems`*. 2004.
102. Josephson, B. D., Possible New Effects in Superconductive Tunnelling. *Physics Letters* **1962**, 1 (7), 251-253.
103. Barone, A., *Principles and Applications of Superconducting Quantum interference devices*. World Scientific Publishing Co. Pte. Ltd.: Singapore, 1992.
104. Testo-845 <http://www.testo350.com/845.html>.
105. Tipler, P., *Physik*. 2000.
106. Plunkett, K. N.; Zhu, X.; Moore, J. S.; Leckband, D. E., PNIPAM Chain Collapse Depends on the Molecular Weight and Grafting Density. *Langmuir* **2006**, 22, 4259-4266.
107. Balamurugan, S.; Mendez, S.; Balamurugan, S. S.; O'Brien, M. J.; Lopez, G. P., Thermal response of poly(N-isopropylacrylamide) brushes probed by surface plasmon resonance. *Langmuir* **2003**, 19 (7), 2545-2549.
108. Queralto, N.; Bumbu, G. G.; Francesch, L.; Knoll, W.; Borros, S.; Berger, R.; Foerch, R., Investigation into the Chemical Reactivity of Plasma-Deposited Perfluorophenyl Methacrylate Using Infrared Reflection Absorption Spectroscopy and Microcantilever Studies. *Plasma Process. Polym.* **2007**, 4, S790-S793.

109. Beines, P. W.; Klosterkamp, I.; Menges, B.; Jonas, U.; Knoll, W., Responsive thin hydrogel layers from photo-cross-linkable poly(N-isopropylacrylamide) terpolymers. *Langmuir* **2007**, *23* (4), 2231-2238.
110. Beines, P. W. Synthese und Charakterisierung einer Hydrogelmatrix für die Multianalyt-Sensorik. Gutenberg Universität, Mainz, 2007.
111. Toomey, R.; Freidank, D.; Ruhe, J., Swelling behavior of thin, surface-attached polymer networks. *Macromolecules* **2004**, *37* (3), 882-887.
112. Kuckling, D.; Adler, H. J. P.; Ling, L.; Habicher, W. D.; Arndt, K. F., Temperature sensitive polymers based on 2-(dimethyl maleinimido)-N-ethyl-acrylamide: Copolymers with N-isopropylacrylamide. *Polymer Bulletin* **2000**, *44* (3), 269-276.
113. Vo, C. D.; Kuckling, D.; Adler, H. J. P.; Schohoff, M., Preparation of thermosensitive nanogels by photo-cross-linking. *Colloid and Polymer Science* **2002**, *280* (5), 400-409.
114. Kuckling, D.; Adler, H. J. P.; Arndt, K. F.; Ling, L.; Habicher, W. D., Temperature and pH dependent solubility of novel poly(N-isopropylacrylamide) copolymers. *Macromolecular Chemistry and Physics* **2000**, *201* (2), 273-280.
115. Prucker, O.; Naumann, C. A.; Ruhe, J.; Knoll, W.; Frank, C. W., Photochemical attachment of polymer films to solid surfaces via monolayers of benzophenone derivatives. *Journal of the American Chemical Society* **1999**, *121* (38), 8766-8770.
116. Ulman, A., Formation and structure of self-assembled monolayers. *Chemical Reviews* **1996**, *96* (4), 1533-1554.
117. Dorman, G.; Prestwich, G. D., Benzophenone Photophores in Biochemistry. *Biochemistry* **1994**, *33* (19), 5661-5673.
118. Horie, K.; Morishita, K.; Mita, I., Photochemistry in Polymer Solids .3. Kinetics for Nonexponential Decay of Benzophenone Phosphorescence in Acrylic and Methacrylic Polymers. *Macromolecules* **1984**, *17* (9), 1746-1750.
119. Horie, K.; Ando, H.; Mita, I., Photochemistry in Polymer Solids .8. Mechanism of Photoreaction of Benzophenone in Poly(vinyl-Alcohol). *Macromolecules* **1987**, *20* (1), 54-58.
120. Zweifel, H., Polymers with Pendent Dimethylmaleimide Groups as Highly Sensitive Photocrosslinkable Systems. *Photographic Science and Engineering* **1983**, *27* (3), 114-118.
121. Deschryv.Fc; Smets, G.; Boens, N., Photopolymerization .5. Unsensitized Solution Photocyclopolymerization of N,N'-Alkylenebismaleimides. *Journal of Polymer Science Part a-1-Polymer Chemistry* **1972**, *10* (6), 1687-&.
122. Burda, C.; Chen, X. B.; Narayanan, R.; El-Sayed, M. A., Chemistry and properties of nanocrystals of different shapes. *Chemical Reviews* **2005**, *105* (4), 1025-1102.
123. El-Sayed, M. A., Small is different: Shape-, size-, and composition-dependent properties of some colloidal semiconductor nanocrystals. *Accounts of Chemical Research* **2004**, *37* (5), 326-333.

124. Seo, W. S.; Jo, H. H.; Lee, K.; Kim, B.; Oh, S. J.; Park, J. T., Size-dependent magnetic properties of colloidal Mn₃O₄ and MnO nanoparticles. *Angewandte Chemie-International Edition* **2004**, *43* (9), 1115-1117.
125. Li, X. G.; Chiba, A.; Takahashi, S.; Ohsaki, K., Preparation, oxidation and magnetic properties of Fe-Cr ultrafine powders by hydrogen plasma-metal reaction. *Journal of Magnetism and Magnetic Materials* **1997**, *173* (1-2), 101-108.
126. Lin, X. M.; Samia, A. C. S., Synthesis, assembly and physical properties of magnetic nanoparticles. *Journal of Magnetism and Magnetic Materials* **2006**, *305* (1), 100-109.
127. Taboada, E.; Rodriguez, E.; Roig, A.; Oro, J.; Roch, A.; Muller, R. N., Relaxometric and magnetic characterization of ultras-small iron oxide nanoparticles with high magnetization. Evaluation as potential T-1 magnetic resonance imaging contrast agents for molecular imaging. *Langmuir* **2007**, *23* (8), 4583-4588.
128. Jana, N. R.; Chen, Y. F.; Peng, X. G., Size- and shape-controlled magnetic (Cr, Mn, Fe, Co, Ni) oxide nanocrystals via a simple and general approach. *Chemistry of Materials* **2004**, *16* (20), 3931-3935.
129. Kwon, S. G.; Piao, Y.; Park, J.; Angappane, S.; Jo, Y.; Hwang, N. M.; Park, J. G.; Hyeon, T., Kinetics of monodisperse iron oxide nanocrystal formation by "heating-up" process. *Journal of the American Chemical Society* **2007**, *129* (41), 12571-12584.
130. Du, G. H.; Liu, Z. L.; Xia, X.; Chu, Q.; Zhang, S. M., Characterization and application of Fe₃O₄/SiO₂ nanocomposites. *Journal of Sol-Gel Science and Technology* **2006**, *39* (3), 285-291.
131. Sun, J.; Zhou, S. B.; Hou, P.; Yang, Y.; Weng, J.; Li, X. H.; Li, M. Y., Synthesis and characterization of biocompatible Fe₃O₄ nanoparticles. *Journal of Biomedical Materials Research Part A* **2007**, *80A* (2), 333-341.
132. Sun, Y. B.; Ding, X. B.; Zheng, Z. H.; Cheng, X.; Hu, X. H.; Peng, Y. X., Magnetic separation of polymer hybrid iron oxide nanoparticles triggered by temperature. *Chemical Communications* **2006**, (26), 2765-2767.
133. Tsang, S. C.; Yu, C. H.; Gao, X.; Tam, K., Silica-encapsulated nanomagnetic particle as a new recoverable biocatalyst carrier. *Journal of Physical Chemistry B* **2006**, *110* (34), 16914-16922.
134. Sun, S. H.; Zeng, H.; Robinson, D. B.; Raoux, S.; Rice, P. M.; Wang, S. X.; Li, G. X., Monodisperse MFe₂O₄ (M = Fe, Co, Mn) nanoparticles. *Journal of the American Chemical Society* **2004**, *126* (1), 273-279.
135. Kim, M.; Chen, Y. F.; Liu, Y. C.; Peng, X. G., Super-stable, high-quality Fe₃O₄ dendron-nanocrystals dispersible in both organic and aqueous solutions. *Advanced Materials* **2005**, *17* (11), 1429-+.
136. Hassner, A.; Wiederke, R.; Kaschere, A., Reaction of Aldehydes with N-Hydroxybenzenesulfonamide - Acetal Formation Catalyzed by Nucleophiles. *Journal of Organic Chemistry* **1970**, *35* (6), 1962-8.

137. Mohapatra, S.; Mallick, S. K.; Maiti, T. K.; Ghosh, S. K.; Pramanik, P., Synthesis of highly stable folic acid conjugated magnetite nanoparticles for targeting cancer cells. *Nanotechnology* **2007**, *18* (38), -.
138. Lee, D. C.; Mikulec, F. V.; Pelaez, J. M.; Koo, B.; Korgel, B. A., Synthesis and magnetic properties of silica-coated FePt nanocrystals. *Journal of Physical Chemistry B* **2006**, *110* (23), 11160-11166.
139. Ling, X. Y.; Reinhoudt, D. N.; Huskens, J., Ferrocenyl-functionalized silica nanoparticles: Preparation, characterization, and molecular recognition at interfaces. *Langmuir* **2006**, *22* (21), 8777-8783.
140. Suzuki, K.; Siddiqui, S.; Chappell, C.; Siddiqui, J. A.; Ottenbrite, R. M., Modification of porous silica particles with poly(acrylic acid). *Polymers for Advanced Technologies* **2000**, *11* (2), 92-97.
141. Takahara, Y. K.; Ikeda, S.; Ishino, S.; Tachi, K.; Ikeue, K.; Sakata, T.; Hasegawa, T.; Mori, H.; Matsumura, M.; Ohtani, B., Asymmetrically modified silica particles: A simple particulate surfactant for stabilization of oil droplets in water. *Journal of the American Chemical Society* **2005**, *127* (17), 6271-6275.
142. Wu, Z. J.; Xiang, H.; Kim, T.; Chun, M. S.; Lee, K., Surface properties of submicrometer silica spheres modified with aminopropyltriethoxysilane and phenyltriethoxysilane. *Journal of Colloid and Interface Science* **2006**, *304* (1), 119-124.
143. Wu, W.; He, Q. G.; Chen, H., Silane bridged surface tailoring on magnetite nanoparticles. *IEEE Transactions on Magnetics* **2007**.
144. Mohapatra, S.; Pramanik, N.; Mukherjee, S.; Ghosh, S. K.; Pramanik, P., A simple synthesis of amine-derivatised superparamagnetic iron oxide nanoparticles for bioapplications. *J Mater Sci* **2007**, *42*, 7566-7574.
145. Lattuada, M.; Hatton, T. A., Functionalization of monodisperse magnetic nanoparticles. *Langmuir* **2007**, *23* (4), 2158-2168.
146. Guenther, M.; Gerlach, G.; Wallmersperger, T., Non-linear Effects in Hydrogel-based Chemical Sensors: Experiment and Modeling. *Journal of Intelligent Material Systems and Structures* **2009**, *20* (8), 949-961.
147. Milner, S. T., Polymer Brushes. *Science* **1991**, *251*, 905-914.
148. Tokarev, I.; Minko, S., Stimuli-responsive hydrogel thin films. *Soft Matter* **2009**, *5* (3), 511-524.
149. Chen, G. H.; Hoffman, A. S., Graft-Copolymers That Exhibit Temperature-Induced Phase-Transitions over a Wide-Range of Ph. *Nature* **1995**, *373* (6509), 49-52.
150. Brazel, C. S.; Peppas, N. A., Pulsatile local delivery of thrombolytic and antithrombotic agents using poly(N-isopropylacrylamide-co-methacrylic acid) hydrogels. *Journal of Controlled Release* **1996**, *39* (1), 57-64.

151. Zhao, Z. X.; Li, Z.; Xia, Q. B.; Xi, H. X.; Lin, Y. S., Fast synthesis of temperature-sensitive PNIPAAm hydrogels by microwave irradiation. *European Polymer Journal* **2008**, *44* (4), 1217-1224.
152. Varga, I.; Gilanyi, T.; Meszaros, R.; Filipcsei, G.; Zrinyi, M., Effect of cross-link density on the internal structure of Poly(N-isopropylacrylamide) microgels. *Journal of Physical Chemistry B* **2001**, *105* (38), 9071-9076.
153. Schmaljohann, D.; Nitschke, M.; Schulze, R.; Eing, A.; Werner, C.; Eichhorn, Y. J., In situ study of the thermoresponsive behavior of micropatterned hydrogel films by imaging ellipsometry. *Langmuir* **2005**, *21* (6), 2317-2322.
154. Dostalek, J.; Roskamp, R. F.; Knoll, W., Coupled long range surface plasmons for the investigation of thin films and interfaces. *Sensors and Actuators B-Chemical* **2009**, *139* (1), 9-12.
155. Zhang, G. Z., Study on conformation change of thermally sensitive linear grafted poly(N-isopropylacrylamide) chains by quartz crystal microbalance. *Macromolecules* **2004**, *37* (17), 6553-6557.
156. Liu, G. M.; Zhang, G. Z., Reentrant behavior of poly(N-isopropylacrylamide) brushes in water-methanol mixtures investigated with a quartz crystal microbalance. *Langmuir* **2005**, *21* (5), 2086-2090.
157. Liu, G. M.; Zhang, G. Z., Collapse and swelling of thermally sensitive Poly(N-isopropylacrylamide) brushes monitored with a quartz crystal microbalance. *Journal of Physical Chemistry B* **2005**, *109* (2), 743-747.
158. Bumbu, G.-G.; Kircher, G.; Wolkenhauer, M.; Berger, R.; Gutman, J., S., Synthesis and Characterization of Polymer Brushes on Micromechanical Cantilevers. *Macromolecular Chemistry and Physics* **2004**, *205*, 1713-1720.
159. Igarashi, S.; Itakura, A., N.; Kitajima, M.; Chifen, A., N.; Försch, R.; Berger, R., Surface stress control using ultraviolet light irradiation of plasma-polymerized thin films. *Applied Physics Letters* **2006**, *88* (1413119).
160. Fritz, J.; Baller, M. K.; Lang, H. P.; Rothuizen, H.; Vettiger, P.; Meyer, E.; Güntherodt, H.-J.; Gerber, C.; Gimzewski, J. K., Translating Biomolecular Recognition into Nanomechanics. *Science* **2000**, *288*, 316-318.
161. Shu, W.; Liu, D.; Watari, M.; Riener, C. K.; Strunz, T.; Welland, M. E.; Balasubramanian, S.; McKendry, R., A., DNA Molecular Motor Driven Micromechanical Cantilever Arrays. *Journal of American Chemical Society* **2005**, *127*, 17054-17060.
162. Zhou, F.; Biesheuvel, M.; Choi, E.-Y.; Shu, W.; Poetes, R.; Steiner, U.; Huck, W., T.S., Polyelectrolyte Brush Amplified Electroactuation of Microcantilevers. *NanoLetters* **2008**, *8* (2), 725-730.
163. Snow, D.; Weeks, B., L.; Kim, D. J.; Loui, A.; Hart, B., R.; Hope-Weeks, L. J., Static deflection measurements of cantilever arrays reveal polymer film expansion and contraction. *Journal of Colloid and Interface Science* **2007**, *316*, 687-693.

164. Oliviero, G.; Bergese, P.; Canavese, G.; Chiari, M.; Colombi, P.; Cretich, M.; Damin, F.; Fiorilli, S.; Marasso, S., L.; Ricciardi, C.; Rivolo, P.; Depero, L., E., A biofunctional polymeric coating for microcantilever molecular recognition. *Analytica Chimica Acta* **2008**, *630*, 161-167.
165. Bradley, C.; Jalili, N.; Nett, S., K.; Chu, L.; Försch, R.; Gutman, J., S.; Berger, R., Response Characteristics of Thermoresponsive Polymers Using Nanomechanical Cantilever Sensors. *Macromolecular Chemistry and Physics* **2009**, *210*, 1339-1345.
166. Fritz, J.; Baller, M. K.; Lang, H. P.; Strunz, T.; Meyer, E.; Guntherodt, H. J.; Delamarche, E.; Gerber, C.; Gimzewski, J. K., Stress at the Solid-Liquid Interface of Self-Assembled Monolayers on Gold Investigated with a Nanomechanical Sensor. *Langmuir* **2000**, *16* (25), 9694-9696.
167. Hu, K.; Bard, J., Use of Atomic Force Microscopy for the Study of Surface Acid-Base Properties of Carboxylic Acid-Terminated Self-Assembled Monolayers. *Langmuir* **1997**, *13*, 5114-5119.
168. Raiteri, R.; Butt, H. J.; Grattarola, M., Changes in surface stress at the liquid/solid interface measured with a microcantilever. *Electrochimica Acta* **2000**, *46* (2-3), 157-163.
169. Harmon, M. E.; Kucking, D.; Frank, C. W., Photo-cross-linkable PNIPAAm copolymers. 5. Mechanical properties of hydrogel layers. *Langmuir* **2003**, *19* (26), 10660-10665.
170. Butt, H.-J. r., A Sensitive Method to Measure Changes in the Surface Stress of Solids. *Journal of Colloid and Interface Science* **1996**, *180* (1), 251-260.
171. Pomozzi, A., Fluorescence close to dielectric interfaces. 2008.
172. Harmon, M. E.; Jakob, T. A. M.; Knoll, W.; Frank, C. W., A Surface Plasmon Resonance Study of Volume Phase Transitions in N-Isopropylacrylamide Gel Films. *Macromolecules* **2002**, *35* (15), 5999-6004.
173. Pareek, P.; Adler, H.-J.; Kuckling, D., Tuning the Swelling Behavior of Chemisorbed Thin PNIPAAm Hydrogel Layers by N,N-Dimethyl Acrylamide Content. In *Characterization of Polymer Surfaces and Thin Films*, 2006; pp 145-151.
174. Tamai, Y.; Tanaka, H.; Nakanishi, K., Molecular dynamics study of polymer-water interaction in hydrogels .1. Hydrogen-bond structure. *Macromolecules* **1996**, *29* (21), 6750-6760.
175. Watari, M.; Galbraith, J.; Lang, H.-P.; Sousa, M.; Hegner, M.; Gerber, C.; Horton, M. A.; McKendry, R. A., Investigating the Molecular Mechanisms of In-Plane Mechanochemistry on Cantilever Arrays. *Journal of the American Chemical Society* **2006**, *129* (3), 601-609.
176. Klein, C. A., How accurate are Stoney's equation and recent modifications. *Journal of Applied Physics* **2000**, *88* (9), 5487-5489.
177. Sader, J. E., Surface stress induced deflections of cantilever plates with applications to the atomic force microscope: Rectangular plates. *Journal of Applied Physics* **2001**, *89* (5), 2911-2921.
178. Schafer, J. D.; Nafe, H.; Aldinger, F., Macro- and microstress analysis in sol-gel derived $\text{Pb}(\text{Zr}_{x}\text{Ti}_{1-x})\text{O}_3$ thin films. *Journal of Applied Physics* **1999**, *85* (12), 8023-8031.

179. Bumbu, G.-G.; Wolkenhauer, M.; Kircher, G.; Gutman, J., S.; Berger, R., Micromechanical Cantilever Technique: A tool for Investigating the Swelling of Polymer Brushes. *Langmuir* **2007**, *23*, 2203-2207.
180. Wang, J.; Gan, D.; Lyon, L. A.; El-Sayed, M. A., Temperature-Jump Investigations of the Kinetics of Hydrogel Nanoparticle Volume Phase Transitions. *Journal of the American Chemical Society* **2001**, *123* (45), 11284-11289.
181. Zhang, X. Z.; Xu, X. D.; Cheng, S. X.; Zhuo, R. X., Strategies to improve the response rate of thermosensitive PNIPAAm hydrogels. *Soft Matter* **2008**, *4* (3), 385-391.
182. Chen, X. J.; Tsujii, K., A novel hydrogel showing super-rapid shrinking but slow swelling behavior. *Macromolecules* **2006**, *39* (25), 8550-8552.
183. Yoshida, R.; Uchida, K.; Kaneko, Y.; Sakai, K.; Kikuchi, A.; Sakurai, Y.; Okano, T., Comb-Type Grafted Hydrogels with Rapid De-Swelling Response to Temperature-Changes. *Nature* **1995**, *374* (6519), 240-242.
184. Kaneko, Y.; Yoshida, R.; Sakai, K.; Sakurai, Y.; Okano, T., Temperature-Responsive Shrinking Kinetics of Poly(N-Isopropylacrylamide) Copolymer Gels with Hydrophilic and Hydrophobic Comonomers. *Journal of Membrane Science* **1995**, *101* (1-2), 13-22.
185. Zhang, X. Z.; Yang, Y. Y.; Wang, F. J.; Chung, T. S., Thermosensitive poly(N-isopropylacrylamide-co-acrylic acid) hydrogels with expanded network structures and improved oscillating swelling-deswelling properties. *Langmuir* **2002**, *18* (6), 2013-2018.
186. Brom, C. c. d.; Anac, I.; Roskamp, R.; Retsch, M.; Jonas, U.; Menges, B.; Preece, J. A., The swelling Behaviour of the Thermoresponsive Hydrogel-Silica Nanoparticle Composites. *in preparation* **2010**.
187. Matsuo, E. S.; Tanaka, T., Kinetics of discontinuous volume--phase transition of gels. *The Journal of Chemical Physics* **1988**, *89* (3), 1695-1703.
188. Gan, D. J.; Lyon, L. A., Fluorescence nonradiative energy transfer analysis of crosslinker heterogeneity in core-shell hydrogel nanoparticles. *Analytica Chimica Acta* **2003**, *496* (1-2), 53-63.
189. Zhang, N.; Knoll, W., Thermally Responsive Hydrogel Films Studied by Surface Plasmon Diffraction. *Analytical Chemistry* **2009**, *81* (7), 2611-2617.
190. Junk, M. J. N.; Jonas, U.; Hinderberger, D., EPR Spectroscopy Reveals Nanoinhomogeneities in the structure and reactivity of thermoresponsive hydrogels *Small* **2008**, *4* (9), 1485-1493.
191. Morrish, A. H.; Haneda, K., Surface Magnetic-Properties of Fine Particles. *Journal of Magnetism and Magnetic Materials* **1983**, *35* (1-3), 105-113.
192. Chen, J.; Yang, L. M.; Liu, Y. F.; Ding, G. W.; Pei, Y.; Li, J.; Hua, G. F.; Huang, J., Preparation and characterization of magnetic targeted drug controlled-release hydrogel microspheres. *Macromolecular Symposia* **2005**, *225*, 71-80.

193. Bergey, E. J.; Levy, L.; Wang, X. P.; Krebs, L. J.; Lal, M.; Kim, K. S.; Pakatchi, S.; Liebow, C.; Prasad, P. N., DC magnetic field induced magnetocytolysis of cancer cells targeted by LH-RH magnetic nanoparticles in vitro. *Biomedical Microdevices* **2002**, *4* (4), 293-299.
194. McHenry, M. E.; Laughlin, D. E., Nano-scale materials development for future magnetic applications. *Acta Materialia* **2000**, *48* (1), 223-238.
195. Wu, W.; He, Q. G.; Jiang, C. Z., Magnetic Iron Oxide Nanoparticles: Synthesis and Surface Functionalization Strategies. *Nanoscale Research Letters* **2008**, *3* (11), 397-415.
196. Wu, M.; Ma, Y.; Liu, Y.; Bi, O.; Fang, Q.; Niu, H.; Chen, Q., Chainlike assembly of magnetite coated with SiO₂ nanostructures induced by an applied magnetic field. *Materials Research Billeting* **2007**.
197. Alexiou, C.; Arnold, W.; Klein, R. J.; pARAK, F. G.; Hulin, P.; Bergemann, C.; Erhardt, W.; Wagenpfiel, S.; Lubbe, A. S., Locoregional cancer treatment with magnetic drug targeting. *Cancer Research* **200**, *60* (6641-8).
198. Rosensweig, R. E., Heating magnetic fluid with alternating magnetic field. *Journal of Magnetism and Magnetic Materials* **2002**, *252* (1-3), 370-374.
199. Jordan, A.; Scholz, R.; Wust, P.; Fahling, H.; Felix, R., Magnetic fluid hyperthermia (MFH): Cancer treatment with AC magnetic field induced excitation of biocompatible superparamagnetic nanoparticles. *Journal of Magnetism and Magnetic Materials* **1999**, *201*, 413-419.
200. Hergt, R.; Dutz, S.; Muller, R.; Zeisberger, M., Magnetic particle hyperthermia: nanoparticle magnetism and materials development for cancer therapy. *Journal of Physics-Condensed Matter* **2006**, *18* (38), S2919-S2934.
201. Glockl, G.; Hergt, R.; Zeisberger, M.; Dutz, S.; Nagel, S.; Weitschies, W., The effect of field parameters, nanoparticle properties and immobilization on the specific heating power in magnetic particle hyperthermia. *Journal of Physics-Condensed Matter* **2006**, *18* (38), S2935-S2949.
202. Ivkov, R.; DeNardo, S. J.; Daum, W.; Foreman, A. R.; Goldstein, R. C.; Nemkov, V. S.; DeNardo, G. L., Application of high amplitude alternating magnetic fields for heat induction of nanoparticles localized in cancer. *Clinical Cancer Research* **2005**, *11* (19), 7093S-7103S.
203. Caruntu, D.; Caruntu, G.; O'Connor, C. J., Magnetic properties of variable-sized Fe₃O₄ nanoparticles synthesized from non-aqueous homogeneous solutions of polyols. *Journal of Physics D-Applied Physics* **2007**, *40* (19), 5801-5809.
204. Schwind, M. Magnetic Ferrite Nanoparticles. Synthesis and Characterization of Ferrite Nanocrystals with Different Shapes and Elemental Compositions. Gutenberg Universität, Mainz, 2008.
205. Song, Q.; Zhang, Z. J., Correlation between spin-orbital coupling and the superparamagnetic properties in magnetite and cobalt ferrite spinel nanocrystals. *Journal of Physical Chemistry B* **2006**, *110* (23), 11205-11209.
206. Goya, G. F.; Berquo, T. S.; Fonseca, F. C.; Morales, M. P., Static and dynamic magnetic properties of spherical magnetite nanoparticles. *Journal of Applied Physics* **2003**, *94* (5), 3520-3528.

207. Stoner, E. C.; Wohlfarth, E. P., A Mechanism of Magnetic Hysteresis in Heterogeneous Alloys. *IEEE Transactions on Magnetics* **1991**, *27*, 3475-3518.
208. Liu, Y.; Sellmyer, D. J.; Shindo, D., *Handbook of advanced magnetic materials Volume 1. Nanostructural effects*. 2006.
209. Roca, A. G.; Morales, M. P.; O'Grady, K.; Serna, C. J., Structural and magnetic properties of uniform magnetite nanoparticles prepared by high temperature decomposition of organic precursors. *Nanotechnology* **2006**, *17* (11), 2783-2788.
210. Park, J.; An, K. J.; Hwang, Y. S.; Park, J. G.; Noh, H. J.; Kim, J. Y.; Park, J. H.; Hwang, N. M.; Hyeon, T., Ultra-large-scale syntheses of monodisperse nanocrystals. *Nature Materials* **2004**, *3* (12), 891-895.
211. Guskos, N.; Glenis, S.; Likodimos, V.; Typek, J.; Maryniak, M.; Roslaniec, Z.; Kwiatkowska, M.; Baran, M.; Szymczak, R.; Petridis, D., Matrix effects on the magnetic properties of gamma-Fe₂O₃ nanoparticles dispersed in a multiblock copolymer. *Journal of Applied Physics* **2006**, *99* (8), -.
212. Wang, X. M.; Gu, H. C.; Yang, Z. Q., The heating effect of magnetic fluids in an alternating magnetic field. *Journal of Magnetism and Magnetic Materials* **2005**, *293* (1), 334-340.
213. Hergt, R.; Hiergeist, R.; Zeisberger, M.; Glockl, G.; Weitschies, W.; Ramirez, P.; Hilger, I.; Kaiser, W. A., Enhancement of AC-losses of magnetic nanoparticles for heating applications. *Journal of Magnetism and Magnetic Materials* **2004**, *280* (2-3), 358-368.
214. Hergt, R.; Hiergeist, R.; Hilger, I.; Kaiser, W. A.; Lapatnikov, Y.; Margel, S.; Richter, U., Maghemite nanoparticles with very high AC-losses for application in RF-magnetic hyperthermia. *Journal of Magnetism and Magnetic Materials* **2004**, *270* (3), 345-357.
215. Chemla, Y. R.; Crossman, H. L.; Poon, Y.; McDermott, R.; Stevens, R.; Alper, M. D.; Clarke, J., Ultrasensitive magnetic biosensor for homogeneous immunoassay. *Proceedings of the National Academy of Sciences of the United States of America* **2000**, *97* (26), 14268-14272.
216. Ma, M.; Wu, Y.; Zhou, H.; Sun, Y. K.; Zhang, Y.; Gu, N., Size dependence of specific power absorption of Fe₃O₄ particles in AC magnetic field. *Journal of Magnetism and Magnetic Materials* **2004**, *268* (1-2), 33-39.
217. Murray, C. B.; Kagan, C. R.; Bawendi, M. G., Synthesis and characterization of monodisperse nanocrystals and close-packed nanocrystal assemblies. *Annual Review of Materials Science* **2000**, *30*, 545-610.
218. Yamamuro, S.; Farrell, D. F.; Majetich, S. A., Direct imaging of self-assembled magnetic nanoparticle arrays: Phase stability and magnetic effects on morphology. *Physical Review B* **2002**, *65* (22), -.
219. Whetten, R. L.; Shafiqullin, M. N.; Khoury, J. T.; Schaaff, T. G.; Vezmar, I.; Alvarez, M. M.; Wilkinson, A., Crystal structures of molecular gold nanocrystal arrays. *Accounts of Chemical Research* **1999**, *32* (5), 397-406.
220. Talapin, D. V.; Shevchenko, E. V.; Kornowski, A.; Gaponik, N.; Haase, M.; Rogach, A. L.; Weller, H., A new approach to crystallization of CdSe nanoparticles into ordered three-dimensional superlattices. *Advanced Materials* **2001**, *13* (24), 1868-+.

221. Murray, C. B.; Kagan, C. R.; Bawendi, M. G., Self-Organization of CdSe Nanocrystallites into 3-Dimensional Quantum-Dot Superlattices. *Science* **1995**, *270* (5240), 1335-1338.
222. Farrell, D.; Cheng, Y.; Kan, S.; Sachan, M.; Ding, Y.; Majetich, S. A.; Yang, L., Iron nanoparticle assemblies: structures and magnetic behavior. *Fifth International Conference on Fine Particle Magnetism* **2005**, *17*, 185-195
206.
223. Murray, C. B.; Sun, S. H.; Doyle, H.; Betley, T., Monodisperse 3d transition-metal (Co, Ni, Fe) nanoparticles and their assembly into nanoparticle superlattices. *Mrs Bulletin* **2001**, *26* (12), 985-991.
224. Song, Q.; Ding, Y.; Wang, Z. L.; Zhang, Z. J., Formation of orientation-ordered superlattices of magnetite magnetic nanocrystals from shape-segregated self-assemblies. *Journal of Physical Chemistry B* **2006**, *110* (50), 25547-25550.
225. Zheng, R. K.; Gu, H. W.; Xu, B.; Fung, K. K.; Zhang, X. X.; Ringer, S. P., Self-assembly and self-orientation of truncated octahedral magnetite nanocrystals. *Advanced Materials* **2006**, *18* (18), 2418-+.
226. Satarkar, N. S.; Hilt, J. Z., Hydrogel nanocomposites as remote-controlled biomaterials. *Acta Biomaterialia* **2008**, *4* (1), 11-16.
227. Osterman, N.; Poberaj, I.; Dobnikar, J.; Frenkel, D.; Zihlerl, P.; Babic, D., Field-Induced Self-Assembly of Suspended Colloidal Membranes. *Physical Review Letters* **2009**, *103* (22), -
228. Abramchuk, S.; Kramarenko, E.; Grishin, D.; Stepanov, G.; Nikitin, L. V.; Filipcsei, G.; Khokhlov, A. R.; Zrinyi, M., Novel highly elastic magnetic materials for dampers and seals: part II. Material behavior in a magnetic field. *Polymers for Advanced Technologies* **2007**, *18* (7), 513-518.
229. Abramchuk, S.; Kramarenko, E.; Stepanov, G.; Nikitin, L. V.; Filipcsei, G.; Khokhlov, A. R.; Zrinyi, M., Novel highly elastic magnetic materials for dampers and seals: Part I. Preparation and characterization of the elastic materials. *Polymers for Advanced Technologies* **2007**, *18* (11), 883-890.
230. Pavan Kumar, V. S.; Jagadeesh Babu, V.; Raghuraman, G. K.; Dhamodharan, R.; Natarajan, T. S., Giant magnetoresistance of Fe₃O₄-polymethylmethacrylate nanocomposite aligned fibers via electrospinning. *Journal of Applied Physics* **2007**, *101* (11), -.
231. Godovsky, D. Y.; Varfolomeev, A. V.; Efremova, G. D.; Cherepanov, V. M.; Kapustin, G. A.; Volkov, A. V.; Moskvina, M. A., Magnetic properties of polyvinyl alcohol-based composites containing iron oxide nanoparticles. *Advanced Materials for Optics and Electronics* **1999**, *9* (3), 87-93.
232. Szabo, D.; Barsi, L.; Buki, A.; Zrinyi, M., Studies on nonhomogeneous deformation in magnetic field sensitive gels. *Ach-Models in Chemistry* **1997**, *134* (2-3), 155-167.
233. Zrinyi, M.; Barsi, L.; Buki, A., Deformation of ferrogels induced by nonuniform magnetic fields. *Journal of Chemical Physics* **1996**, *104* (21), 8750-8756.

234. Zrinyi, M.; Barsi, L.; Szabo, D.; Kilian, H. G., Direct observation of abrupt shape transition in ferrogels induced by nonuniform magnetic field. *Journal of Chemical Physics* **1997**, *106* (13), 5685-5692.
235. Shamim, N.; Hong, L.; Hidajat, K.; Uddin, M. S., Thermosensitive-polymer-coated magnetic nanoparticles: Adsorption and desorption of bovine serum albumin. *Journal of Colloid and Interface Science* **2006**, *304* (1), 1-8.
236. Ang, K. L.; Venkatraman, S.; Ramanujan, R. V., Magnetic PNIPA hydrogels for hyperthermia applications in cancer therapy. *Materials Science & Engineering C-Biomimetic and Supramolecular Systems* **2007**, *27* (3), 347-351.
237. Kato, N.; Yamanobe, S.; Takahashi, F., Property of magneto-driven poly (N-isopropylacrylamide) gel containing gamma-Fe₂O₃ in NaCl solution as a chemomechanical device. *Materials Science & Engineering C-Biomimetic and Supramolecular Systems* **1997**, *5* (2), 141-147.
238. Schmidt, A. M., Electromagnetic activation of shape memory polymer networks containing magnetic nanoparticles. *Macromolecular Rapid Communications* **2006**, *27* (14), 1168-1172.
239. Lattermann, G.; Krekhova, M., Thermoreversible ferrogels. *Macromolecular Rapid Communications* **2006**, *27* (16), 1373-1379.
240. Guo, J.; Yang, W. L.; Deng, Y. H.; Wang, C. C.; Fu, S. K., Organic-dye-coupled magnetic nanoparticles encaged inside thermoresponsive PNIPAM microcapsules. *Small* **2005**, *1* (7), 737-743.
241. Frimpong, R. A.; Fraser, S.; Hilt, J. Z., Synthesis and temperature response analysis of magnetic-hydrogel nanocomposites. *Journal of Biomedical Materials Research Part A* **2007**, *80A* (1), 1-6.
242. Lin, C. L.; Chiu, W. Y., Thermally responsive complex polymer networks containing Fe₃O₄ nanoparticles: Composition/morphology/property relationship. *Journal of Polymer Science Part a-Polymer Chemistry* **2005**, *43* (23), 5923-5934.
243. Pich, A.; Bhattacharya, S.; Lu, Y.; Boyko, V.; Adler, H. A. P., Temperature-sensitive hybrid microgels with magnetic properties. *Langmuir* **2004**, *20* (24), 10706-10711.
244. Deng, Y. H.; Wang, C. C.; Shen, X. Z.; Yang, W. L.; An, L.; Gao, H.; Fu, S. K., Preparation, characterization, and application of multistimuli-responsive microspheres with fluorescence-labeled magnetic cores and thermoresponsive shells. *Chemistry-a European Journal* **2005**, *11* (20), 6006-6013.
245. Zhang, J. L.; Srivastava, R. S.; Misra, R. D. K., Core-shell magnetite nanoparticles surface encapsulated with smart stimuli-responsive polymer: Synthesis, characterization, and LCST of viable drug-targeting delivery system. *Langmuir* **2007**, *23* (11), 6342-6351.
246. Lai, J. J.; Hoffman, J. M.; Ebara, M.; Hoffman, A. S.; Estournes, C.; Wattiaux, A.; Stayton, P. S., Dual magnetic-/temperature-responsive nanoparticles for microfluidic separations and assays. *Langmuir* **2007**, *23* (13), 7385-7391.
247. Correa-Duarte, M. A.; Giersig, M.; Kotov, N. A.; Liz-Marzan, L. M., Control of packing order of self-assembled monolayers of magnetite nanoparticles with and without SiO₂ coating by microwave irradiation. *Langmuir* **1998**, *14* (22), 6430-6435.

248. Crisp, M. T.; Kotov, N. A., Preparation of nanoparticle coatings on surfaces of complex geometry. *Nano Letters* **2003**, *3* (2), 173-177.
249. Gates, B.; Xia, Y. N., Photonic crystals that can be addressed with an external magnetic field. *Advanced Materials* **2001**, *13* (21), 1605-+.
250. Grigoriev, D.; Gorin, D.; Sukhorukov, G. B.; Yashchenok, A.; Maltseva, E.; Mohwald, H., Polyelectrolyte/magnetite nanoparticle multilayers: Preparation and structure characterization. *Langmuir* **2007**, *23* (24), 12388-12396.
251. Mamedov, A.; Ostrander, J.; Aliev, F.; Kotov, N. A., Stratified assemblies of magnetite nanoparticles and montmorillonite prepared by the layer-by-layer assembly. *Langmuir* **2000**, *16* (8), 3941-3949.
252. Bryant, S. J.; Nuttelman, C. R.; Anseth, K. S., Cytocompatibility of UV and visible light photoinitiating systems on cultured NIH/3T3 fibroblasts in vitro. *Journal of Biomaterials Science-Polymer Edition* **2000**, *11* (5), 439-457.
253. Thompson, D. W.; Snyder, P. G.; Castro, L.; Yan, L.; Kaipa, P.; Woollam, J. A., Optical characterization of porous alumina from vacuum ultraviolet to midinfrared. *Journal of Applied Physics* **2005**, *97* (11), -.
254. Xiong, Y. M.; Synder, P. G.; Woollam, J. A.; Aljumaily, G. A.; Gagliardi, F. J.; Krosche, E. R., Controlled Index of Refraction Silicon Oxynitride Films Characterized by Variable Angle Spectroscopic Ellipsometry. *Thin Solid Films* **1991**, *206* (1-2), 248-253.
255. Wing, Z. N.; Wang, B.; Halloran, J. W., Permittivity of porous titanate dielectrics. *Journal of the American Ceramic Society* **2006**, *89* (12), 3696-3700.
256. Zeng, H.; Sun, S. H., Syntheses, properties and potential applications of multicomponent magnetic nanoparticles. *Advanced Functional Materials* **2008**, *18* (3), 391-400.
257. Burda, C.; Chen, X.; Narayanan, R.; El-Sayed, M. A., Chemistry and Properties of Nanocrystals of different shapes. *Chemical Reviews* **2005**, *105* (1025-1102).
258. Daniel, M.-C.; Astruc, D., Gold nanoparticles: Assembly, supramolecular chemistry, quantum-size-related properties, and applications towards Biology, Catalysis, and Nanotechnology. *Chemical Reviews* **2004**, *104*, 293-346.
259. Yu, B. L.; Zhu, C. S.; Gan, F. X., Large nonlinear optical properties of Fe₂O₃ nanoparticles. *Physica E-Low-Dimensional Systems & Nanostructures* **2000**, *8* (4), 360-364.
260. Shannon, R. D.; Shannon, R. C.; Medenbach, O.; Fischer, R. X., Refractive index and dispersion of fluorides and oxides. *Journal of Physical and Chemical Reference Data* **2002**, *31* (4), 931-970.
261. Ziolo, R. F.; Giannelis, E. P.; Weinstein, B. A.; Ohoro, M. P.; Ganguly, B. N.; Mehrotra, V.; Russell, M. W.; Huffman, D. R., Matrix-Mediated Synthesis of Nanocrystalline Gamma-Fe₂O₃ - a New Optically Transparent Magnetic Material. *Science* **1992**, *257* (5067), 219-223.
262. Filipcsei, G.; Csetneki, I.; Szilagyi, A.; Zrinyi, M., Magnetic field-responsive smart polymer composites. *Oligomers Polymer Composites Molecular Imprinting* **2007**, *206*, 137-189.

263. Kilian, H. G.; Schenk, H.; Wolff, S., Large Deformation in Filled Networks of Different Architecture and Its Interpretation in Terms of the Van Der Waals Network Model. *Colloid and Polymer Science* **1987**, *265* (5), 410-423.
264. Junk, M. J. N.; Berger, R.; Jonas, U., Atomic Force Spectroscopy of Thermoresponsive Photo-Cross-Linked Hydrogel Films. *Langmuir*.
265. FEMLAB <http://www.comsol.com/>.

Publications and Presentations

PUBLICATIONS

Nuria Queralto, Luis Heritier, Robert Roskamp, Rüdiger Berger, Wolfgang Knoll
"Study of Poly N-isopropylacrylamide hydrogel thin film through nanomechanical cantilever sensors: pH effects and temperature" in preparation (Chapter 4.1)

Nuria Queralto, Robert Roskamp, Wolfgang Knoll "Thin film ferrogel study" in preparation (Chapter 4.2 and 4.3)

Luis Duque, Nuria Queralto, Laia Francesch, G.G. Bumbu, Salvador Borros, Rüdiger Berger and Renate Förch. "Properties of plasma polymerized pentafluorophenyl methacrylate" *Plasma Processes and Polymers*, in press

Diego Pallarola, Nuria Queralto, Fernando Battaglini and Omar Azzaroni
"Supramolecular Assembly of Glucose Oxidase on Concanavalin A-Modified Gold Electrodes" *Physical Chemistry Chemical Physics*, in press.

Diego Pallarola, Nuria Queralto, Wolfgang Knoll, Marcelo Ceolín, Omar Azzaroni and Fernando Battaglini. "Redox-Active Concanavalin A: Synthesis, Characterization and Recognition-Driven Assembly of Interfacial Architectures for Bioelectronic Applications" *Langmuir*, submitted

Mark E. Roberts, Nuria Queralto, Stefan C. B. Mannsfeld, Benjamin N. Reinecke, Wolfgang Knoll, and Zhenan Bao "Cross-Linked Polymer Gate Dielectric Films for Low-Voltage Organic Transistors" *Chem. Mater.* 2009, 21, 2292–2299

Mark E. Roberts, Stefan C. B. Mannsfeld, Núria Queraltó, Colin Reese, Jason Locklin, Wolfgang Knoll and Zhenan Bao "Water-stable organic transistors and their application in chemical and biological sensors" *PNAS*, 2008, 105, 34, 12134-12139

Nuria Queralto, Gabriela G. Bumbu, Laia Francesch, Wolfgang Knoll, Salvador Borros, Rüdiger Berger, Renate Förch. "Investigation into the Chemical Reactivity of Plasma-Deposited Perfluorophenyl Methacrylate Using Infrared Reflection Absorption Spectroscopy and Microcantilever Studies." *Plasma Processes and Polymers* Volume 4, Issue S1, Date: April 2007, Pages: S790-S793

B. R. Rogers, Z. Song, J. Marschall, N. Queraltó, and C. A. Zorman, "The Effect of Dissociated Oxygen on the Oxidation of Si, Polycrystalline SiC and LPCVD Si₃N₄," in *High Temperature Corrosion and Materials Chemistry V*, edited by E. Opila *et al.*, The Electrochemical Society Proceedings Series, Pennington, New Jersey, 2004.

PRESENTATIONS

N.Queralto "Towards magnetic hydrogels" Workshop: Magnetic Nanoparticles and Magnetic Soft Matter. MPI for Polymer Research, Mainz, Deutschland January 2008

Mark E. Roberts, Núria Queraltó, Wolfgang Knoll, and Zhenan Bao "Dielectric Materials for Low Operating Voltage Organic Thin-Film Transistors" AICHE Annual Meeting, 2006.

N. Queralto, L. Francesch, L. Chu, S. Borros, R. Berger, G. Bumbu, W. Knoll and R. Förch, "Reactions at plasma polymer/ liquid interfaces" Plasma Surface Engineering conference (PSE 2006) in September.

Poster contributions

N. Queralto, G. Bumbu, L. Francesch, S. Borros, W. Knoll, R. Berger, R. Förch "Infrared Reflection Absorption Spectroscopy and Microcantilever studies of chemical reactions at plasma polymer film surfaces." Workshop Micromechanical Cantilevers MPIP (Mainz, Germany) 2008

Núria Queraltó, Beinn V.O. Muir, Shuhua Liu, Wolfgang Knoll, Curtis W. Frank "Properties of magnetic nanoparticles-thermoreponsive hydrogel composite materials" Workshop Center on Polymer Interfaces and Macromolecular Assemblies (CPIMA) Stanford, CA. August 2007

N. Queralto Gratacos, M. Roberts, W. Knoll, Z. Bao "Towards Planar and Smooth Microarray Electrodes." MRS Spring Meeting 2007 (Poster)

Mark E. Roberts¹, Nuria Queralto^{2,1}, Stefan C.B. Mannsfeld¹, Zhenan Bao¹ and Wolfgang Knoll² „Dielectric Materials for Low Operating Voltage Organic Thin-film Transistors.“ MRS Spring Meeting 2007 (Poster)
